

OFFSET ATTACHING PLANAR JETS WITH AND WITHOUT A CO-FLOWING JET

OFFSET ATTACHING PLANAR JETS WITH AND WITHOUT A CO-FLOWING JET

By

NAN GAO, M.ENG., B.ENG.

A Thesis

Submitted to the School of Graduate Studies

in Partial Fulfilment of the Requirements

for the Degree

Doctor of Philosophy

McMaster University

© Copyright by Nan Gao, November 2006

DOCTOR OF PHILOSOPHY (2006)
(Mechanical Engineering)

MCMASTER UNIVERSITY
Hamilton, Ontario

TITLE: Offset Attaching Planar Jets With and Without a Co-Flowing
Jet

AUTHOR: Nan Gao
M. Eng.(Mechanical Engineering)
McMaster University, Hamilton, Canada, 2000
B. ENG.(Thermal Engineering)
Tsinghua University, Beijing, China, 1997

SUPERVISOR: Drs. Dan Ewing and Chan Y. Ching

NUMBER OF PAGES: xxvii, 183

To my grandmother and my parents

Acknowledgements

The author wishes to express his gratitude to his supervisors Dr. Dan Ewing and Dr. Chan Ching for their guidance and constant encouragement throughout the course of this study. The author would like to thank other members of the supervisory committee Dr. Nicholas Kevlahan and Dr. John Vlachopoulos for their valuable suggestions and comments in the last few years. The author would also like to give sincere thanks to Dr. Jonathan W. Naughton for his guidance in the measurements of skin friction and providing the software.

The author also appreciates Dr. Joe Hall and Dr. Hongguang Sun for their work in building some of the instrumentation used here. Gratitude is also extended to the technicians Mr. Ron Lodewyks, Mr. Mark MacKenzie, Mr. Jim McLaren, Mr. Dave Schick, and Mr. Joe Verhaeghe for their kindly help. The author also thanks the financial support from the Natural Sciences and Engineering Research Council of Canada.

Abstract

An experimental study of turbulent planar offset attaching jets with and without a co-flowing jet was performed for jets with offset distances less than approximately 1.0 jet height and Reynolds numbers of 21 800 to 54 500. The development of the jets were characterized using the measurements of the flow velocities, static and fluctuating wall pressure, skin friction and heat transfer. The development of the large scale flow structures was also characterized using the two-point and two-time measurements of the wall pressure and velocity fluctuations.

The results show that the initial development of the offset attaching jets can be divided into 5 different regions, three associated with the reattachment process and two associated with the wall jet. The measurements showed three characteristic motions in the offset attaching jets. Upstream of the reattachment point, the fluctuations are predominantly determined by the downstream propagating large scale flow structures in the inner shear layer. There is also evidence of upstream propagating low frequency motions that seem to be in the recirculation region and a very low frequency flapping motion. After the reattachment, the inner shear layer structures gradually merge with wall jet like structures that formed away from the wall and these merged structures convect downstream similar to the flow structures in a developed planar wall jet.

The results showed that the effect of the co-flowing jet depends on the velocity, mass, momentum flux and the size of the jet. The fluctuations in the inner shear layer decrease when a co-flowing jet with a velocity less than 20% of the main jet velocity is added. When the velocity of the inner jet is more than 20% of the main jet velocity there is evidence that wake like structures form downstream of the splitter plate between the jets. In the case when the size of the inner jet is half of the main jet, the fluctuating wall pressure and the heat transfer continue to decrease when the inner jet velocity increases despite a large increase in the vertical fluctuating velocity in the attaching shear layer. This is different

from the case where the inner jet height is 18% of the main jet height, where the fluctuating pressure and heat transfer increase with the inner jet velocity. In this case, the frequencies of the wake like structures and inner shear layer structures seem to coincide resulting in strong structures that interact with the wall, dramatically increasing the fluctuating wall pressure and heat transfer.

Nomenclature

| | |
|----------|--|
| C_P | Static wall pressure coefficient, $2(P - P_\infty)/\rho U_U^2$ |
| $C_{p'}$ | Fluctuating wall pressure coefficient, $2p'/\rho U_U^2$ |
| C_f | Skin friction coefficient, $2\tau_w/\rho U_U^2$ |
| c_p | Specific heat of air, J/kgK |
| f | Frequency, Hz |
| f_F | Forcing frequency, Hz |
| F_{uu} | Power spectrum of the streamwise fluctuating velocity, $(m/s)^2/Hz$ |
| F_{vv} | Power spectrum of the vertical fluctuating velocity, $(m/s)^2/Hz$ |
| F_{pp} | Power spectrum of the fluctuating pressure, Pa^2/Hz |
| F_{pu} | Cross spectrum of the fluctuating pressure and the streamwise velocity, $Pa(m/s)/Hz$ |
| F_{pv} | Cross spectrum of the fluctuating pressure and the vertical velocity, $Pa(m/s)/Hz$ |
| H_c | Height of the splitter plate between the two jets, m |
| H_s | Offset distance from the lower edge of the outer jet to the wall, m |
| H_j | Height of the outer jet, m |
| H'_j | Height of the inner jet, m |
| h | Convective heat transfer coefficient, W/m^2K |
| h_f | Thickness of the oil-film, m |
| m | Mass flow rate at the exit of the outer jet per unit width, kg/sm |
| m' | Mass flow rate at the exit of the inner jet per unit width, kg/sm |
| M | Momentum flux at the exit of the outer jet per unit width, kg/s^2 |
| M' | Momentum flux at the exit of the inner jet per unit width, kg/s^2 |
| Nu | Nusselt number, hH_j/k_a |
| P | Static pressure, Pa |
| p' | RMS value of the fluctuating wall pressure, Pa |
| q | Dynamic head of the outer jet, $\rho U_U^2/2, Pa$ |

| | |
|----------------------|---|
| \hat{p} | Fourier transform of the fluctuating wall pressure, Pa/Hz |
| \hat{p}^* | Complex conjugate of \hat{p} , Pa/Hz |
| \dot{q}_{conv} | Convective heat flux to the flow over the foil, W/m^2 |
| \dot{q}_{elec} | Total Joulean heating, W/m^2 |
| \dot{q}_{rad} | Radiation heat loss from the foil, W/m^2 |
| R_{pp} | Correlation of fluctuating wall pressure, Pa^2 |
| Re | Reynolds number of the outer jet, $U_U H_j / \nu$ |
| Re' | Reynolds number of the inner jet, $U_L H'_j / \nu$ |
| St | Stanton number, $h / \rho c_p U_U$ |
| T_j | Jet temperature, K |
| T_w | Foil temperature, K |
| t | Time, s |
| U | Streamwise component of the local mean velocity, m/s |
| U_c | Mean convection velocity of the fluctuations, m/s |
| U_L | Flow rate averaged velocity of the inner jet at the exit, m/s |
| U_{max} | Maximum local mean streamwise velocity, m/s |
| U'_o | Maximum mean streamwise velocity at the exit of the inner jet, m/s |
| U_o | Maximum mean streamwise velocity at the exit of the outer jet, m/s |
| U_U | Flow rate averaged velocity of the outer jet at the exit, m/s |
| U_∞ | Free stream velocity, m/s |
| u' | RMS value of the streamwise component of the velocity fluctuations, m/s |
| $u'_{i,max}$ | Maximum u' along the inner shear layer, m/s |
| $u'_{o,max}$ | Maximum u' along the outer shear layer, m/s |
| $\langle uv \rangle$ | Turbulent Reynolds shear stress, m^2/s^2 |
| V | Vertical component of the local mean velocity, m/s |
| v' | RMS value of the vertical component of the velocity fluctuations, m/s |
| X_r | Attachment length, m |

| | |
|---------------|--|
| x | Spatial coordinate in the streamwise direction, m |
| x_1 | Location of the reference microphone in the two-point measurements, m |
| x_2 | Location of the second microphone in the two-point measurements, m |
| y | Spatial coordinate in the vertical direction, m |
| $y_{+1/2}$ | Outer half width of the jet, m |
| y_{max} | Distance from the location with U_{max} to the wall, m |
| z | Spatial coordinate in the cross-stream direction, m |
| δ | Boundary layer thickness of the incoming flow, m |
| Φ | Single line cross spectrum of fluctuating pressure, Pa^2/Hz |
| γ_{pp} | Coherence of the fluctuating wall pressure |
| γ_{pv} | Coherence of the fluctuating wall pressure and the fluctuating vertical velocity |
| ν | Kinematic viscosity of air, m^2/s |
| ρ | Density of air, kg/m^3 |
| ρ_{pp} | Correlation coefficient of fluctuating wall pressure |
| ρ_{pu} | Correlation coefficient of fluctuating wall pressure and streamwise fluctuating velocity |
| ρ_{pv} | Correlation coefficient of fluctuating wall pressure and vertical fluctuating velocity |
| τ | Time interval, s |
| τ_w | Skin friction, Pa |
| θ | Momentum thickness of the incoming flow, m |
| θ_{pp} | Phase angle of the cross spectrum for the fluctuating wall pressure, rad |
| θ_{pv} | Phase angle of the pressure-vertical velocity cross spectrum, rad |
| ξ | Uncertainty due to the sampling time |

Contents

| | | |
|----------|---|-----------|
| 1 | Introduction | 1 |
| 2 | Literature Review | 4 |
| 2.1 | Offset Attaching Jets | 4 |
| 2.2 | Flow Control Using a Co-flowing Jet | 8 |
| 2.2.1 | Flow field produced by dual-lip air ring | 8 |
| 2.2.2 | Counter-current shear control in combustion chamber | 10 |
| 2.2.3 | Radial reattaching jet with co-flow | 11 |
| 2.2.4 | Other flows controlled using constant injection | 12 |
| 2.3 | Other Generic Reattaching Flows | 13 |
| 2.3.1 | Size of the separation bubble | 13 |
| 2.3.2 | Static wall pressure | 14 |
| 2.3.3 | Skin friction | 15 |
| 2.3.4 | Turbulence quantities and heat transfer | 16 |
| 2.3.5 | Periodic forcing of a separated shear layer | 20 |
| 3 | Experimental Methodology | 27 |
| 3.1 | Experimental Facility | 27 |
| 3.2 | Hotwire anemometry | 30 |
| 3.2.1 | Calibration | 31 |

| | | |
|----------|---|------------|
| 3.2.2 | Errors in hot-wire measurements | 33 |
| 3.3 | Static and fluctuating wall pressure measurements | 38 |
| 3.4 | Skin friction measurements | 42 |
| 3.5 | Heat transfer measurements | 46 |
| 4 | Offset Attaching Planar Jets - Single Point Measurements | 50 |
| 4.1 | Effect of Offset Distance | 50 |
| 4.1.1 | Effect of Offset Distance on the Mean Flow Field | 50 |
| 4.1.2 | Effect of Offset Distance on the Fluctuating Flow Field | 57 |
| 4.2 | Effect of Reynolds number | 67 |
| 5 | Large Scale Flow Structures in Offset Attaching Planar Jets | 73 |
| 5.1 | Single point spectral measurements | 73 |
| 5.2 | Two-point two-time pressure measurements | 77 |
| 5.2.1 | Transition from a reattaching flow to a planar wall jet | 77 |
| 5.2.2 | Dominant motions in the reattaching region | 84 |
| 5.3 | Two-point two-time pressure-velocity measurements | 92 |
| 6 | Co-flowing Jets - Single Point Measurements | 108 |
| 6.1 | Offset jet with a co-flowing jet of $H'_j/H_j = 0.5$ | 108 |
| 6.2 | Single point spectral measurements | 117 |
| 6.3 | Offset jet with a co-flowing jet of $H'_j/H_j = 0.18$ | 122 |
| 6.4 | Effect of mass flow and momentum flux ratios | 129 |
| 7 | Co-flowing Jets - Multi-point Measurements | 132 |
| 7.1 | Effect of co-flowing jet with $U'_o/U_o \leq 0.2$ | 132 |
| 7.2 | Effect of co-flowing jet with velocity $U'_o/U_o \geq 0.35$ | 141 |
| 7.2.1 | Offset jet with a co-flowing jet of $H'_j/H_j = 0.5$ | 141 |
| 7.2.2 | Offset jet with a co-flowing jet of $H'_j/H_j = 0.18$ | 145 |

| | |
|---|------------|
| 8 Conclusions | 150 |
| 9 Recommendations | 155 |
| Appendices | 169 |
| Appendix A: Velocity profiles of the offset and free jets | 170 |
| Appendix B: Heat flux losses | 176 |
| Appendix C: Uncertainties in Stanton number | 178 |
| Appendix D: POD analysis of fluctuating wall pressure for an offset attaching jet with $H_s/H_j = 1$ | 181 |

List of Tables

| | | |
|-----|--|-----|
| 2.1 | Summary of experimental investigations of offset planar jet. | 21 |
| 2.2 | Summary of investigations on the dynamics of reattaching shear layers over a bluff body. | 22 |
| 2.2 | continued | 23 |
| 2.3 | Summary of investigations on the flow over a backward facing step after 1980. | 24 |
| 2.3 | continued | 25 |
| 2.3 | continued | 26 |
| 3.1 | Cross-flow errors in hot-wire measurements (Shabbir <i>et al.</i> , 1996) | 35 |
| 4.1 | Summary of flow parameters of single offset jet. | 63 |
| 5.1 | Summary of characteristic motions in offset attaching jets | 107 |
| 6.1 | Summary of flow parameters of offset jet with a co-flowing jet. | 109 |

List of Figures

| | | |
|-----|---|----|
| 1.1 | Schematics of the dual jet air ring used in blown film manufacturing process. | 2 |
| 2.1 | Attachment length measured by ● Lund (1986) and modeled by — Bourque (1967) | 5 |
| 2.2 | Schematics of the offset jets used by (a) Sawyer (1960), (b) Lund (1986), (c) Nozaki <i>et al.</i> (1979, 1981) and (d) Nasr & Lai (1997, 1998) | 6 |
| 2.3 | Schematic of the coutercurrent shear control of a backward facing step used by Forliti & Strykowski (2005) | 10 |
| 2.4 | Schematic of the control of radial reattaching jet using steady co-flowing jet by Tanaka <i>et al.</i> (1986 <i>a,b,c</i>) | 11 |
| 2.5 | Schematic of the flows over (a) a backward facing step, (b) a blunt plate and (c) a splitter plate with fence | 14 |
| 2.6 | Spectra of the fluctuating wall pressure and the fluctuating skin friction (Spazzini <i>et al.</i> , 2001) for flow over — a backward facing step and —— a bluff body measured at (a) $x/X_r \approx 1$ (b) $x/X_r \lesssim 0.25$ | 18 |
| 3.1 | Schematic of the experimental facility, units in cm. | 28 |
| 3.2 | Schematics of the experimental facility | 30 |
| 3.3 | Cross-wire geometry | 32 |
| 3.4 | Schematic showing rectification using a cross-wire probe | 34 |
| 3.5 | Scatter plots of effective cooling velocities at (a) $x/H_j = 4$, $y/H_j = 0.4$ (b) $x/H_j = 5$, $y/H_j = 0.4$ in an offset attaching jet with $H_s/H_j=1$ | 34 |

| | | |
|------|---|----|
| 3.6 | Estimation of cross flow errors in (a) the streamwise mean velocity and (b) the mean square value of the streamwise fluctuating velocity in an offset attaching jet with $H_s/H_j = 1.0$ and $Re = 44000$ | 36 |
| 3.7 | Estimated errors due to limited sampling time for 95% confidence interval in (a) the streamwise mean velocity and (b) the mean square value of the streamwise fluctuating velocity in an offset attaching jet with $H_s/H_j = 1.0$ and $Re = 44000$ | 37 |
| 3.8 | Sketch of typical frequency response curve of Panasonic WM-61B microphones given by the manufacturer (Panasonic, 2006). | 40 |
| 3.9 | Schematic showing how the microphone was embedded in the wall. | 41 |
| 3.10 | The spectra of fluctuating wall pressure near the reattachment location, $x/H_j = 4.5$, for the jet with $H_s/H_j = 1$ measured using a microphone flush mounted on the wall and through the pinhole. | 41 |
| 3.11 | Schematic of the setup for the oil-film interferometry measurements. | 44 |
| 3.12 | Typical fringe patterns (a) in the recirculation region, (b) near the attachment point and (c) downstream of the attachment point. | 44 |
| 3.13 | A model with known geometry and reference points was used to reduce the photogrammetry error. | 46 |
| 3.14 | Schematic of the heat transfer facility | 47 |
| 4.1 | Changes in the attachment location with the offset distance for the \circ 3.8cm height jet, the \triangle 1.9cm jet and the attachment location reported by \bullet Lund (1986). | 51 |
| 4.2 | Profiles of the mean streamwise velocity in the region $x/H_j \leq 6$ for jets with $H_s/H_j =$ (a) 0, (b) 0.2, (c) 0.6 and (d) 1.0. | 52 |
| 4.3 | Profiles of the mean streamwise velocity in the region $x/H_j \geq 6$ for offset ratio of — 0, \circ 0.2, \square 0.6 and \triangle 1.0. | 52 |

| | | |
|------|--|----|
| 4.4 | Changes in the jet half width with streamwise position for jets with offset ratio of $\circlearrowleft 0$, $\square 0.2$, $\triangle 0.4$, $\triangledown 0.6$, $\diamond 0.8$ and $* 1$ in term of (a) x/X_r and (b) x/H_j (from the single wire measurements). | 53 |
| 4.5 | Changes in the maximum local mean velocity for jets with offset ratio of $\circlearrowleft 0$, $\square 0.2$, $\triangle 0.4$, $\triangledown 0.6$, $\diamond 0.8$ and $* 1$ in term of (a) x/X_r and (b) x/H_j (from the single wire measurements). | 54 |
| 4.6 | Distribution of the static wall pressure coefficient for jets with $H_s/H_j = \triangle 0.2 \square 0.4 \triangledown 0.6 \diamond 0.8$ and $\circlearrowleft 1.0$, and \bullet for a flow over a backward facing step (Heenan & Morrison, 1998). The results for the 1.9cm height jet with $H_s/H_j = * 1.0$ are also shown. | 55 |
| 4.7 | Distribution of the skin friction coefficient for \circlearrowleft a planar wall jet, offset jets with $H_s/H_j = \square 0.2$, $\triangle 0.4$ and $* 1$, and flows over backward facing step with $Re_{H_s} = \bullet 39000$ (Bradshaw & Wong, 1972), $Re_{H_s} = \boxminus 10400$, $\otimes 37200$ (Jovic & Driver, 1995) and $Re_{H_s} = \oplus 28000$ (Vogel & Eaton, 1985). | 56 |
| 4.8 | Profiles of the streamwise fluctuating velocity in the region $x/H_j \leq 6$ for (a) the planar wall jet $H_s/H_j = 0$ and the offset jets with H_s of (b) $0.2H_j$ (c) $0.6H_j$ (d) H_j , the Reynolds number in all cases was approximately 44 000. | 57 |
| 4.9 | Profiles of the vertical fluctuating velocity in the region $x/H_j \leq 6$ for (a) the planar wall jet $H_s/H_j = 0$ and the offset jets with H_s of (b) $0.2H_j$ (c) $0.6H_j$ (d) H_j | 58 |
| 4.10 | Profiles of the Reynolds shear stress in the region $x/H_j \leq 6$ for (a) planar wall jet $H_s/H_j = 0$ and offset jets with H_s of (b) $0.2H_j$ (c) $0.6H_j$ (d) H_j . | 58 |
| 4.11 | Profiles of the rms value of (a) the streamwise and (b) the vertical fluctuating velocities and (c) the Reynolds shear stress in the region $x/H_j \geq 6$ for H_s/H_j of — $0 \circlearrowleft 0.2 \square 0.6$ and $\triangle 1.0$ and Reynolds number of approximately 44 000. | 59 |

| | |
|---|----|
| 4.12 Distributions of the maximum u' in the (a) inner and (b) outer shear layer, the maximum v' in the (c) inner and (d) outer shear layer and the maximum magnitude of $\langle uv \rangle$ in the (e) inner and (f) outer shear layer of ● the planar wall jet and the offset jets with $H_s/H_j = \square 0.2, \triangle 0.6$ and $\triangledown 1.0$, and for \otimes a free jet with $Re \approx 44\,000$ | 61 |
| 4.13 Distributions of the maximum u' in the (a) inner and (b) outer shear layer, the maximum v' in the (c) inner and (d) outer shear layer and the maximum magnitude of $\langle uv \rangle$ in the (e) inner and (f) outer shear layer of the offset jets with $H_s/H_j = \square 0.2, \triangle 0.6$ and $\triangledown 1.0$ with $Re \approx 44\,000$ | 62 |
| 4.14 Distributions of the fluctuating wall pressure coefficient for jets with $H_s/H_j =$ $\blacktriangle 0 \square 0.1 \blacksquare 0.2 \triangledown 0.4 \blacktriangledown 0.6 \circ 0.8 \bullet 1.0$ and results from backward facing step \boxtimes Driver <i>et al.</i> (1987) \otimes Heenan & Morrison (1998) and bluff body reattachment \odot Cherry <i>et al.</i> (1984) \oplus Hudy <i>et al.</i> (2003). | 64 |
| 4.15 Distribution of the Stanton number for \circ a planar wall jet and offset jets with $H_s/H_j = \square 0.2, \triangle 0.4, \triangledown 0.6, \diamond 0.8 * 1.0$ and $Re \approx 44\,000$. The results by Kim <i>et al.</i> (1996) for offset jets with $H_s/H_j = \bullet 0.5$ and \blacksquare 1.5 and results by Vogel & Eaton (1985) for the backward facing step with $\delta/H_s = \otimes 0.15$ and $\boxtimes 1.1$ are also shown. | 65 |
| 4.16 Distributions of the static wall pressure coefficient for jets with $H_s/H_j = 1$ and a Reynolds number of $\bigcirc 21\,800, \square 32\,500, \triangle 44\,400$ and $* 54\,500$. . . | 68 |
| 4.17 Distributions of the skin friction coefficient for jets with $H_s/H_j = 1$ and a Reynolds number of $\bigcirc 21\,800, \square 32\,500, \triangle 44\,400$ and $* 54\,500$ | 68 |
| 4.18 Distributions of the fluctuating wall pressure coefficient for jets with $H_s/H_j =$ 1 and a Reynolds number of $\bigcirc 21\,800, \square 32\,500, \triangle 44\,400$ and $* 54\,500$. . . | 69 |
| 4.19 Distributions of the Stanton number for jets with $H_s/H_j = 1$ and a Reynolds number of $\bigcirc 21\,800, \square 32\,500, \triangle 44\,400$ and $* 54\,500$ | 69 |

| | |
|--|----|
| 4.20 Distributions of the normalized Stanton number for jets with $H_s/H_j = 1$ and a Reynolds number of $\bigcirc 21\,800$, $\square 32\,500$, $\triangle 44\,400$ and $* 54\,500$, the error bars indicate the uncertainties for 95% confidence interval in the case with $Re = 21\,800$ | 71 |
| 4.21 Distributions of the maximum Stanton number for jets with different Reynolds numbers and $H_s/H_j = \diamond 0.2$, $\triangledown 0.4$, $\triangle 0.6$, $\square 0.8$ and $\bigcirc 1.0$ in the current investigation, the error bars indicate the uncertainties for 95% confidence interval. | 71 |
| 4.22 Distributions of the maximum Stanton number for a backward facing step with $\delta/H_s = \bullet 0.15$, $\blacksquare 0.19$, $\blacktriangle 0.7$, $\blacktriangledown 1.1$ and $\blacklozenge 1.6$ for different Reynolds numbers computed from the results reported by Vogel & Eaton (1985). . . . | 72 |
| 4.23 Distributions of the location of the maximum Stanton number for jets with different Reynolds numbers and offset distance $H_s/H_j = \diamond 0.2$, $\triangledown 0.4$, $\triangle 0.6$, $\square 0.8$ and $\bigcirc 1.0$ | 72 |
| 5.1 Spectra of the fluctuating wall pressure for (a) a planar wall jet and jets with $H_s/H_j =$ (b) 0.2, (c) 0.6 and (d) 1.0 and and $Re \approx 44000$ | 74 |
| 5.2 Spectra of the fluctuating wall pressure for jets $H_s/H_j =$ (a) 0.2, (b) 0.6 and (c) 1.0 and $Re \approx 44000$ | 74 |
| 5.3 Spectra of fluctuating wall pressure and fluctuating streamwise and vertical fluctuating velocities measured at different distance above wall at $x/H_j =$ (a) 2, (b) 4, (c) 8 and (d) 12 for an offset jet with $H_s/H_j = 1$ and $Re \approx 44000$. 76 | 76 |
| 5.4 Correlation coefficient, ρ_{pp} , of the fluctuating wall pressure for the reference microphone at $x_1/H_j =$ (a) 1.5, (b) 3, (c) 5 and (d) 7 for a planar wall jet (left) and an offset jet with $H_s/H_j = 0.6$ (right), the locations of other microphones indicated by left tick marks. | 78 |

| | | |
|------|---|----|
| 5.5 | Correlation coefficient, ρ_{pp} , of the fluctuating wall pressure with a reference microphone in region III (left) and region IV (right) for jets with $H_s/H_j =$ (a)&(b) 0.4, (c)&(d) 0.6, (e)&(f) 0.8 and (g)&(h) 1.0 and $Re \approx 44000$ | 79 |
| 5.6 | Distributions of the convection velocity for the dominant flow structures in jets with $H_s/H_j = \circ 0.2 \square 0.4 \triangle 0.6 \triangledown 0.8 \diamond 1.0$ and $Re \approx 44000$ based on equation 5.2 and for \otimes the flow over a backward facing step (Heenan & Morrison, 1998). | 81 |
| 5.7 | Phase angles of the cross spectra for (a) the planar wall jet and offset jets with $H_s/H_j =$ (b) 0.2 (c) 0.6 and (d) 1.0 and $Re \approx 44000$ with reference microphone at $x_1/H_j = 2$ | 82 |
| 5.8 | The convection velocities for fluctuations with different frequencies in the region $7 \leq x/H_j \leq 16$ for a planar wall jet and offset jets with $H_s/H_j = 0.2$ to 1 and $Re \approx 44000$ based on equation 5.3. | 85 |
| 5.9 | Correlation coefficient, ρ_{pp} , of the fluctuating wall pressure for the reference microphone in the region I near $x_1/X_r \approx 0.4$ for an offset jets with $H_s/H_j =$ (a) 0.4, (b) 0.6, (c) 0.8 and (d) 1.0 and $Re \approx 44000$, the locations of other microphones, x_2 , indicated using the tick marks on the right. | 85 |
| 5.10 | The (a) cross spectra (b) phase angle and (c) coherence of the cross spectra between the fluctuating pressure at $x_1/X_r = 0.43$ ($x_1/H_j = 2$) and x_2/X_r for offset jet with $H_s/H_j = 1.0$ and $Re \approx 44000$. The auto spectra at x_2/X_r are also shown in figure (a) using a solid line. | 86 |
| 5.11 | The phase angle of cross spectra between the fluctuating pressure at $x_1/X_r = 0.43$ ($x_1/H_j = 2$) and x_2/X_r for the offset jet with $H_s/H_j = 1.0$ and $Re \approx 44000$ | 87 |
| 5.12 | The convection velocity for different frequencies in the region $0.75 \leq x/X_r \leq 1.2$ ($3.5 \leq x/H_j \leq 5.5$) for offset jet with $H_s/H_j = 1.0$ and $Re \approx 44000$, based on the cross spectra of the fluctuating wall pressure. | 88 |

| | |
|---|-----|
| 5.13 Distributions of phase angles of the cross spectra for reference location $x_1/X_r = 0.11, 0.32, 0.54$ and 0.75 ($x_1/H_j = 0.5, 1.5, 2.5$ and 3.5) for an offset jet with $H_s/H_j = 1.0$ and $Re \approx 44000$ | 89 |
| 5.14 Convection velocity calculated using phase angle of the fluctuating wall pressure in the region $1 \leq x_2/H_j \leq 2$ ($0.22 \leq x_2/X_r \leq 0.43$) with reference location $x_1/X_r = 0.32$ for an offset jet with $H_s/H_j = 1.0$ and $Re \approx 44000$ | 91 |
| 5.15 Correlation coefficients of the fluctuating wall pressure and the streamwise fluctuating velocity ρ_{pu} (left) and the vertical fluctuating velocity ρ_{pv} (right) for a planar wall jet with $Re \approx 44\,000$ at different streamwise locations. | 93 |
| 5.16 Correlation coefficient ρ_{pu} (left) and ρ_{pv} (right) for the the fluctuating wall pressure at $x_1/H_j = 1.5$ and the fluctuating velocity at different locations for time delays $\tau U_U/H_j \approx -2$ to 5 in the planar wall jet with $Re \approx 44\,000$ | 94 |
| 5.17 Correlation coefficients of the fluctuating wall pressure and the streamwise fluctuating velocity ρ_{pu} (left) and the vertical fluctuating velocity ρ_{pv} (right) at the positions above the wall for the offset jet with $H_s/H_j = 1$ and $Re \approx 44\,000$ at different streamwise locations. | 96 |
| 5.18 Correlation coefficient ρ_{pu} (left) and ρ_{pv} (right) for the fluctuating wall pressure at $x_1/H_j = 4$ and the fluctuating velocities at different locations for time delays $\tau U_U/H_j \approx -0.5$ to 2.4 in an offset jet with $H_s/H_j = 1$ and $Re \approx 44\,000$ | 97 |
| 5.19 Correlation coefficient ρ_{pu} (left) and ρ_{pv} (right) for the fluctuating wall pressure at $x_1/H_j = 8$ and the fluctuating velocities at different locations for time delays $\tau U_U/H_j \approx -0.96$ to 1.2 in an offset jet with $H_s/H_j = 1$ and $Re \approx 44\,000$ | 100 |

| | |
|--|-----|
| 5.20 The coherence between the fluctuating wall pressure at $x_1/X_r \approx 0.4$ and fluctuating streamwise velocities, (left) γ_{pu} and (right) γ_{pv} , for an offset jet with $H_s/H_j = 1.0$ and $Re \approx 44\,000$ for frequencies of $fX_r/U_U = 0.08$ to 1.0. | 101 |
| 5.21 The phase angles of the cross spectra between the fluctuating wall pressure at $x_1/X_r \approx 0.4$ and fluctuating streamwise velocities, (left) $ \theta _{pu}$ and (right) $ \theta _{pv}$, for an offset jet with $H_s/H_j = 1.0$ and $Re \approx 44\,000$ for frequencies of $fX_r/U_U = 0.08$ to 1.0. | 103 |
| 5.22 Distributions of the phase angles of the cross spectra of the fluctuating pressure and vertical fluctuating velocity for an offset jet with $H_s/H_j = 1.0$ and $Re \approx 44\,000$ | 104 |
| 5.23 Distributions of the convection velocities computed using the phase angles of the cross spectra $\circ \theta_{pv}$ and $\bullet \theta_{pp}$ in the attachment region $0.8 \leq x/Xr \leq 1$ for different frequencies for an offset jet with $H_s/H_j = 1.0$ and $Re \approx 44\,000$ | 105 |
| 5.24 Distributions of the convection velocities in the attachment region $0.7 \leq x/X_r \leq 1.4$ for different frequencies for offset jets with $H_s/H_j = 0.1$ to 1.0 and $Re \approx 44\,000$ | 106 |
| 6.1 Distributions of the vectors and streamlines of the mean velocity for (a) a single offset jet and co-flowing jets with $H'_j/H_j = 0.5$ and U'_o/U_o of (b) 0.10, (c) 0.20, (d) 0.28, (e) 0.38, Reynolds numbers are given in Table. 6.1. | 110 |
| 6.2 Distributions of the vectors and streamlines of the mean velocity for co-flowing jets with $H'_j/H_j = 0.5$ and U'_o/U_o of (a) 0.59 and (b) 0.74. | 111 |
| 6.3 Distribution of (a) the static wall pressure coefficient and (b) the mean skin friction coefficient for \bullet a planar wall jet, \circ a single offset jet and co-flowing jets with $H'_j/H_j = 0.5$ and $U'_o/U_o = \diamond 0.10, \square 0.20, \triangle 0.28, \otimes 0.38, \triangledown 0.59$ and $* 0.74$ | 111 |

| | | |
|------|--|-----|
| 6.4 | Distributions of (a) the maximum local streamwise velocity and (b) y_{max} for \circ the single offset jet and jets with velocity ratio $U'_o/U_o = \square 0.10, \triangle 0.20, \nabla 0.28, \diamond 0.38, * 0.59$ and $\times 0.74$ | 113 |
| 6.5 | Distributions of the outer half jet width of the outer jet for \circ the single offset jet and jets with velocity ratio $U'_o/U_o = \square 0.10, \triangle 0.20, \nabla 0.28, \diamond 0.38, * 0.59$ and $\times 0.74$ | 113 |
| 6.6 | Profiles of the mean streamwise velocity, the fluctuating streamwise and vertical velocities and the Reynolds shear stress for — a single offset jet and jets with $H'_j/H_j = 0.5$ and $U'_o/U_o = \circ 0.20, \square 0.38$ and $\triangle 0.59$ | 115 |
| 6.7 | Distributions of (a) the fluctuating wall pressure coefficients and (b) the Stanton number for \bullet a single offset jet and co-flowing jets with $H'_j/H_j = 0.5$ and $U'_o/U_o = \circ 0.10, \square 0.20, \triangle 0.28, \nabla 0.38, \diamond 0.59$ and $* 0.74$ | 116 |
| 6.8 | The spectra of the fluctuating wall pressure for (a) the single offset jet with $H_s/H = 1$ and offset jet with a co-flowing jet with $H_s/H_j = 1, H'_j/H_j = 0.5$ and $U'_o/U_o = (b) 0.20, (c) 0.38$ and (d) 0.59 | 118 |
| 6.9 | The spectra of the fluctuating wall pressure for offset jet with a co-flowing jet with $H_s/H_j = 1, H'_j/H_j = 0.5$ and $U'_o/U_o = 0$ to 0.74 measured at $x/H_j = 16$, frequency is normalized using outer jet half width $y_{+1/2}$ measured at $x/H_j = 16$ | 118 |
| 6.10 | Spectra of fluctuating wall pressure and fluctuating streamwise and vertical fluctuating wall pressure measured at different distance above wall at $x/H_j = (a) 2, (b) 4, (c) 8$ and (d) 12 for an offset jet with $H_s/H_j = 1$ and a co-flowing jet with $H'_j/H_j = 0.5$ and $U'_o/U_o = 0.20$ | 120 |
| 6.11 | Spectra of fluctuating wall pressure and fluctuating streamwise and vertical fluctuating wall pressure measured at different distance above wall at $x/H_j = (a) 2, (b) 4, (c) 8$ and (d) 12 for an offset jet with $H_s/H_j = 1$ and a co-flowing jet with $H'_j/H_j = 0.5$ and $U'_o/U_o = 0.38$ | 121 |

| | |
|---|-----|
| 6.12 Distributions of the vectors and streamlines of the mean velocity for co-flowing jets with size ratio $H'_j/H_j \approx 0.18$ and velocity ratios $U'_o/U_o =$ (a) 0.27 and (b) 0.63. | 123 |
| 6.13 Distributions of (a) the static wall pressure coefficient and (b) the skin friction coefficient for co-flowing jets with size ratio $H'_j/H_j \approx 0.18$ and velocity ratios $U'_o/U_o = \circ 0, \square 0.27, \otimes 0.42, \triangledown 0.63$ and $\ast 0.86$, and \bullet for the planar wall jet. | 123 |
| 6.14 Profiles of (a) the mean streamwise velocity, (b) u' , (c) v' and (d) $\langle uv \rangle$ for — the single offset jet and jets with $H'_j/H_j = 0.18$ and $U'_o/U_o = \circ 0.27$ and $\triangle 0.63$ | 124 |
| 6.15 The distributions of the local maximum vertical fluctuating velocity along the inner shear layer for \otimes the single offset jet with $H_s/H_j = 1$ and co-flowing jets with $H'_j/H_j = 0.5$ and $U'_o/U_o = \circ 0.1, \square 0.2, \triangle 0.28, \triangledown 0.38, \diamond 0.59, \ast 0.74$ and co-flowing jets with $H'_j/H_j = 0.18$ and $U'_o/U_o = \bullet 0.27$ and $\blacktriangle 0.63$ | 125 |
| 6.16 Distributions of (a) the fluctuating wall pressure coefficients and (b) the Stanton number for \bullet the single offset jet with $H_s/H_j = 1$ and co-flowing jets with $H'_j/H_j = 0.18$ and $U'_o/U_o = \diamond 0.1, \circ 0.27, \square 0.42, \triangle 0.63, \triangledown 0.86$ and $\ast 1$ | 125 |
| 6.17 The spectra of the fluctuating wall pressure for (a) the single offset jet with $H_s/H_j = 1$ and co-flowing jets with $H'_j/H_j = 0.18$ and $U'_o/U_o =$ (b) 0.27, (c) 0.42 and (d) 0.63. | 127 |
| 6.18 The spectra of the fluctuating wall pressure for co-flowing jets with $H'_j/H_j = 0.18$ and $U'_o/U_o =$ (a) 0.42 and (b) 0.63. | 127 |
| 6.19 Effect of the ratios of the (a) maximum velocity, (b) mass flow rate and (c) streamwise momentum on the reattachment location for co-flowing jets with height ratio of $H'_j/H_j = \circ 0.5$ and $\bullet 0.18$ | 130 |

| | |
|--|-----|
| 6.20 Effect of the ratios of the (a) maximum velocity, (b) mass flow rate and (c) streamwise momentum on the maximum static wall pressure coefficient for co-flowing jets with height ratio of $H'_j/H_j = \circ 0.5$ and $\blacksquare 0.18$ | 131 |
| 7.1 Correlation coefficients of the fluctuating wall pressure for (left) the single offset jet with $H_s/H_j = 1.0$ and (right) the co-flowing jets with velocity ratio of $U'_o/U_o \approx 0.2$ and $H'_j/H_j = 0.5$ for reference locations at $x_1/H_j = 12, 9$ and 5 (from top to bottom) indicated using \circ | 133 |
| 7.2 The \circ cross spectra of fluctuating wall pressure with reference location at $x_1/H_j = 2$ ($x_1/X_r \approx 0.4$) and — the auto spectra at x_2 for (left) single offset jet and (right) co-flowing jets with $U'_o/U_o \approx 0.2$, $H_s/H_j = 1$ and $H'_j/H_j = 0.5$ | 134 |
| 7.3 The coherence of fluctuating wall pressure with the reference location at $x_1/H_j = 2$ ($x_1/X_r \approx 0.4$) for (left) the single offset jet and (right) the co-flowing jets with $U'_o/U_o \approx 0.2$ and $H'_j/H_j = 0.5$ | 134 |
| 7.4 The phase angle of the fluctuating wall pressure between $x_1/H_j = 2$ ($x_1/X_r \approx 0.4$) and different streamwise position x_2 for frequencies of $0.2 \leq f X_r/U_U \leq 0.8$ for (a) single offset jet and (b) co-flowing jets with $U'_o/U_o \approx 0.2$ and $H'_j/H_j = 0.5$ | 136 |
| 7.5 The convection velocity for different frequencies computed from $d\theta_{pp}/dx_2$ ● for the single offset jet with $H_s/H_j = 1.0$ and \circ for the offset jet with $H_s/H_j = 1.0$ and a co-flowing jet with $U'_o/U_o \approx 0.2$ and $H'_j/H_j = 0.5$, both for the region $0.9 \leq x/Xr \leq 1.2$ ($4.5 \lesssim x/H_j \lesssim 6$). | 137 |
| 7.6 The convection velocity for different frequencies computed from $d\theta_{pp}/dx_2$ ● for a single offset jet with $H_s/H_j = 1.0$ and \circ for an offset jet with $H_s/H_j = 1.0$ and a co-flowing jet with $U'_o/U_o \approx 0.2$ and $H'_j/H_j = 0.5$, both for the region $7 \leq x/H_j \leq 14$ | 137 |

| | | |
|------|---|-----|
| 7.7 | Correlation coefficient and phase angles for frequencies of $0.08 \leq f X_r / U_U \leq 0.28$ of the fluctuating wall pressure in the region $x_2 / H_j \leq 8$ for $x_1 / H_j = 0.5$ in the offset jet with $H_s / H_j = 1.0$ and co-flowing jet with $H'_j / H_j = 0.5$ and $U'_o / U_o \approx 0.2$ | 138 |
| 7.8 | Correlation coefficients of fluctuating wall pressure and fluctuating velocities, ρ_{pu} (left) and ρ_{pv} (right), at three different time when $x_1 / H_j = 4$ for the offset jet with $H_s / H_j = 1.0$ and a co-flowing jet with $H'_j / H_j = 0.5$ and $U'_o / U_o \approx 0.2$ | 138 |
| 7.9 | Coherence of the fluctuating wall pressure at $x_1 / H_j = 4$ and fluctuating vertical velocity, γ_{pv} , of different frequencies for (left) single offset jet with $H_s / H_j = 1.0$ and (right) the offset jet with a co-flowing jet of $U'_o / U_o \approx 0.2$ | 140 |
| 7.10 | Correlation coefficient of fluctuating wall pressure for the offset jet with a co-flowing jet of $H'_j / H_j = 0.5$ and velocity ratio of $U'_o / U_o \approx 0.38$, when the reference location is at $x_1 / H_j =$ (a) 1, (b) 6.5, (c) 9 and (d) 12. | 142 |
| 7.11 | The coherence and the phase angles of fluctuating wall pressure with reference to $x_1 / H_j = 2$ ($x_1 / X_r \approx 0.63$) for the offset jet with $H_s / H_j = 1.0$ and a co-flowing jet with $H'_j / H_j = 0.5$ and $U'_o / U_o \approx 0.38$ | 142 |
| 7.12 | Correlation coefficients of the fluctuating wall pressure and the fluctuating velocities above the microphone, ρ_{pu} (left) and ρ_{pv} (right), measured at $x / H_j = 2, 4, 6$ and 8 for the offset jet with a co-flowing jet of $H'_j / H_j = 0.5$ and velocity ratio of $U'_o / U_o \approx 0.38$ | 144 |
| 7.13 | Correlation coefficients of fluctuating wall pressure at $x_1 / H_j = 4$ and fluctuating velocities, (left) ρ_{pu} and (right) ρ_{pv} , for three different time delays in the offset jet with $H_s / H_j = 1.0$ and a co-flowing jet with $H'_j / H_j = 0.5$ and $U'_o / U_o \approx 0.38$ | 145 |

| | | |
|------|---|-----|
| 7.14 | Correlation coefficient of fluctuating wall pressure for the offset jet with a co-flowing jet of $H'_j/H_j = 0.18$ and velocity ratio of $U'_o/U_o \approx 0.63$ when the reference location is at $x_1/H_j =$ (a) 1 and (b) 7. | 146 |
| 7.15 | The coherence and the phase angles of fluctuating wall pressure with reference to $x_1/H_j = 2$ ($x_1/X_r \approx 0.62$) for the offset jet with $H_s/H_j = 1.0$ and a co-flowing jet with $H'_j/H_j = 0.18$ and $U'_o/U_o \approx 0.63$ | 147 |
| 7.16 | Correlation coefficients of fluctuating wall pressure and fluctuating velocities above the microphone, ρ_{pu} (left) and ρ_{pv} (right), measured at $x/H_j = 2, 4, 6$ and 8 for the offset jet with H_s/H_j a co-flowing jet of $H'_j/H_j = 0.18$ and velocity ratio of $U'_o/U_o \approx 0.63$ | 148 |
| 7.17 | Correlation coefficients of fluctuating wall pressure at $x_1/H_j = 4$ and fluctuating velocities, (left) ρ_{pu} and (right) ρ_{pv} , at three different time delays for the offset jet with $H_s/H_j = 1.0$ and a co-flowing jet with $H'_j/H_j = 0.18$ and $U'_o/U_o \approx 0.63$ | 149 |
| A-1 | Distributions of (a) the mean streamwise velocity (b) the fluctuating velocity and (c) the Reynolds shear stress for a planar free jet at $x \approx 0.05H_j$ measured using the jet with $H_j = 0.38cm$ (solid symbols) and the jet with $H_j = 0.19cm$ (open symbols), U_o represents the maximum streamwise velocity. | 171 |
| A-2 | Profiles of the mean velocity measured using a single hot-wire at $x \approx 0.05H_j$ for an offset attaching planar jet with $H_s/H_j = 1$ and (a) $H'_j/H_j = 0.5$ with $U'_o/U_o = \bigcirc 0.1, \square 0.2, \triangle 0.28, \nabla 0.38, \diamond 0.47, \times 0.59, *\ 0.74$, and (b) $H'_j/H_j = 0.18$ with $U'_o/U_o = \bigcirc 0.27, \square 0.42, \triangle 0.63, \nabla 0.86$ | 171 |
| A-3 | Profile of mean and fluctuating streamwise velocity for a free jet along centerline of the jet, $y = H_j/2$, at the jet exit for $Re \approx 44\,000$ | 172 |
| A-4 | Profile of mean streamwise velocity for a planar free jet along centerline of the jet, $y = H_j/2$, at $x/H_j = \bigcirc 0, \square 6, \triangle 12, \nabla 18$ for $Re \approx 44\,000$ | 172 |

| | | |
|-----|--|-----|
| A-5 | Contours of fluctuating velocities (a) u'/U_{max} , (b) v'/U_{max} and (c) w'/U_{max} for an offset attaching jet with $H_s/H_j = 1$ at $x/H_j = 12$ for $Re \approx 44\,000$. . . | 173 |
| A-6 | Profiles of the mean streamwise velocity and turbulent stresses of a planar free jet measured using the jet with $H_j = 0.38\,cm$ at $x/H_j = \circ 0, \square 2, \Delta 4, \nabla 6, \bullet 8$ for $Re \approx 44\,000$ | 174 |
| A-7 | Profiles of the mean streamwise velocity and turbulent stresses of a planar free jet measured using the jet with $H_j = 0.19\,cm$ at $x/H_j = \circ 0, \square 2, \Delta 4, \nabla 6, \bullet 8$ for $Re \approx 44\,000$ | 175 |
| B-1 | Illustration of the heat losses. | 177 |
| B-2 | Distribution of \circ wall temperature for a typical offset jet with $H_s/H_j = 1$ and $Re = 44\,000$ and the estimated ----- radiation heat loss from the top of the wall, —— heat loss through bottom air gap ($T_b = T_\infty + 5^\circ C$) and — lateral conduction within the foil. | 177 |
| C-1 | Electrical resistivity of 304 Stainless steel for different temperatures (Davis, 1996). | 180 |
| D-1 | The (a) modal energy contain $\varepsilon^{(n)}/\varepsilon$, (b) eigenspectra for the first 3 modes, $\lambda^{(n)}/\varepsilon$, and (c) real part of the eigenvectors for selected frequencies for offset jet with $H_s/H_j = 1.0$ | 182 |

Chapter 1

Introduction

Offset turbulent planar jets initially traveling parallel to an adjacent wall curve toward that wall and eventually attach to the wall and then recover to a two-dimensional wall jet. The flows can cause a maximum in the local convective heat transfer rate at the reattachment location making these flows useful in a range of thermal management applications. These include the cooling and drying flows in the polymer and textile industries, the mixing flows in the combustion chamber of gas turbine and others. The original motivation for this investigation was from the investigations on the cooling jets produced by dual-lip air rings used to produce thin polyethylene films shown in Fig. 1.1. In this process, the polymer melt extruded through an annular die forms a thin-walled tube that expands in diameter over the initial region due to the difference in the air pressure across the tube and forms a bubble. The bubble is cooled by air jets that exit an air ring surrounding the bubble, causing the polymer to solidify at some distance above the die exit before it is collapsed to a sheet. The cooling jets used in this process have a significant effect on the stability of the film bubble. As the flow rate increases, disturbances from the cooling flow appear to cause periodic variations in the film bubble diameter or helical motions of bubble that eventually break the bubble (Ghaneh-Fard *et al.*, 1996, 1997). Thus, there is considerable interest in improving the design and use of these cooling flows to increase the heat transfer, the bubble

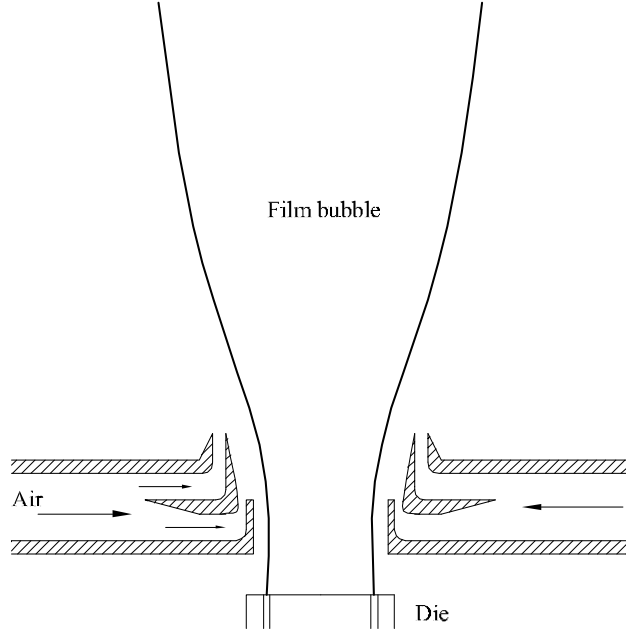


Figure 1.1: Schematics of the dual jet air ring used in blown film manufacturing process.

stability, and hence the production rate.

In dual lip air rings, an inner jet with a relatively low flow rate is used to initially cool the base of the bubble and increase the rigidity of the film. A second jet with a larger flow rate is then used to cool the upper part of the bubble. Modeling and measurements of the flow produced by a typical dual lip air ring (e.g. Sidiropoulos & Vlachopoulos, 2000; Gao *et al.*, 2005; Li *et al.*, 2005) showed that the interaction of the two jets in the region above the forming cone had a significant effect on the flow in this region. In particular, the entrainment of the inner jet into the outer jet affected the location where the outer jet attached to the surface and effectively provide a means of controlling the reattaching outer jet. This would also change the heat transfer produced by these jets.

Heretofore, there have only been limited investigations of the flow produced by offset attaching jets with small initial offset distances similar to the distances used in the dual-lip air ring, and few or no investigations of offset jets with a co-flowing jet below the outer jet. Thus, the objective of this investigation is to study the development of the offset

planar attaching jets at offset distances smaller than the jet height, and to characterize the development of offset jets with a co-flowing jet. The development of the flow structures in the offset jet with and without a co-flowing jet will also be examined.

The previous investigations on the development of offset jets and other reattaching flows are reviewed in Chapter 2. The experimental facility and methodology will then be discussed in Chapter 3. The single point measurement results for the single offset jets are discussed in Chapter 4, while the development of the large scale structures in the single offset jet is discussed in Chapter 5. The single point measurements of offset jets with a co-flowing jet are presented in Chapter 6, and the results of the two-point and two-time measurements are discussed in Chapter 7. Finally, the conclusions of the investigation are included in Chapter 8, and recommendations are given in Chapter 9.

Chapter 2

Literature Review

The development of planar offset attaching jets with a low flow rate co-flowing jet has not been investigated before. The investigations of turbulent planar offset attaching jets will be reviewed first. Investigations that considered flow control using constant flow rate injection or suction flows below an attaching jet or shear layer will then be reviewed. Finally, the investigations of the dynamics of the large scale structures in attaching flows, such as flows over backward facing steps and bluff bodies, are reviewed.

2.1 Offset Attaching Jets

Previous investigations have characterized the development of the Reynolds averaged flow field in turbulent offset planar jets analytically (Bourque & Newman, 1960; Sawyer, 1963; Bourque, 1967), experimentally (Sawyer, 1960; Hoch & Jiji, 1981; Lund, 1986; Pelfrey & Liburdy, 1986; Nasr & Lai, 1997, 1998), and numerically using RANS models (Nasr & Lai, 1998). The heat transfer from the wall to the flow has also been considered (Kim *et al.*, 1996; Bremhorst & Agnew, 1999; Song *et al.*, 2000). A list of the experimental investigations of offset attaching planar jets is included in Table 2.1.

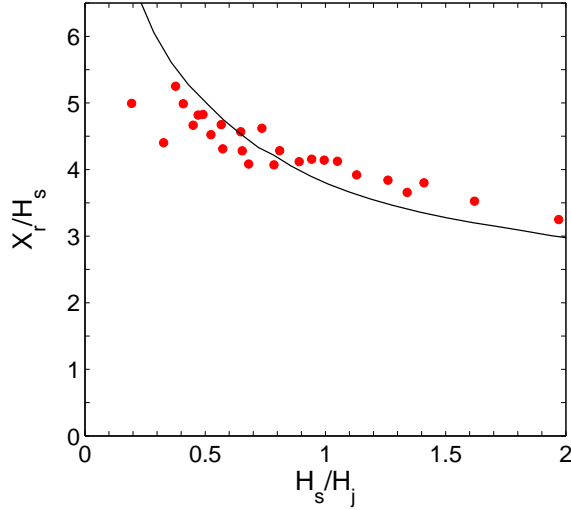


Figure 2.1: Attachment length measured by ● Lund (1986) and modeled by — Bourque (1967).

The results show that the offset jets curve toward the adjacent wall and eventually attach to the wall. A recirculation region is formed between the jet and the wall upstream of the reattachment location. The jets then evolve downstream after this reattachment region and gradually recover to a flow similar to a two-dimensional wall jet. There is a maximum in the distributions of the static pressure on the wall and the heat transfer near the reattachment location. The development of the offset jet is affected by several factors including offset distance, nozzle geometry, initial turbulence level, Reynolds number, aspect ratio and presence of side walls.

Most investigations of turbulent offset jets focused on jets with offset distances that are larger than the jet height, $H_s \geq H_j$. In these cases, the jet tends to interact with the wall after the shear layers in the near field interact so the jet is fully turbulent before attaching to the wall. The reattachment length (X_r) increases with offset distance (H_s), but the ratio of these distance X_r/H_s decreases when the offset distance increases as shown in Fig. 2.1. The results for offset distance $H_s \geq 0.4H_j$ agree with the model proposed by Bourque (1967) for fully developed jets, but the measurements and model differ for small offset

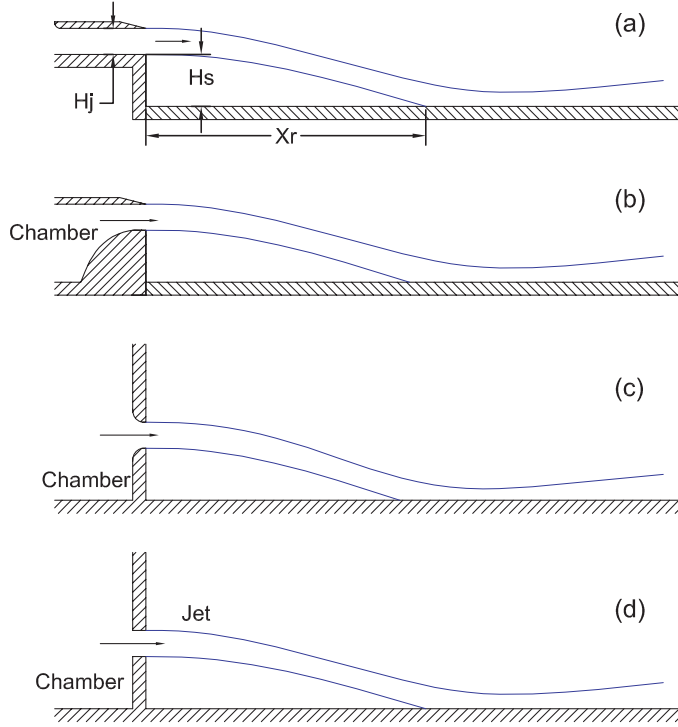


Figure 2.2: Schematics of the offset jets used by (a) Sawyer (1960), (b) Lund (1986), (c) Nozaki *et al.* (1979, 1981) and (d) Nasr & Lai (1997, 1998).

ratios, $H_s/H_j < 0.4$. At some point, one would expect this ratio may approach a constant value similar to in a backward facing step (Eaton & Johnson, 1981). Lund's measurements showed no obvious evidence of this, however, even for offset ratios H_s/H_j as small as 0.2.

Results from different investigations indicate that the development of the offset jet depends on the nozzle geometry. The reattachment location differs by as much as 20% for jets exiting short channel (Sawyer, 1960), orifice plates (Nasr & Lai, 1997, 1998), orifice plates with a contoured inlet (Nozaki *et al.*, 1979, 1981) and the nozzle used by Lund (1986) that are all shown in Fig. 2.2. The jets produced by different nozzles will have different initial momentum thickness that may cause the jets to develop differently as in the case for free round jet (Mi *et al.*, 2001).

Nasr & Lai (1998) found that the distribution of the static pressure on the wall was independent of Reynolds number when $Re \geq 10\,000$, while Nozaki *et al.* (1979) found the

critical Reynolds number was 20 000 for jet with aspect ratio larger than 8. Lund (1986) also found the flow was Reynolds number independent when $Re \geq 20\,000$.

Nasr & Lai (1998) showed that the maximum static wall pressure measured at the center of the bottom wall decreased when the confining walls at the two sides of the flow were removed. The location of this maximum also shifted from $x/H_j \approx 4.5$ to 6. The effect of a confining wall behind the nozzle exit does not appear to be considered in any previous investigation but different configurations have been used. Nozaki *et al.* (1979, 1981) used a confining wall behind the nozzle with a height of approximately 10 jet heights. Sawyer (1960) and Lund (1986) did not use a confining plate. Instead, the top plate of the nozzle had a sharp edge to allow direct entrainment of air from the top of the jet. This could also cause the differences observed in the development of the jets.

Nozaki *et al.* (1981) also examined the effect of changing the initial turbulence in an offset jet with $H_s/H_j = 11$ from 0.4% to 6%. They found that the increase in the initial turbulence promoted the development of the shear layer and reduced the attachment location from $X_r/H_j \approx 26$ to 21. The minimum and the maximum static pressure on the wall decreased approximately 20%.

The aspect ratio (jet width/jet height) of the jet can also affect the development of the flow when it is less than a critical aspect ratio. Lund (1986) compared the distributions of static wall pressure on the jet centerline for jets with initial aspect ratios of 10 and 18. He showed that there was not a significant difference between the results for jets with aspect ratios of 10 and 18, indicating the flow in the center of the jet was independent of the jet aspect ratio when the aspect ratio was larger than 10.

Kim *et al.* (1996) and Song *et al.* (2000) measured the heat transfer from a heated surface to the offset attaching jet for Reynolds numbers of 6500 to 39000 and offset distances of $0.5H_j$ to $15H_j$. The heat transfer to the offset jet was initially small in the recirculation region and increased to a maximum near the reattachment region. The heat transfer then decreased gradually as the flow developed downstream. The maximum in the heat transfer

was larger for jets with smaller offset distances. For example, the maximum Nusselt number was approximately 180 for the jet with $H_s/H_j = 0.5$ and decreased to 120 for jet with $H_s/H_j = 5$. Kim *et al.* (1996) reported that the maximum Nusselt number could be scaled using $Re^{0.49}$ for $Re = 6\,000$ to 30 000.

2.2 Flow Control Using a Co-flowing Jet

Passive and active flow control has been used in a range of applications to reduce the form drag and increase the stall margin of an air foil (e.g. Zaman, 1992; Seifert *et al.*, 1996; Wu *et al.*, 1998), to suppress resonance of a cavity flow (e.g. Cattafesta *et al.*, 2003; Rowley & Williams, 2006), to enhance the mixing in combustion chambers (e.g. Forliti & Strykowski, 2005) and in other flows reviewed by Gad-el-Hak & Bushnell (1991) and Gad-el-Hak (1996). Passive control strategies modify the geometry and extract energy from the flow while the active flow control strategies provide external energy into the system. Open-loop active control with periodic forcing near the separation point appears to be the most widely examined method to control a separated shear layer. Flow control using a co-flowing jet of interest here is also in the category of open-loop active control (cf Cattafesta *et al.*, 2003; Rowley & Williams, 2006).

2.2.1 Flow field produced by dual-lip air ring

There have been a few investigations of the flow field produced by a dual-lip air ring used in the blown film manufacturing process, where the development of main cooling jet was in part controlled using a co-flowing jet. Sidiropoulos (2000) and Sidiropoulos & Vlachopoulos (2000) performed numerical investigations of this flow using $k - \epsilon$ model for a range of dual lip air ring designs. They found that the outer jet turned toward the wall downstream of the jet exits due to the entrainment process, often termed the Coanda effect. The outer jet produced a more uniform pressure on the bubble in the region above the forming cone

when the outer jet exited approximately parallel to the bubble rather than impinging onto the surface. They found that the pressure distribution and the heat transfer on the bubble surface depended on the size of the recirculation region, that was determined by the flow rate and the design of the forming cone.

Gao *et al.* (2005) later measured the static and fluctuating pressure on the surface of a solid bubble model for a typical dual lip air ring with a range of upper and lower jet velocities. The outer jet curved to the wall downstream the tip of the forming cone, while the inner jet seemed to be entrained into the outer jet. The static wall pressure reached a maximum near the location where the outer jet appeared to attach to the wall due to the streamline curvature in the flow. The fluctuating wall pressure reached a maximum slightly upstream of the maximum of the static wall pressure. In many cases, the magnitude of the pressure fluctuation were on the order of the static pressure. The magnitude of the maxima in the static and fluctuating wall pressure did not scale with the dynamic head of either the inner or the outer jets, indicating the the flow above the forming cone was determined by both jets in this region. Further above the forming cone, both the static and the fluctuating wall pressure decreased after the jet attached to the wall and developed parallel to the wall. The fluctuating wall pressure scaled with the dynamic head of the outer jet, indicating the flow were determined by the outer jet velocity in this region.

Gao *et al.* (2005) showed that there was a peak in the spectra of the fluctuating wall pressure at a frequency of $fH_j/U_U \approx 0.21 - 0.27$ measured in the reattachment region. The peak decreased in magnitude as the flow evolved downstream, and a low frequency peak with a frequency of $fH_j/U_U \approx 0.05$ emerged. Gao *et al.* (2005) also measured the spectra of the fluctuating streamwise velocity and found that the high frequency wall pressure fluctuations seem to be associated with the large scale structures in the attaching inner shear layer of the outer jet, while the low frequency wall pressure fluctuations seemed to be caused by the large-scale flow structures from the outside shear layer of the outer jet.

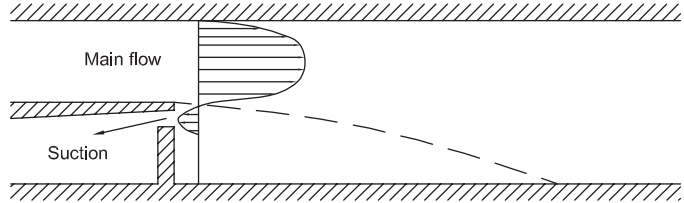


Figure 2.3: Schematic of the coutercurrent shear control of a backward facing step used by Forliti & Strykowski (2005).

Gao & Ewing (2005) used the measurements of the two-point and two-time correlation of fluctuating pressure on the wall to characterize the development and convection of the large-scale structures. They found in the region where the inner shear layer attached to the wall (near the jet exit), the fluctuating wall pressure was only correlated over a short distance, indicating the structures in the inner shear layer diminished soon after the shear layer attached to the wall. Downstream of the reattaching region, the fluctuating wall pressure was correlated over a long distance indicating that the large scale flow structures in this region were convected downstream. The convection velocity was 0.5 to 0.7 of the maximum outer jet velocity in the reattaching region and 0.45 to 0.5 of the maximum outer jet velocity in the downstream region. The flow in their investigation was not a generic flow and their measurements were only taken with a small range of velocity ratios limited by the facility.

2.2.2 Counter-current shear control in combustion chamber

Flow control using a steady co-flowing jet can also be found in other applications. For example, Forliti & Strykowski (2005) studied counter-current shear control on a backward facing step using PIV, where suction with a constant flow rate was applied through a gap located $0.05H_s$ below the tip of the step as shown in Fig. 2.3. They found that when the suction flow rate was increased from 0 to approximately 10% of the main flow, the mean reattachment location decreased from $7H_s$ to $4H_s$. They argued that the mean velocity

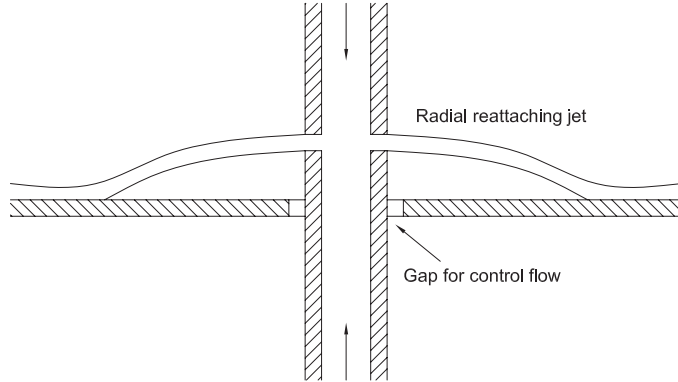


Figure 2.4: Schematic of the control of radial reattaching jet using steady co-flowing jet by Tanaka *et al.* (1986a,b,c).

gradients across the shear layer increased when suction was applied, so that the shear layer grew much faster. The Reynolds stresses along the shear layer and the reverse velocity in the recirculation region increased with the suction flow rate, but that there was no noticeable transition in the stability. They also found stronger three-dimensionality for the flow with a higher suction flow rate.

2.2.3 Radial reattaching jet with co-flow

Tanaka *et al.* (1986a,b,c) studied the effect of blowing or sucking flow through a gap in the corner of the recirculation region of a turbulent radial attaching jet discharged from a cylindrical nozzle as shown in Fig. 2.4. The width of the gap was 0.9 nozzle widths and the configuration was such that the initial direction of the control flow was perpendicular to the initial direction of the attaching jet. The control flow had a significant effect on the distributions of the static wall pressure and mean velocity. When the suction flow rate was increased, the maximum streamwise mean velocity decayed at a faster rate in the near field ($x/H_s \leq 8$). In these cases, the maximum in the static pressure associated with the attachment process was also more pronounced, and the location of this maximum shifted upstream. When the blowing flow rate was increased, the maximum in the streamwise

mean velocity decayed at a slower rate in the region $x/H_s \lesssim 15$. In fact, the decay rate approached that of a free radial jet when the velocity ratio between the control flow and the main flow was increased to approximately 0.4. The maximum static pressure on the wall also decreased and the attachment point shifted to a downstream location. The effect of adding a control flow on the radial attaching jet was also studied for offset distances from 2 to $10H_j$. This effect was more pronounced for smaller offset distances.

2.2.4 Other flows controlled using constant injection

There are other flows in the literature that are similar to the attaching jet with a co-flow. For example, Kim & Lee (2002) studied the velocity field in the turbulent wake of a porous plate with a porosity of 38.5% and a height of 30mm located 0mm to 9mm above a flat wall. The flow separated around this plate forming a shear layer over the plate and an inner jet between the plate and the wall (when the plate was elevated from the wall). The ratio between the maximum velocity in the inner and outer flows was 0.3 to 0.75 depending on the height of the plate above the wall. They found that the outer shear layer formed at the top of the plate moved away from the wall when the inner flow rate increased. Only the region near the plate $x/H_s \leq 5$ was studied. Thus, the outer flow had not reattached to the wall in this region, so the reattachment process was not studied.

Injection of mass with constant flow rate was also used in applications such as suppressing the resonance over open cavities caused by the feedback of acoustic disturbance. Sarohia & Massier (1977) found the noise can be suppressed when the steady injection flow rate was larger than 0.05 to $0.15\rho U_\infty A$, where U_∞ is the free stream velocity and A is the area of the cavity. Vakili & Gauthier (1994) suppressed the resonance by injecting flow into boundary layer through the porous wall upstream of the cavity. The boundary layer thickness increased with the injection flow rate and the noise decreased.

2.3 Other Generic Reattaching Flows

Heretofore, there does not appear to have any investigation that have characterized the flow fields of the offset attaching jets with small offset distances, nor any investigations of the large-scale structures present in the offset jet for any height. Other reattaching flows such as the flow over a backward facing step and the flow separated from a bluff body shown in Fig. 2.5 have been studied extensively because of the simplicity in their geometry and wide existence. In these flows, the separation occurs at a fixed location and there is a recirculation region between the main flow and the wall. The shear layer entrains mass in the separation region and the main flow curves toward the wall and finally attaches to the wall producing a peak in the surface fluctuating pressure and local heat transfer rate. Eaton & Johnson (1981) gave a detailed review of the investigations of the backward facing step, and later Simpson (1989) reviewed the dynamics of the reattaching shear layers in detail. A summary of some recent investigations of the reattaching process in the flow over a bluff body and a backward facing step are listed in Table 2.2 and 2.3, respectively.

2.3.1 Size of the separation bubble

The mean reattachment length, X_r , was 5.6 to 8.2 step heights, H_s , for the backward facing step (Eaton & Johnson, 1981) and approximately 4.5 to 10 half plate thickness ($H/2$) for a blunt plate (Kiya & Sasaki, 1983, 1985; Saathoff & Melbourne, 1997) or 17.2 to 25.6 fence heights ($H/2$) for a thin splitter plate with a fence (Ruderich & Ferngolz, 1986; Castro & Haque, 1987; Hudy *et al.*, 2003). Eaton & Johnson (1981) noted that the mean reattachment length for a backward facing step can be affected by a number of parameters including whether the boundary layer of the incoming flow was laminar or turbulent, the boundary layer thickness of the incoming flow, δ , the free stream turbulence intensity, the external pressure gradient due to the expansion ratio in the wind tunnel and the aspect ratio of the flow apparatus if it was less than a critical aspect ratio. The attachment length for

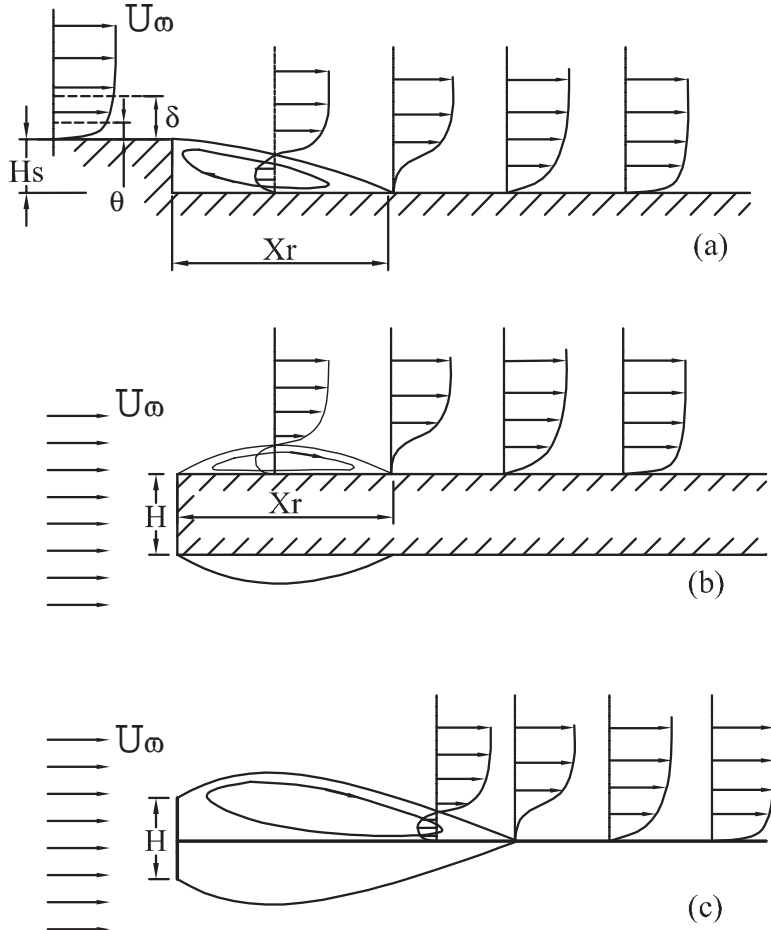


Figure 2.5: Schematic of the flows over (a) a backward facing step, (b) a blunt plate and (c) a splitter plate with fence.

bluff bodies also decreased when the free stream turbulence intensity increased (Saathoff & Melbourne, 1997) due to the enhanced mixing in the shear layer.

2.3.2 Static wall pressure

The static wall pressure coefficients for different reattaching flows are different but the changes are similar and are related to the entrainment process and the streamline curvature of the flow. Initially the static wall pressure decreased slightly to a minimum at $x/X_r \approx 0.4$

to 0.6, before increasing significantly as the separated flow attached to the wall. The local maximum occurred at a location slightly downstream of the reattachment point (Cherry *et al.*, 1984; Hudy *et al.*, 2003; Farabee & Casarella, 1986; Driver *et al.*, 1987; Heenan & Morrison, 1998). The difference between the maximum and minimum static wall pressure ΔC_p was approximately 0.3 for a backward facing step (Farabee & Casarella, 1986; Adams & Johnston, 1988a; Heenan & Morrison, 1998). Adams & Johnston (1988a) noted that ΔC_p increased from 0.24 to 0.34 when the initial boundary layer thickness, δ/H_s , decreased from 1.53 to 0.06.

2.3.3 Skin friction

The distributions of the mean wall shear stress for a backward facing step was also measured using a preston tube technique (Bradshaw & Wong, 1972), a laser-oil interferometer technique (Driver & Seegmiller, 1985; Jovic & Driver, 1995), a pulsed wire probe technique (Vogel & Eaton, 1985; Adams & Johnston, 1988b), a double hotwire probe technique (Spazzini *et al.*, 2001), an electrodiffusion technique (Tihon *et al.*, 2001) and an oscillating hot-wire technique (Li & Naguib, 2003). It was also determined from direct numerical simulation (Le *et al.*, 1997). The skin friction was initially negative in the recirculation region. The mininum skin friction occurred at $x/X_r \approx 0.65$, indicating the strongest reverse flow occurred near this location. The skin friction then increased to zero at the mean reattachment point, and increased further to a maximum at $x/X_r \approx 3$. The maximum and minimum in the skin friction coefficient varied with the Reynolds number. The maximum skin friction coefficient, C_f , changed from 3×10^{-3} to 2×10^{-3} when the Reynolds number changed from 4000 to 27000, while the minimum C_f changed from -2×10^{-3} to -1×10^{-3} (Adams & Johnston, 1988b; Jovic & Driver, 1995; Spazzini *et al.*, 2001).

2.3.4 Turbulence quantities and heat transfer

The turbulent Reynolds stresses in the separated shear layer of the flow over a backward facing step appear to be similar to a free mixing layer in the first half of the separation bubble, but decrease significantly when the shear layer attached to the wall (Chandrsuda & Bradshaw, 1981). Adams & Johnston (1988a) showed that the maximum fluctuating velocity in the separated shear layer of a backward facing step decreased when the initial boundary layer thickness δ/H_s increased. This indicates again that δ/H_s is an important parameter in determining the development of the shear layer and the interaction of the shear layer with the wall.

The periodic sweeping of the wall by the reattaching shear layer caused a significant increase in the fluctuating wall pressure (Cherry *et al.*, 1984; Driver *et al.*, 1987; Heenan & Morrison, 1998; Hudy *et al.*, 2003) and the local heat transfer (Baughn *et al.*, 1984; Vogel & Eaton, 1985; Baughn *et al.*, 1987; Inaoka *et al.*, 2004). The maximum fluctuating wall pressure occurred at a location slightly upstream of the reattachment point in all investigations but the magnitude of the fluctuation varied significantly. Heenan & Morrison (1998) argued that this was caused by the differences in δ/H_s for the case of the backward facing step, where the maximum $C_{p'}$ varied from 0.03 when $\delta/H_s = 1.5$ (Driver *et al.*, 1987) to $C_{p'} = 0.065$ when $\delta/H_s = 0.2$ (Heenan & Morrison, 1998). The value of $C_{p'}$ is much larger in the flow separated from a bluff body, *e.g.* $C_{p'} = 0.13$ to 0.16 (Cherry *et al.*, 1984; Hudy *et al.*, 2003). This may due in part to a smaller initial shear layer thickness of this flow. Eaton & Johnson (1981) noted this earlier and Vogel & Eaton (1985) and Adams & Johnston (1988b) also gave evidence of the relation between δ/H_s and the fluctuations. They found the maximum fluctuating skin friction occurred at the reattachment location and the magnitude increased from $C'_f \approx 1.4 \times 10^{-3}$ to 1.8×10^{-3} when δ/H_s decreased from 1.1 to 0.15.

Vogel & Eaton (1985) showed that the heat transfer from the wall to the flow over a

backward facing step increased significantly and reached a maximum at the same location as the maximum of the fluctuating wall pressure. The maximum heat transfer rate was approximately twice the heat transfer rate for a channel flow. Vogel & Eaton (1985) also found δ/H_s has a significant effect on the convective heat transfer. The Stanton number, $St = h/\rho c_p U$, increased from 3.2×10^{-3} to 4.2×10^{-3} when δ/H_s decreased from 1.1 to 0.15. The heat transfer in the reattachment region was closely associated with the turbulence fluctuations. Far downstream of the reattachment point the heat transfer seemed to associate with the local mean skin friction, and Vogel & Eaton (1985) argued that Reynolds analogy seemed to apply here.

The dynamics of the motions in the reattaching flow has been examined in many investigations using flow visualizations, measurements of the fluctuating velocities, wall pressure, skin friction and numerical simulations. The shear layer formed due to the Kelvin-Helmholtz instability grew similar to a free mixing layer in the first half of the separation region unaffected by the wall (Chandrsuda & Bradshaw, 1981). The initial frequency of the shear layer scaled with the initial momentum thickness, θ , and the free stream velocity (Sigurdson, 1995). The structures in the shear layer underwent pair, triple and even quadruple merging (Smits, 1987) so the characteristic frequency of the shear layer continued to decrease in this region, but did not change significantly in the region $x/X_r > 0.5$ (e.g. Cherry *et al.*, 1984; Farabee & Casarella, 1986). The large scale structures in the shear layer attached to the wall with a convection velocity of approximately $0.5U_\infty$ in the reattaching region. This increased to approximately $0.65U_\infty$ at $x/X_r \approx 2$ (Heenan & Morrison, 1998) indicating the structures were accelerating downstream of the reattachment location. In visualization and numerical studies this attaching process appeared to be like the bursting of separation bubble with vortical structures shed from this bubble so this was usually called shedding type of instability (Kiya & Sasaki, 1983; Hudy *et al.*, 2003). Wee *et al.* (2004) related this shedding to an absolute instability of the separation bubble using a linear instability analysis of DNS data. The characteristic frequency of the shedding varied

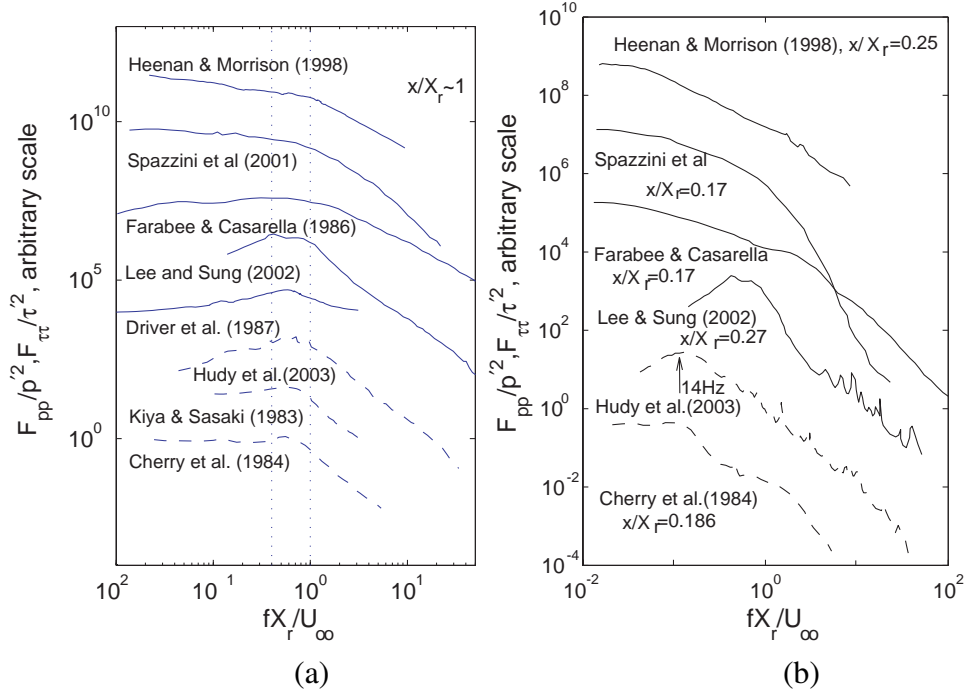


Figure 2.6: Spectra of the fluctuating wall pressure and the fluctuating skin friction (Spazzini *et al.*, 2001) for flow over — a backward facing step and — — a bluff body measured at (a) $x/X_r \approx 1$ (b) $x/X_r \lesssim 0.25$.

in every investigation, but were in the range $fX_r/U_\infty \approx 0.5$ to 1 (e.g. Cherry *et al.*, 1984; Farabee & Casarella, 1986; Driver *et al.*, 1987; Heenan & Morrison, 1998; Lee & Sung, 2002; Hudy *et al.*, 2003) as shown in Fig. 2.6(a).

There is also considerable evidence of another instability with a very low frequency of $fX_r/U_\infty < 0.15$ (Simpson, 1989) that is an order of magnitude smaller than the shedding frequency (e.g. Kiya & Sasaki, 1983, 1985; Cherry *et al.*, 1984; Driver *et al.*, 1987). For example, the pressure spectra measured in the region $x/X_r \approx 0.25$ shown in Fig. 2.6(b) show that the fluctuating energy is concentrated in this low frequency range (Cherry *et al.*, 1984; Farabee & Casarella, 1986; Heenan & Morrison, 1998; Spazzini *et al.*, 2001). Lee & Sung (2002) did not measure the spectrum at low frequency and the peak shown by Hudy *et al.* (2003) may be caused by the poor response of the microphone in the low frequency range $f < 14\text{Hz}$. This instability was often called 'flapping' of the shear layer (e.g. Lee &

Sung, 2002; Spazzini *et al.*, 2001). This name caused confusion because only the flapping in the first half of shear layer seemed to be related to this low frequency instability (Cherry *et al.*, 1984), and the flapping of the streamline in the area $x/X_r > 0.5$ was obviously related to the shedding type of instability (Cherry *et al.*, 1984; Le *et al.*, 1997; Wee *et al.*, 2004). There are a few hypotheses for the cause of this low frequency instability including the instantaneous imbalance of the mass into and out of the separation bubble (Eaton & Johnson, 1981) and a quasi-periodic motion of the secondary separation bubble (Spazzini *et al.*, 2001). Heenan & Morrison (1998) and Hudy *et al.* (2003) found that disturbances were convected both downstream and upstream in the separation bubble with velocities of $U_c \approx 0.5U_\infty$ and $U'_c \approx -0.2U_\infty$, respectively. Heenan & Morrison (1998) showed that the upstream convection and the low frequency unsteadiness was not present when permeable walls was used below the backward facing step. Thus, the results suggested that the low frequency instability was related to the upstream convection. It should be noted this instability contributes only a small part of the total fluctuations near the reattachment point, and not every experimental investigation observed evidence of this instability (e.g. Chandrsuda & Bradshaw, 1981; Ruderich & Ferngolz, 1986).

The large scale vortical structures shed from the separation region keep developing along the wall downstream of the reattachment region. There is a strong correlation between the fluctuating velocity and wall pressure in the region downstream of the reattachment point, indicating the pressure fluctuations were primarily caused by the passing of flow structures (Lee & Sung, 2002). The effect of these traveling structures on the fluctuating wall pressure exists even at 72 step heights away from the separation point (Farabee & Casarella, 1986). The spacing between adjacent large-scale structures was approximately $0.5X_r$ for flow over a backward facing step (Lee & Sung, 2002) and approximately 0.6 to $0.8X_r$ for a reattaching flow over a bluff plate (Cherry *et al.*, 1984; Kiya & Sasaki, 1985).

2.3.5 Periodic forcing of a separated shear layer

Open-loop active control of the separated shear layer was widely used to reduce the size of the separation bubble. Flow control on a backward facing step or a bluff body can be performed using an external loudspeaker (e.g. Bhattacharjee *et al.*, 1986), a zero-injection-mass internal oscillator (e.g. Hasan, 1992; Sigurdson, 1995; Chun & Sung, 1996; Kiya *et al.*, 1997; Yoshioka *et al.*, 2001*a,b*) or miniature oscillating flaps near the lip of the step (e.g. Roos & Kegelman, 1986; Inaoka *et al.*, 2004). The effect of forcing frequency on the length of the separation bubble was discussed in detail by Sigurdson (1995); Kiya *et al.* (1997); Chun & Sung (1996); Yoshioka *et al.* (2001*b*) and others. The most effective forcing frequency was $f_F H_s/U_\infty \approx 0.2$ to 0.55 for backward facing step flows and $f_F H/U_\infty \approx 1.6$ for bluff body flows. In these cases, the reattachment length can be reduced by as much as 30% (Hasan, 1992; Hasan & Khan, 1992; Chun & Sung, 1996; Kiya *et al.*, 1997; Yoshioka *et al.*, 2001*b*; Dejoan & Leschziner, 2004). Chun & Sung (1996) and Dejoan & Leschziner (2004) found that the most effective forcing frequency in the previous investigations when scaled using the initial momentum thickness of the shear layer were $f_F \theta/U_\infty \approx 0.01$. This is similar to the frequency of the unforced Kelvin-Helmholtz instability. The effect of the forcing increases with the forcing amplitude. Sigurdson (1995) found the relation was linear but Kiya *et al.* (1997) found it is logarithmic. Inaoka *et al.* (2004) also found the maximum heat transfer coefficient for a backward facing step flow can be increased by as much as 20% when the forcing frequency is $f_F H_s/U_\infty \approx 0.2$ to 0.35 .

Table 2.1: Summary of experimental investigations of offset planar jet.

| Authors | Aspect ratio | H_s/H_j | Re_{Hj} | Measurements | Main findings |
|----------------------------------|----------------------|--------------|--------------------|---|--|
| Sawyer (1960) | ≥ 48 | 3-24 | 8000 -15 000 | pressure | <ul style="list-style-type: none"> measure the static wall pressure for $Hs/Hj = 3$ to 24. |
| Tanaka & Tanaka (1978a,b, 1981) | radial jet, 28-94 | 0.8-25 | 10 000 - 25 000 | pressure, velocity | <ul style="list-style-type: none"> effect of offset ratio and oblique angle on distributions of static pressure and velocity. |
| Nozaki <i>et al.</i> (1979) | 1-8 | 1.5-65 | 20 000 - 70 000 | velocity, pressure | <ul style="list-style-type: none"> flow was Re dependent when aspect ratio less than 8. |
| Nozaki <i>et al.</i> (1981) | 8 | 1-20 | 10 000 - 50 000 | velocity, pressure | <ul style="list-style-type: none"> when initial u'/U_o increased from 0.4% to 6%, X_r and maximum static wall pressure, P_{max}, decreased 20%, when u'/U_o increased from 6% to 9%, X_r and maximum static wall pressure unchanged. |
| Hoch & Jiji (1981) | 10,19 | 3-8.7 | 1300- 27 000 | pressure, ve- locity | <ul style="list-style-type: none"> reported mean flow, static wall pressure. |
| Lund (1986) | 10, 18 | 0.2- 21.8 | 20 000 | pressure, X_r | <ul style="list-style-type: none"> reported change of X_r with Hs/Hj reported static wall pressure |
| Pelfrey & Liburdy (1986) | 12 | 7 | 15 000 | velocity | <ul style="list-style-type: none"> measured the mean velocity and turbulence intensity. |
| Tanaka <i>et al.</i> (1986a,b,c) | radial jet, 47 | 2-10 | 16 000 | pressure, ve- locity | <ul style="list-style-type: none"> examined effect of blowing and suction control when suction flow rate increase, X_r decreased, P_{max} increased, when blowing flow rate increase, X_r increased, P_{max} decreased. |
| Kim <i>et al.</i> (1996) | 40 in wind tunnel | 0-20 | 6500 - 39 000 | velocity, pressure, heat transfer | <ul style="list-style-type: none"> profile of mean velocity self-similar at $x/H_j \geq 20$ for $Hs/Hj = 5$, maximum Nusselt number $Nu_{max} \propto Re^{0.49}$ for $Hs/Hj = 5$, location of maximum Nusselt number $x \propto (Hs/Hj)^{0.72}$ for $Re=39\,000$. |
| Nasr & Lai (1997) | 30 | 1.625 | 11 000 | velocity | <ul style="list-style-type: none"> reported comparison of U,V, $\langle u^2 \rangle, \langle v^2 \rangle, \langle uv \rangle$ measured for an offset jet and those measured for two parallel plane jets. |
| Nasr & Lai (1998) | 30 | 1.625 | 3300- 15 200 | velocity, pressure | <ul style="list-style-type: none"> reported contours of mean velocity, wall pressure, reported CFD using different RANS models, proposed $x_r/H_j = 2.63(Hs/Hj + 0.5)^{0.855}$ |
| Bremhorst & Agnew (1999) | radial jet, 55 | 9.1 | 7600 | velocity, heat transfer | <ul style="list-style-type: none"> found heat transfer for radial reattaching jets higher than normal impinged jet. |
| Song <i>et al.</i> (2000) | 12 in wind tunnel | 2.5-10 | 53 200 | velocity, pressure, heat transfer | <ul style="list-style-type: none"> locations of maximum Nusselt number and static wall pressure coincide with X_r when oblique angle $\alpha = 0^\circ$, location of maximum Nusselt number coincide with X_r but P_{max} occurs at a downstream location when $\alpha > 0^\circ$. |

Table 2.2: Summary of investigations on the dynamics of reattaching shear layers over a bluff body.

| Authors | Re_H | Measurements | Main findings |
|-------------------------------|--------------------|--|--|
| Kiya & Sasaki (1983) | | velocity, pressure | <ul style="list-style-type: none"> shear layer has a lower growth rate and larger turbulent stresses than a free mixing layer, large scale structures shedding from separation bubble, $f \approx 0.65U_\infty/X_r$ at $x = X_r$ spacing between large scale structures $\Delta x_s = 0.7-0.8X_r$ height of the center of these structures $h_c \approx 0.2X_r$ convection velocity of structures $U_c \approx 0.5U_\infty$ streamwise and spanwise integral length scale $L_{11} = 0.12X_r$, $L_{33} = 0.3X_r$ for $x/X_r \geq 0.8$ |
| Cherry <i>et al.</i> (1984) | 32000 | velocity, pressure, flow vis. | <ul style="list-style-type: none"> low frequency unsteadiness found, cause flapping of shear layer near separation in $x/X_r < 0.6$, shear layer grows like a free shear layer, dominant frequency in shear layer decreases. spacing large scale structure 0.6-0.8X_r convection velocity $U_c \approx 0.5U_\infty$ near reattachment location. three dimensionality increases after reattachment. |
| Kiya & Sasaki (1985) | 26 000 | velocity, pressure | <ul style="list-style-type: none"> flow dominated by large scale structure from shear layer and low frequency unsteadiness of separation bubble showed evidence of hairpin structures in attachment region, with spacing $0.6X_r$. skrinkage faster than enlargement. |
| Ruderich & Ferngolz (1986) | 9 000 - 14 000 | velocity, pressure, skin friction, flow vis. | <ul style="list-style-type: none"> minimum $C_f \approx 0.0029$ to 0.0033 for $Re \approx 9\,000$ to 14 000, occurred at $x/X_r \approx 0.65$ integral length scale increases as flow develops after separation no peak found in the pressure spectra low frequency 'flapping' of shear layer not found |
| Castro & Haque (1987) | 20 000 | velocity, pressure, skin friction | <ul style="list-style-type: none"> minimum $C_f \approx 0.0025$ to 0.0035 for $Re \approx 15\,000$ to 23 000, occurred at $x/X_r \approx 0.65$ shear layer growth not linear, initially higher then gradually decreased at x/X_r, flow dominated by passage of large scale structures. near the separation, there is a unsteady motion with much longer time scale |
| Sigurdson (1995) | 55 000- 132 000 | periodic forcing a axisymmetric separation bubble | <ul style="list-style-type: none"> argue two dominant instability, Kelvin-Helmholtz instability of the shear layer, $f_{KH}\theta/U = \text{const}$, and the shedding of the separation bubble, $f_s h/U \approx 0.08$. f_s much lower than f_{KH} when forcing frequency $f_F \gg f_{KH}$, little effect, when $f_s \ll f_F \lesssim f_{KH}$, shear layer amplified, X_r decreases, when $f_F \approx f_s$, most significant effect on X_r, when $f_F \ll f_s$, little effect |

continue to next page ...

Table 2.2: continued

| Authors | Re_H | Method | Main findings |
|---------------------------------------|--------|--|--|
| Kiya <i>et al.</i> (1997) | 0 000 | forcing axisymmetric separation bubble at double frequencies | <ul style="list-style-type: none"> argued self-excited flow maintained by feedback loop, natural frequency $fX_r/U \approx 0.5$ most effective when forcing frequency $f_F \approx 2^n f_s$, X_r was a logarithmic function of forcing amplitude, integral scale of forced flow was 0.3 to 0.4π at $x/X_r \approx 0.5$, 0.15 to 0.2π at $x/X_r \approx 1$, most effect double frequency forcing $f_{F2} \approx 2f_{F1}$ and phase angle π. |
| Saathoff & Melbourne (1997) | 40 000 | pressure, velocity, flow vis | <ul style="list-style-type: none"> flow vis. simultaneously with wall pressure measurements X_r decreases when free stream turbulence intensity increases |
| Suksangpanomrung <i>et al.</i> (2000) | 50 000 | CFD(LES) | <ul style="list-style-type: none"> 3 subgrid models were compared, selective structure function model give better results than structure function and Smagorinsky models |
| Chun & Sung (2003) | 5600 | velocity, pressure | <ul style="list-style-type: none"> effect of unsteady wake from a cylinder on separation bubble from bluff plate were examined, X_r decreased by the wake, separation bubble 'saw-tooth' movement found. |
| Hudy <i>et al.</i> (2003) | 7900 | pressure | <ul style="list-style-type: none"> disturbance convects up and downstream in region $x/X_r \leq 0.25$, upstream convection velocity $U_c \approx 0.21U_\infty$, upstream convection velocity $0.21U_\infty$ downstream convection velocity $U_c \approx 0.57U_\infty x/X_r > 0.25$ vortex shedding frequency $fX_r/U = 0.6 - 0.9$ at $x/X_r \approx 1$. evidence of absolute instability of the bubble found. |
| Abdalla & Yang (2005) | 6500 | CFD(LES) | <ul style="list-style-type: none"> vortex shedding frequency $fX_r/U = 0.7 - 0.88$. low frequency unsteadiness not found |

Table 2.3: Summary of investigations on the flow over a backward facing step after 1980.

| Authors | Re_{H_s} | Measurements | Main findings |
|------------------------------------|-------------------|------------------------------|---|
| Chandrsuda & Bradshaw (1981) | 10 000 | velocity | <ul style="list-style-type: none"> shear layer develops similar to free shear layer except near wall, Reynolds stresses decreases near wall due to confinement of large eddies. |
| Vogel & Eaton (1985) | 13 000- 42 000 | heat transfer, skin friction | <ul style="list-style-type: none"> reattachment caused a increase in heat transfer by a factor of two slightly upstream of the reattachment point, for $Re=28000$, when δ/H_s increased from 0.15 to 1.1, Stanton number decreased from 0.0042 to 0.0032, at $x/X_r \approx 1$, no mean flow, heat transfer determined by turbulence fluctuations, fluctuating C_f changed from 0.0014 to 0.0018 when δ/H_s decreased from 1.1 to 0.15, at $x/X_r \gg 1$, heat transfer decreased rapidly to flat plate behavior where it was determined by local skin friction, Reynolds analogy applies. |
| Bhattacharjee <i>et al.</i> (1986) | 39 000 | | <ul style="list-style-type: none"> force the flow using external loud speaker, found optimum forcing frequency $f_F H_s/U \approx 0.22$ |
| Farabee & Casarella (1986) | 23 000 | pressure | <ul style="list-style-type: none"> found there were two dominant frequencies in the flow, near the separation, $x/H_s \approx 1$, spectrum rich in very low frequency energy, near the reattachment, $x/X_r \approx 1$, spectrum rich in both the low and high frequency energy, there were two peaks in the spectrum, after reattachment, $x/X_r > 1$, low frequency contents in spectra decreased significantly, high frequency contents decrease gradually but the flow did not reach equilibrium state even at $x/H_s = 72$, within the separation bubble, disturbance only convected downstream. |
| Roos & Kegelman (1986) | 26 000- 76 000 | | <ul style="list-style-type: none"> force the flow using oscillating flaps, found optimum forcing frequency $f_F H_s/U \approx 0.2-0.4$. |
| Driver <i>et al.</i> (1987) | 37 000 | pressure, velocity | <ul style="list-style-type: none"> two type of fluctuations, random flapping of shear layer with $f H_s/U \approx 0.06$ and spanwise vortical structures with $f H_s/U \approx 0.2$, conditional sampling shows amplitude of flapping less than 20% of the thickness of the shear layer, flapping of shear layer contribute little to fluctuating energy, Reynolds shear stress changes when shear layer is flapping, flapping might be caused by the momentary disorder of shear layer that alters the reverse flow rate. |
| Adams & Johnston (1988a) | 800- 40 000 | pressure, velocity | <ul style="list-style-type: none"> studied the effect of Re and initial boundary layer thickness on pressure and turbulence stresses static wall pressure coef. collapsed in $x/X_r < 0.8$ for all the initial boundary layer thickness maximum static wall pressure coef. increases when boundary layer thickness decreases. static wall pressure coef. unchanged when Re was changed and δ/H_s unchanged |

continue to next page ...

Table 2.3: continued

| Authors | Re_{H_s} | Method | Main findings |
|---|--------------------|-------------------------------|--|
| Adams & Johnston (1988b) | 800- 40 000 | skin friction, velocity | <ul style="list-style-type: none"> when initial boundary layer changes from laminar to turbulent , X_r increases sharply, after the transition into the turbulent initial boundary layer, X_r decreases gradually with increasing Re, fluctuating C_f changed from 0.0011 to 0.0013 when δ/H_s decreased from 0.9 to 0.37, X_r independent of Re when $Re > 100\,000$. skin friction seems to be more related to boundary layer thickness, rather than laminar or turbulent. |
| Hasan (1992); Hasan & Khan (1992) | 11 000, 30 000 | | <ul style="list-style-type: none"> force the flow using internal oscillator, found optimum forcing frequency $f_F H_s/U \approx 0.185$. |
| Jovic & Driver (1995) | 5000 - 37 500 | skin friction | <ul style="list-style-type: none"> $C_{f-min} \approx -0.003$ for $Re=5000$, -0.001 for $Re=27500$ at $x/X_r \approx 0.6$ $C_{f-max} \approx 0.003$ for $Re=5000$, 0.002 for $Re=27500$ at $x/X_r \approx 3$. |
| Kasagi & Matsunaga (1995) | 5540 | velocity (PTV) | <ul style="list-style-type: none"> velocity, Reynolds stresses were measured using PTV, $X_r/H_s = 6.51$. |
| Chun & Sung (1996) | 13 000 - 33 000 | | <ul style="list-style-type: none"> force the flow using internal oscillator, found optimum forcing frequency $f_F H_s/U \approx 0.25-0.275$. |
| Le <i>et al.</i> (1997) | 5100 | CFD(DNS) | <ul style="list-style-type: none"> computed flow fields agree with experiments, attachment length $X_r = 6.28H_s$, dominant fluctuations with $fH_s/U \approx 0.06$. |
| Chun & Sung (1998) | 1200 | velocity, pressure, flow vis. | <ul style="list-style-type: none"> flow forced by internal oscillator at $f_F H_s/U = 0.305$ to 0.955, $f_F H_s/U = 0.477$ most effective for laminar separation, X_r decreased by 60% when forcing amplitude was 0.3U. |
| Craft (1998) | 5100 | CFD(k- ϵ) | <ul style="list-style-type: none"> velocity and Reynolds stresses agree Le <i>et al.</i> (1997) |
| Heenan & Morrison (1998) | 190 000 | pressure | <p>examined the flow with impermeable and porous bottom wall, for impermeable wall</p> <ul style="list-style-type: none"> two dominant instabilities, flapping of shear layer with $fX_r/U \approx 0.1$ and large eddy in shear layer $fX_r/U \approx 1$, downstream convection velocity 0.5U-0.7U increases while reattaching, upstream convection velocity -0.2U inside separation bubble, size of the large scale structures from 'busting' of separation bubble $\approx 2.2H_s$, size of structure in shear layer $\approx 0.7H_s$ at $x/H_s \geq 4$, porous bottom wall increases X_r, reduces pressure fluctuation and drag, |
| Scarano <i>et al.</i> (1999) | 5000 | velocity (PIV) | <ul style="list-style-type: none"> structure in shear layer length scale $0.12 - 0.44H_s$, spanwise roller spreading linearly in region $0.8 \leq x/H_s \leq 3.5$, showed evidence of early 3 dimensional broke down of primary rollers. |
| Manceau <i>et al.</i> (2000) | 5100 | CFD($v^2 - f$) | <ul style="list-style-type: none"> velocity and Reynolds stresses agree Le <i>et al.</i> (1997) |

continue to next page . . .

Table 2.3: continued

| Authors | Re_{H_s} | Method | Main findings |
|----------------------------------|-------------|---|--|
| Rhee & Sung (2000) | 33 000 | CFD(modified $k - \epsilon$) | <ul style="list-style-type: none"> force the flow using internal oscillator, found optimum forcing frequency $f_F H_s/U \approx 0.275$. good agreement with experiments(Chun & Sung, 1996) |
| Lee & Sung (2001) | 33 000 | pressure | <ul style="list-style-type: none"> two dominant frequencies found, low frequency related to flapping, high frequency from shear layer. |
| Spazzini <i>et al.</i> (2001) | 3500-16 000 | skin friction | <ul style="list-style-type: none"> X_r evaluated using locations of $C_f = 0$ and 50% forward flow rate agree $X_r \approx 5$ for $Re=3500$, $X_r \approx 6.5$ for $Re=16000$, $C_{f-min} \approx -0.0028$ for $Re=3500$, -0.0013 for $Re=16000$ occurred at $x/X_r \approx 0.65$, $C_{f-max} \approx 0.0031$ for $Re=3500$, 0.002 for $Re=16000$ at $x/X_r = 3$, there exists a secondary bubble with a very low frequency quasi periodic motion corresponding to the flapping of the shear layer. |
| Yoshioka <i>et al.</i> (2001a,b) | 3700 | velocity (PIV) | <ul style="list-style-type: none"> measured U, V, u', v', $\langle uv \rangle$ unforced and forced at $f_F H_s/U = 0.04$ to 0.3, forcing at $f_F H_s/U = 0.19$ most effective, which is twice as the vortex shedding frequency, X_r reduced 30%. the decrease in X_r is correlated with the increase in the production of Reynolds shear stress. when $f_F H_s/U \approx 0.19$, Reynolds stresses at $x \approx X_r$ increases. when $f_F H_s/U > 0.19$, Reynolds stresses in the early stages of the recirculation region increases. when $f_F H_s/U < 0.19$, Reynolds stresses at $x > X_r$ increases. |
| Bredberg <i>et al.</i> (2002) | 5100 | CFD($k-\omega$) | <ul style="list-style-type: none"> velocity and Reynolds stresses agree Le <i>et al.</i> (1997) |
| Lee & Sung (2002) | 33000 | pressure, velocity | <ul style="list-style-type: none"> found the wall pressure fluctuations were primarily caused by the vortical structures in the shear layer, convection velocity of these structures $U_c \approx 0.6U$ these structures were modulated by the flapping of shear layer, illustrated using a band pass filter with $0.05 \leq f H_s/U \leq 0.08$. |
| Dejoan & Leschziner (2004) | 3700 | CFD(LES) | <ul style="list-style-type: none"> shedding type of instability with $f H_s/U = 0.077$ dominate the flow near $x/X_r \approx 1$, these structure convected downstream at $0.4U$, most effective forcing frequency $f_F H_s/U = 0.2$, X_r decreased by 30%. |
| Inaoka <i>et al.</i> (2004) | 1000 | heat transfer, forced by oscillating flap | <ul style="list-style-type: none"> forced at $f_F H_s/U = 0.2$ to 4, most effective at $f_F H_s/U = 0.2$ to 0.35, X_r decreases 30%, h increased 20% |

Chapter 3

Experimental Methodology

This chapter describes the experimental facility and the techniques used in the current investigation. The experimental facility will be described first. The experimental techniques used to measure the flow velocity, wall pressure, skin friction and convective heat transfer are then discussed.

3.1 Experimental Facility

The development of the jets was examined using a facility shown in Fig. 3.1 where the two jets in this facility exited long channels. The air flow, supplied from a blower with a 10 HP motor, was split into a 122cm by 72.4cm by 45.7cm settling chamber attached to the upper channel, and a 81.3cm by 40.6cm by 22.9cm settling chamber attached to the lower channel. The hose connections included gate valves that were used to adjust the flow rate to the jets. Both settling chambers included layers of foam and perforated plates to condition the flow. The width of both channels were 74.3cm. The height of the upper channel was 3.8cm so the ratio of the outer jet width to its height is 19.5, while the height of the inner jet was 1.9cm so the aspect ratio of this jet was 39. The length of the upper channel was 81.3cm so the ratio of the outer jet length to its height was 21, while the length of the lower channel was 50.8cm so the ratio of the inner jet length to its height was 27. The entrances

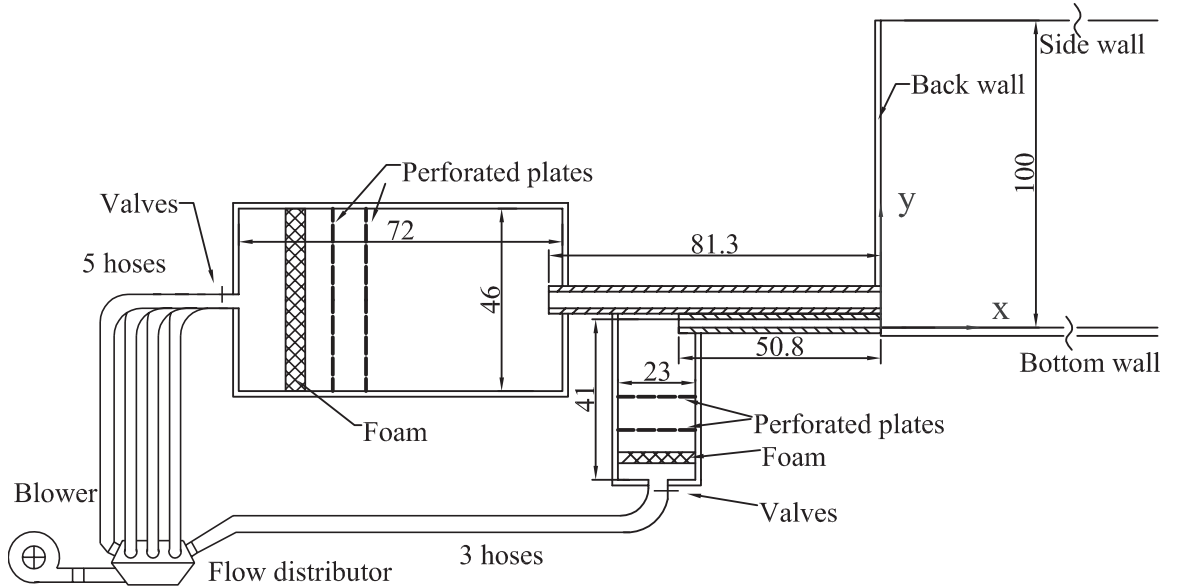


Figure 3.1: Schematic of the experimental facility, units in *cm*.

and the exits of both channels had machined square edges. The facility initially included bell mouths at the entrance of the channels, but it was found that the exit profiles were more uniform for the square channel entrance.

The profiles of the mean velocity and turbulent stresses measured at the exit of the jets (shown in Fig. A-1 in the Appendix) are reasonably symmetric when the flow was configured as two dimensional free jets. The flow at the channel exit are similar to fully developed channel flow. For example, the distribution of the Reynolds stress $\langle uv \rangle$ varies linearly across the exit of the jets. The profiles measured along both channels outlet, shown in Fig. A-3, are uniform over the central region of the jet from $-6 \leq z/H_j \leq 6$ with variations in mean and rms velocity less than $\pm 1\%$ and $\pm 2.5\%$, respectively.

The flow exiting the channels develops over a 1.8m long bottom plate that was mounted parallel to the channels. The facility was aligned by initially aligning the streamwise axes of the channels with the axis of the traversing mechanism. After alignment, the angle between the axes of the upper channel and the traversing mechanism was found to be less than 0.2° based on the velocity profiles of the upper jet measured at different streamwise

locations when it was configured as a free jet, shown in Fig. A-6. The angle between the axes of the lower channel and the traversing mechanism was found to be less than 0.1° . The angle between the bottom wall and the streamwise axis of the traversing mechanism was checked using a dial indicator and it was found the angle was less than 0.2° .

The flow was here confined on both sides using two 100cm high and 180cm long side walls and behind the jet using a 80cm high back wall. The effect of the side walls on the two dimensionality of the jets was also checked by measuring the boundary layer on the side walls as the flow evolved downstream, shown in Fig. A-4. The distributions of the fluctuating velocities in the y-z planes were also measured at 17 by 21 equally spaced locations at $x/H_j = 12$ and the contours are shown in Fig. A-5. The measurements show that the thickness of the boundary layer over the side wall grows slowly and the profiles of fluctuating velocities are nearly identical in the region $-4 \leq z/H_j \leq 4$ at $x/H_j = 12$. In the experiments of the single offset jet, the jet not in use was sealed using tape. The offset distance of the jet was changed by adjusting the supporting threaded rods to move the bottom wall in the vertical direction. The ratio of the offset distance of the jet to the jet height, H_s/H_j , was changed between 0 and 1.2. In the co-flowing jet experiments, the lower edge of the outer jet was positioned 3.8 cm above the wall, so ratio of the offset distance to the jet height, H_s/H_j , was 1. The height of the splitter plate between the two jets, H_c , in most of the measurements was 1.9 cm. Measurements were also performed for a second case when a 50.8cm long and 74.8cm wide removable center plate was added in the lower channel as shown in Fig. 3.2. This removable plate was held in place using screws in the four corners. The total height of the splitter plate in that case was 3.1 cm, so the height of the lower jet was 0.7 cm.

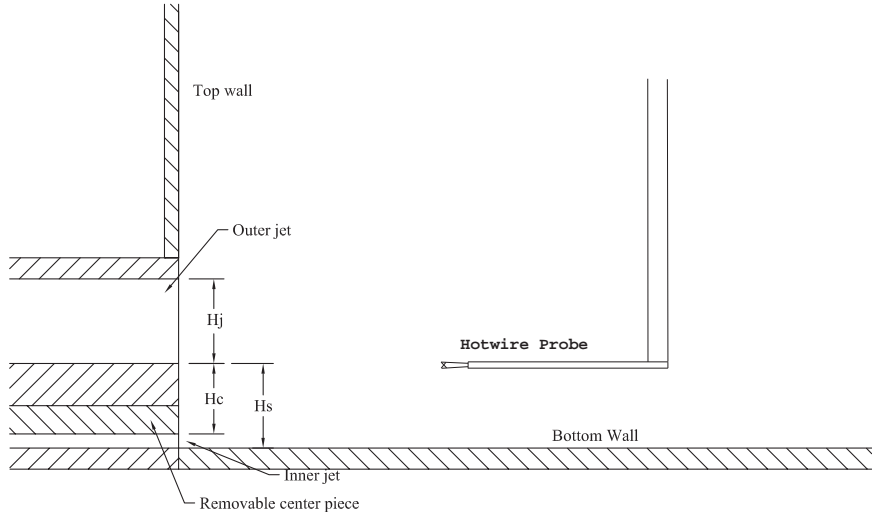


Figure 3.2: Schematics of the experimental facility.

3.2 Hotwire anemometry

The development of the flow field in the offset jets was measured using single and cross hot-wire probes and an in-house anemometry system designed based on the bridge proposed by Perry (1982). Sun (2002) commissioned the in-house anemometry system and compared its performance with that of a Dantec DISA 55M system and a A.A. LAB AN-2000 system. Sun (2002) found they were in good agreement. The measurements were performed using single and cross-wire probes with wire diameters of $5\mu\text{m}$ and length of approximately 1.5 mm . The flow field was measured by moving the hot-wire probes on a computer controlled traverse that could be positioned with an accuracy less than 0.05mm . The probe was held using a 4.8 mm diameter probe holder that was mounted on the traversing mechanism using a 12.7 mm diameter 50 cm long rod at a position 12 cm downstream of the hot-wire sensor.

3.2.1 Calibration

The hot-wire probes were calibrated in a separate round jet facility where the jet exited a contoured nozzle with an outlet diameter of 9.9mm. The uniformity of the mean velocity at the exit of the nozzle was found to be within 1% and the turbulence intensity was less than 1%. The probe was placed approximately 0.5 diameter downstream of the nozzle. The velocity of the jet was determined using the static pressure measured 10cm upstream of the contraction. The pressure was measured using a VALIDYNE DP45 differential pressure transducer with a 6-26 D209-96A diaphragm, which was calibrated using a Crystal IS33 pressure gauge.

The single wire probes were calibrated by measuring the output voltages of hot-wire anemometer for different velocities at jet exit. The voltage was recorded for 15 to 20 velocities in the range of the experiment. The voltage was sampled at 1024Hz for a total time of 10 seconds for each velocity. The result was then fitted using a fourth degree polynomial to form the calibration curve given by (Bruun, 1995)

$$U = C_0 + C_1 E + C_2 E^2 + C_3 E^3 + C_4 E^4 \quad (3.1)$$

where C_0 to C_4 are the calibration constants, E is the voltage output from anemometer and U is the streamwise components of mean velocity. The typical error in the fit was less than 0.2%.

The cross-wire probes were calibrated in the same facility using the method proposed by Champagne & Sleicher (1967) where the effective cooling velocities were given by

$$U_{eff1}^2 = U^2 [\sin^2(\phi_1) + k_1^2 \cos^2(\phi_1)], \quad (3.2)$$

and

$$U_{eff2}^2 = U^2 [\sin^2(\theta - \phi_1) + k_2^2 \cos^2(\theta - \phi_1)]. \quad (3.3)$$

Here, U_{eff1} and U_{eff2} are the effective velocities sensed by the two wires, U is the actual velocity k_1^2 and k_2^2 are the angular sensitivity for the two wires, ϕ_1 is the angle between

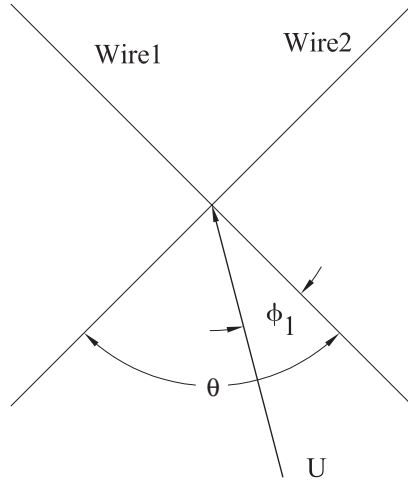


Figure 3.3: Cross-wire geometry.

wire 1 and U and θ is the angle between the two wires as shown in Fig. 3.3.

The procedure of the calibration follows that given by Glauser (1987), Sun (2002) and Hall (2005). The cross-wire probe was initially exposed to a known flow velocity, and was rotated at a step of 1° using a stepper motor until θ was found. Each wire was then positioned perpendicular to the flow direction and calibrated similar to a single wire probe. The angular sensitivity coefficients were determined by measuring the voltage output for different angles for fixed jet velocity. Equations 3.2 and 3.3 were then fit to curves of $U_{eff}(\phi)$. The angle between the wires was found to be $\theta \approx 90^\circ$ and the angular sensitivity coefficients were determined to be $k_1^2 = k_2^2 = 0.15 \pm 0.03$ for $\phi = 5^\circ$ to 60° in agreement with Champagne *et al.* (1967). The angular sensitivity of the wire was essentially independent of the velocity for a range $U = 8$ to 45 m/s.

When the cross-wire probe was mounted on the traverse in the experiments, the probe was first visually aligned to the wall. The alignment of the probe was then checked by measuring the mean velocity profiles at 20 jet heights downstream of the jet exit, where the jet develops similar to a planar wall jet. In all cases the measured angle of mean flow near the wall was less than 0.5° . It was assumed the actual angle at this point should be

approximately zero so this measured angle was taken as the error in aligning the probe. This angle was then used through all further measurements until the probe was removed from the flow for recalibration.

3.2.2 Errors in hot-wire measurements

There are several error sources for hot-wire measurements, including cross-flow error, rectification error, error due to the limited sample time and error due to changes in the flow temperature. The sources of these errors and the estimations of each of these errors are discussed in detail below.

Rectification error

Rectification error in hot-wire measurements occurs when the actual velocity vector falls outside of the cone of acceptance in multi-wire measurements. As a result, the computed velocity is on the other side of the wire as shown in Fig. 3.4. The rectification error becomes significant in the flow with large turbulence intensity. Following Tutu & Chevany (1975), the occurrence of rectification can be examined using the phase diagram of the effective velocities. The cone of acceptance, where the velocity that can be unambiguously resolved, was defined as the region between lines (Tutu & Chevany, 1975)

$$U_{eff1} = k_1 U_{eff2} \quad (3.4)$$

and

$$U_{eff2} = k_2 U_{eff1}. \quad (3.5)$$

If the density of the effective velocity points falling near the boundary lines is large, the measurements include a significant rectification error.

The phase diagrams of the effective velocities were checked for a number of locations near the reattachment region where the turbulence intensity was the largest in the current flow. The phase diagrams of the effective velocities measured at $y/H_j = 0.5$ and $x/H_j = 4$

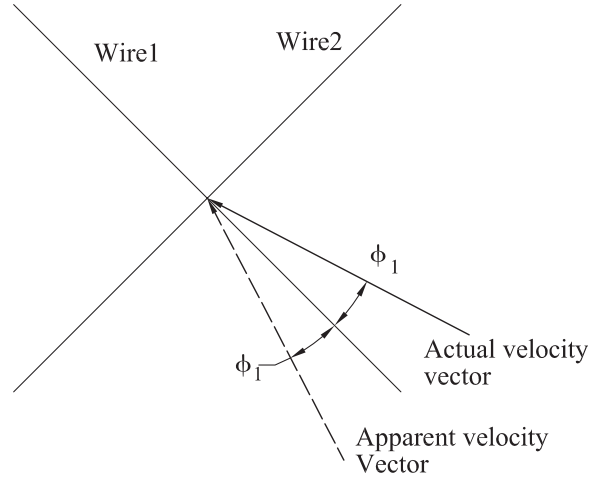


Figure 3.4: Schematic showing rectification using a cross-wire probe.

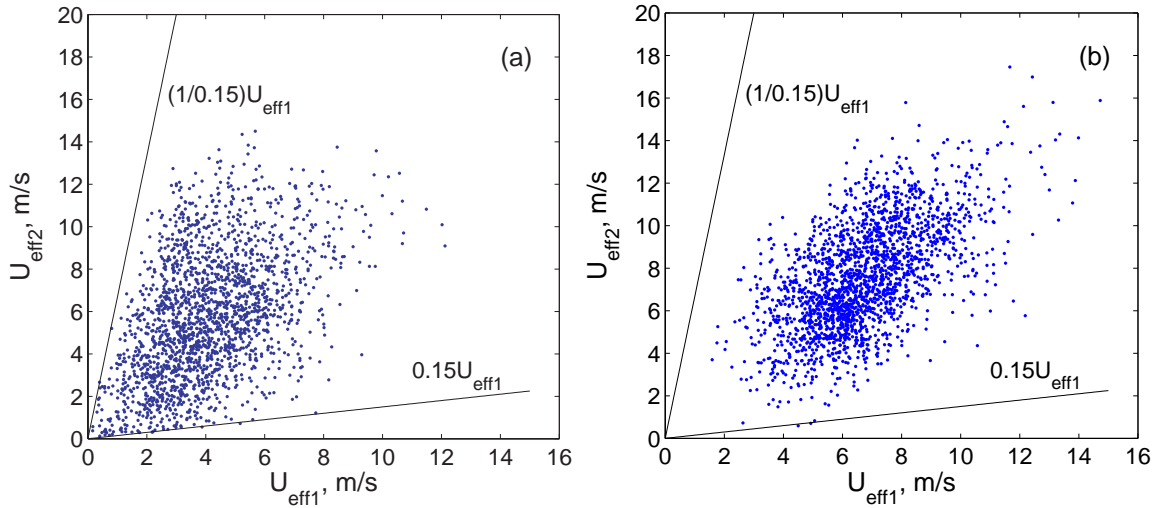


Figure 3.5: Scatter plots of effective cooling velocities at (a) $x/H_j = 4$, $y/H_j = 0.4$ (b) $x/H_j = 5$, $y/H_j = 0.4$ in an offset attaching jet with $H_s/H_j=1$.

Table 3.1: Cross-flow errors in hot-wire measurements (Shabbir *et al.*, 1996)

Single wire:

$$\Delta U = \frac{1}{2} \frac{V^2 + \bar{v}^2}{U} - \frac{1}{2} \frac{\bar{u}\bar{v}}{\bar{U}^2} - \frac{V\bar{u}\bar{v}}{\bar{U}^2} + \dots$$

$$\Delta \bar{u}^2 = \frac{2V\bar{u}\bar{v} + \bar{u}\bar{v}^2}{U} + \frac{V^2\bar{v}^2 - V^2\bar{u}^2 + V\bar{v}^3 - \bar{u}^2\bar{v}^2 - 2V\bar{u}^2\bar{v}}{\bar{U}^2} + \frac{1}{4} \frac{\bar{v}^4 + \bar{v}^2}{\bar{U}^2} + \dots$$

Cross wire:

$$\Delta U = \frac{1}{1+k^2} \left[\frac{\bar{w}^2}{U} - \frac{\bar{u}\bar{w}^2}{\bar{U}^2} + \frac{\bar{u}^2\bar{w}^2}{\bar{U}^3} - 2 \frac{\bar{w}^4}{\bar{U}^3} + \dots \right]$$

$$\Delta \bar{u}^2 = \frac{2\bar{u}^2}{1+k^2} \left[\frac{\bar{u}\bar{w}^2}{\bar{u}^2 U} - \frac{\bar{u}^2\bar{w}^2}{\bar{u}^2\bar{U}^2} + \frac{1}{2} \left(\frac{\bar{w}^4 - (\bar{w}^2)^2}{\bar{u}^2\bar{U}^2} \right) + \dots \right]$$

and 5 are shown in Fig. 3.5 (a) and (b), respectively. It is clear the distributions were away from the boundary at $x/H_j = 5$ indicating the rectification error are small in the area downstream of the attachment point. However, there are a significant number of points near the boundary lines in the first graph indicating significant errors. Data measured in the region with large rectification errors are excluded.

Cross flow error

The cross-flow error is caused by the contribution from the velocity component perpendicular to the hot-wire sensors, \tilde{w} , that can not be resolved. The cross-flow error for the current investigation are listed in Table 3.1 following the approach outlined by Shabbir *et al.* (1996) and Sun (2002) where Δ represents the error. Estimation of the cross-flow errors in the streamwise mean and fluctuating velocity using a cross-wire probe for an offset attaching jet with $H_s/H_j = 1.0$ are shown in Fig. 3.6. The largest cross flow error is approximately 4% in the mean streamwise velocity and 8% in the square mean value of the streamwise fluctuating velocity, occur near the reattachment location and in the outer part

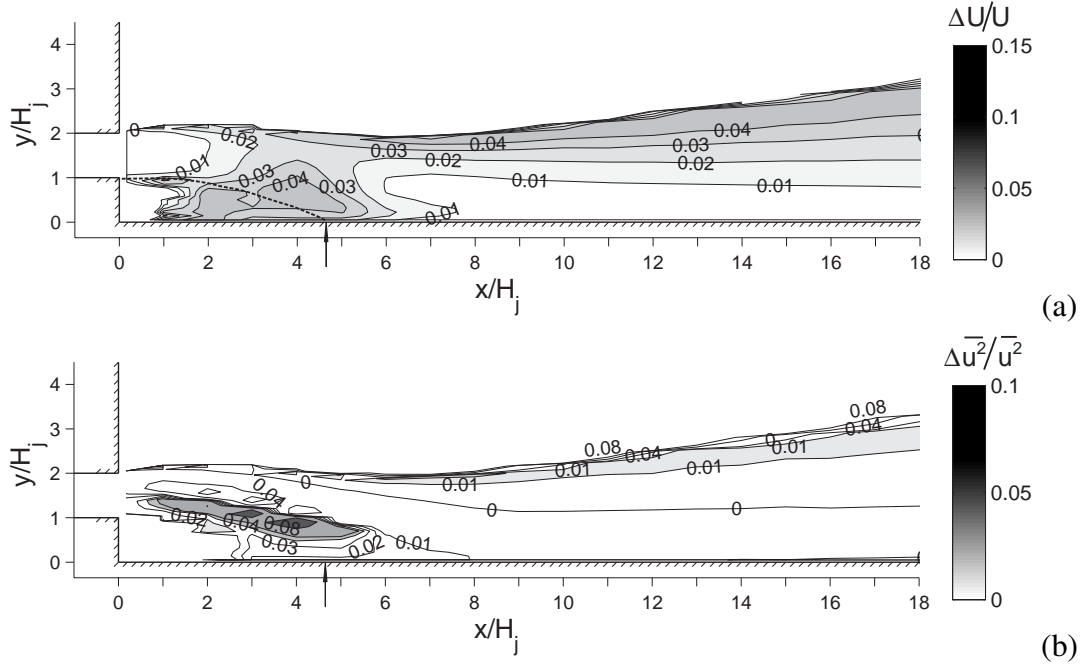


Figure 3.6: Estimation of cross flow errors in (a) the streamwise mean velocity and (b) the mean square value of the streamwise fluctuating velocity in an offset attaching jet with $H_s/H_j = 1.0$ and $Re = 44000$.

of the jet downstream of the reattachment location where the rms velocities are large.

Errors associated with the limited sample time

The sampling time t_s required to accurately resolve the single point measurements can be estimated following the approach given by George *et al.* (1978). For example, the relative errors in the mean streamwise velocity and the mean square value of the fluctuating streamwise velocity are given by (George *et al.*, 1978)

$$\xi_U = \frac{\sqrt{\bar{u}^2}/U}{\sqrt{N}}, \quad (3.6)$$

$$\xi_{\bar{u}^2} = \frac{1}{\sqrt{N}} \sqrt{\frac{\bar{u}^4}{\bar{u}^2^2}}, \quad (3.7)$$

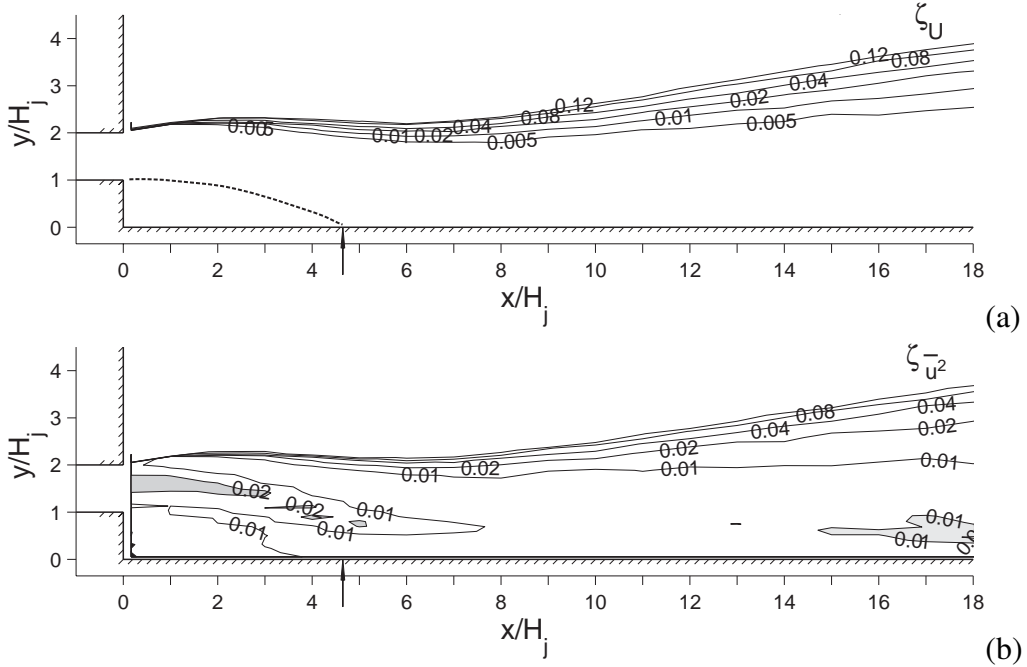


Figure 3.7: Estimated errors due to limited sampling time for 95% confidence interval in (a) the streamwise mean velocity and (b) the mean square value of the streamwise fluctuating velocity in an offset attaching jet with $H_s/H_j = 1.0$ and $Re = 44000$.

where N , the number of independent measurement points, is given by

$$N = t_s/2\tau_l. \quad (3.8)$$

Here, t_s is the total sampling time and τ_l is the integral time scale of the flow given by

$$\tau_l = \frac{1}{\bar{u}^2} \int_o^\infty R_{uu}(\tau) d\tau, \quad (3.9)$$

where R_{uu} is the two-time correlation of streamwise fluctuating velocity. The two-time correlation was determined by inverse Fourier transforms of the spectrum at different locations in order to estimate the error.

At each location of the single point measurements, the output signal from the anemometry system was sampled using a 14-bit A/D board at a frequency of 4096Hz for a total time of 50 seconds. The errors in the mean streamwise velocity and the mean square value

of the fluctuations velocity due to the sampling time in a typical case are shown in Fig. 3.7. The errors were less than 1% for the mean streamwise velocity and 2% for the mean square value of the fluctuating streamwise velocity at the 95% confidence interval. This is typical of all the experiments. Thus, the sampling time was sufficient.

Errors associated with air temperature variations

The ambient air temperature during the measurements was measured using a RTD temperature sensor with a resolution of 0.1°C . The temperature varied less than $\pm 1^{\circ}\text{C}$ in all cases, and the effect of the temperature on the velocity measurements was compensated using the technique proposed by Beuther (1980). The calibration constants for the hot-wire were modified, so that the equation 3.1 became

$$U = C_0 + C_1 E \left(\frac{T_s - T_{f,c}}{T_s - T_{f,m}} \right)^{1/2} + C_2 E^2 \left(\frac{T_s - T_{f,c}}{T_s - T_{f,m}} \right)^1 \\ + C_3 E^3 \left(\frac{T_s - T_{f,c}}{T_s - T_{f,m}} \right)^{3/2} + C_4 E^4 \left(\frac{T_s - T_{f,c}}{T_s - T_{f,m}} \right)^2, \quad (3.10)$$

where T_s is the probe temperature set at 230°C for over heat ratio of 1.8 (Bruun, 1995), and $T_{f,c}$ and $T_{f,m}$ are the air temperature during the calibration and measurement, respectively. Sun (2002) showed this was effective when the room temperature changed from 22.8°C to 25.5°C . The resulting error in the mean velocity measurements was approximately $0.4\%/\text{ }^{\circ}\text{C}$.

3.3 Static and fluctuating wall pressure measurements

The static pressure on the bottom wall was measured using a series of pressure taps mounted along the jet centerline of the wall. The pressure taps were 0.16 cm diameter stainless steel tubes. The pressure taps were located at a spacing of $0.5H_j$ in the region $1 \leq x/H_j \leq 8$, and at a spacing of H_j in $9 \leq x/H_j \leq 12$. The pressure was measured using a VALIDYNE

DP45 differential pressure transducer with a 6-26 D209-96A diaphragm, which was calibrated using a Crystal IS33 pressure gauge.

The fluctuating pressure was measured using 16 Panasonic WM-61B microphones that have a flat response for 20Hz to 5000Hz. A sketch of the typical frequency response curve for this type of microphone given by the manufacturer are shown in Fig. 3.8. The microphones were mounted directly into blind cavities drilled from the bottom of the wall on a line 0.75 cm off the centerline of the jet. The cavities were located at a spacing of $0.25H_j$ in the region $0.25 \leq x/H_j \leq 2$, at a spacing of $0.5H_j$ in $2 \leq x/H_j \leq 8$ and at a spacing of H_j in $8 \leq x/H_j \leq 16$. The microphones sense the flow through a 1mm-diameter, 5mm-long pinhole drilled through the wall to the top of the cavity as shown in Fig. 3.9. The use of the pinhole instead of flush mounting the microphone on the surface reduced any potential interference of the flow field by the microphones. The microphones were calibrated using a piston phone at 1000Hz before they were mounted. The signals from microphone were simultaneously acquired with the 14-bit A/D board in 100 independent blocks of 4096 data points at a frequency of 4096Hz. The uncertainties for the fluctuating wall pressure due to the sample time were less than 2% for 95% confidence interval.

The spectra of the fluctuating wall pressure measured through the pinholes were compared with the spectra measured with the flush mounted microphones. The spectra of the fluctuating wall pressure measured near the reattachment location for a single offset attaching jet with $H_s/H_j = 1.0$ using these two setups are compared in Fig. 3.10. The difference in the fluctuations with frequency less than 500Hz was small. This frequency was larger than frequency of interest in the current study indicating the error in the fluctuating wall pressure associated with the damping in the pinhole was small.

The development of the large scale structures was examined by studying the correlation coefficient of the fluctuating wall pressure measured at different streamwise locations, given by

$$\rho_{pp}(x_1, x_2, \tau) = R_{pp}(x_1, x_2, \tau)/p'(x_1)p'(x_2), \quad (3.11)$$

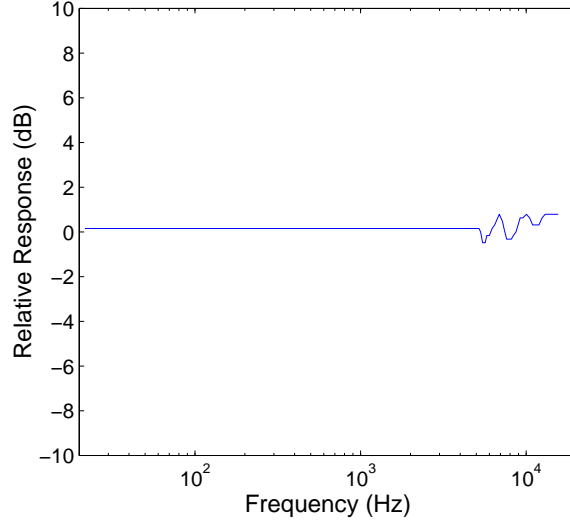


Figure 3.8: Sketch of typical frequency response curve of Panasonic WM-61B microphones given by the manufacturer (Panasonic, 2006).

where τ is the time delay and the cross correlation $R_{pp}(x_1, x_2, \tau)$ was computed by inverse Fourier transforming the cross spectra, *i.e.* ,

$$R_{pp}(x_1, x_2, \tau) = \int_{-\infty}^{\infty} \Phi(x_1, x_2, f) e^{i2\pi f \tau} df. \quad (3.12)$$

The cross spectra $\Phi(x_1, x_2, f)$ was given by

$$\overline{\hat{p}(x_1, f) \hat{p}^*(x_2, f')} = \Phi(x_1, x_2, f) \delta(f - f'), \quad (3.13)$$

where δ is the Dirac delta function, \hat{p} is the Fourier transform of the transient wall pressure, and $*$ represents the complex conjugate. These spectra were computed by averaging the results for different blocks

$$\Phi(x_1, x_2, f) = \frac{\overline{\hat{p}(x_1, f) \hat{p}^*(x_2, f)}}{T}, \quad (3.14)$$

where T is the sampling time for each data block. The spectra here were presented in terms of half-line spectra, $|F_{pp}(x_1, x_2, f)|$. The uncertainty in the magnitude of the spectra was less than $\pm 2/\sqrt{N}$ at the 95% confidence interval (Bruun, 1995), where N is the number

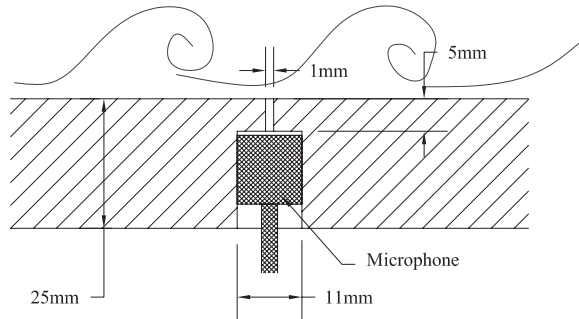


Figure 3.9: Schematic showing how the microphone was embedded in the wall.

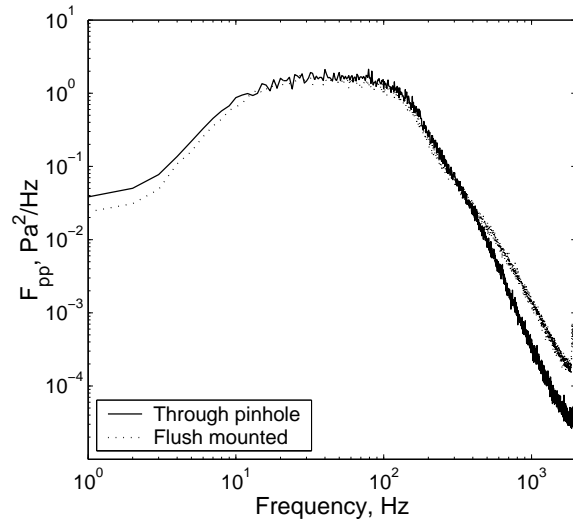


Figure 3.10: The spectra of fluctuating wall pressure near the reattachment location, $x/H_j = 4.5$, for the jet with $H_s/H_j = 1$ measured using a microphone flush mounted on the wall and through the pinhole.

of independent data blocks. The spectra were computed here using 100 blocks of data so the uncertainty in the magnitude of the spectra of fluctuating wall pressure was less than $\pm 20\%$ in the current investigation.

The nature of the relationship between the pressure at the two points was also examined using the coherence of the pressure fluctuations measured at two locations given by,

$$\gamma_{pp}^2(x_1, x_2, f) = \frac{|\Phi(x_1, x_2, f)|^2}{\Phi(x_1, x_1, f)\Phi(x_2, x_2, f)}, \quad (3.15)$$

and the phase angle of the cross spectrum, $\theta_{pp}(x_1, x_2, f)$ given by

$$\theta_{pp}(x_1, x_2, f) = \tan^{-1} \left(\frac{\text{img}(\Phi(x_1, x_2, f))}{\text{real}(\Phi(x_1, x_2, f))} \right). \quad (3.16)$$

The development of the structures in the flow was examined by performing simultaneously measurements of the fluctuating wall pressure and fluctuating velocities. The output signals of microphones and hot-wires were sampled at a frequency of 2048Hz for 150 independent blocks of 1024 data points per block. The cross correlations of the fluctuating wall pressure and the fluctuating velocities, R_{pu} and R_{pv} , and the cross spectra, F_{pu} and F_{pv} , were computed using the equations shown above, with $\hat{p}^*(x_2, f)$ replaced with $\hat{u}^*(x, y, f)$ or $\hat{v}^*(x, y, f)$. The spectra were computed here using 150 blocks of data so the uncertainty in the magnitude of the cross spectra was less than $\pm 15\%$ at the 95% confidence interval.

3.4 Skin friction measurements

The skin friction, τ_w , on the wall was measured using a thin-oil-film interferometry technique, which is based on the behavior of a thin oil film applied on the wall surface subjected to a shear from the flow. In this approach, the change in the oil film thickness over time is used to characterize the skin friction. The thickness of the oil film was determined here by examining the interference fringe pattern on the surface of the oil film illuminated with a single wave length light source. The background and development of this method and other related methods are reviewed in detail in Naughton & Sheplak (2002).

The relationship between the thickness of the oil film and the viscous shear of the flow, the pressure gradient, gravity and surface tension is given by (Brown & Naughton, 1999)

$$\begin{aligned} \frac{\partial h_f}{\partial t} + \frac{\partial}{\partial x} \left[\frac{\tau_{w,x} h_f^2}{2\mu} - \frac{h_f^3}{3\mu} \left(\frac{\partial P}{\partial x} - \frac{\partial}{\partial x} \left\{ \sigma \left(\frac{\partial^2 h_f}{\partial x^2} + \frac{\partial^2 h_f}{\partial z^2} \right) \right\} - \rho g_x \right) \right] \\ + \frac{\partial}{\partial z} \left[\frac{\tau_{w,z} h_f^2}{2\mu} - \frac{h_f^3}{3\mu} \left(\frac{\partial P}{\partial z} - \frac{\partial}{\partial z} \left\{ \sigma \left(\frac{\partial^2 h_f}{\partial x^2} + \frac{\partial^2 h_f}{\partial z^2} \right) \right\} - \rho g_z \right) \right] = 0, \end{aligned} \quad (3.17)$$

where P is the external static pressure, h_f is the thickness of the oil film and μ is the viscosity of the oil. The thickness of the oil-film is small in most applications (usually 1 to $2\mu m$), so the skin friction term is 2 to 3 orders of magnitude larger than the pressure gradient and gravitational terms and much larger than the surface tension term (Naughton *et al.*, 2006). The flow in the current investigation is two-dimensional. Thus, the oil film equation can be reduced to

$$\frac{\partial h_f}{\partial t} + \frac{\partial}{\partial x} \left(\frac{\tau_{w,x} h_f^2}{2\mu} \right) = 0. \quad (3.18)$$

The solution to this equation can be obtained by solving the iterative equation (Naughton *et al.*, 2006)

$$C_{f,i+1}^{1/2} = \frac{\int_0^x (n/C_{f,i})^{1/2}}{h_f \sqrt{n} \int_0^t (q/\mu) dt}, \quad (3.19)$$

where C_f is the skin friction coefficient, q is the dynamic head of the free stream and n is the streamline divergence (which is 1 for two dimensional flows). The initial guess for the iteration process is normally the solution for the case with constant skin friction (Naughton *et al.*, 2006)

$$C_{f,1} = \frac{\mu x}{q h_f t}. \quad (3.20)$$

The thickness of the oil film was monitored using an image-based global interferometry measurements technique (Garrison & Ackman, 1998; Brown & Naughton, 1999). The central part of the bottom wall was covered using a 91cm by 13cm thin Mylar film (Monokote Industries, Topflight black) as shown in Fig. 3.11. Dow Corning 200 Fluid with a nominal viscosity of 20cts was applied on the Mylar film before the test was started. In most of

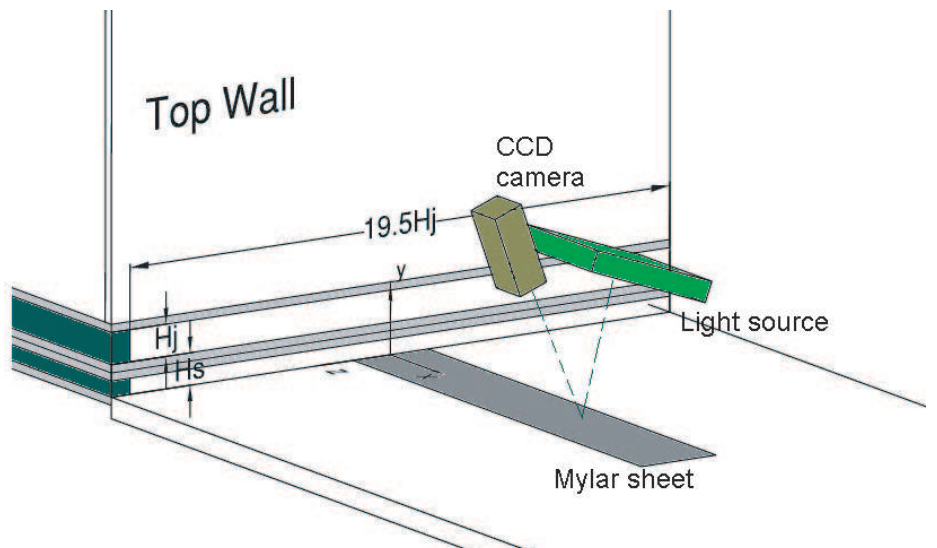


Figure 3.11: Schematic of the setup for the oil-film interferometry measurements.

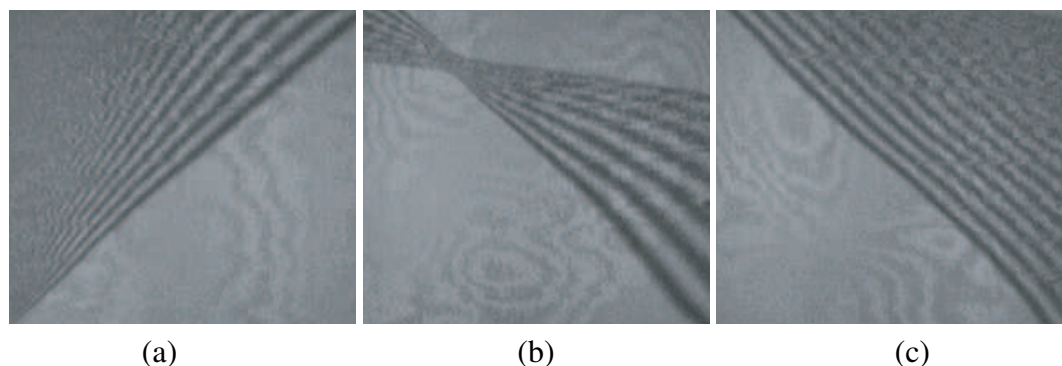


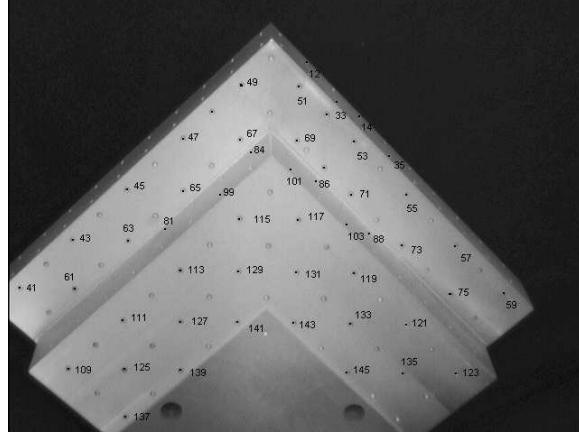
Figure 3.12: Typical fringe patterns (a) in the recirculation region, (b) near the attachment point and (c) downstream of the attachment point.

the cases, the oil was applied as a line approximately 45° to the direction of the main flow. The oil film was illuminated using a green mono lamp with wave length $\lambda = 546nm$. The test was then started and run at the desired condition. The resulting fringe patterns were acquired using A Pulnix TMC-7DSP CCD camera and a Matrox Meteor II frame grabber. After the experiment was started, computer sent a trigger signal to the frame grabber to take an image every 5 minutes. The dynamic head of the jet at the center of the jet exit was monitored using a pitot tube and the jet temperature was monitored using a RTD sensor mounted at the jet exit. The typical size of the image is 75mm by 75mm. The camera and light source were mounted on a traverse that was moved to 9 locations in streamwise direction to cover the area of interest.

The phase angle of the fringe pattern relative to the leading edge was determined by examining the image along lines in the streamwise direction. The profiles of intensity on these lines were Fourier transformed and correlated with cosine curves. The peaks and valleys can then be obtained. The phase angle, film thickness and the skin friction coefficient could then be calculated from these results. The current investigation closely followed the procedures discussed in Naughton *et al.* (2006). The software used in analyzing the interferograms was developed by Naughton *et al.* (2003).

The uncertainty in the measurements is caused by the uncertainties in the oil viscosity, photogrammetry inaccuracies, and precision uncertainties. Among these, the uncertainty in the changes of the oil viscosity with the wall temperature is thought to be the largest source of error (Naughton *et al.*, 2006). The viscosity of the oil used in this investigation was measured at different temperature by Naughton (2005). The temperature of the jet was monitored using a RTD temperature sensor.

The photogrammetry error was reduced by taking an image of a model with known geometry and reference points shown in Fig. 3.13. The prospective center and the orientation angle were then determined using photogrammetry (Liu *et al.*, 2000). The physical location of the wall for the pixels were determined by taking an image of a map with equally



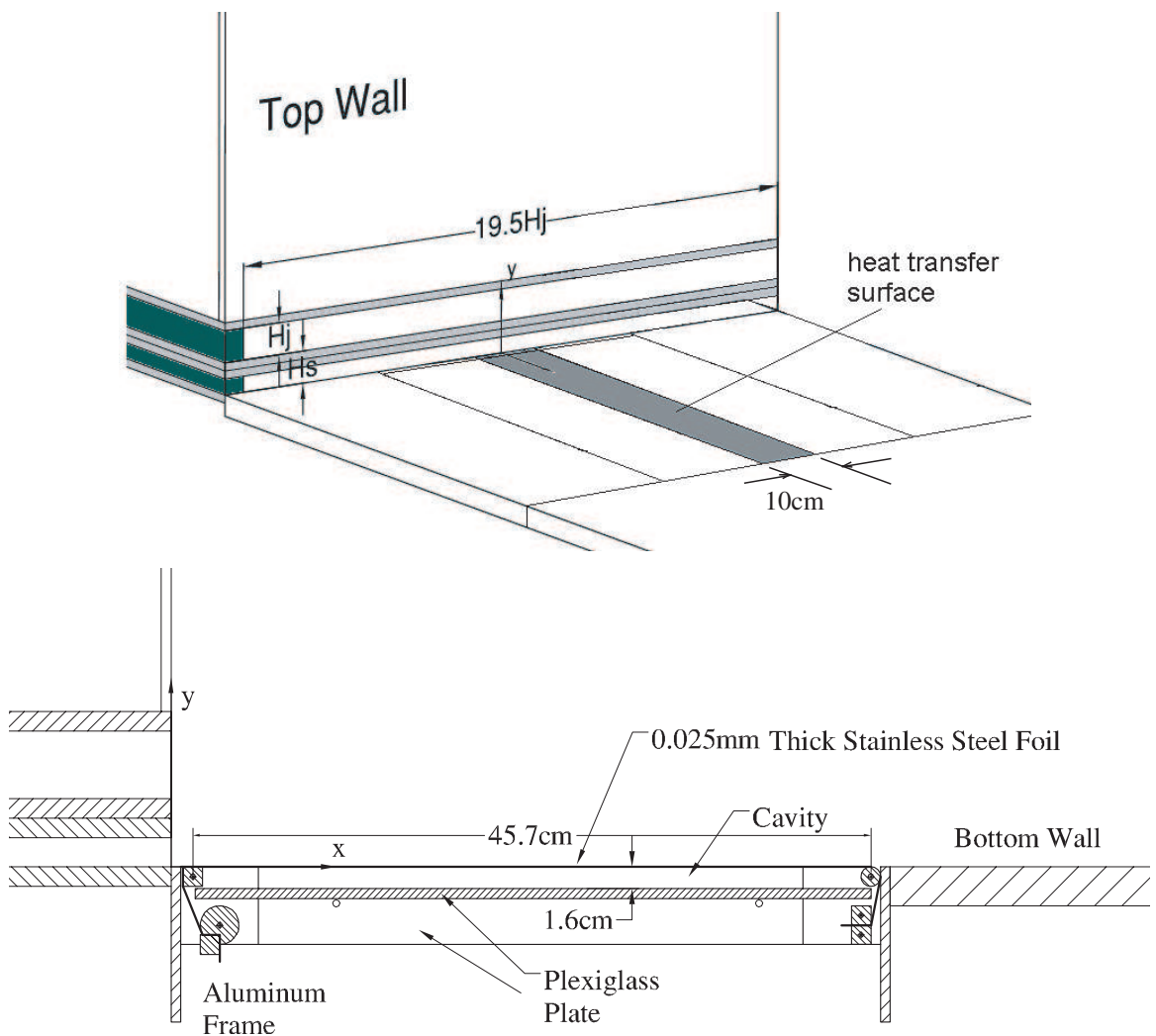


Figure 3.14: Schematic of the heat transfer facility

aluminum frame with a 45.7cm by 10cm gap between the plates. A 0.025mm thick stainless steel foil, that acted as the heat transfer surface, was mounted over this gap. A 1.6mm thick plexiglas plate was located under the foil to form a 1.6cm thick cavity below the foil to reduce the heat loss from the bottom of the foil. The foil was attached to adjustable aluminum mounts positioned below the surface used to tension the foil after it was heated.

The ends of the foil were clamped to the adjustable aluminum mounts using machined square aluminum bars. Heavy gauge wires were then used to connect these bars to a regulated DC power supply (INSTEK GW GPR-1820HD) that could produce approximately 1500 W/m^2 of local electrical heating in the foil. The current through the foil was measured using a meter on the power supply, while the voltage drop across the foil itself was measured using a multi-meter.

The electrical heating of the foil was transferred to the jet, lost through radiation from the foil or transferred to the air below the foil. The heat transfer to the air below the foil was estimated by assuming the air was stratified in the cavity below the plexiglass plate and the loss was estimated to be less than 1% of the local heating. Similarly, the lateral heat conduction in the foil based on the temperature gradients was less than 0.5% of the total electrical heating. These two parts of the heat losses were neglected and considered in the uncertainty analysis. The radiation heat transfer from the top of the foil, \dot{q}_{rad} , was less than 14% of the local electrical heating in the separation region. The radiation loss was less than 7% of the total heating in other regions. Further details on the estimation of these losses are included in Appendix B.

Thus, the local heat transfer coefficient for the impinging jet was given by

$$h = \frac{\dot{q}_{conv}}{T_w(x) - T_j} = \frac{\dot{q}_{elec} - \dot{q}_{rad}}{T_w(x) - T_j}. \quad (3.21)$$

The total electrical heating was computed using

$$\dot{q}_{elec} = \frac{IU}{A}, \quad (3.22)$$

where I and U were the current and voltage drop across the foil and A is the area of the foil. The radiation from the upper surface of the foil to the room was evaluated using

$$\dot{q}_{rad} = \varepsilon\sigma(T_w^4 - T_\infty^4). \quad (3.23)$$

The top of the foil was coated with candle-soot black paint that was found to have an emissivity of $\varepsilon \approx 0.96 \pm 0.01$.

The jet temperature, T_j , was measured using a thermocouple located in the upper settling chamber and a Fluke 52II thermometer. The foil temperature distributions, $T_w(x)$, were measured using a FLIR THERMACAM SC3000 infrared camera located approximately 1m directly above the foil. There are 480 by 320 pixels in each thermal image which give a typical spatial resolution of approximately $0.027H_j$. Each temperature distribution reported here was determined by averaging the wall temperature in the region $-0.8 \leq z/H_j \leq 0.8$ at the same streamwise location from 100 samples of the instantaneous temperature distribution measured at 1 Hz. The heat transfer coefficient was reported in terms of the Stanton number ($St = h/\rho c_p U_U$), which is typical in the investigations of the reattaching flow (Vogel & Eaton, 1985).

The uniformity of the heating in the foil was checked by measuring the temperature distribution on the foil for modest heating without the cooling flow. The temperature of the foil was found to be uniform to within experimental uncertainty. The uncertainty of Stanton number was estimated using the approach outlined by Coleman & Steele (1998) and the process is shown in Appendix C. The uncertainty for the Stanton number was found to be less than $\pm 7\%$ for 95% confidence interval.

Chapter 4

Offset Attaching Planar Jets - Single Point Measurements

Heretofore, there have not been any systematic measurements of the flow field or heat transfer in offset jets with small offset distances (typical of the size used in the dual lip air ring). Thus, the development of these flows are examined first. The development of the single offset jet was first characterized using single point measurements. The distributions of the velocity, static and fluctuating wall pressure, heat transfer from a heated wall to the jet and skin friction are presented in this chapter. The effect of the offset distance and Reynolds number and the development of the jet are also discussed. The development of the large-scale structures in these flows is considered in the next chapter.

4.1 Effect of Offset Distance

4.1.1 Effect of Offset Distance on the Mean Flow Field

The changes in the attachment locations in the offset jets with H_s/H_j of 0.1 to 1.2 are shown in Fig. 4.1 with the corresponding results from Lund (1986) for an offset jet exiting a nozzle with contoured lower surface and a wall behind the jet. The attachment

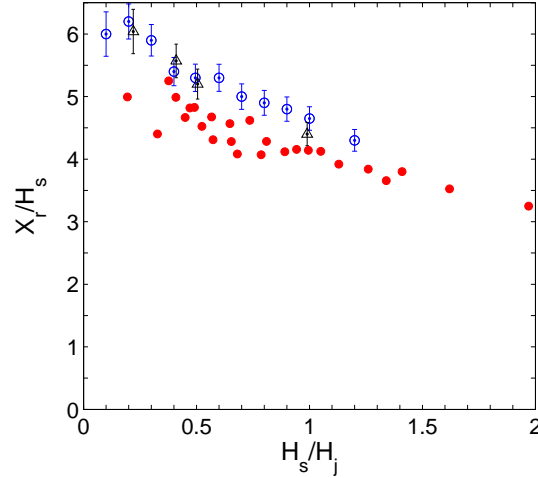


Figure 4.1: Changes in the attachment location with the offset distance for the \circ 3.8cm height jet, the \triangle 1.9cm jet and the attachment location reported by \bullet Lund (1986).

locations determined for the two jets examined here agree indicating the location was independent of the nozzle aspect ratio. The results here show that the attachment location was approximately constant with $X_r \approx 6H_j$ for jets with $H_s \leq 0.3H_j$, similar to the results for a backward facing step (Driver *et al.*, 1987; Heenan & Morrison, 1998). The normalized reattachment length, X_r/H_s , decreased gradually with offset ratio for jets with $H_s \gtrsim 0.3H_j$, similar to the results of Lund (1986). The reattachment lengths here were systematically larger than those reported by Lund; this may be caused by the difference in the nozzle geometry.

The profiles of the mean streamwise velocity in the near field of the offset jets with $H_s/H_j = 0.2$ to 1.0 and a planar wall jet with $H_s/H_j = 0$ are shown in Fig. 4.2. Here the mean velocity, U , has been normalized using the mass-averaged velocity measured at the jet exit, U_U . The profiles of the mean velocity at the jet exit were in good agreement with each other with the difference in the maximum streamwise velocity less than $\pm 1\%$. The results show that the offset jets curved toward the wall and attached to the wall, as expected. The attachment location determined from the oil film visualization is indicated here by the end of the dashed line in the plots. The velocity profiles gradually change downstream

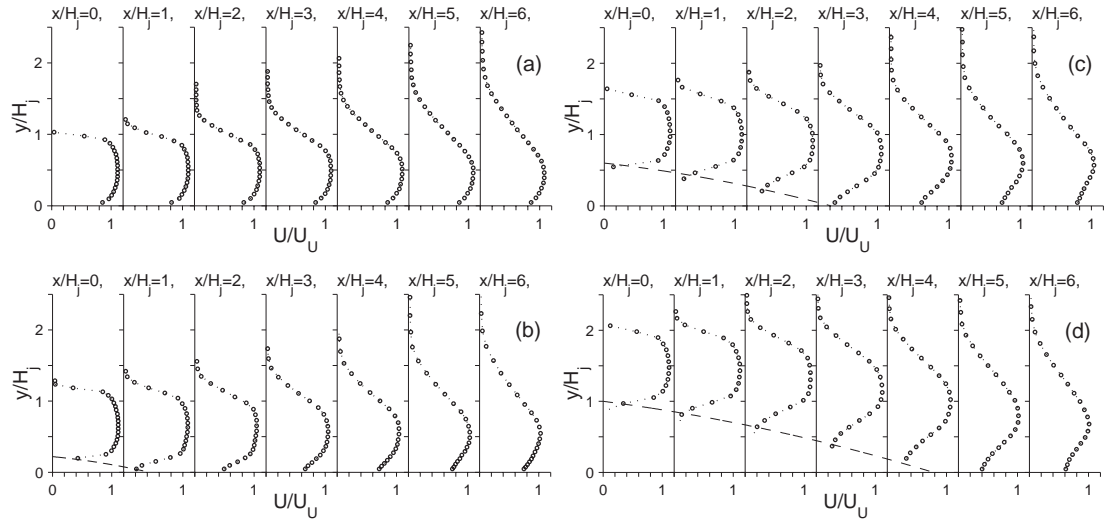


Figure 4.2: Profiles of the mean streamwise velocity in the region $x/H_j \leq 6$ for jets with $H_s/H_j =$ (a) 0, (b) 0.2, (c) 0.6 and (d) 1.0.

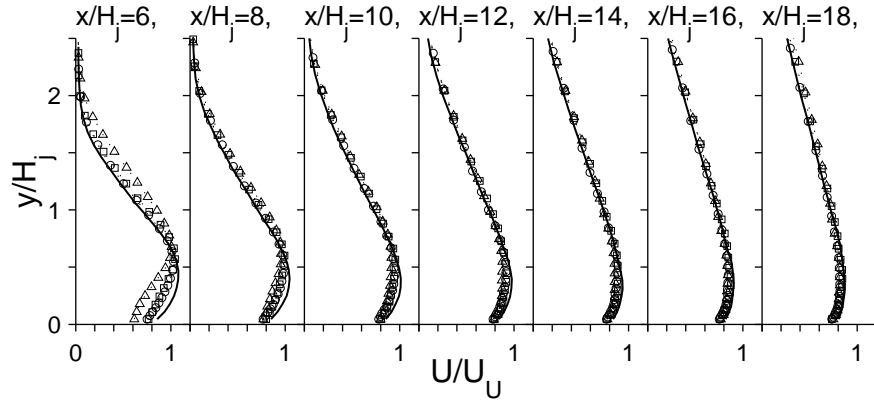


Figure 4.3: Profiles of the mean streamwise velocity in the region $x/H_j \geq 6$ for offset ratio of — 0, \circ 0.2, \square 0.6 and \triangle 1.0.

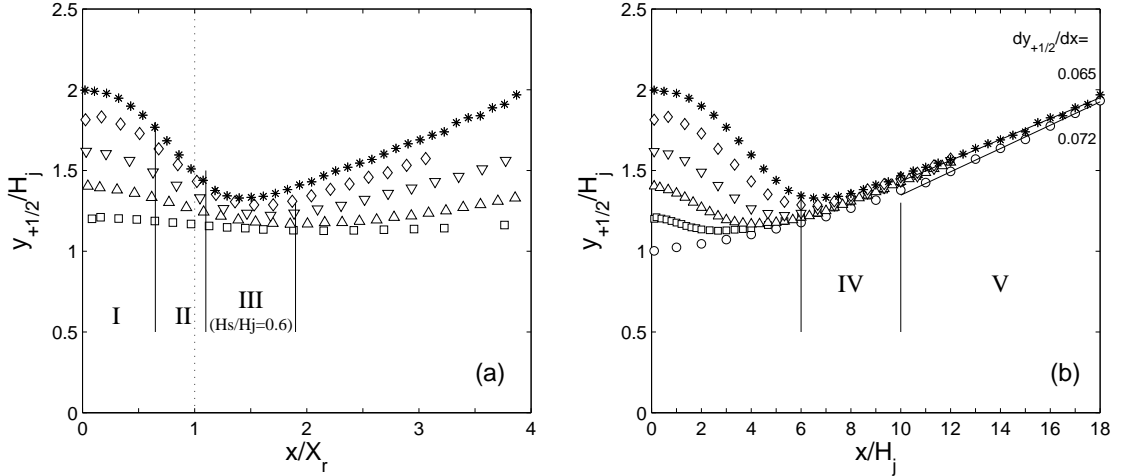


Figure 4.4: Changes in the jet half width with streamwise position for jets with offset ratio of \circ 0, \square 0.2, \triangle 0.4, \triangledown 0.6, \diamond 0.8 and $*$ 1 in term of (a) x/X_r and (b) x/H_j (from the single wire measurements).

of the attachment location and become similar to those in the wall jet exiting the channel without an initial offset. The mean profiles from all the offset jets collapse at $x/H_j \gtrsim 8$, as shown Fig. 4.3, but they differ from the profile for the planar wall jet even at $x/H_j = 12$. The differences persisted to at least $x/H_j = 18$, where there was a 3% difference in the maximum velocity. The difference was found to be repeatable and exceeded the 95% confidence interval. Thus, the results showed that the effect of even a small initial step persists well beyond the attachment location of the jet.

The development of the jets for different offset ratios can be characterized by examining the change in the outer jet half-width, $y_{+1/2}$, and the maximum velocity, U_{max} , with downstream location. The results determined from the single hot-wire measurements are shown in Fig. 4.4 and Fig. 4.5. Here, the outer half-width is the local distance from the wall to the outer point where the mean velocity is half the maximum velocity. The streamwise coordinate has been normalized using both H_j to compare the overall development of the jets, and X_r to compare the development of the jets in the reattaching region. The results show that the development of the offset jets can be divided into five regions, three defined by the

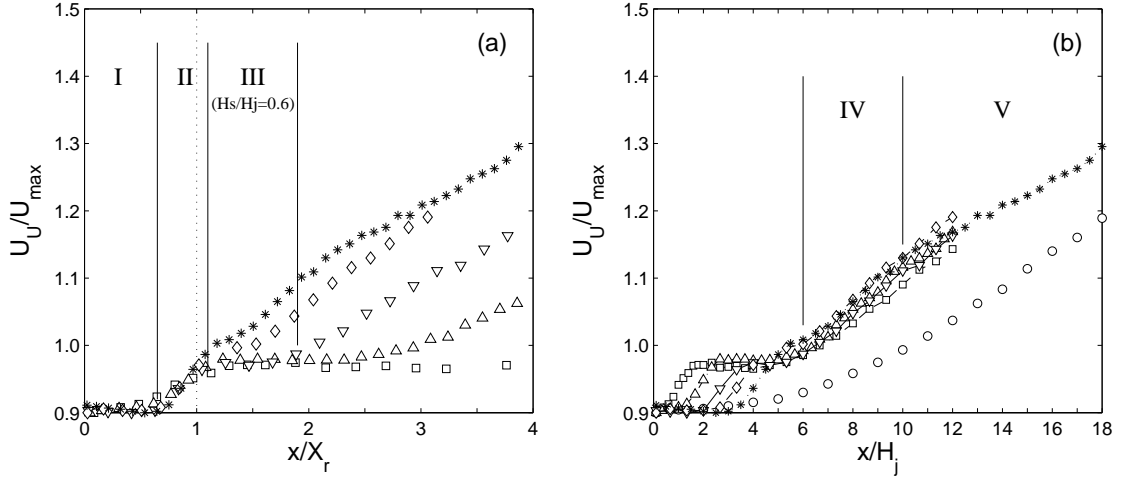


Figure 4.5: Changes in the maximum local mean velocity for jets with offset ratio of \circ 0, \square 0.2, \triangle 0.4, ∇ 0.6, \diamond 0.8 and $*$ 1 in term of (a) x/X_r and (b) x/H_j (from the single wire measurements).

reattachment process and two in the wall jet region. In the first region, $x/X_r \leq 0.65$, the maximum velocity does not decay significantly and the outer half width $y_{+1/2}$ decreases gradually as the jets curve toward the wall. In the second region, $0.65 < x/X_r \leq 1.1$, the jets attach to the wall. This process is characterized by a rapid decrease in both the half-width of the jet and the maximum velocity. In the third region, $x/X_r > 1.1$, the jets reorganize after attaching to the wall. The jet half width and the maximum velocity initially remain unchanged in this region for the jets with small offset ratios. The size of this third region is not as clearly defined and is different for jets with different offset ratios. It appears to end with the end of the near field (potential core) of the jet due to the interaction between the outer and the inner shear layer. This occurs at $x/H_j \approx 6$, whereafter the velocity begins to decay quite rapidly. The fourth region, $6 \lesssim x/H_j \lesssim 10$, is a transitional region where the maximum velocity decays and the half width grows for all the jets. The jets eventually develop into a flow similar to a planar wall jet in the fifth region $x/H_j \gtrsim 10$, where the jet half width grows at a constant rate of $dy_{+1/2}/dx \approx 0.07$ that is quite similar to the regular planar wall jet. The maximum velocities decay at a similar rate to the planar wall jet, but

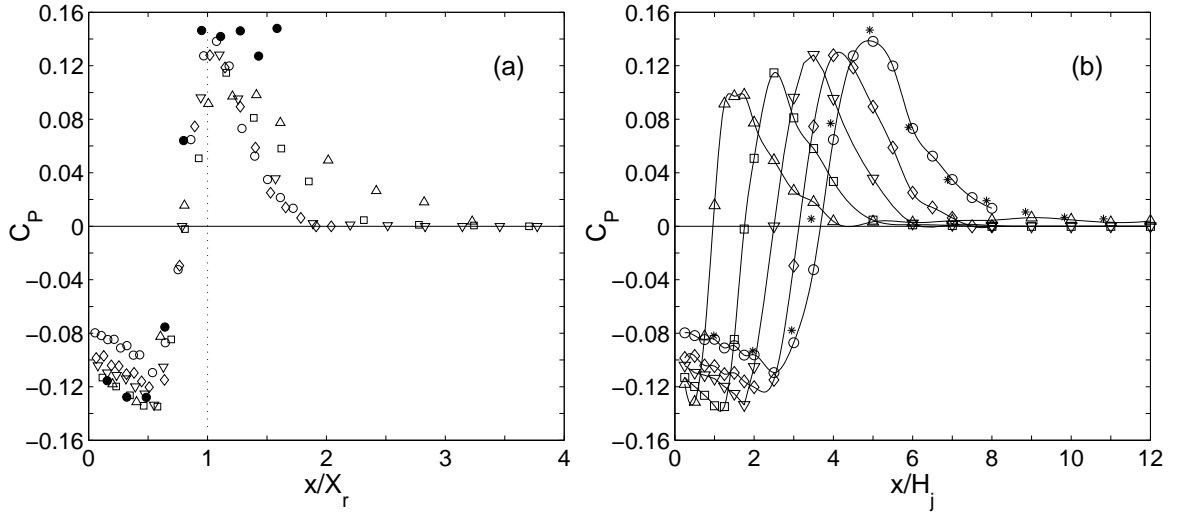


Figure 4.6: Distribution of the static wall pressure coefficient for jets with $H_s/H_j = \Delta 0.2$ $\square 0.4$ $\nabla 0.6$ $\diamond 0.8$ and $\circ 1.0$, and \bullet for a flow over a backward facing step (Heenan & Morrison, 1998). The results for the 1.9cm height jet with $H_s/H_j = *$ 1.0 are also shown.

the maximum velocity in the offset jets are slightly smaller than the planar wall jet. This is true even for smallest offset distance considered here thus showing again that even a small offset distance seem to impact the development of the jet.

The change in the static wall pressure coefficient, C_P , with streamwise position for the jets with offset distance H_s/H_j of 0 to 1.0 is shown in Fig. 4.6, where $C_P = (P - P_\infty)/0.5\rho U_U^2$. The streamwise coordinate has again been normalized by both X_r and H_j to highlight the changes in the different regions. The results here were in good agreement with the results for the larger aspect ratio nozzle. The static wall pressure is initially below the atmospheric pressure due to the entrainment by the inner shear layer or the Coanda effect and reaches a local minimum at $x/X_r \approx 0.65$ or the end region I. The minimum static pressure coefficient at this point varies from -0.14 for the jets with $H_s/H_j \leq 0.6$ to -0.11 for a jet with an offset ratio of 1.0. The static wall pressure increased rapidly in the reattachment region and reached to a maximum slightly downstream of the attachment location similar to other attaching flows (e.g. Farabee & Casarella, 1986; Driver *et al.*,

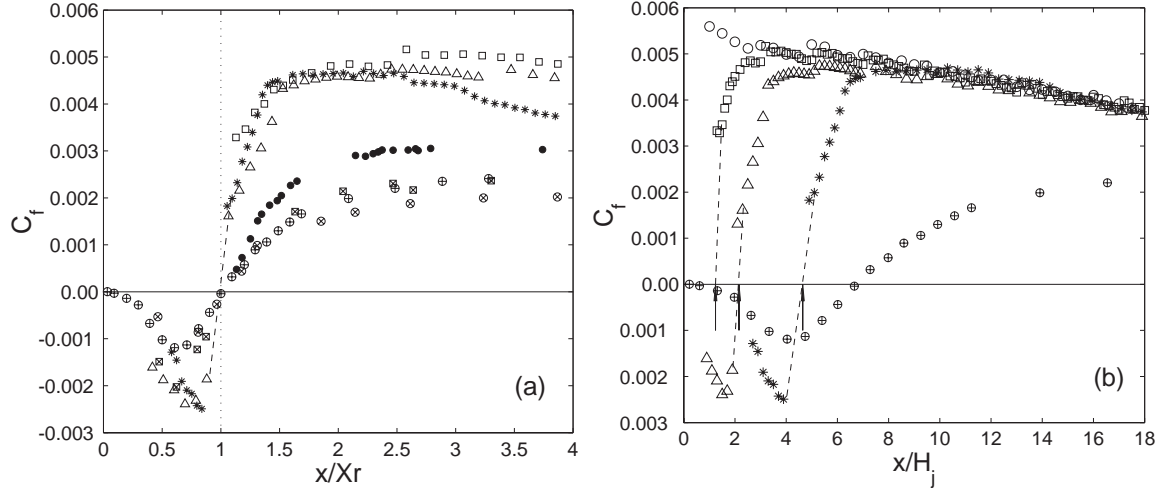


Figure 4.7: Distribution of the skin friction coefficient for \circ a planar wall jet, offset jets with $H_s/H_j = \square 0.2$, $\triangle 0.4$ and $*$ 1, and flows over backward facing step with $Re_{H_s} = \bullet 39000$ (Bradshaw & Wong, 1972), $Re_{H_s} = \boxtimes 10400$, $\otimes 37200$ (Jovic & Driver, 1995) and $Re_{H_s} = \oplus 28000$ (Vogel & Eaton, 1985).

1987; Heenan & Morrison, 1998). The maximum in the static wall pressure coefficient increased with the offset ratio from $C_P \approx 0.1$ for the jet with $H_s/H_j = 0.2$ to $C_P \approx 0.14$ for the jet with $H_s/H_j = 1.0$ likely due to the larger curvature in the jet with $H_s/H_j = 1.0$. The static wall pressure decreased rapidly to the atmospheric pressure after the flow attaches to the wall. The pressure decreased more gradually for jets with the smaller offset ratios, suggesting again that they recovered more gradually, consistent with the change in the mean velocity observed in region III.

The distributions of the skin friction coefficient, given by $C_f = \tau_w / 0.5 \rho U_U^2$, for a planar wall jet and offset jets with $H_s = 0.2H_j$, $0.4H_j$ and H_j are shown in Fig. 4.7. The skin friction coefficients for flows over a backward facing step with different Reynolds numbers are also shown (Bradshaw & Wong, 1972; Vogel & Eaton, 1985; Jovic & Driver, 1995). The skin friction was initially negative in the recirculation region and decreased as the jet curved toward the wall reaching a minimum at $x/X_r \approx 0.85$, indicating to strong reverse flow near this location. The skin friction then increased to 0 at the mean attachment location

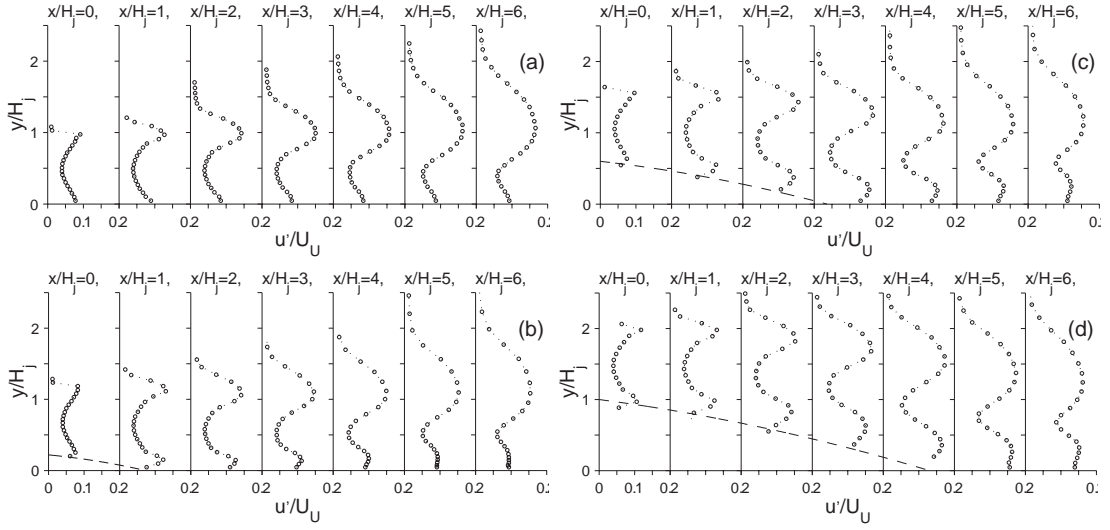


Figure 4.8: Profiles of the streamwise fluctuating velocity in the region $x/H_j \leq 6$ for (a) the planar wall jet $H_s/H_j = 0$ and the offset jets with H_s of (b) $0.2H_j$ (c) $0.6H_j$ (d) H_j , the Reynolds number in all cases was approximately 44 000.

(by definition) and further increased in the region $1 \leq x/X_r \leq 1.5$. This was due in part to the acceleration of the flow near the wall due to the favorable pressure gradient. The skin friction for the offset jets became similar to the results for the planar wall jet after the reattachment point and decreased approximately linearly as the flow evolved further downstream. The skin friction for the offset jet was much larger than the backward facing step for a similar Reynolds number based on the step height. The difference between them decreased as the flow evolved to $x/X_r \approx 4$.

4.1.2 Effect of Offset Distance on the Fluctuating Flow Field

Profiles of rms value of the streamwise fluctuating velocity, u' , the vertical fluctuating velocity, v' , and the Reynolds shear stress, $\langle uv \rangle$, measured in the region $x/H_j \leq 6$ in the different jets are shown in Fig. 4.8 to Fig. 4.10, while profiles measured in the region $x/H_j \geq 6$ are shown in Fig. 4.11. The changes in the magnitude of the fluctuating velocities and Reynolds shear stress in both shear layers of the offset jets differed from those for the

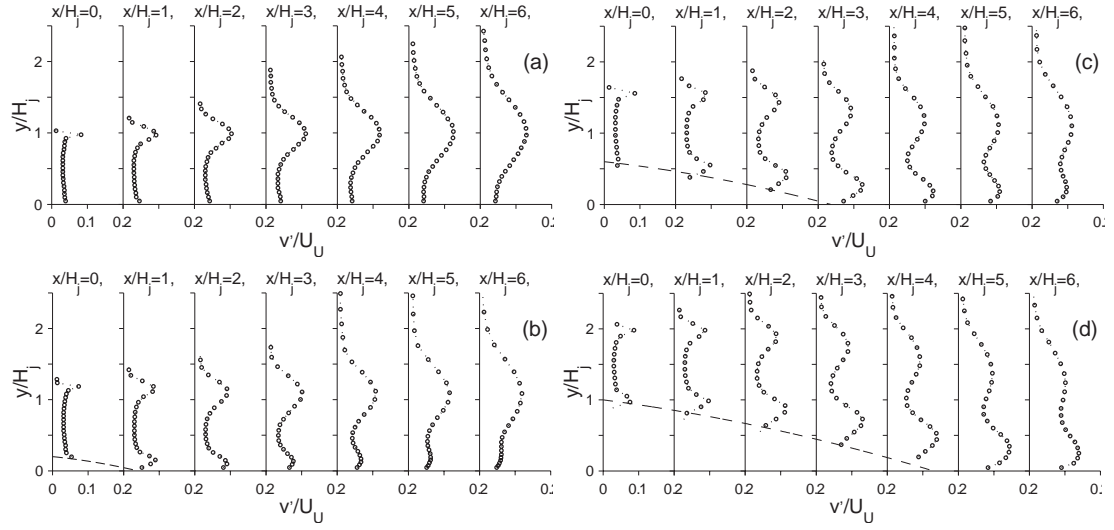


Figure 4.9: Profiles of the vertical fluctuating velocity in the region $x/H_j \leq 6$ for (a) the planar wall jet $H_s/H_j = 0$ and the offset jets with H_s of (b) $0.2H_j$ (c) $0.6H_j$ (d) H_j .

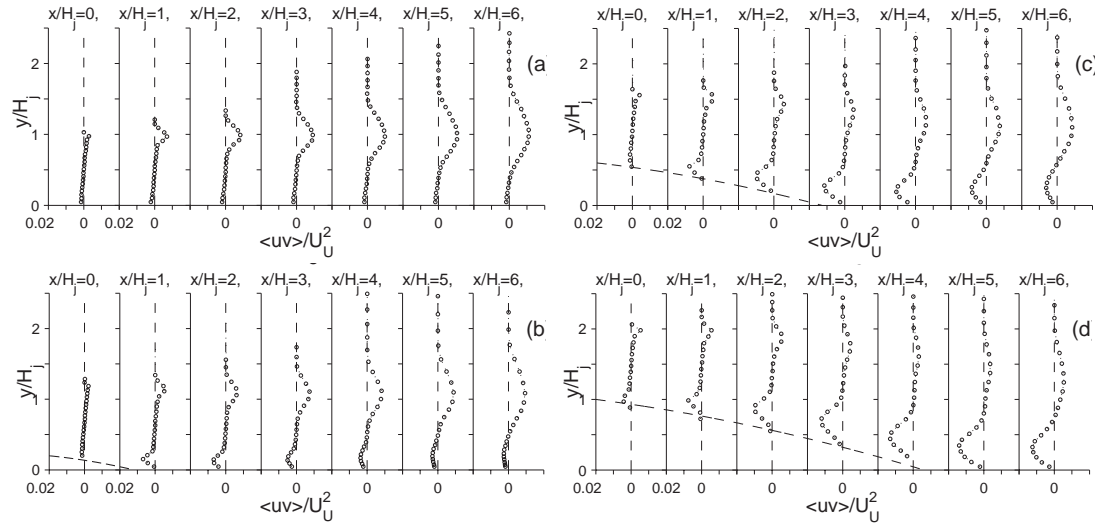


Figure 4.10: Profiles of the Reynolds shear stress in the region $x/H_j \leq 6$ for (a) planar wall jet $H_s/H_j = 0$ and offset jets with H_s of (b) $0.2H_j$ (c) $0.6H_j$ (d) H_j .

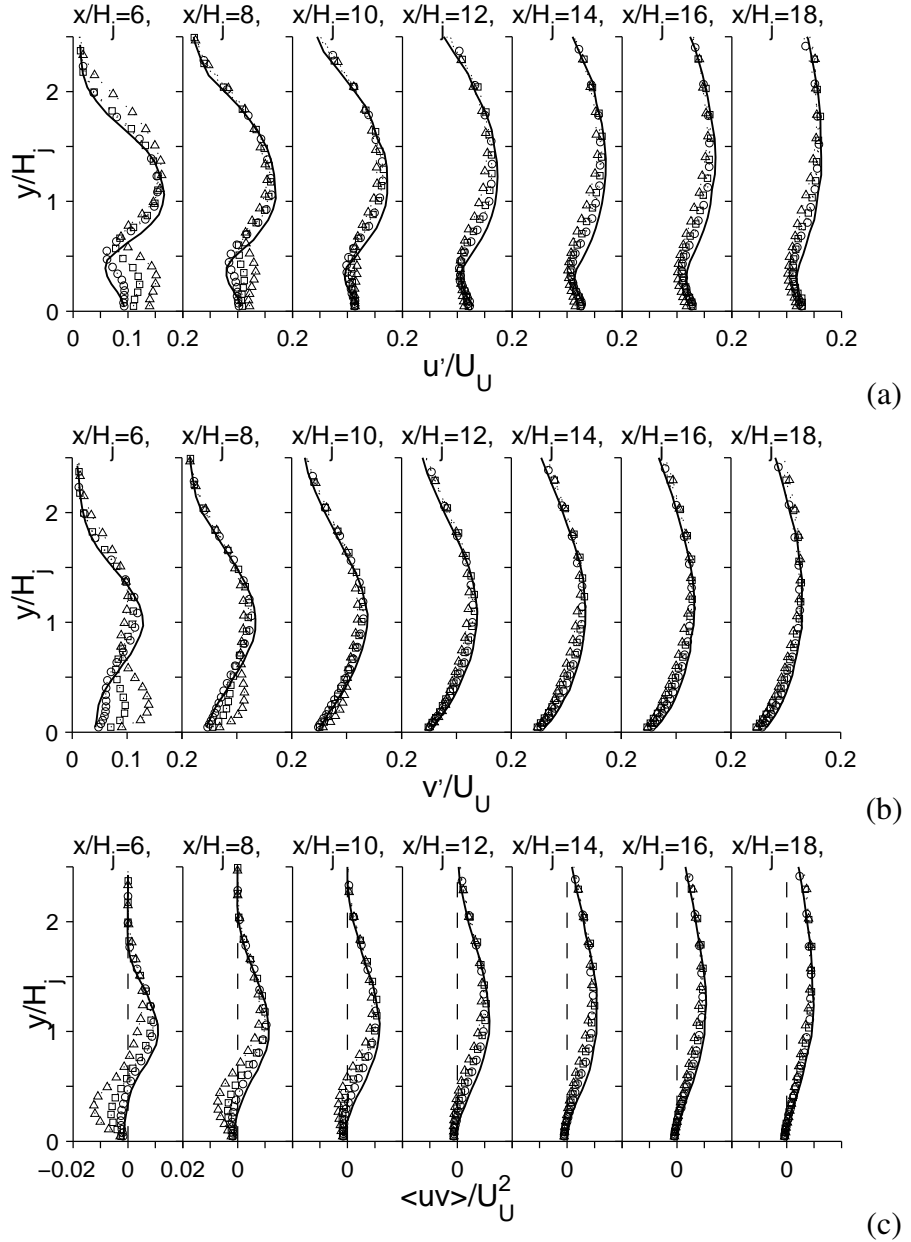


Figure 4.11: Profiles of the rms value of (a) the streamwise and (b) the vertical fluctuating velocities and (c) the Reynolds shear stress in the region $x/H_j \geq 6$ for H_s/H_j of — 0 ○ 0.2 □ 0.6 and △ 1.0 and Reynolds number of approximately 44 000.

planar wall jets. There is a local maximum in the turbulent fluctuations, u' and v' , in the shear layers formed on either side of the jet near the jet exit. Both shear layers spread and curves toward the wall as the jets evolve downstream. The rms velocities along both shear layers increase from separation point to near the attachment point as the length scale of the large scale flow structures increases through pairing and merging of smaller structures. The Reynolds shear stress, $-\langle uv \rangle_{max}$, also increases indicating the momentum transport across the shear layer increases for all the jets. After the jet attaches to the wall, the outer shear layer continues to grow similar to the outer shear layer in the planar wall jet, while the rms velocities in the near wall layer decrease due to the interactions between flow structures and the wall, similar to the backward facing step (Bradshaw & Wong, 1972). The difference between the offset jets and the planar wall jet becomes smaller as the flow develops further downstream into the wall jet region.

The change in the magnitude of the fluctuating velocities and Reynolds shear stress in the shear layers of the offset jets can be better illustrated by contrasting the maximum local rms fluctuating velocities and Reynolds shear stress at different streamwise locations along the shear layers. The changes in the maximum streamwise and vertical fluctuating velocity and the Reynolds shear stress with the streamwise position for the inner and outer shear layers in term of x/H_j are shown in Fig. 4.12, while the changes in terms of x/X_r are shown in Fig. 4.13. The results for the shear layer in the free jet ($H_s/H_j \rightarrow \infty$) and the outer shear layer in the planar wall jet ($H_s/H_j = 0$) measured using the same jet are also shown for comparison. The rms velocities for the inner shear layer of the planar wall jet are not shown here because it is not clear whether the cross-wire probe was close enough to the wall to fully capture the maximum rms velocities in the inner shear layer. The maximum local streamwise fluctuating velocities in the outer shear layer of all the offset jets, $u'_{o,max}$, were similar to the planar wall jet in the region $x/H_j \lesssim 1.5$, indicating the offset distance did not have a significant effect on the initial part of the outer shear layer in the offset jets with $H_s/H_j \leq 1.0$. The maximum streamwise fluctuating velocity continued

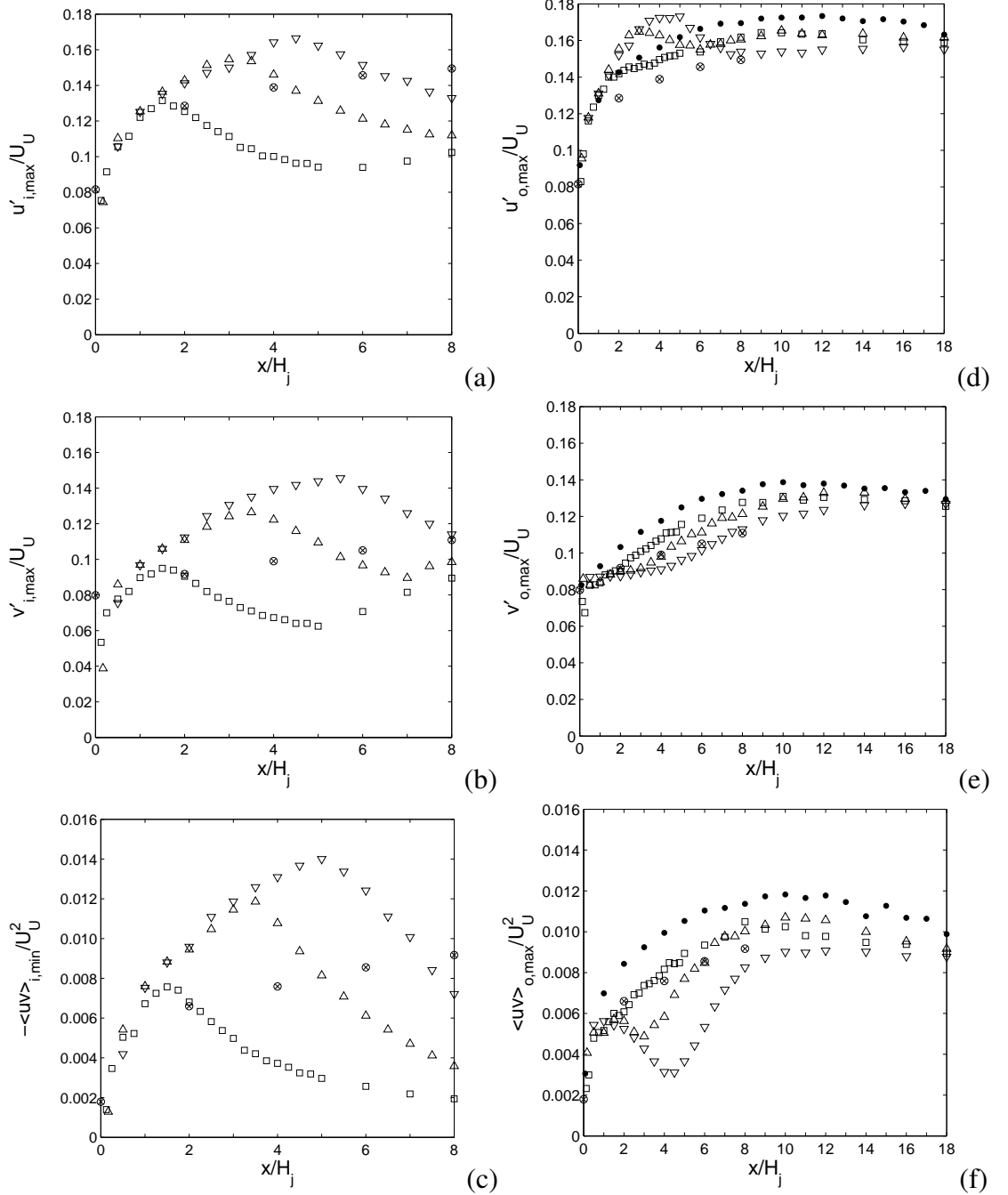


Figure 4.12: Distributions of the maximum u' in the (a) inner and (b) outer shear layer, the maximum v' in the (c) inner and (d) outer shear layer and the maximum magnitude of $\langle uv \rangle$ in the (e) inner and (f) outer shear layer of ● the planar wall jet and the offset jets with $H_s/H_j = \square 0.2$, $\triangle 0.6$ and $\nabla 1.0$, and for \otimes a free jet with $Re \approx 44\,000$.

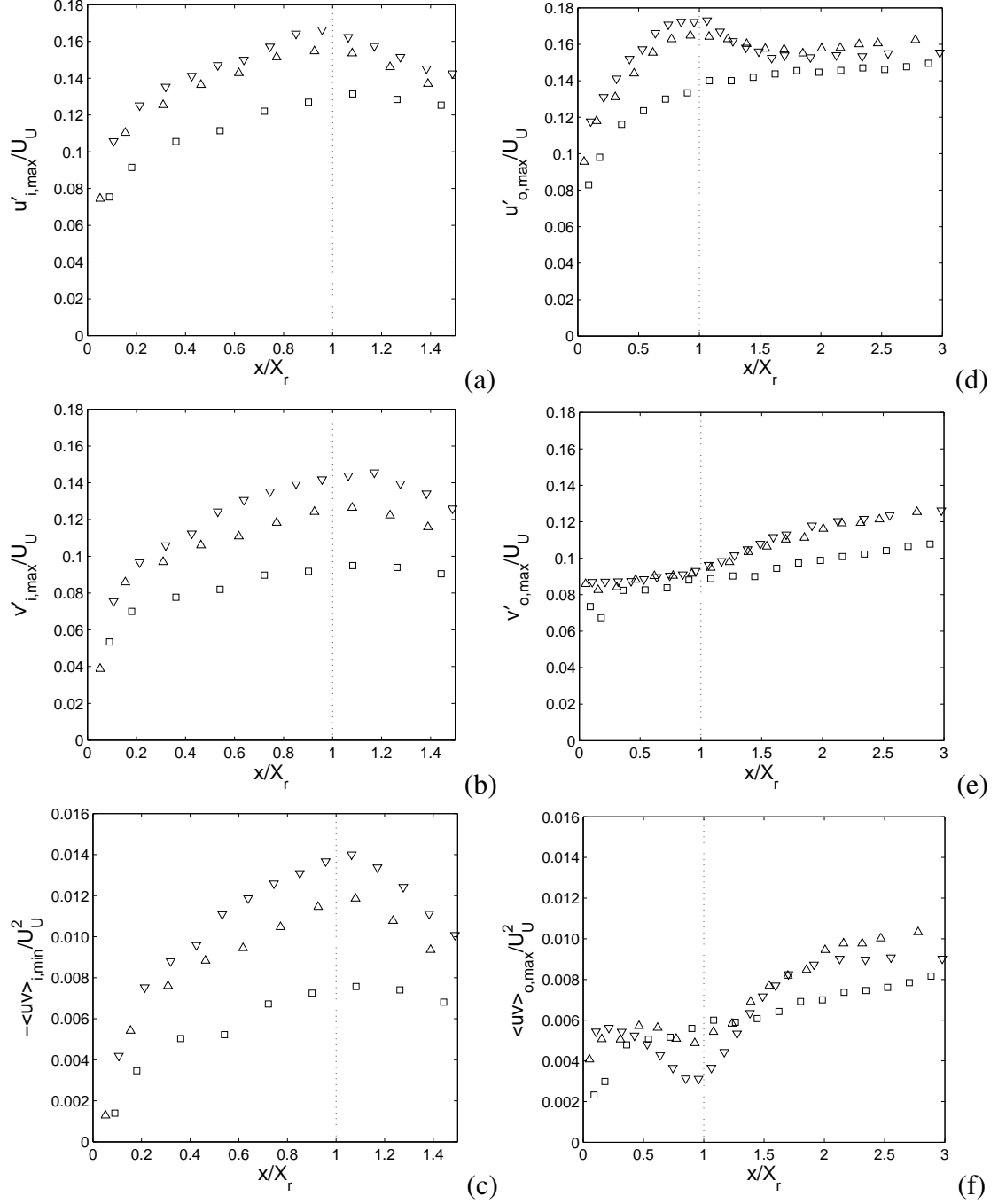


Figure 4.13: Distributions of the maximum u' in the (a) inner and (b) outer shear layer, the maximum v' in the (c) inner and (d) outer shear layer and the maximum magnitude of $\langle uv \rangle$ in the (e) inner and (f) outer shear layer of the offset jets with $H_s/H_j = \square 0.2$, $\triangle 0.6$ and $\nabla 1.0$ with $Re \approx 44\,000$.

Table 4.1: Summary of flow parameters of single offset jet.

| H_s/H_j | $U_U(m/s)$ | $U_U H_j/\nu$ | θ/H_j | θ/H_s | X_r/H_s |
|-----------|------------|---------------|--------------|--------------|-----------|
| 0.1 | 18.2 | 44000 | 0.027 | 0.270 | 6.0 |
| 0.2 | 18.3 | 44200 | 0.029 | 0.145 | 6.2 |
| 0.4 | 18.4 | 44400 | 0.026 | 0.065 | 5.4 |
| 0.6 | 18.5 | 44700 | 0.025 | 0.042 | 5.3 |
| 0.8 | 18.3 | 44200 | 0.024 | 0.030 | 4.9 |
| 1.0 | 18.4 | 44400 | 0.027 | 0.027 | 4.6 |

to increase as the flow evolved downstream, and there seemed to be a transition between the offset jets with $H_s/H_j = 0.2$ and 0.6 . For example, $u'_{o,max}$ for the offset jets with $H_s/H_j = 0.2$ is approximately 5% less than the planar wall jet, while $u'_{o,max}$ for offset jets with $H_s/H_j \geq 0.6$ became larger than the planar wall jet while $v'_{o,max}$ became smaller than that for the planar wall jet. The Reynolds shear stress, $\langle uv \rangle_{o,max}$, decreased significantly to the attachment location, likely due to the interaction of the flow structures with the wall. The Reynolds shear stress then increased slightly after the reattachment but did not recover to the results for the planar jet. In the regions downstream of the attachment point, $u'_{o,max}$ for offset jets with large offset distances $H_s/H_j \geq 0.6$ decreased and became less than the planar jet indicating the fluctuations in the reattaching flow was reduced by the interactions between the flow and the wall.

The maximum of local fluctuating velocities, $u'_{i,max}$ and $v'_{i,max}$, and the Reynolds shear stress, $\langle uv \rangle_{i,max}$, in the inner shear layer of offset jets increased significantly in the streamwise direction and reached maxima near the reattachment location. The maximum fluctuating velocities and the Reynolds shear stress in the inner shear layer were significantly larger than the largest values observed in the wall jet at the same streamwise location. The fluctuations were also slightly larger than the shear layer in the free jet, likely due to the presence of the recirculating flow.

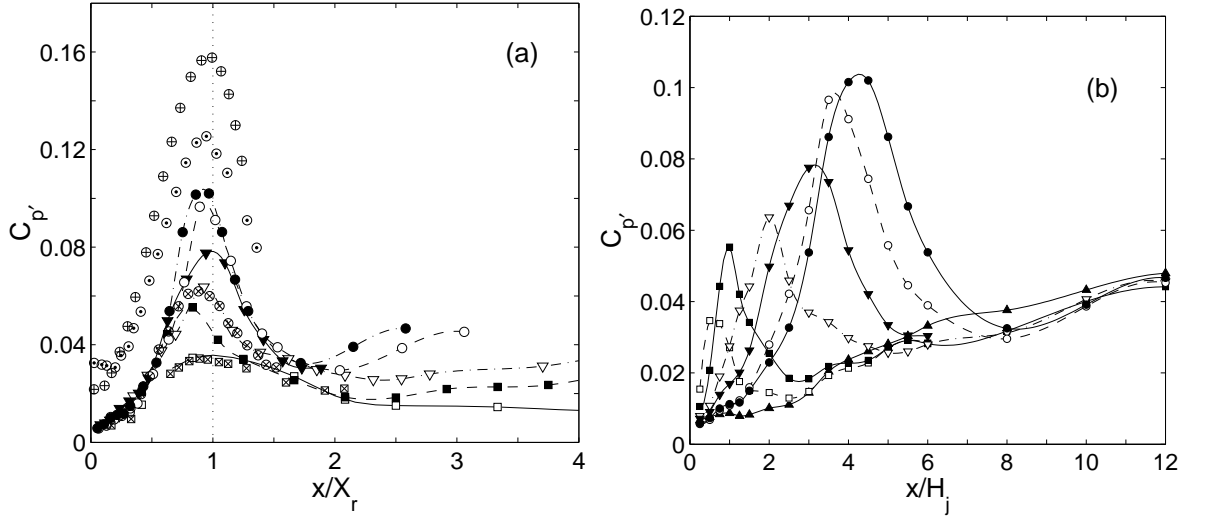


Figure 4.14: Distributions of the fluctuating wall pressure coefficient for jets with $H_s/H_j = \blacktriangle 0 \square 0.1 \blacksquare 0.2 \triangledown 0.4 \triangledown 0.6 \circ 0.8 \bullet 1.0$ and results from backward facing step \boxtimes Driver *et al.* (1987) \otimes Heenan & Morrison (1998) and bluff body reattachment \odot Cherry *et al.* (1984) \oplus Hudy *et al.* (2003).

The size of the fluctuations at the reattachment point increased with the offset distance of the jet. In particular, the largest $u'_{i,max}$ was approximately $0.13U_U$ for the jet with $H_s/H_j = 0.2$ and $0.17U_U$ for the jet with $H_s/H_j = 1$, while the largest $v'_{i,max}$ were approximately $0.09U_U$ and $0.15U_U$, respectively. The difference seemed to be associated with the ratio between the initial momentum thickness of the lower side of the jet and the offset distance, θ/H_s , similar to other reattachment flows (Adams & Johnston, 1988b; Heenan & Morrison, 1998). The initial momentum thickness of the lower edge in the jets studied here were approximately $0.025H_j$, and are listed in Table 4.1. The ratio θ/H_s decreased as the offset height increased, causing increases in the maximum rms fluctuating velocities. The presence of the wall disturbed the growth of the shear layer, and the fluctuating velocities $u'_{i,max}$ and $v'_{i,max}$ decreased downstream of the attachment point due to the interaction between the flow and the wall.

The increase in the fluctuating velocities in the inner shear layer caused a corresponding increase in the fluctuating wall pressure coefficients, $C_{p'}$, shown in Fig. 4.14, where

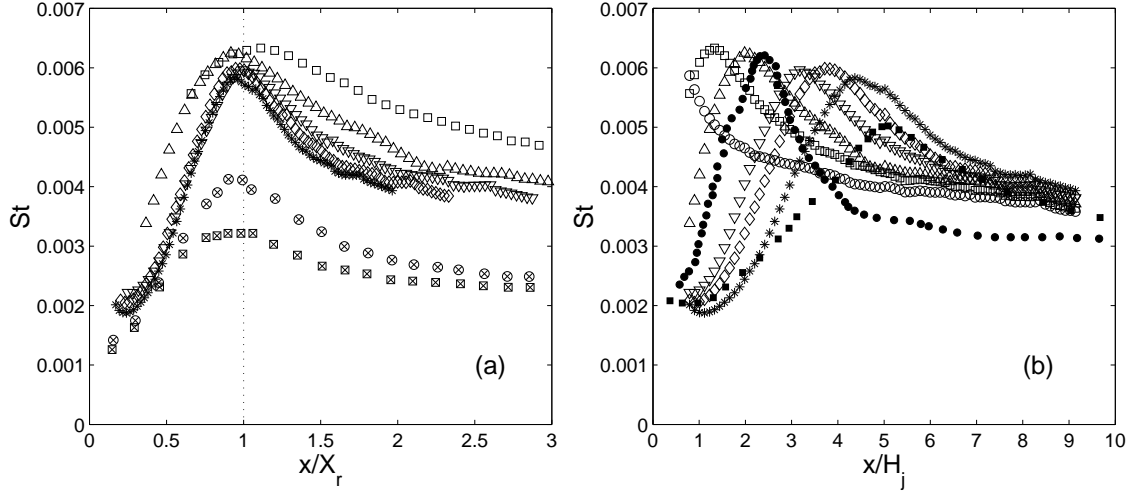


Figure 4.15: Distribution of the Stanton number for \circ a planar wall jet and offset jets with $H_s/H_j = \square 0.2, \triangle 0.4, \nabla 0.6, \diamond 0.8 * 1.0$ and $Re \approx 44\,000$. The results by Kim *et al.* (1996) for offset jets with $H_s/H_j = \bullet 0.5$ and $\blacksquare 1.5$ and results by Vogel & Eaton (1985) for the backward facing step with $\delta/H_s = \otimes 0.15$ and $\boxtimes 1.1$ are also shown.

$C_{p'} = p'/0.5\rho U_U^2$ and p' was the rms value of the fluctuating wall pressure. The fluctuating wall pressure for all the offset jets initially collapsed in region I, $x/X_r \leq 0.65$. Thereafter, the fluctuating pressure increased rapidly reaching a maximum slightly upstream of the attachment location, similar to other reattaching flows. The maximum in the fluctuating wall pressure increases significantly from $C_{p'} \approx 0.035$ for the jet with $H_s/H_j = 0.1$ to $C_{p'} \approx 0.1$ for $H_s/H_j = 1$, similar to the maxima in the fluctuating velocities. The magnitude of the fluctuating pressure for the case with $H_s/H_j = 0.1$ (or $\theta/H_s \approx 0.27$) was similar to that reported for flow over a backward facing step with $\delta/H_s \approx 1.4$ (Driver *et al.*, 1987), while the case with $H_s/H_j = 0.4$ (or $\theta/H_s \approx 0.065$) was similar to the results for flow over a backward facing step with $\delta/H_s \approx 0.2$ (Heenan & Morrison, 1998). The maximum fluctuating wall pressure for the reattaching flow over a bluff body was much larger (Cherry *et al.*, 1984; Hudy *et al.*, 2003) likely because the initial momentum thickness was much smaller.

The distributions of the Stanton number for jets with offset distance of $0.2H_j$ to H_j

are shown in Fig. 4.15, where $St = h/\rho c_p U_U$. The Stanton number for planar wall jet measured in the current investigation and the Stanton number computed from the Nusselt number for offset jets with $H_s/H_j = 0.5$ and 1.5 reported by Kim *et al.* (1996) are shown in Fig. 4.15. The measurements by Kim *et al.* (1996) agree with the current results set both in the magnitude and the location of the heat transfer peaks. The Stanton number for the offset jets was initially smaller than the results for the planar wall jet in the region below the recirculating flow, but increased to a maximum slightly upstream of reattachment point similar to the distributions of the fluctuating wall pressure. The Stanton numbers near the reattachment point of the offset jets were significantly larger than those for the planar wall jet. The heat transfer peak was broader for cases with small offset distance, $H_s/H_j \leq 0.4$, in Fig. 4.15 (a). For the jets with larger offset distances, $H_s/H_j \geq 0.6$, the distributions of the Stanton number were similar when plotted in terms of x/X_r and the peaks were narrower than the cases with small offset distances, consistent with the shorter recovery of these jets in the velocity and pressure measurements.

The Stanton numbers for flow over a backward facing step with $\delta/H_s = 0.15$ and 1.1 reported by Vogel & Eaton (1985) were also shown in Fig. 4.15 (a). The maxima in the Stanton numbers for the flow over the backward facing step were significantly smaller than in the offset jets examined here. The maximum rms value of the streamwise fluctuating velocity near the reattachment point for the backward facing step was approximately $0.16U_U$ (Vogel & Eaton, 1985), that was similar to the offset jets with $H_s/H_j \geq 0.6$, and was much larger than the jet with $H_s/H_j \leq 0.4$. The jets with $H_s/H_j \leq 0.4$ produced largest Stanton number and the backward facing step produced the least. Thus, it seemed that the maximum Stanton numbers for the reattaching flow were caused by factors other than just the local turbulence intensity.

Downstream of the reattachment location, the Stanton number decreased gradually and approached the results for the planar wall jet. This is similar to the mean skin friction. In the region away from the attachment point, $x/X_r \gtrsim 3$, the Stanton number become similar

to the skin friction coefficient, or $St/C_f \approx 1$. This suggests the momentum and the heat transfer between the jet and the wall may be caused by similar turbulent transport processes or the Reynolds analogy approximately holds. A similar result was also found for the flow over the backward facing step by Vogel & Eaton (1985).

4.2 Effect of Reynolds number

The effect of the Reynolds number on the development of the offset attaching planar jets was examined by measuring the static and fluctuating wall pressure, the skin friction and heat transfer for offset planar jets with $H_s = H_j$ and Reynolds numbers of 21 800, 32 500, 44 400 and 54 500. The changes in the ratio of the initial momentum thickness and the offset distance (θ/H_s) were less than 5% in these cases.

The distributions of the static wall pressure coefficient for Reynolds number of 21 800 to 54 500 are shown in Fig. 4.16. The static wall pressure coefficient only changed slightly with Reynolds number in the reattachment region or region II. The maximum static wall pressure coefficient increased gradually with Reynolds number. The difference between the results for the largest and the smallest Reynolds number was approximately 15%. The results for the skin friction shown in Fig. 4.17 changed similarly with Reynolds number. The minimum in the skin friction coefficient in the recirculation region decreased while the maximum in the skin friction coefficient downstream of the attachment point increased when the Reynolds number decreased similar to the results for the flow over the backward facing step reported by Jovic & Driver (1995). This is opposite to the trend observed in the static wall pressure.

The distributions of the fluctuating wall pressure coefficient for Reynolds number of 21 800 to 54 500 are shown in Fig. 4.18. The fluctuating pressure coefficient near the attachment location for the jet with $Re = 54 500$ were approximately 25% larger than the jet

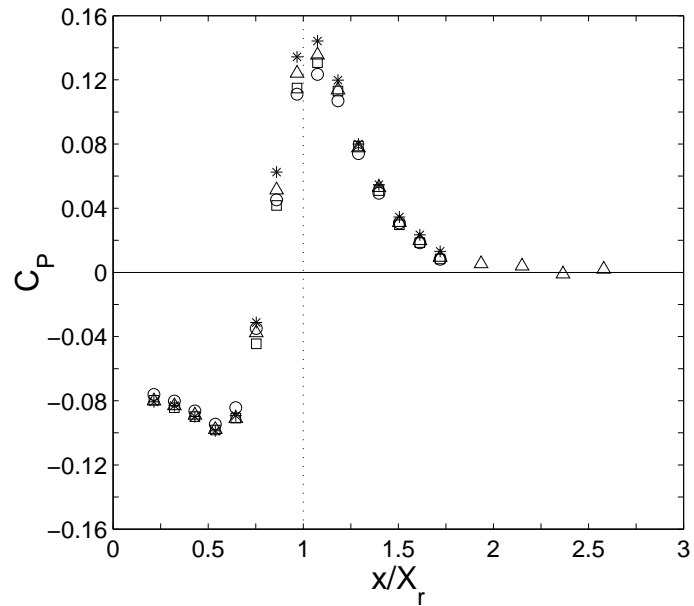


Figure 4.16: Distributions of the static wall pressure coefficient for jets with $H_s/H_j = 1$ and a Reynolds number of \bigcirc 21 800, \square 32 500, \triangle 44 400 and $*$ 54 500.

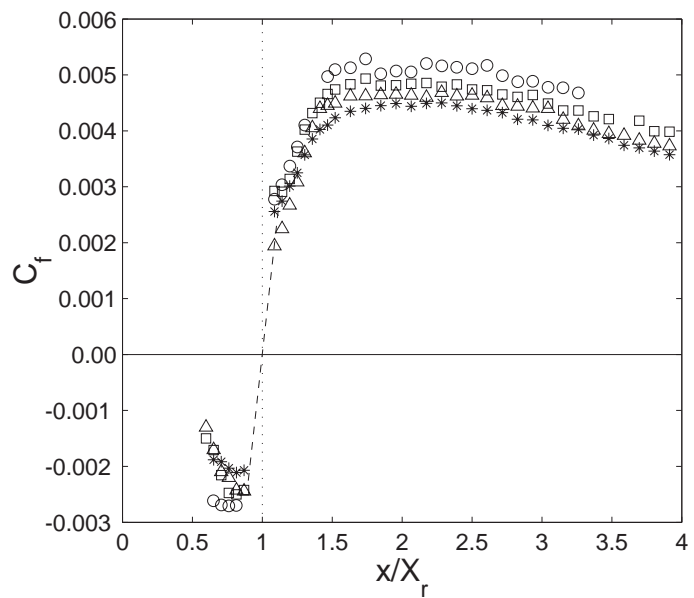


Figure 4.17: Distributions of the skin friction coefficient for jets with $H_s/H_j = 1$ and a Reynolds number of \bigcirc 21 800, \square 32 500, \triangle 44 400 and $*$ 54 500.

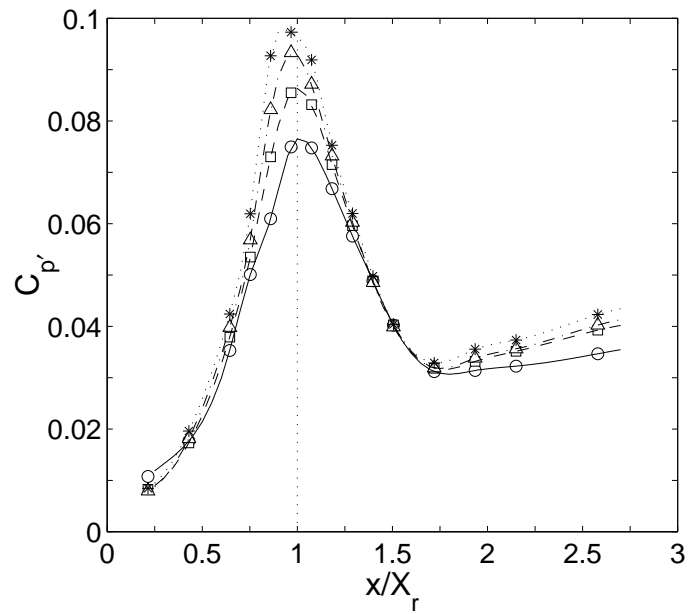


Figure 4.18: Distributions of the fluctuating wall pressure coefficient for jets with $H_s/H_j = 1$ and a Reynolds number of $\bigcirc 21\,800$, $\square 32\,500$, $\triangle 44\,400$ and $*$ 54 500.

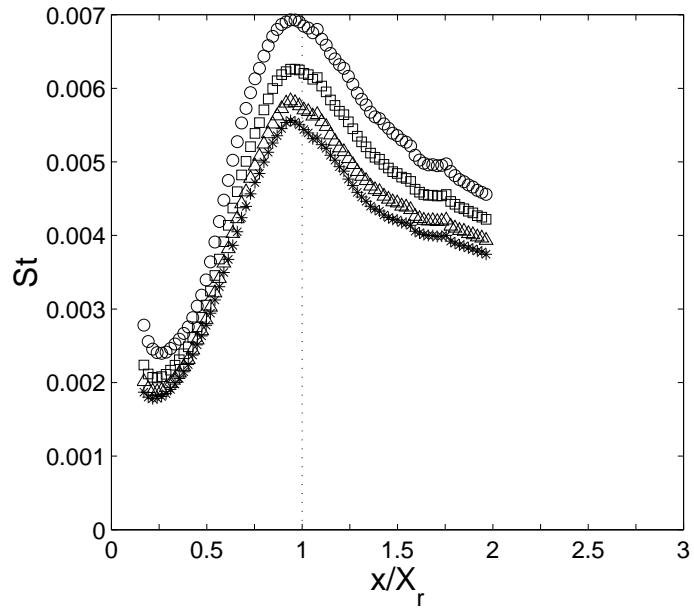


Figure 4.19: Distributions of the Stanton number for jets with $H_s/H_j = 1$ and a Reynolds number of $\bigcirc 21\,800$, $\square 32\,500$, $\triangle 44\,400$ and $*$ 54 500.

with $Re = 21\,800$ (that was much larger than the 95% confidence interval of 2%), indicating the fluctuations were larger in the jets with higher Reynolds numbers. The distributions of the Stanton number for Reynolds number of 21 800 to 54 500 are shown in Fig. 4.19. The Stanton number decreased when the Reynolds number increased. The distributions of the Stanton number normalized using $Re^{-0.24}$ are shown in Fig. 4.20. The results showed that the normalized Stanton number collapsed in the region $0.3 \leq x/X_r < 2$ well within the 95% confidence interval of $\pm 7\%$ indicating the scaling with $Re^{-0.24}$ works throughout the reattachment region. This was different from the offset attaching jet with $H_s/H_j = 5$ where Kim *et al.* (1996) reported that the maximum Nusselt number scaled as $Nu_{max} \propto Re^{0.49}$ or $St_{max} \propto Re^{-0.51}$.

The heat transfer measurements were repeated for offset jets with different offset distances. The change in the maximum Stanton number with the Reynolds number for different offset distance are shown in Fig. 4.21. The maximum Stanton number appeared to change as $St_{max} \propto Re^{-0.34}$ for jets with $H_s/H_j \leq 0.4$, similar to the backward facing step shown in Fig. 4.22. The maximum Stanton number for the backward facing step was computed from the experimental results reported by Vogel & Eaton (1985). The power in this correlation changed gradually as the offset distance increased until it reached $St_{max} \propto Re^{-0.24}$ for jets with $H_s/H_j = 1$. The variations are less than the 95% confidence interval. The trend though seem to be confirmed when the whole distribution is compared and was found to be repeatable in multiple experiments.

The locations of the maximum Stanton numbers for offset jets with $H_s/H_j = 0.2$ to 1.0 are shown in Fig. 4.23. The location with the maximum Stanton number shifted downstream slightly when the Reynolds number increased for the jets with $H_s/H_j \leq 0.6$, while the changes for jet with $H_s/H_j = 1$ were small.

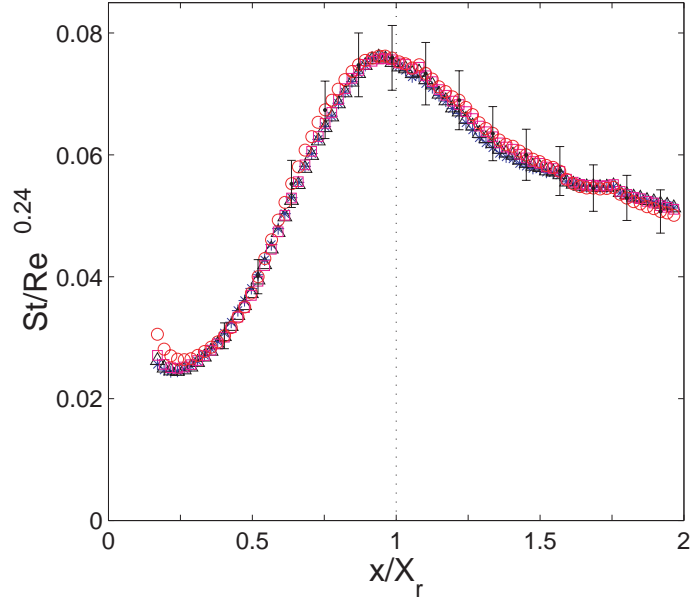


Figure 4.20: Distributions of the normalized Stanton number for jets with $H_s/H_j = 1$ and a Reynolds number of $\circ 21\,800$, $\square 32\,500$, $\triangle 44\,400$ and $*$ $54\,500$, the error bars indicate the uncertainties for 95% confidence interval in the case with $Re = 21\,800$.

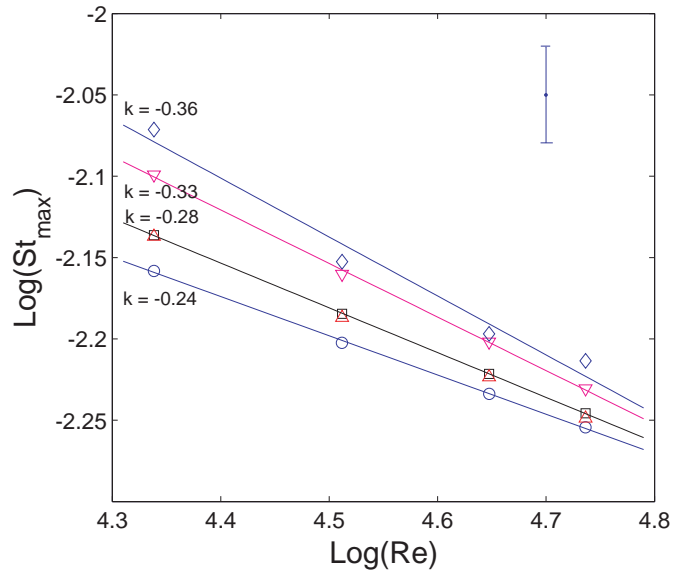


Figure 4.21: Distributions of the maximum Stanton number for jets with different Reynolds numbers and $H_s/H_j = \diamond 0.2$, $\triangledown 0.4$, $\triangle 0.6$, $\square 0.8$ and $\circ 1.0$ in the current investigation, the error bars indicate the uncertainties for 95% confidence interval.

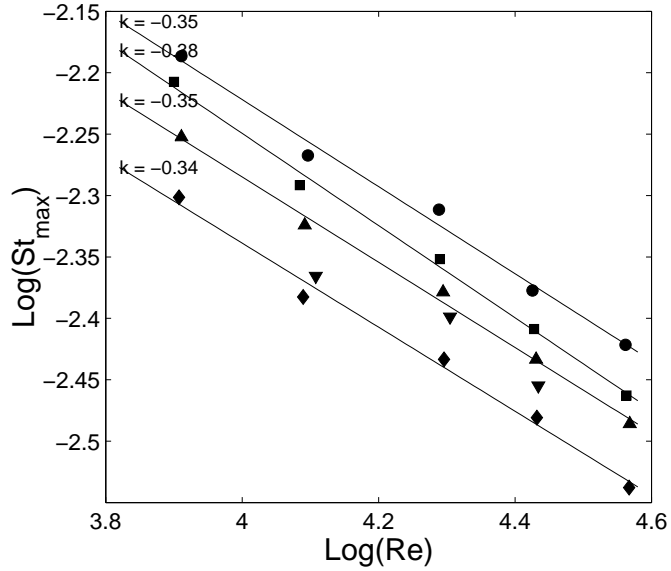


Figure 4.22: Distributions of the maximum Stanton number for a backward facing step with $\delta/H_s = \bullet 0.15$, $\blacksquare 0.19$, $\blacktriangle 0.7$, $\blacktriangledown 1.1$ and $\blacklozenge 1.6$ for different Reynolds numbers computed from the results reported by Vogel & Eaton (1985).

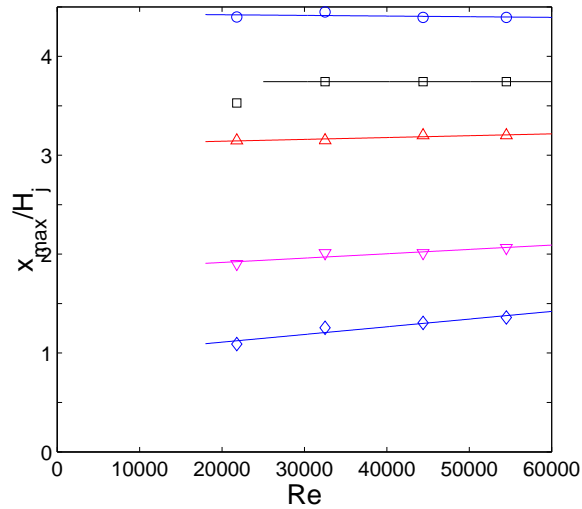


Figure 4.23: Distributions of the location of the maximum Stanton number for jets with different Reynolds numbers and offset distance $H_s/H_j = \diamond 0.2$, $\triangledown 0.4$, $\triangle 0.6$, $\square 0.8$ and $\circ 1.0$.

Chapter 5

Large Scale Flow Structures in Offset Attaching Planar Jets

The evolution of the large scale flow structures in offset jets with different offset distances was studied using the single point spectral measurements and the two-point and two-time measurements of the fluctuating wall pressure and fluctuating velocities in the flows. The results from the single point spectral measurements are first discussed in this chapter. The simultaneous measurements of fluctuating wall pressure are then discussed and compared with the results for the planar wall jet. Finally, joint measurements of the fluctuating wall pressure and velocities for different cases are presented.

5.1 Single point spectral measurements

The evolution of the large scale flow structures in the offset jet was initially examined using the spectra of the fluctuating wall pressure, F_{pp} , and fluctuating streamwise and vertical velocities, F_{uu} and F_{vv} . The spectra of the fluctuating wall pressure, F_{pp} , for jets with different offset ratios are shown in Fig. 5.1. The results for the planar wall jet ($H_s/H_j = 0$) are also shown in this figure. The fluctuating energy in the area near the exit of all the offset jets, $x/X_r \leq 0.26$, was concentrated in the low frequency range. There seemed to be a low

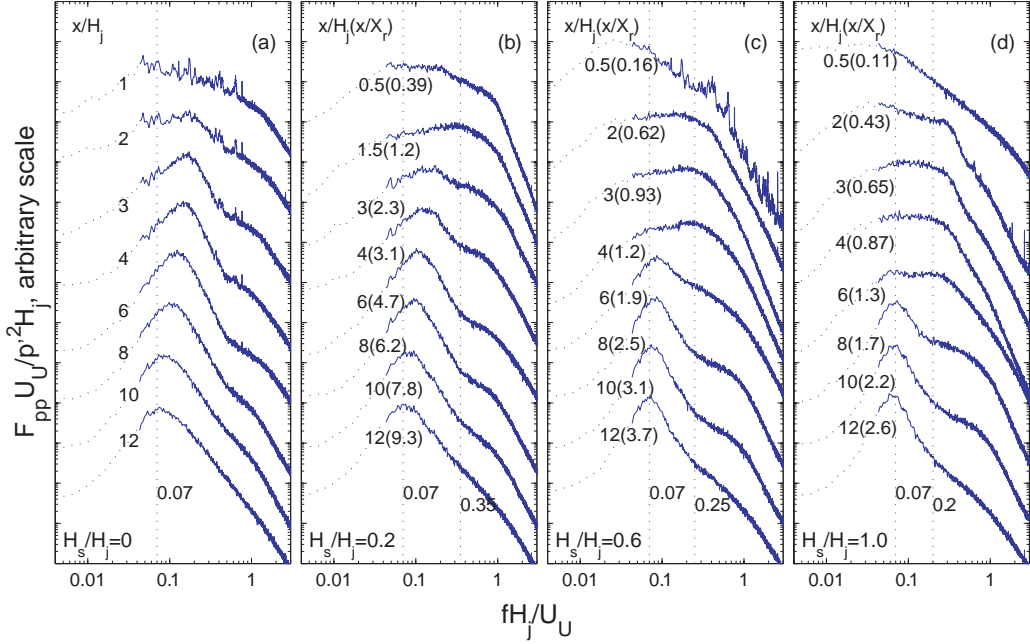


Figure 5.1: Spectra of the fluctuating wall pressure for (a) a planar wall jet and jets with $H_s/H_j =$ (b) 0.2, (c) 0.6 and (d) 1.0 and $Re \approx 44000$.

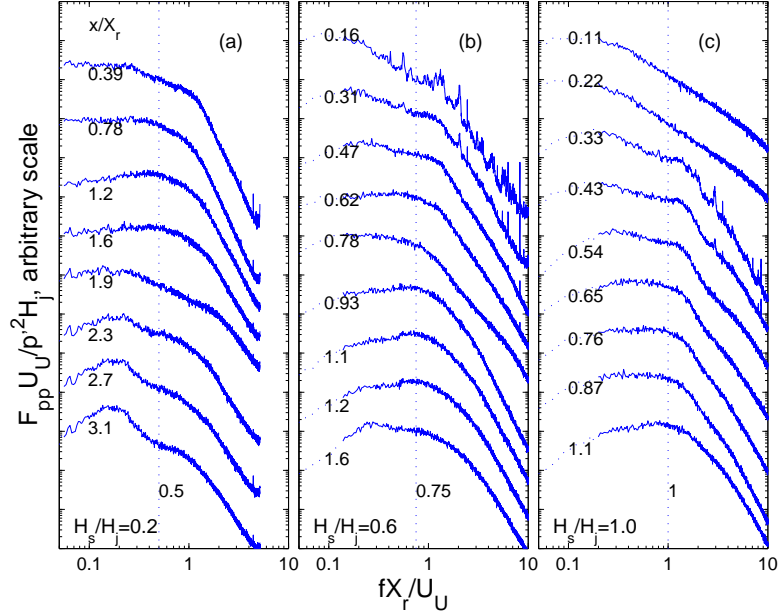


Figure 5.2: Spectra of the fluctuating wall pressure for jets $H_s/H_j =$ (a) 0.2, (b) 0.6 and (c) 1.0 and $Re \approx 44000$.

frequency peaks in the pressure spectra, but the peak was likely associated with the roll-off of the microphone at low frequencies. The spectra for frequencies less than 20Hz are dotted here. A higher frequency peak emerged as the flow evolved downstream to $x/X_r \approx 0.5$ that is likely associated with the large scale flow structures in the attaching inner shear layer. The frequency of this peak decreased as the flow evolved further downstream and formed a dominant peak near the attachment point, similar to the separated shear layer from a bluff body studied by Cherry *et al.* (1984). Here, this frequency shifted from $fH_j/U_U \approx 0.3$ at $x/X_r = 0.43$ to $fH_j/U_U \approx 0.2$ at $x/X_r = 1.1$ for jet with $H_s/H_j = 1$. The frequencies of the peak in the spectra near the attachment point are higher for jets with smaller offset distance, varying from $fH_j/U_U \approx 0.35$ for the jet with $H_s/H_j = 0.2$ to $fH_j/U_U \approx 0.2$ for the jet with $H_s/H_j = 1.0$. The cause of this difference in the frequency will be discussed in more detail later. This peak associated with the attaching inner shear layer gradually disappeared as the flow evolved downstream, which is different from other reattaching flows (Cherry *et al.*, 1984; Hudy *et al.*, 2003), where the peak associated with the inner shear layer was observed well downstream of the reattachment point. In the offset jets, a low frequency peak at $fH_j/U_U \approx 0.07$ emerged near the end of region III. This low frequency peak is very similar to the spectra for the planar wall jet in region $x/H_j \geq 3$, suggesting the flow structures in the offset jet may have changed into ones similar to those in a planar wall jet.

The pressure spectra near the jet exit are shown in Fig. 5.2. Here, the frequency was normalized using X_r . The spectra in region I and II ($x/X_r \leq 1.1$) show similar features for offset ratios of 0.2, 0.6 and 1.0. In the reattachment region, the dominant frequency was $fX_r/U_U \approx 0.3$ to 0.6 for jet with $H_s/H_j = 0.2$, and increased to $fX_r/U_U \approx 0.6$ to 1.2 for jet with $H_s/H_j = 1.0$. The difference in the dominant frequency can also be seen in the spectra from the other reattaching flows measured near the attachment location, shown in Fig. 2.6 (a). The dominant frequencies for these spectra occurred in the range of $0.5 \lesssim fX_r/U_o \lesssim 1.0$.

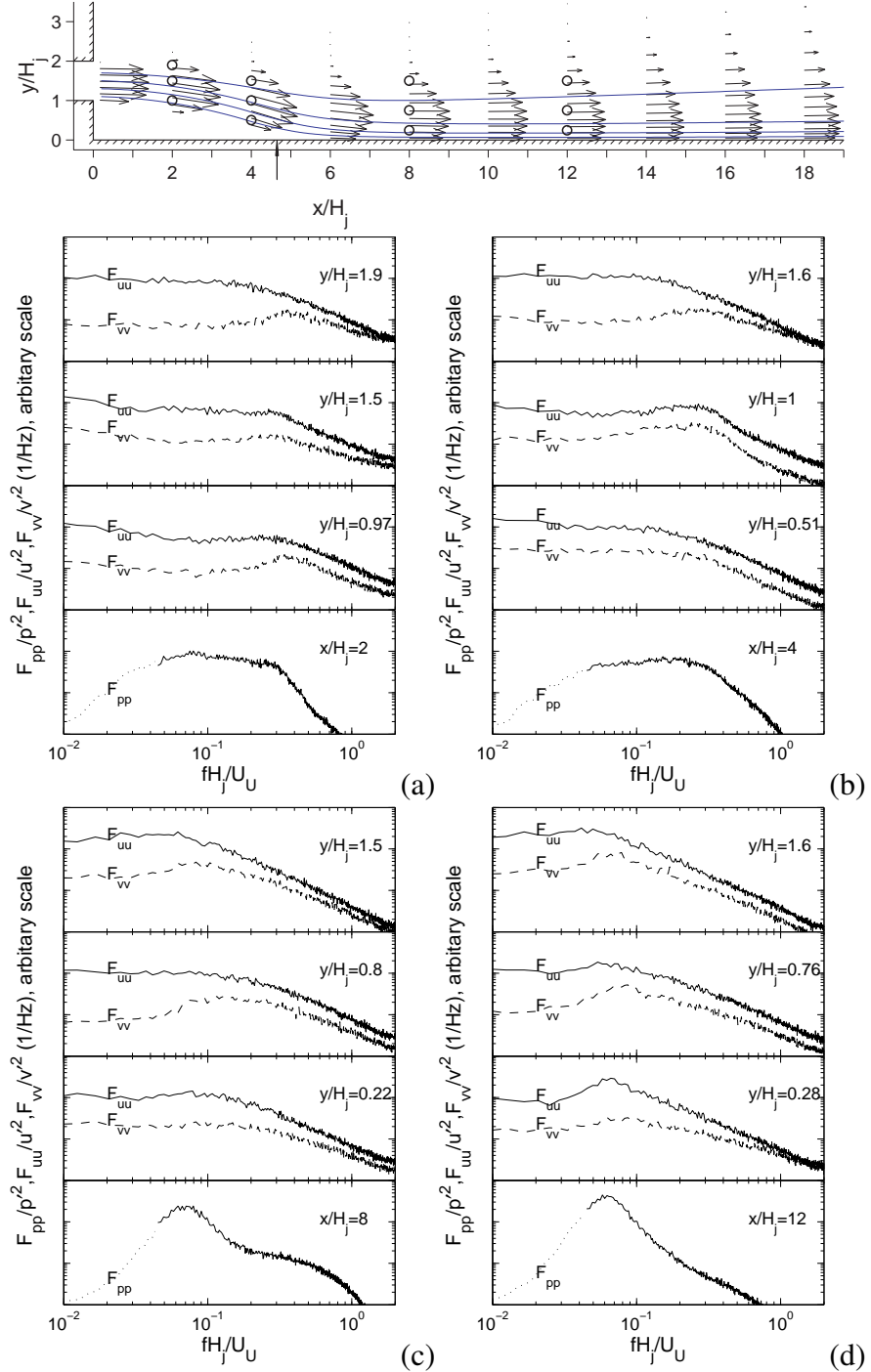


Figure 5.3: Spectra of fluctuating wall pressure and fluctuating streamwise and vertical fluctuating velocities measured at different distance above wall at x/H_j = (a) 2, (b) 4, (c) 8 and (d) 12 for an offset jet with $H_s/H_j = 1$ and $Re \approx 44000$.

The spectra of fluctuating wall pressure and velocities measured in the offset jet with $H_s/H_j = 1.0$ at $x/H_j = 2, 4, 8$ and 12 are shown in Fig. 5.3. In the region upstream of the reattachment location $x/H_j \leq 4$, there appeared to be two characteristic frequencies in the pressure spectra, one at $fH_j/U_U \approx 0.06$ to 0.08 and a second at $fH_j/U_U \approx 0.2$ to 0.3 . The frequency $fH_j/U_U \approx 0.2$ to 0.3 was the characteristic frequency of the velocity fluctuations in the inner part of the jet ($1 \leq y/H_j \leq 1.5$) indicating this peak was likely caused by the flow structures in the inner shear layer. The low frequency peak with $fH_j/U_U \approx 0.08$ was not an obvious characteristic frequency of the fluctuating velocities in the jet and was likely caused by the recirculating flow.

The characteristic frequency of streamwise fluctuating velocity in the outer part of the jet ($y/H_j \geq 1.6$) was smaller than the characteristic frequency of the flow near the wall in the region $x/H_j \leq 4$. The characteristic frequency of the outer part of the flow decreased gradually as the flow evolved downstream and the motion this frequency associated with became the dominant motion in the jet, particularly at $x/H_j = 12$ where the characteristic frequency of the fluctuating wall pressure and fluctuating velocities coincided.

5.2 Two-point two-time pressure measurements

5.2.1 Transition from a reattaching flow to a planar wall jet

The dynamics of the offset attaching jet can be further studied by examining the correlations of the fluctuating wall pressures, given by

$$\rho_{pp}(x_1, x_2, \tau) = \frac{\overline{p(x_1, t)p(x_2, t + \tau)}}{p'(x_1)p'(x_2)}. \quad (5.1)$$

The correlation coefficients of the fluctuating wall pressure for a planar wall jet and an offset jet with $H_s/H_j = 0.6$ are shown in Figure 5.4. The results here are for cases with the reference microphones located at $x_1/H_j = 1.5, 3, 5$ and 7 . Some of the contours show slight discontinuities due to the spatial resolutions of the microphone array. For the

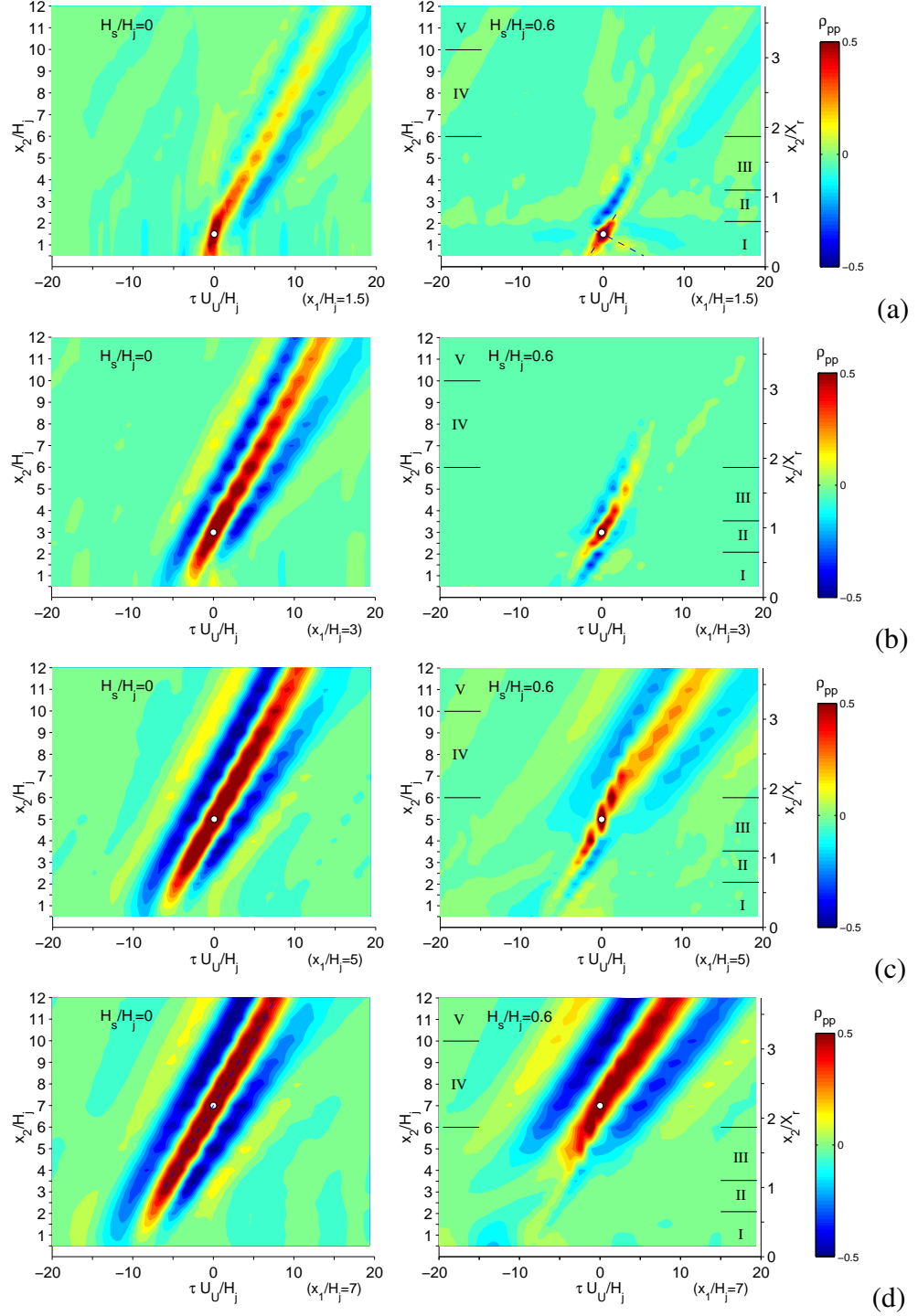


Figure 5.4: Correlation coefficient, ρ_{pp} , of the fluctuating wall pressure for the reference microphone at $x_1/H_j =$ (a) 1.5, (b) 3, (c) 5 and (d) 7 for a planar wall jet (left) and an offset jet with $H_s/H_j = 0.6$ (right), the locations of other microphones indicated by left tick marks.

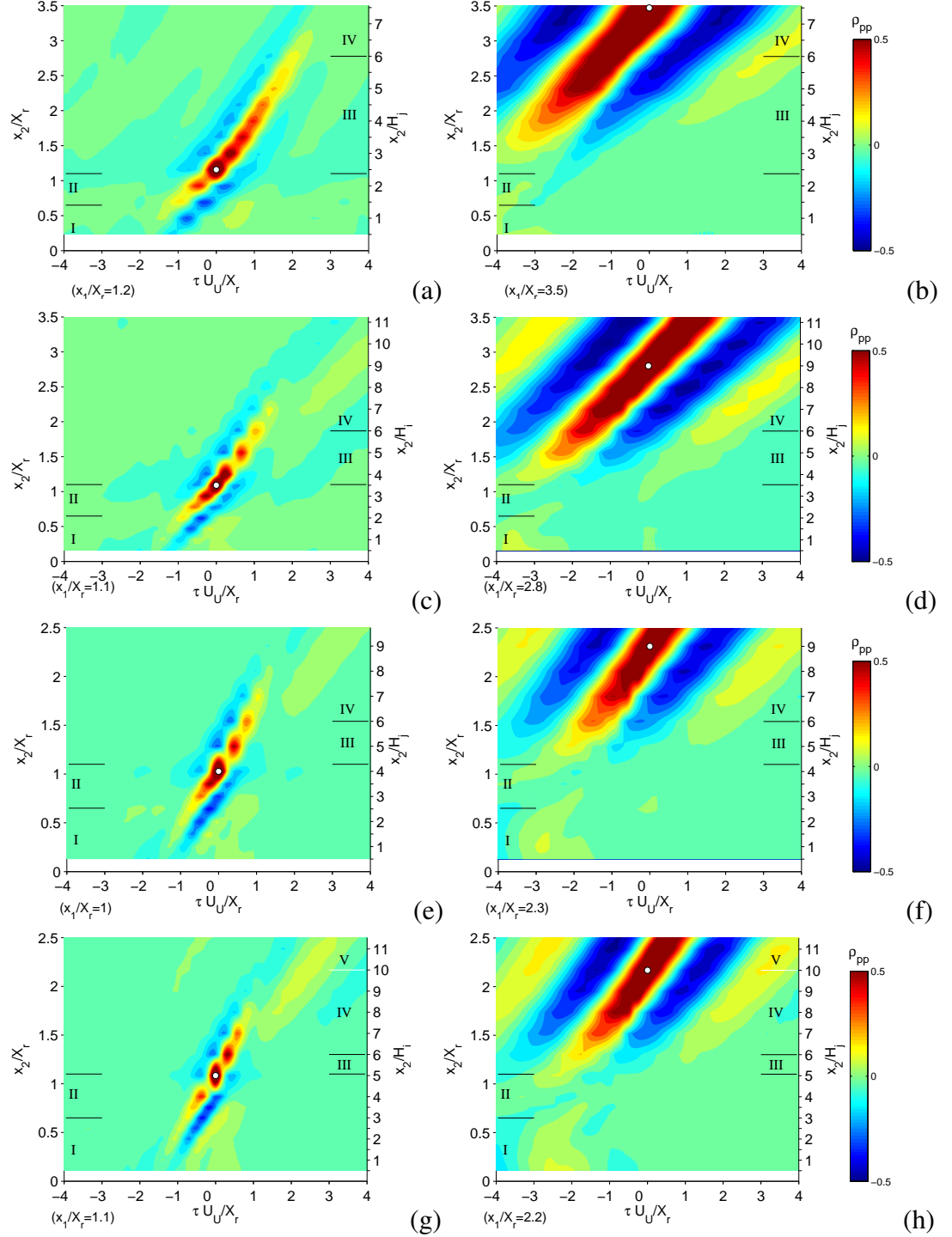


Figure 5.5: Correlation coefficient, ρ_{pp} , of the fluctuating wall pressure with a reference microphone in region III (left) and region IV (right) for jets with $H_s/H_j =$ (a)&(b) 0.4, (c)&(d) 0.6, (e)&(f) 0.8 and (g)&(h) 1.0 and $Re \approx 44000$.

planar wall jet, the fluctuating wall pressure measured at $x/H_j \leq 2.5$ were well correlated and there was a very small time lag in the correlations. This time lag seemed too short to correspond to convection of flow structures as the corresponding velocity would be approximately $3U_U$. Evidence of convection of the disturbances was found in the region $x/H_j > 2.5$ where there was a significant time lag in the maxima in the correlation coefficients that likely corresponds to the passage of the flow structures.

The correlations for the offset jet with $H_s/H_j = 0.6$ were significantly different from the planar wall jet due to the reattachment process. In region I ($x/X_r \leq 0.65$), there is evidence of correlated motions with both positive and negative time lags suggesting there are events convected both downstream and upstream. The correlation associated with the downstream convecting fluctuations gradually diminished in the region $x/H_j \approx 4$ coinciding with the locations where the structures in the inner shear layer of the jet interacted with the wall. The correlations in region III, IV and V indicate that large scale fluctuations emerged in the region $x/H_j \geq 6$, and developed downstream similar to the fluctuations in the planar wall jet flow. The transition of the dominant role between these two types of fluctuations seemed to occur near $x/H_j \approx 6$, which was the beginning of region IV defined in the previous chapter based on the mean flow measurements.

The transition between the reattaching flow region and the planar wall jet region for other offset distances can also be examined using the correlation coefficients of the fluctuating wall pressure. The correlations of the fluctuating wall pressure for jets with $H_s/H_j = 0.4$ to 1.0 are shown in Fig. 5.5. The reference microphones were located at $x/X_r \approx 1.1$ and $x/H_j \approx 9$. These reference locations were selected so that the correlations due to the structures in the reattaching shear layer and the structures in the wall jet can be clearly observed. For all the jets, the correlation associated with the wall-jet type fluctuations appeared to emerge near the beginning of region III ($x/X_r \approx 1.1$) indicating the wall jet structures began to play a role soon after the jets attached to the wall. The correlation from the structures in the attaching shear layer disappeared near the end of region III ($x/H_j \approx 6$)

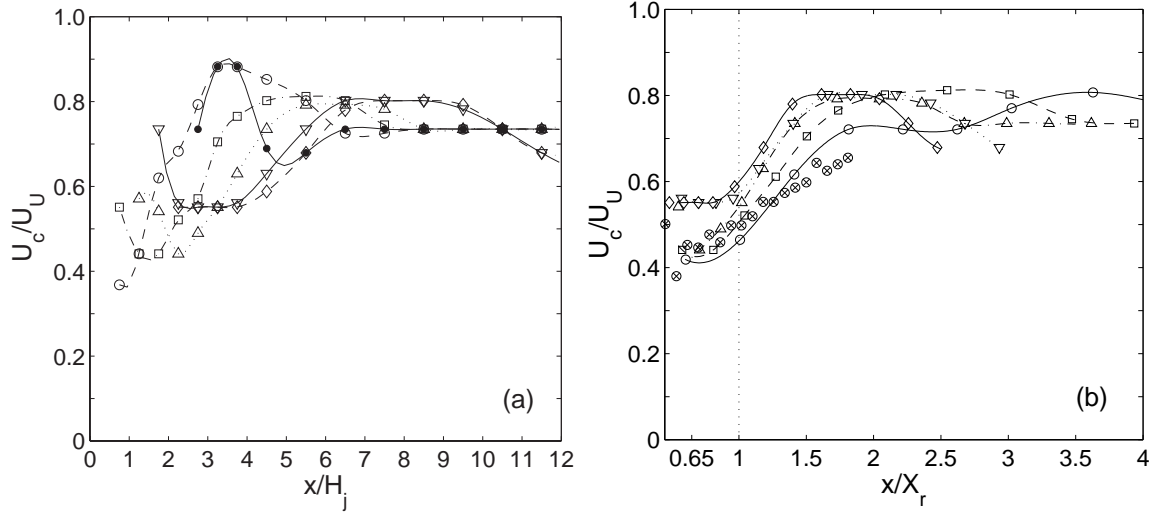


Figure 5.6: Distributions of the convection velocity for the dominant flow structures in jets with $H_s/H_j = \circ 0.2 \square 0.4 \triangle 0.6 \triangledown 0.8 \diamond 1.0$ and $Re \approx 44000$ based on equation 5.2 and for \otimes the flow over a backward facing step (Heenan & Morrison, 1998).

for jet with $H_s/H_j = 0.4$. This location gradually shifted downstream when the offset distance of the jet increased. Thus, the transition location is not fixed in either x/X_r or x/H_j but depends on H_s/H_j .

The convection velocity or the propagation velocity of the fluctuations is often determined from the slope of the locus of the main positive peak in the cross correlation contour (Heenan & Morrison, 1998; Hudy *et al.*, 2003), given by

$$\frac{U_c}{U_U} = \frac{\Delta x/H_j}{\Delta \tau U_U/H_j}. \quad (5.2)$$

The convection velocities, U_c , near the reattachment location determined using this equation for jets with $H_s/H_j = 0.2$ to 1.0 are shown in Fig. 5.6. The average convection velocity was approximately $0.7U_U$ in the region $2.5 < x/H_j \leq 12$ for the planar wall jet. The downstream convection velocities in region I of the offset jet were initially large but decreased to $U_c/U_U \approx 0.45$ to 0.6 as the separated flow attached to the wall in region II ($0.65 \leq x/X_r \leq 1.1$). The velocity U_c were higher for jets with larger offset ratios. The

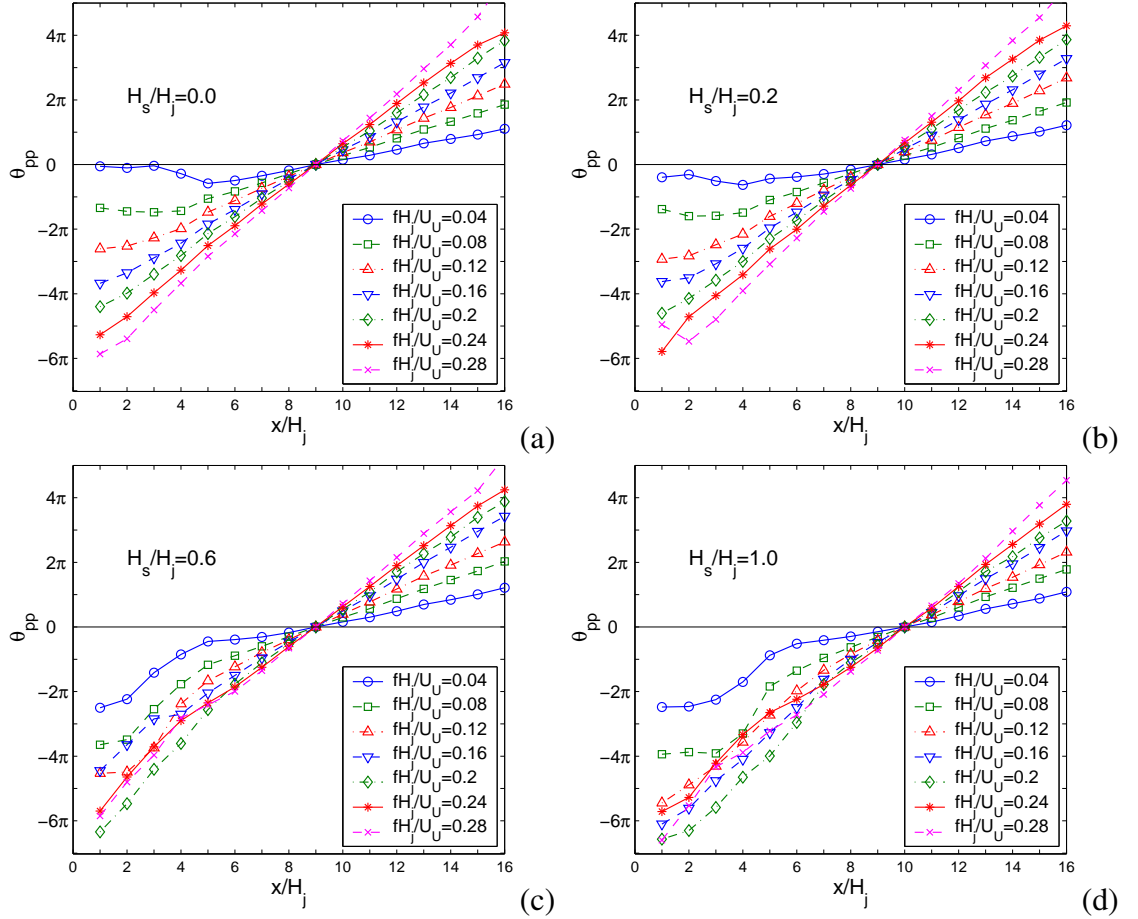


Figure 5.7: Phase angles of the cross spectra for (a) the planar wall jet and offset jets with $H_s/H_j =$ (b) 0.2 (c) 0.6 and (d) 1.0 and $Re \approx 44000$ with reference microphone at $x_1/H_j = 2$.

convection velocities for the jet with $H_s/H_j = 0.4$ agreed with the results from the backward facing step (Heenan & Morrison, 1998) near the reattachment location. Downstream of the reattachment point, the convection velocity increased to $U_c/U_U \approx 0.7$ to 0.8, similar to the planar wall jet, despite the decrease in the local maximum streamwise velocity.

The convection velocity for the fluctuations with individual frequencies can be estimated using the slope of the cross spectra phase angle, $\theta_{pp}(x_1, x_2, f)$, at different streamwise location, x_2 , relative to a fixed location x_1 , *i.e.* (Hudy *et al.*, 2003)

$$\frac{U_c}{U_U} = \frac{2\pi(fH_j/U_U)}{\Delta\theta_{pp}(x_1, x_2, f)/(\Delta x_2/H_j)}. \quad (5.3)$$

The phase angles were initially computed using equation. 3.16. The unwrapped phase angles at different streamwise locations for a range of frequencies in the different jets are plotted in Fig. 5.7. The reference microphone was located at $x_1/H_j = 9$ or 10 in order to track the emergence and the development of wall jet type structures. The phase angle for $fH_j/U_U \geq 0.2$ increased linearly in the streamwise direction for the planar wall jet in the region $2 \leq x_2/H_j \leq 16$ indicating structures with high frequencies were convected with a constant velocity from near the jet exit. The changes of phase angle were not linear with streamwise position for low frequencies. For example, the phase angle for $fH_j/U_U = 0.08$ increased linearly with streamwise position only in the region $4 \leq x/H_j \leq 16$. Thus, the results suggest that these low frequency motions were generated in the initial region of the jet and then were convected downstream. The change in the phase angles with streamwise position for the jet with $H_s/H_j = 0.2$ was similar to the results for the planar wall jet suggesting the flow structures in the offset jet with $H_s/H_j \leq 0.2$ were convected in a way similar to the planar wall jet. For larger offset distances $H_s/H_j \geq 0.6$, the slope of the phase angles increased near the reattachment location suggesting there was a decrease in the convection velocity. After the reattachment, the slope decreased and changed linearly with streamwise position in the region $x/H_j \gtrsim 6$.

The convection velocities computed using the slope of the phase angles in the region $7 \leq x/H_j \leq 16$ are shown in Fig. 5.8. The convection velocity for the planar wall jet was approximately $0.6U_U$ for $fH_j/U_U = 0.08$ and increased gradually to $0.8U_U$ for $fH_j/U_U = 0.24$. Thus, the fluctuations with larger frequencies appeared to be convected faster than the fluctuations with lower frequencies. The convection velocities of fluctuations in the region $7 \leq x/H_j \leq 16$ for offset jets were slightly smaller than the planar wall jet except at $fH_j/U_U \approx 0.2$ where the convection velocities were similar. The convection velocity for the large frequencies ($fH_j/U_U \gtrsim 0.2$) agreed with the convection velocity

estimated from the correlation contours ($U_c/U_U \approx 0.7$ to 0.8) indicating that the convection velocity evaluated using equation 5.2 is a better measure of the propagation velocity of the fluctuations with frequencies larger than the characteristic frequency of dominant motions in the flow. The convection velocity of the most dominant fluctuations in terms of fluctuating energy ($fH_j/U_U \approx 0.06$ to 0.08) was approximately $0.5U_U$ to $0.6U_U$.

5.2.2 Dominant motions in the reattaching region

The dynamics of the pressure fluctuations in the reattaching region were examined using local reference points in the regions I and II. The correlation coefficients of the pressure fluctuations for jets with $H_s/H_j = 0.4, 0.6, 0.8$ and 1.0 with reference location at $x_1/X_r \approx 0.4$ are shown in Fig. 5.9. Here, the length scale was the reattachment length, X_r . The contour for the offset jet with $H_s/H_j = 0.2$ was not shown here due to insufficient spatial resolution in this case. There was evidence of structures being convected both downstream and upstream for all the cases. This was particularly clear in the cases with $H_s/H_j \geq 0.6$ where the spatial resolution was better. Evidence of upstream propagating disturbances with similar convection velocity were also found by Hudy *et al.* (2003) in the reattaching flow over a bluff body and Heenan & Morrison (1998) for the flow over a backward facing step. The characteristics of the motions causing these can again be examined using the coherence of the fluctuations.

The cross spectra, phase angles and the coherence of fluctuating wall pressure measured for $x_1/X_r = 0.43$ and $x_2/X_r \leq 1.2$ in an offset jet with $H_s/H_j = 1$ are shown in Fig. 5.10. There are two frequency ranges with good coherence between the different points. There is a broad peak for the frequency range $fX_r/U_U \lesssim 0.4$ in the region $0.3 \lesssim x_2/X_r \lesssim 1$ (except at $x_2/X_r = 0.65$). This has a similar frequency to the peak in the auto-spectra measured in this region. There is a second frequency range of large coherence $fX_r/U_U \gtrsim 0.4$. The coherence reaches a maximum at $fX_r/U_U \approx 1.2$ to 1.4 . The coherence in this range decreases for $x_2/X_r \gtrsim 1$.

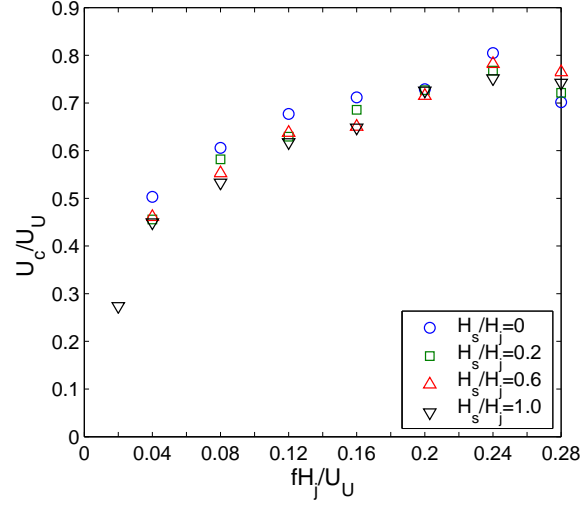


Figure 5.8: The convection velocities for fluctuations with different frequencies in the region $7 \leq x/H_j \leq 16$ for a planar wall jet and offset jets with $H_s/H_j = 0.2$ to 1 and $Re \approx 44000$ based on equation 5.3.

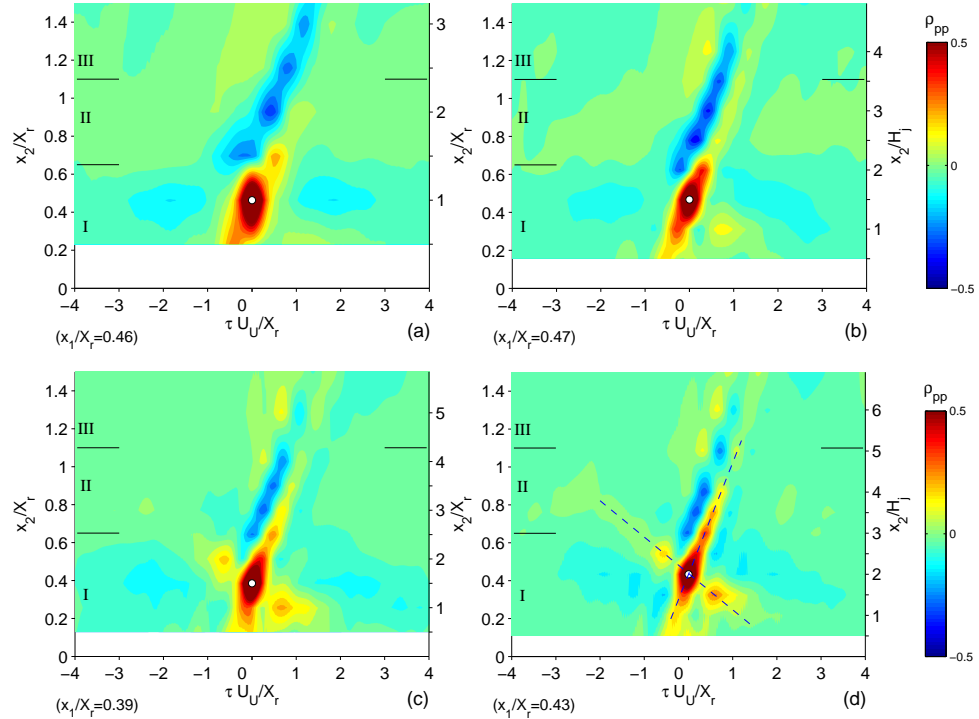


Figure 5.9: Correlation coefficient, ρ_{pp} , of the fluctuating wall pressure for the reference microphone in the region I near $x_1/X_r \approx 0.4$ for an offset jets with $H_s/H_j =$ (a) 0.4, (b) 0.6, (c) 0.8 and (d) 1.0 and $Re \approx 44000$, the locations of other microphones, x_2 , indicated using the tick marks on the right.

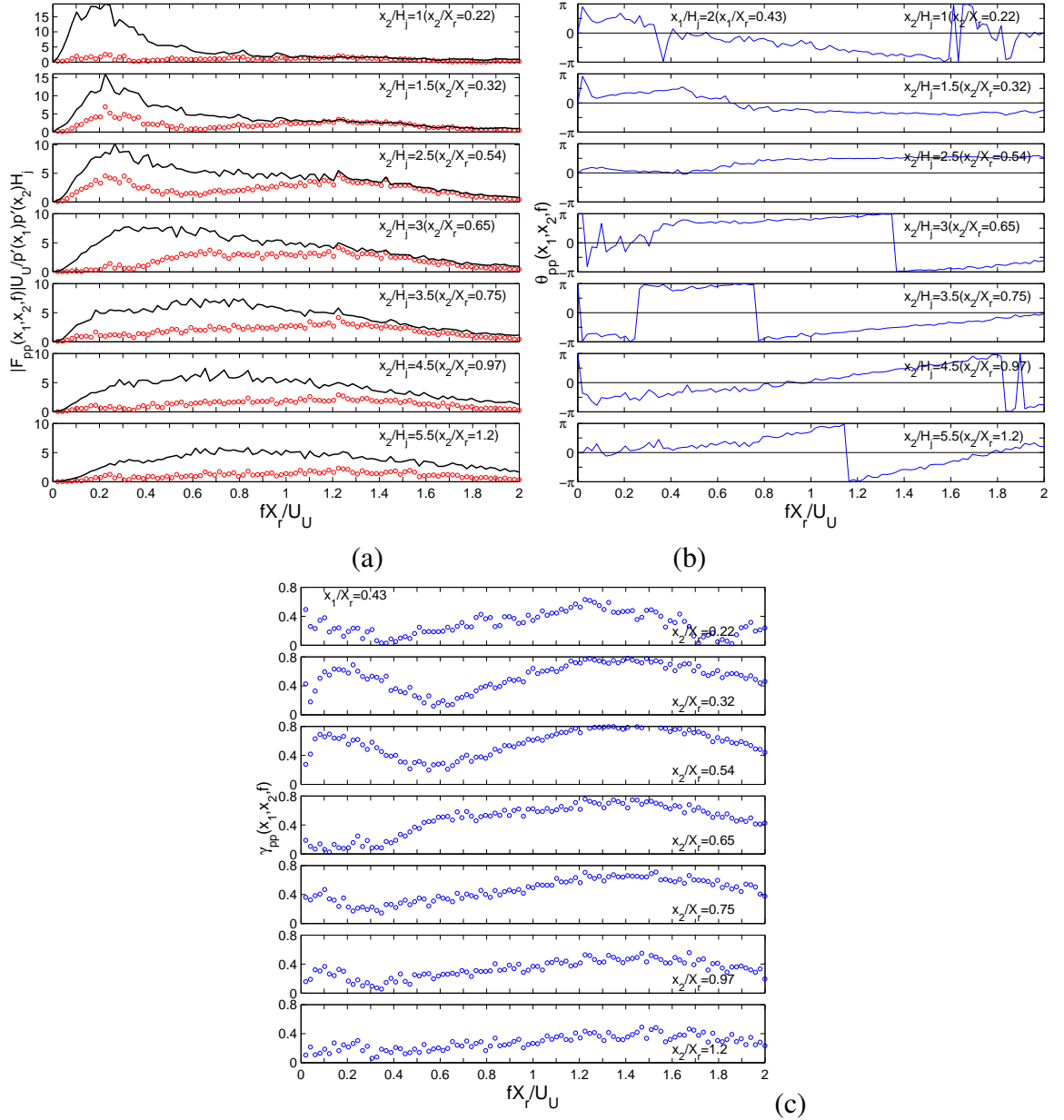


Figure 5.10: The (a) cross spectra (b) phase angle and (c) coherence of the cross spectra between the fluctuating pressure at $x_1/X_r = 0.43$ ($x_1/H_j = 2$) and x_2/X_r for offset jet with $H_s/H_j = 1.0$ and $Re \approx 44000$. The auto spectra at x_2/X_r are also shown in figure (a) using a solid line.

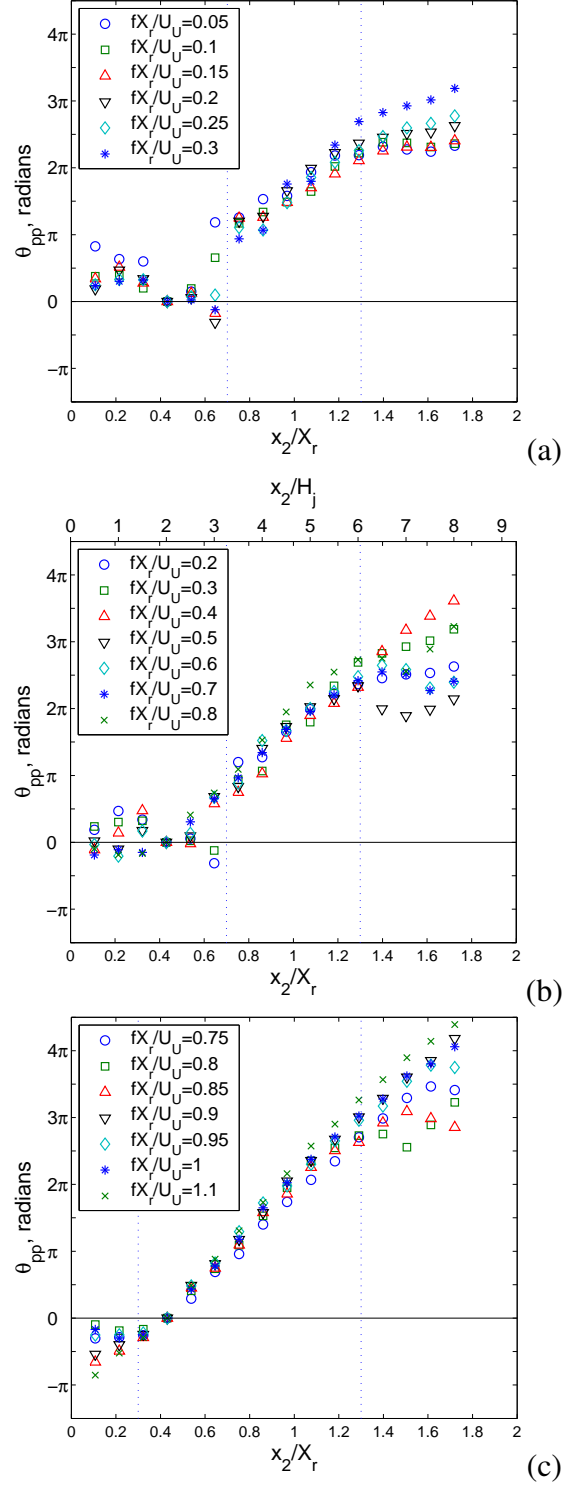


Figure 5.11: The phase angle of cross spectra between the fluctuating pressure at $x_1/X_r = 0.43$ ($x_1/H_j = 2$) and x_2/X_r for the offset jet with $H_s/H_j = 1.0$ and $Re \approx 44000$.

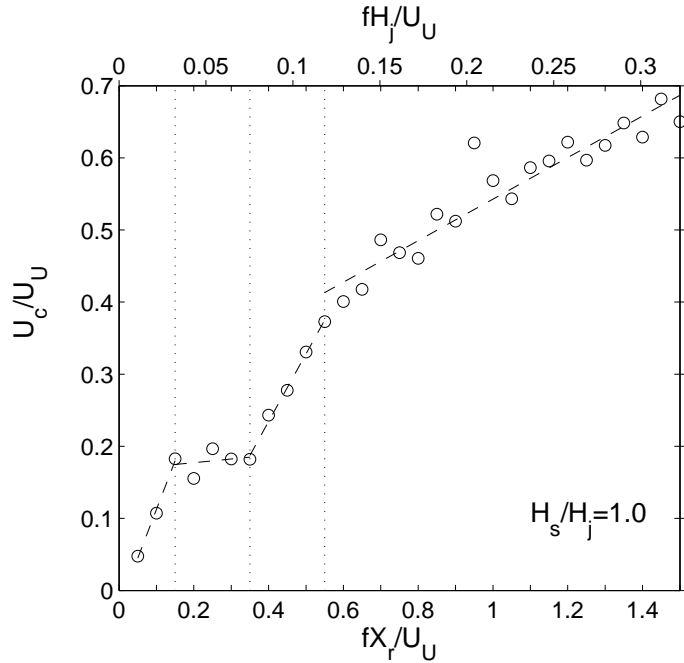


Figure 5.12: The convection velocity for different frequencies in the region $0.75 \leq x/X_r \leq 1.2$ ($3.5 \leq x/H_j \leq 5.5$) for offset jet with $H_s/H_j = 1.0$ and $Re \approx 44000$, based on the cross spectra of the fluctuating wall pressure.

The changes in the phase angles of the cross spectra with frequency for each position shown in Fig. 5.10 (b) do not clearly illustrate the development of the fluctuations. The change of phase angle with streamwise position (x_2/H_j) for a few selected frequencies are shown again in Fig. 5.11. The phase angle for frequencies $fX_r/U_U = 0.15$ to 0.3 decreased in the streamwise direction in region I indicating the convection velocities for fluctuations with these frequencies were negative in this region. There was a phase jump of π at $x/X_r \approx 0.75$ for the fluctuations with $fX_r/U_U = 0.15$ to 0.3 . The phase angles then increased with streamwise position in the region $x/X_r > 0.75$, indicating the fluctuations with these frequencies were propagating downstream in this region. The downstream propagating region started closer to the jet exit for higher frequencies. For example, the frequency of the dominant fluctuations in the reattaching flow ($fX_r/U_U \approx 0.8$) convected downstream in region $x/X_r \gtrsim 0.3$, while the fluctuations with $fX_r/U_U = 1.2$ propagated downstream

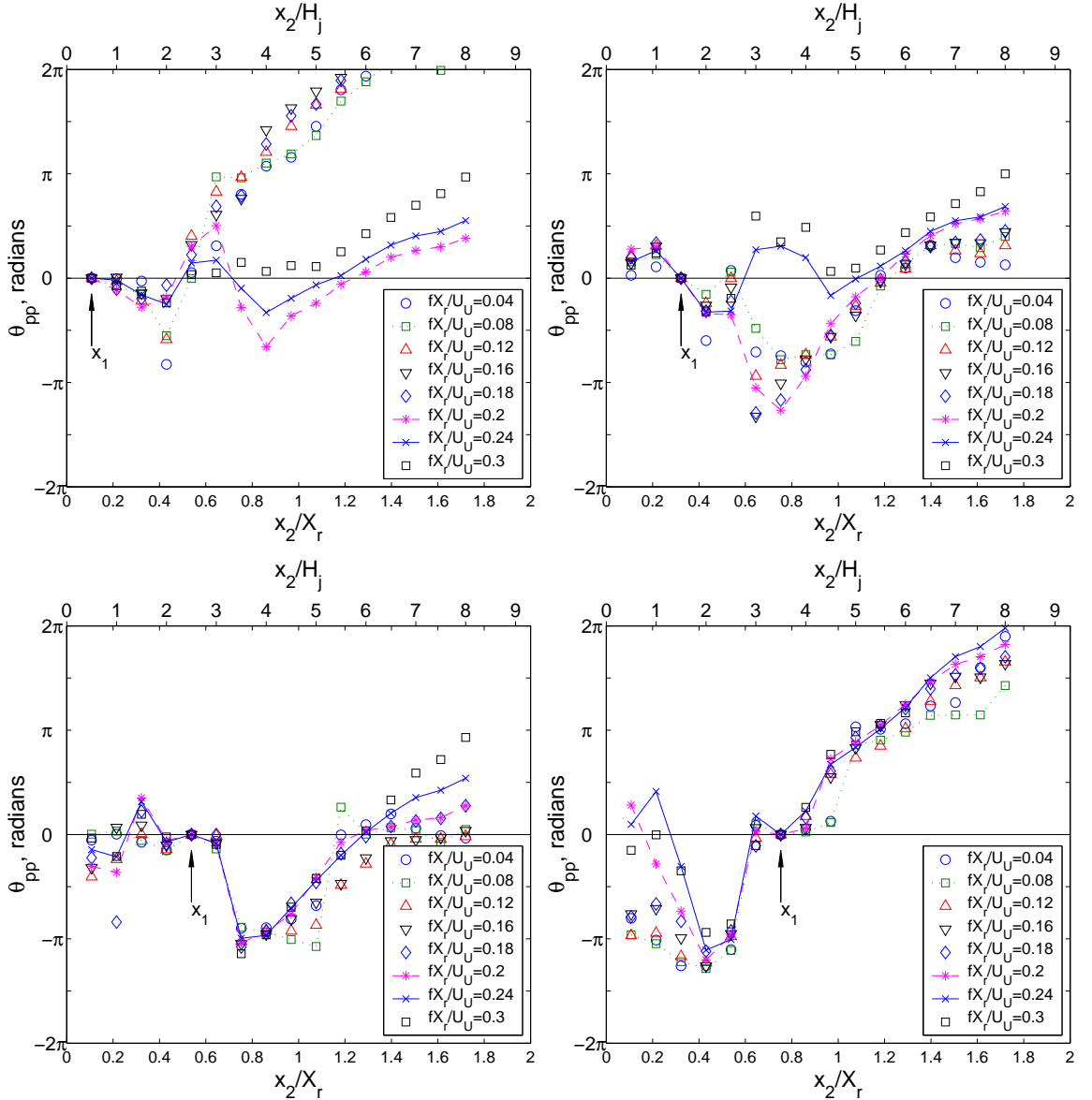


Figure 5.13: Distributions of phase angles of the cross spectra for reference location $x_1/X_r = 0.11, 0.32, 0.54$ and 0.75 ($x_1/H_j = 0.5, 1.5, 2.5$ and 3.5) for an offset jet with $H_s/H_j = 1.0$ and $Re \approx 44000$

throughout the region studied.

The slopes of the phase angles in the reattachment region $0.75 \lesssim x/X_r \lesssim 1.2$ (Region II) were approximately linear for all the frequencies shown here. The averaged convection velocity in this region determined using these slopes is shown in Fig. 5.12. The convection velocity seemed to increase gradually with the frequency for $fX_r/U_U \lesssim 0.15$. The convection velocity was approximately $0.2U_U$ for fluctuations with $0.15 \lesssim fX_r/U_U \lesssim 0.35$ ($0.03 \lesssim fH_j/U_U \lesssim 0.08$). The convection velocity for fluctuations with $fX_r/U_U \gtrsim 0.35$ increased approximately linearly with the frequency. The slope of the convection velocity for different frequencies changed again at $fX_r/U_U \approx 0.6$ indicating the fluctuations with $0.35 \lesssim fX_r/U_U \lesssim 0.65$ might be associated with mechanisms other than the flow structures in the attaching shear layer which have characteristic frequency of $0.6 \lesssim fX_r/U_U \lesssim 1.2$.

The dynamics of the motion in the reattachment region were further studied by examining the phase angles of the cross pressure spectra for four different reference microphone locations, $x_1/X_r = 0.11, 0.32, 0.54$ and 0.75 . The first three are in Region I ($x/X_r \leq 0.65$) while the last is in Region II. The results are shown in Fig. 5.13. This is particularly useful for the motions with $fX_r/U_U \lesssim 0.3$ that make the largest contribution to the fluctuating wall pressure for $x/X_r \leq 0.25$. The results show that the distributions of the phase angle for $x/X_r < 1$ were different for different reference locations. There seemed to be sub-regions where there were different locally dominant motions. The phase angles for frequencies $fX_r/U_U \leq 0.3$ for the cases with $x_1/X_r = 0.11$ and 0.32 decreased in the streamwise direction for $0.2 \lesssim x/X_r \lesssim 0.4$ indicating the fluctuations with these frequencies propagated upstream in this sub-region. The phase angles for frequencies $fX_r/U_U \leq 0.3$ varied less than $\pi/4$ over the sub-region $0.4 \lesssim x_2/X_r \lesssim 0.6$ when $x_1/X_r = 0.54$ or 0.75 indicating the fluctuations with these frequencies were approximately in phase in this sub-region. There was then a jump of π in the phase angle for the frequencies $fX_r/U_U \leq 0.3$ at $x_2/X_r \approx 0.6$ to 0.7 that coincided with the start of the region II (the reattachment region).

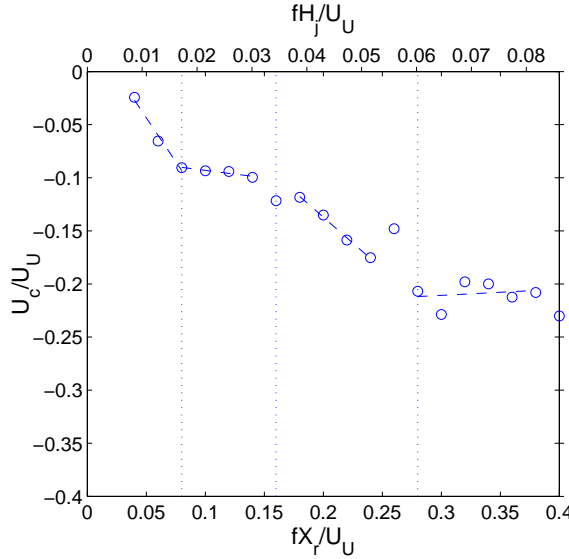


Figure 5.14: Convection velocity calculated using phase angle of the fluctuating wall pressure in the region $1 \leq x_2/H_j \leq 2$ ($0.22 \leq x_2/X_r \leq 0.43$) with reference location $x_1/X_r = 0.32$ for an offset jet with $H_s/H_j = 1.0$ and $Re \approx 44000$.

The nature of the motions with $fX_r/U_U \leq 0.3$ seem to fall into two groups in region II. The phase angle between the fluctuations with $fX_r/U_U \leq 0.08$ at $x_1/X_r = 0.7$ and the fluctuations in the region $0.75 \lesssim x_2/X_r \lesssim 1.0$ were approximately 0 indicating the low frequency fluctuations were in phase in this region. These fluctuations were out of phase with fluctuations in the sub-region $0.4 \lesssim x_2/X_r \lesssim 0.6$. Thus, there appeared to be a low frequency unsteadiness with $fX_r/U_U \lesssim 0.08$ associated with a flapping motion that caused the fluctuations in part of Region I and Region II to be out of phase.

The results for the motions with $fX_r/U_U \gtrsim 0.12$ were different in Region II. The phase angle of the cross spectra measured between $x_1/X_r = 0.75$ and $0.75 \lesssim x_2/X_r \lesssim 1.0$ increased gradually with downstream positions indicating that these higher frequency fluctuations were convected downstream in $x_2/X_r \geq 0.75$ (Region II).

The convection velocity of the fluctuations for $0.2 \lesssim x/X_r \lesssim 0.4$ was calculated using the slope of the phase angle of the cross spectra, $d\theta_{pp}/dx_2$, with $x_1/X_r = 0.32$

and $0.2 \lesssim x_2/X_r \lesssim 0.4$ and shown in Fig. 5.14. The convection velocity was negative suggesting the fluctuations were propagating upstream. The magnitude of the convection velocity was approximately $0.1U_U$ for fluctuations with a frequency of $fX_r/U_U \approx 0.08$ and $0.2U_U$ for frequencies of $0.28 \lesssim fX_r/U_U \lesssim 0.4$. This was similar to the downstream convection velocity in the region $0.75 \lesssim x/X_r \lesssim 1.2$. It seemed that the motions with $0.28 \lesssim fX_r/U_U \lesssim 0.4$ started to interact with the wall in the region $0.4 \lesssim x/X_r \lesssim 0.8$ and convected both upstream and downstream at a similar convection velocity.

5.3 Two-point two-time pressure-velocity measurements

The motions in the reattaching flow and the transition from the reattaching flow to wall jet were examined using joint measurements of fluctuating wall pressure and fluctuating velocities for a planar wall jet and the offset jets. The correlation coefficients of the wall pressure fluctuations and the fluctuating velocity at points above the microphone given by

$$\rho_{pu}(x, y, \tau) = \frac{\overline{p(x, t)u(x, y, t + \tau)}}{p'(x)u'(x, y)} \quad (5.4)$$

and

$$\rho_{pv}(x, y, \tau) = \frac{\overline{p(x, t)v(x, y, t + \tau)}}{p'(x)v'(x, y)}, \quad (5.5)$$

were first examined. Here, x is the location of the reference microphone, y is the locations of the hot-wire probe above the microphone, and τ is the time interval.

The two-point and two-time correlation coefficients of the fluctuating wall pressure and the fluctuating velocities measured above the the microphone in the planar wall jet are shown in Fig. 5.15. The location of the jet outlet is shown on the left of these figures to show its location relative to the motions. The profiles of the rms fluctuating velocities measured at the different locations were also shown on the left. The horizontal axis in these figure are the time separation and should not be misinterpreted as a separation in the streamwise direction. The wall pressure at $x/H_j = 1.5$ was initially poorly correlated with

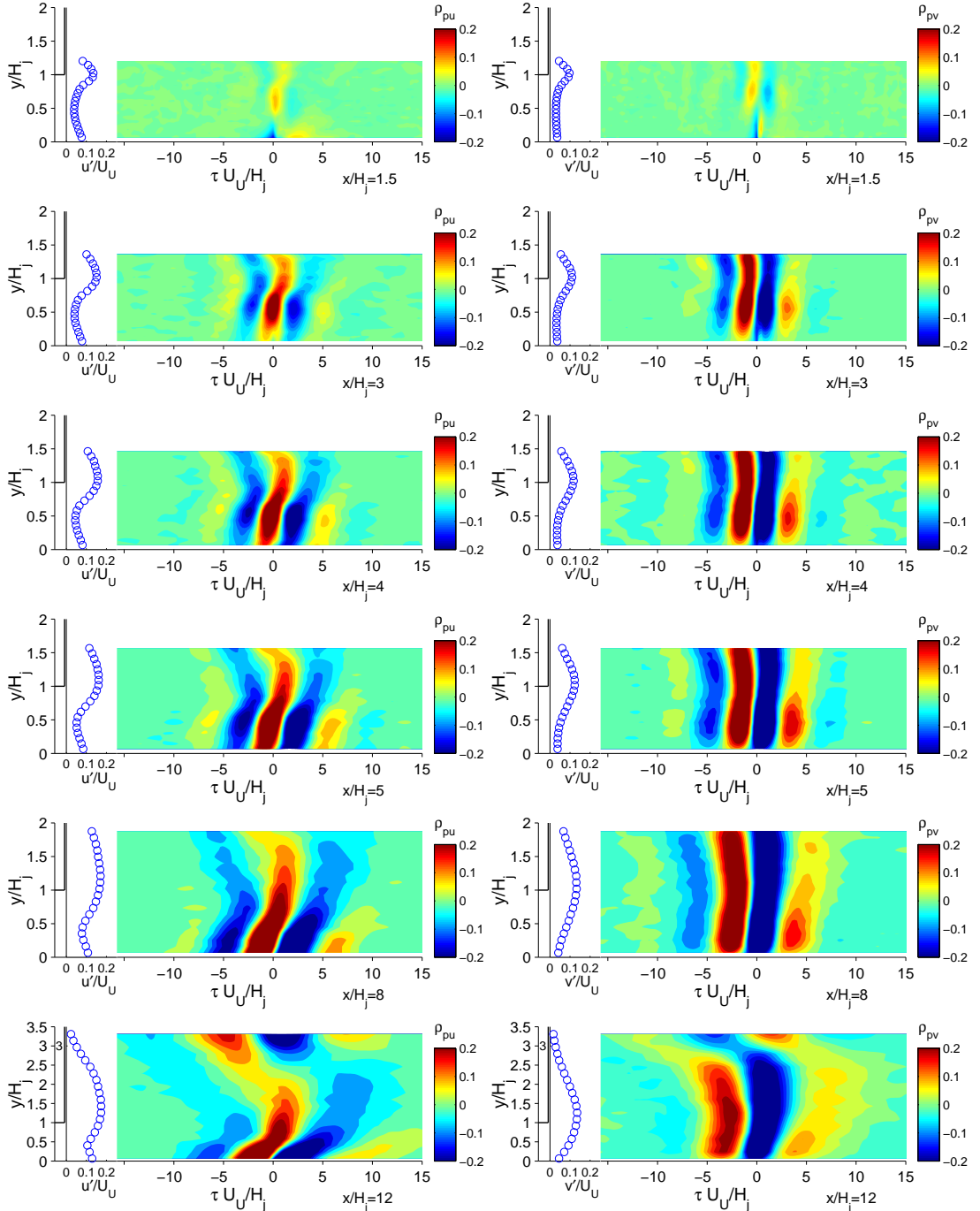


Figure 5.15: Correlation coefficients of the fluctuating wall pressure and the streamwise fluctuating velocity ρ_{pu} (left) and the vertical fluctuating velocity ρ_{pv} (right) for a planar wall jet with $Re \approx 44\,000$ at different streamwise locations.

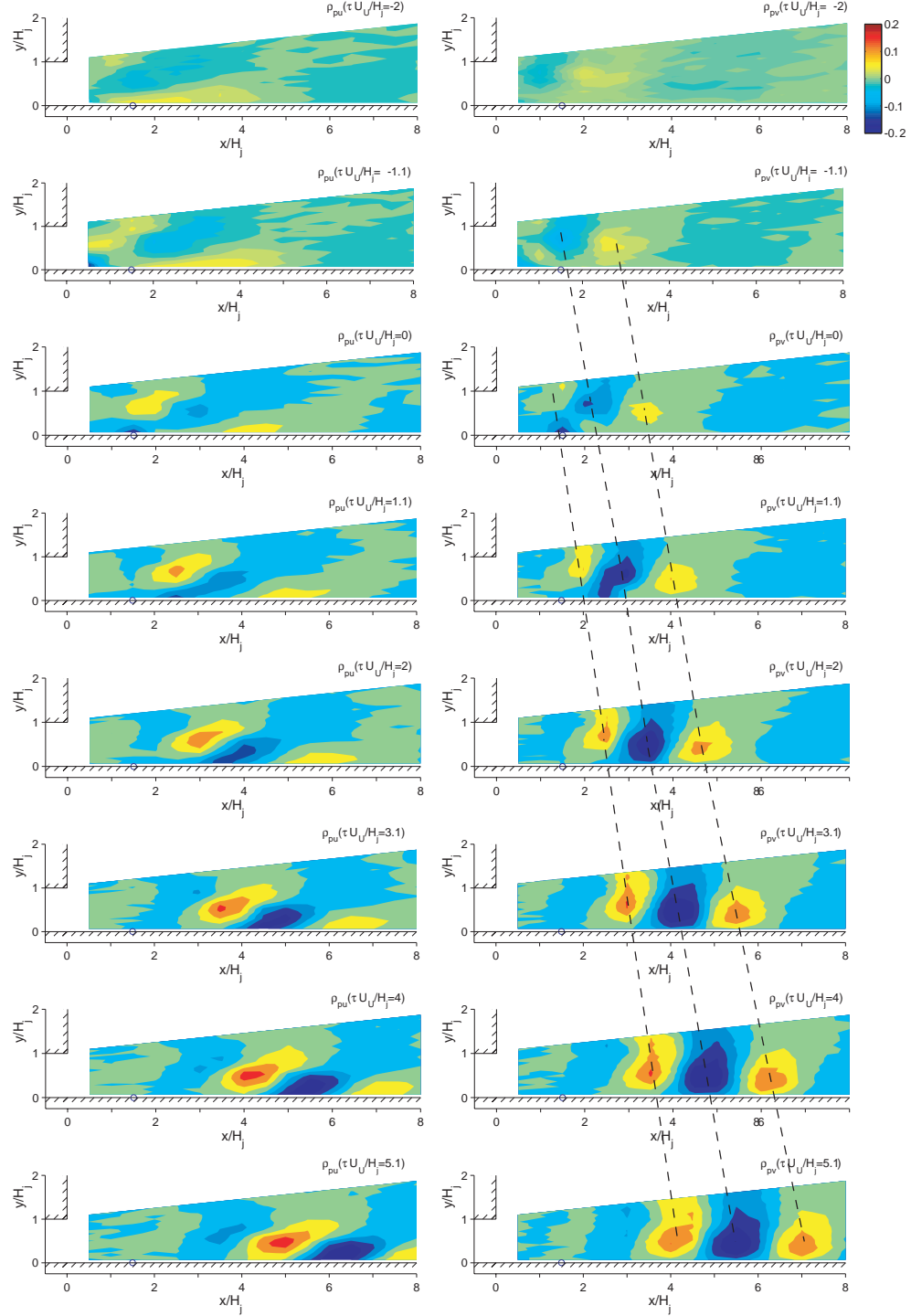


Figure 5.16: Correlation coefficient ρ_{pu} (left) and ρ_{pv} (right) for the fluctuating wall pressure at $x_1/H_j = 1.5$ and the fluctuating velocity at different locations for time delays $\tau U_U / H_j \approx -2$ to 5 in the planar wall jet with $Re \approx 44\,000$.

the fluctuating velocities above this location. There is evidence of large scale structures interacting with the wall at $x/H_j \approx 3$ with a characteristic frequency of $fH_j/U_U \approx 0.2$. At $x/H_j \geq 5$, the fluctuating wall pressure is well correlated with the fluctuating velocities in both the inner and outer parts of the flow. The streamwise fluctuating velocities were out of phase with the fluctuating wall pressure while the vertical fluctuating velocities were in phase with the fluctuating wall pressure. The results showed that the characteristic frequency gradually decreased as the flow evolved downstream.

The evolution of the large scale structures in the offset jet can also be examined using the contours of the correlation coefficients between the wall pressure at one point and the velocity at different spatial locations for a given time delay, *i.e.*

$$\rho_{pu}(x_1, x, y, \tau = \text{const}) = \frac{\overline{p(x_1, t)u(x, y, t + \tau)}}{p'(x_1)u'(x, y)} \quad (5.6)$$

and

$$\rho_{pv}(x_1, x, y, \tau = \text{const}) = \frac{\overline{p(x_1, t)v(x, y, t + \tau)}}{p'(x_1)v'(x, y)}, \quad (5.7)$$

Here, x_1 is the location of the reference microphone, x and y are the locations of the hot-wire probe, and the time interval τ is a constant. The evolution of the structures can then be examined using the correlations for different time delays.

The two-point and two-time correlation coefficients of the fluctuating wall pressure at $x/H_j = 1.5$ and the fluctuating velocities in the planar wall jet for time delays of $\tau U_U/H_j \approx -2$ to 5 are shown in Fig. 5.16. These contours were generated based on velocity measured at 16 by 20 equally spaced locations in the flow. The areas with large positive and negative correlations can be related to the averaged locations of the large scale coherent structures in the flow. The results show that the large scale structures emerged in the outer shear layer of the wall downstream of the jet exit. These structures soon induced co-flowing structures near the wall due to non-slip condition. The structures appeared to form a pair and convected downstream.

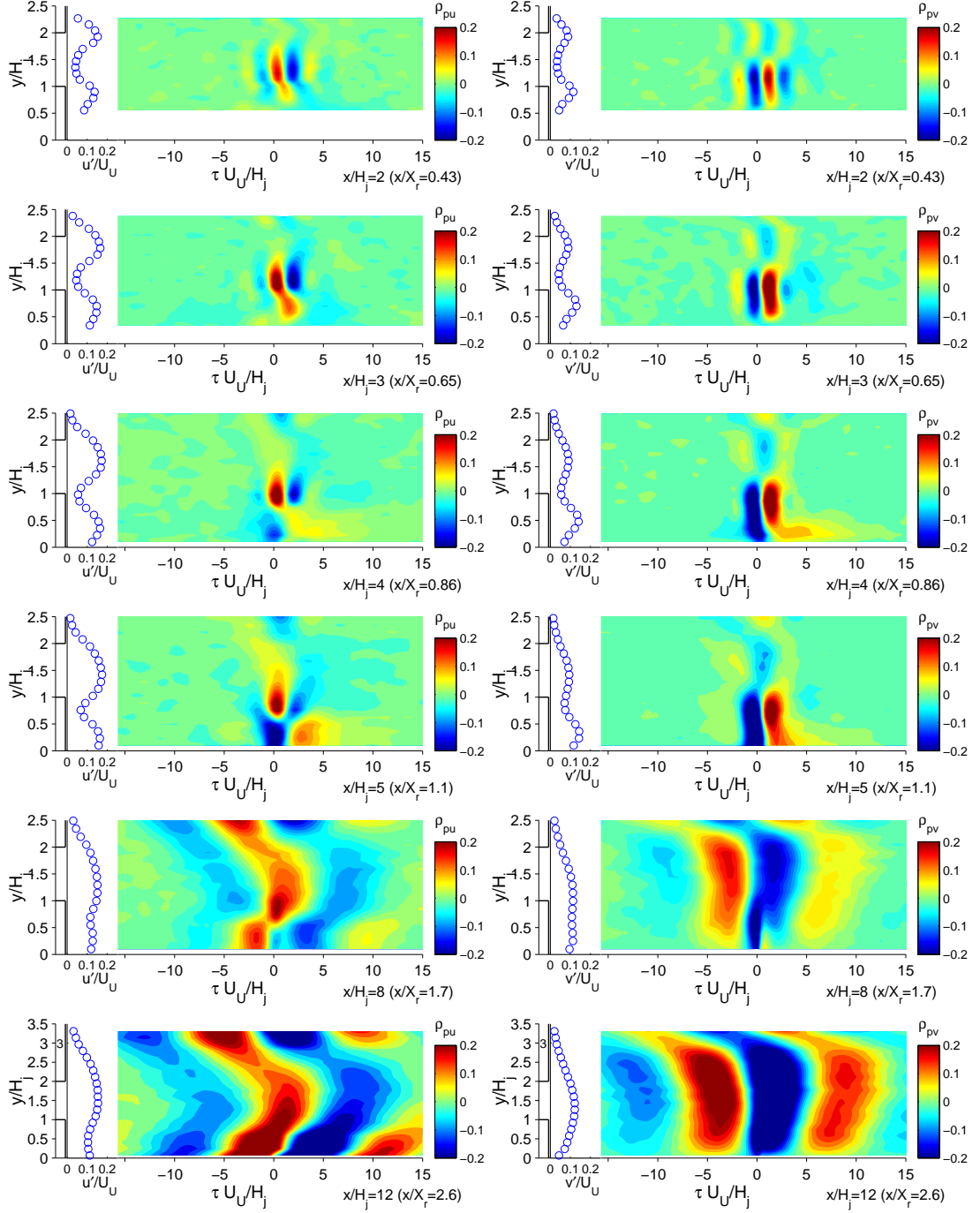


Figure 5.17: Correlation coefficients of the fluctuating wall pressure and the streamwise fluctuating velocity ρ_{pu} (left) and the vertical fluctuating velocity ρ_{pv} (right) at the positions above the wall for the offset jet with $H_s/H_j = 1$ and $Re \approx 44\,000$ at different streamwise locations.

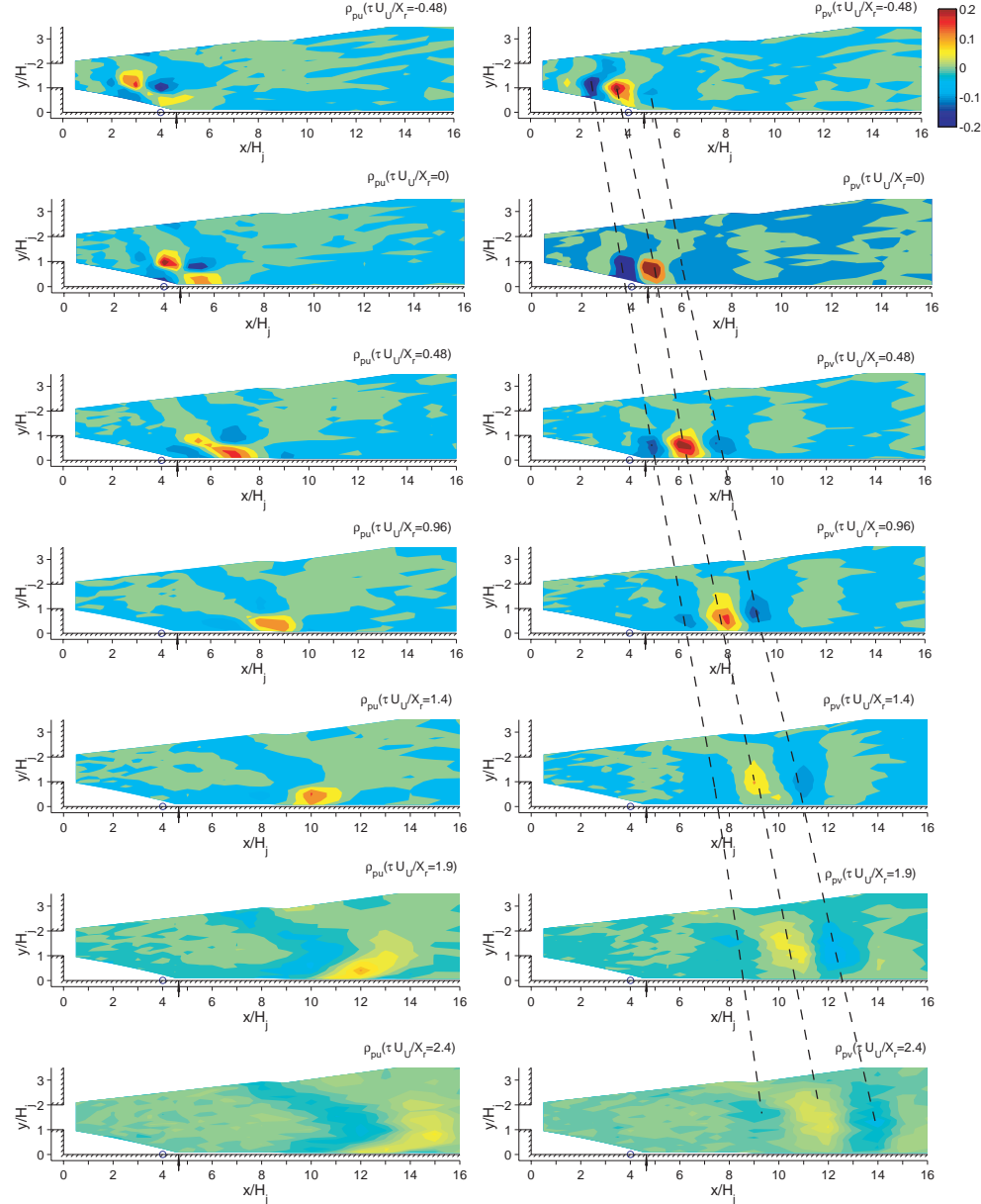


Figure 5.18: Correlation coefficient ρ_{pu} (left) and ρ_{pv} (right) for the fluctuating wall pressure at $x_1/H_j = 4$ and the fluctuating velocities at different locations for time delays $\tau U_U/H_j \approx -0.5$ to 2.4 in an offset jet with $H_s/H_j = 1$ and $Re \approx 44\,000$.

The correlation coefficients between the fluctuating pressure on the wall and the fluctuating velocities at the locations above this point for an offset jet with $H_s/H_j = 1.0$ are shown in Fig. 5.17. The results show that the wall pressure in the region $0.45 \leq x/X_r \leq 1$ are correlated with the fluctuations in both the inner and the outer part of the flow though the correlation is much larger in the inner shear layer. The structures in the inner and outer shear layers seemed to be out of phase with each other. The correlation with these structures gradually disappeared as the flow evolved downstream and there is evidence of another low frequency structure at $x/H_j \approx 5$. This mode makes the dominant contribution to the two-time correlations at $x/H_j = 8$. The contribution from the high frequency structures disappeared in this region and the correlations became similar to the planar wall jet in the region $x/H_j > 8$.

Examples of the two point correlation coefficient, ρ_{pu} and ρ_{pv} , measured between the fluctuating wall pressure at $x/H_j = 4$ ($x/X_r \approx 0.85$) and the fluctuating velocities in different regions in the offset jet with $H_s/H_j = 1$ for different time delays are shown in Fig. 5.18. These contours were generated based on velocity measurements at 16 by 20 equally spaced locations at $x/H_j \leq 8$ and 8 by 20 equally spaced locations at $x/H_j \geq 9$. The measurements in the recirculation region were not shown. The correlation of the velocities and the wall pressure at $x/X_r \approx 1$ showed that there were flow structures are convected along the shear layer in the region $x < X_r$. The velocity in the outer part of the jet are also slightly correlated with the fluctuating wall pressure. The development of the velocity in the outer part that is correlated does seem to be coupled with the inner shear layer. Downstream of the reattaching region $x > X_r$, these structures convected downstream along the wall and grew in size between $8 \leq x/H_j \leq 10$. The change in the structures downstream of the reattachment point can be better understand from the contours of ρ_{pv} determined for the case where the fluctuating wall pressure was measured at $x/H_j = 8$ shown in Fig. 5.19. Regions of correlation from larger scale structures similar to those obtained in wall jet emerge after the jet attached to the wall in the region $x/H_j \geq 6$

(region IV). There is also evidence of the smaller structures from the reattaching shear layer present near the wall in the region $x/H_j \geq 6$. They appear to be convected downstream at a larger velocity than the larger scale outer structures. The results suggest that the faster moving structures from the inner shear layer approached the slower moving outer structures in region III and IV and appeared to merge with them. The correlation indicated that the merged structures traveled downstream similar to a planar wall jet in the region V ($x/H_j \geq 10$).

The relationship between the fluctuating velocities in the flow with the fluctuating wall pressure at different frequencies can be further studied by examining the coherence and the phase angles of the cross spectra between the pressure and velocity for the different frequencies. The coherence between the fluctuating pressure at $x_1/X_r \approx 0.4$ ($x_1/H_j \approx 2$) and velocities in the flow, γ_{pu} and γ_{pv} , for frequencies of $fX_r/U_U = 0.08$ to 1.0 in the offset jet with $H_s/H_j = 1.0$ are shown in Fig. 5.20. The results show that there were two regions with significant coherence ($\gamma \gtrsim 0.3$) in the contours of γ_{pv} for a frequency of $fX_r/U_U = 0.08$ on either side of the reattachment location. The coherence between the fluctuating pressure and velocities was poor for the frequency of $fX_r/U_U = 0.3$. The coherence in the inner part of the offset jet gradually increased for frequencies $0.6 \leq fX_r/U_U \leq 1$, consistent with the coherence of the fluctuating pressure along the wall. Coherence of fluctuating velocities with the fluctuating wall pressure measured at $x_1/X_r < 0.4$ was similar to the case with $x_1/X_r \approx 0.4$ at the frequency $fX_r/U_U \leq 0.1$.

The absolute value of the phase angles of the cross spectra between the fluctuating pressure at $x_1/X_r \approx 0.4$ and velocities in the jet, $|\theta|_{pu}$ and $|\theta|_{pv}$, for an offset jet with $H_s/H_j = 1.0$ at frequencies of $fX_r/U_U = 0.08$ to 1.0 are shown in Fig. 5.21. The contours of the phase angles at large frequencies $fX_r/U_U \geq 0.6$ were similar. There were regions where the fluctuations were in and out of phase with the wall pressure caused by the structures convecting in the jet. The fluctuating wall pressure at low frequency $fX_r/U_U = 0.08$ was in phase with the streamwise velocity fluctuations in the upper part of

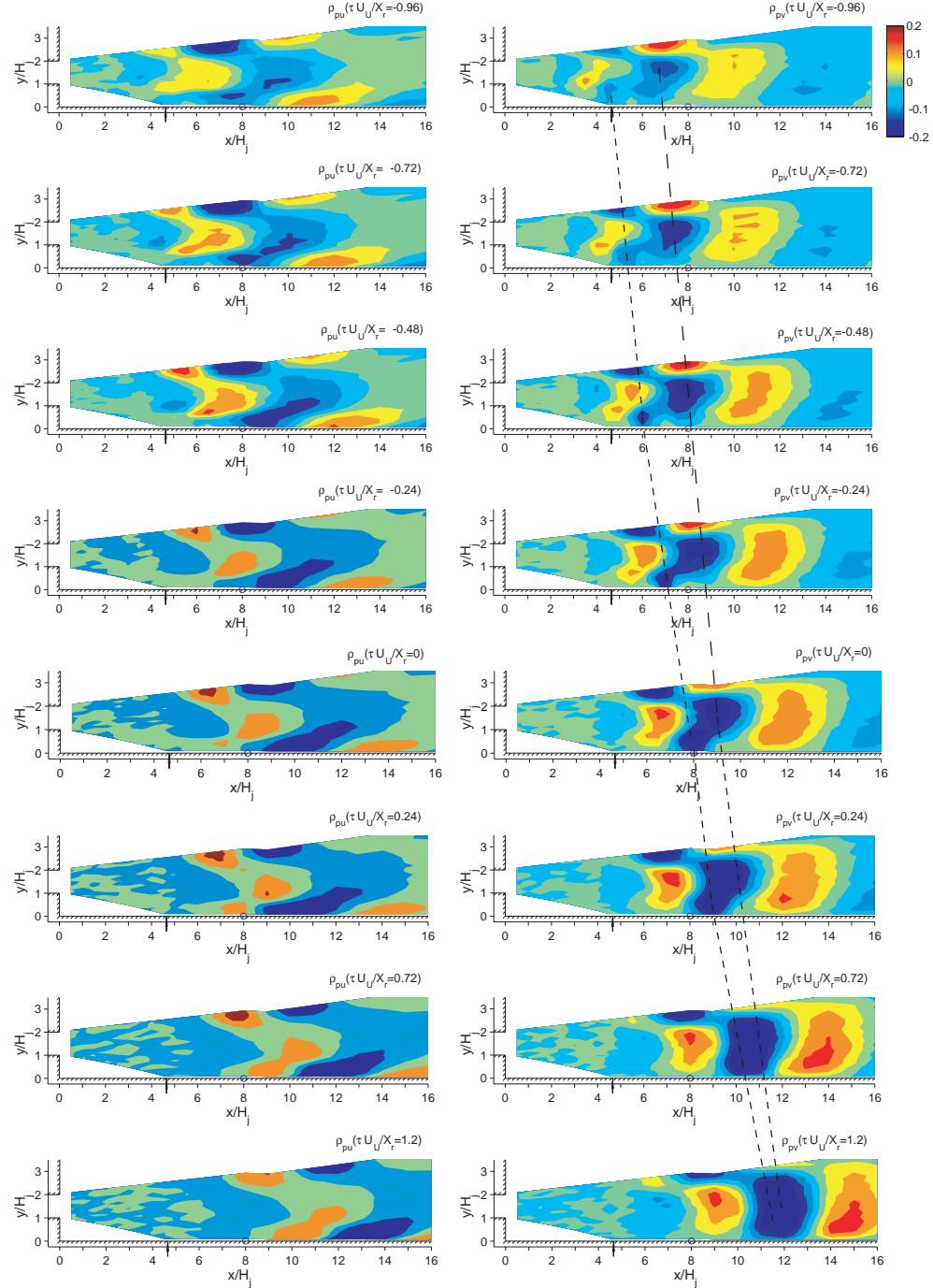


Figure 5.19: Correlation coefficient ρ_{pu} (left) and ρ_{pv} (right) for the fluctuating wall pressure at $x_1/H_j = 8$ and the fluctuating velocities at different locations for time delays $\tau U_U / H_s \approx -0.96$ to 1.2 in an offset jet with $H_s/H_j = 1$ and $Re \approx 44\,000$.

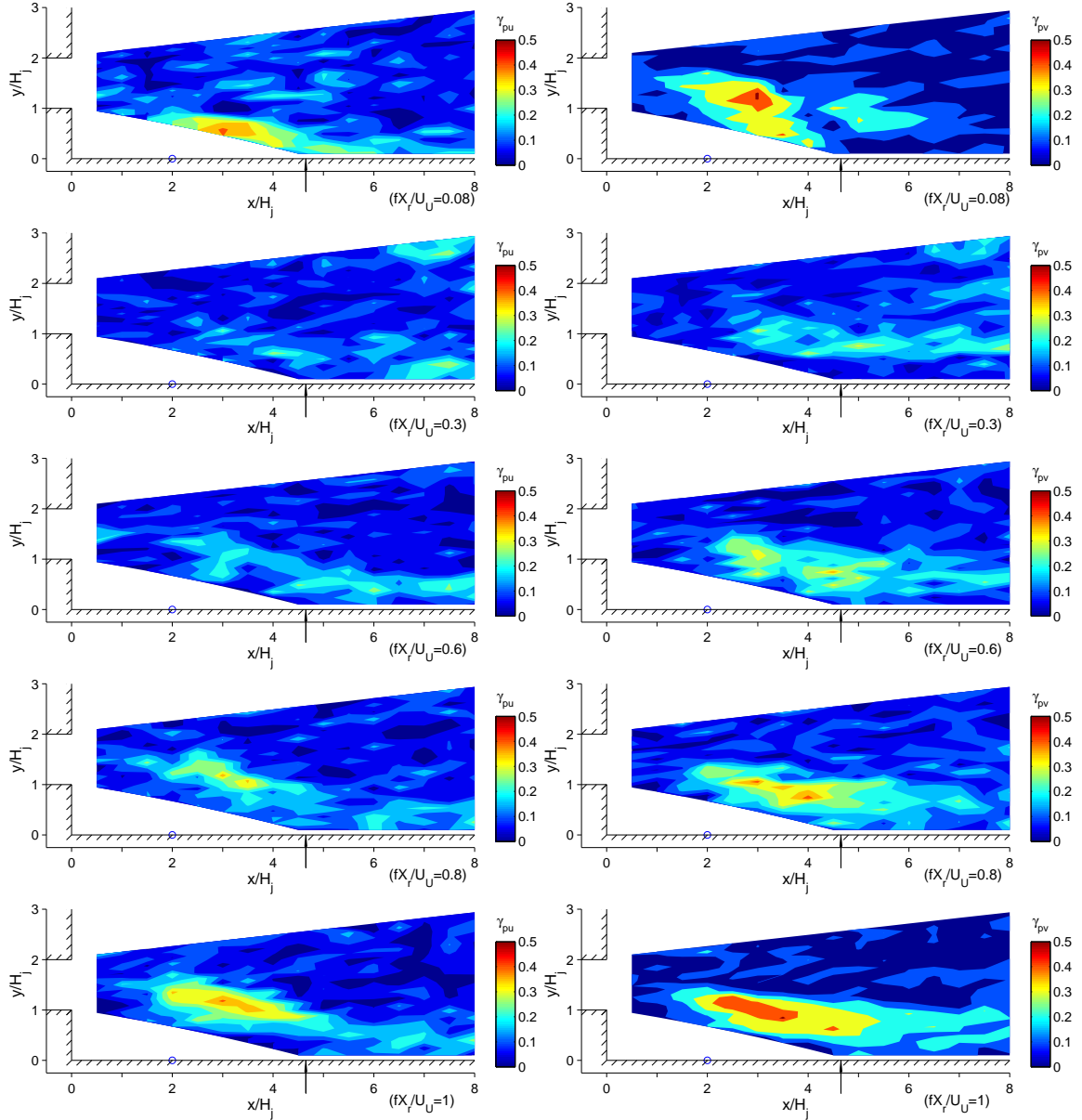


Figure 5.20: The coherence between the fluctuating wall pressure at $x_1/X_r \approx 0.4$ and fluctuating streamwise velocities, (left) γ_{pu} and (right) γ_{pv} , for an offset jet with $H_s/H_j = 1.0$ and $Re \approx 44\,000$ for frequencies of $fX_r/U_U = 0.08$ to 1.0 .

the jet and out of phase with the lower part of the jet. The wall pressure with the frequency of $fX_r/U_U = 0.08$ at $x_1/X_r \approx 0.4$ was out of phase with the vertical velocity fluctuations in the region $x/X_r \lesssim 1$ and in phase with the region $x/X_r \gtrsim 1$ indicating the jet was 'flapping' vertically.

More detailed measurements of the cross spectra between the wall pressure at $x_1/X_r \approx 0.4$ and the fluctuating velocities were performed at 48 equally spaced locations on lines between $y/H_j = 1.25$ at $x/X_r = 0.01$ and $y/H_j = 0.75$ at $x/X_r = 1.5$ shown by a dotted line in the Fig. 5.21. The change in the phase angles with streamwise position for different frequencies are shown in Fig. 5.22. The change in the phase angle of cross spectra with streamwise position for $fX_r/U_U \leq 0.36$ ($fH_j/U_U \leq 0.08$) decreased in the region $0.4 \lesssim x/X_r \lesssim 0.7$ in the streamwise direction suggesting the fluctuations were propagating upstream.

The fluctuating wall pressure with frequency $fX_r/U_U \leq 0.1$ at the reference location $x/X_r \approx 0.4$ seemed to be approximately 0.75π out of phase with the fluctuating vertical velocity at $x/X_r \approx 0.7$, and 1.75π out of phase with fluctuating vertical velocity at $x/X_r \gtrsim 0.9$. These changes in the phase angles indicated that there were oscillations in the region between $0.7 \leq x/X_r \leq 0.9$ in the jet that were out of phase for the very low frequencies $fX_r/U_U \leq 0.1$. The phase angles for fluctuations with $0.12 \leq fX_r/U_U \leq 0.36$ ($0.03 \leq fH_j/U_U \leq 0.08$) increased approximately linearly in the region $0.7 \lesssim x/X_r \lesssim 1.1$ (Region II). The slope of the phase angles for these frequencies were similar indicating the wavelength of the fluctuations with these frequencies were similar. When the frequency further increased $fX_r/U_U > 0.4$, the fluctuations started to propagate downstream at a location closer to the jet exit. The slopes of the phase angles were similar in the region $x/X_r \approx 0.6$ to 0.8 , but different in the region $x/X_r > 0.8$.

Proper Orthogonal Decomposition (POD) of the fluctuating wall pressure in the region $x/X_r \lesssim 1.7$ were performed. The introduction of this method and the results are shown in Appendix D. The eigenvectors of mode 1 for lower frequencies $0.2 \lesssim fX_r/U_U \lesssim$

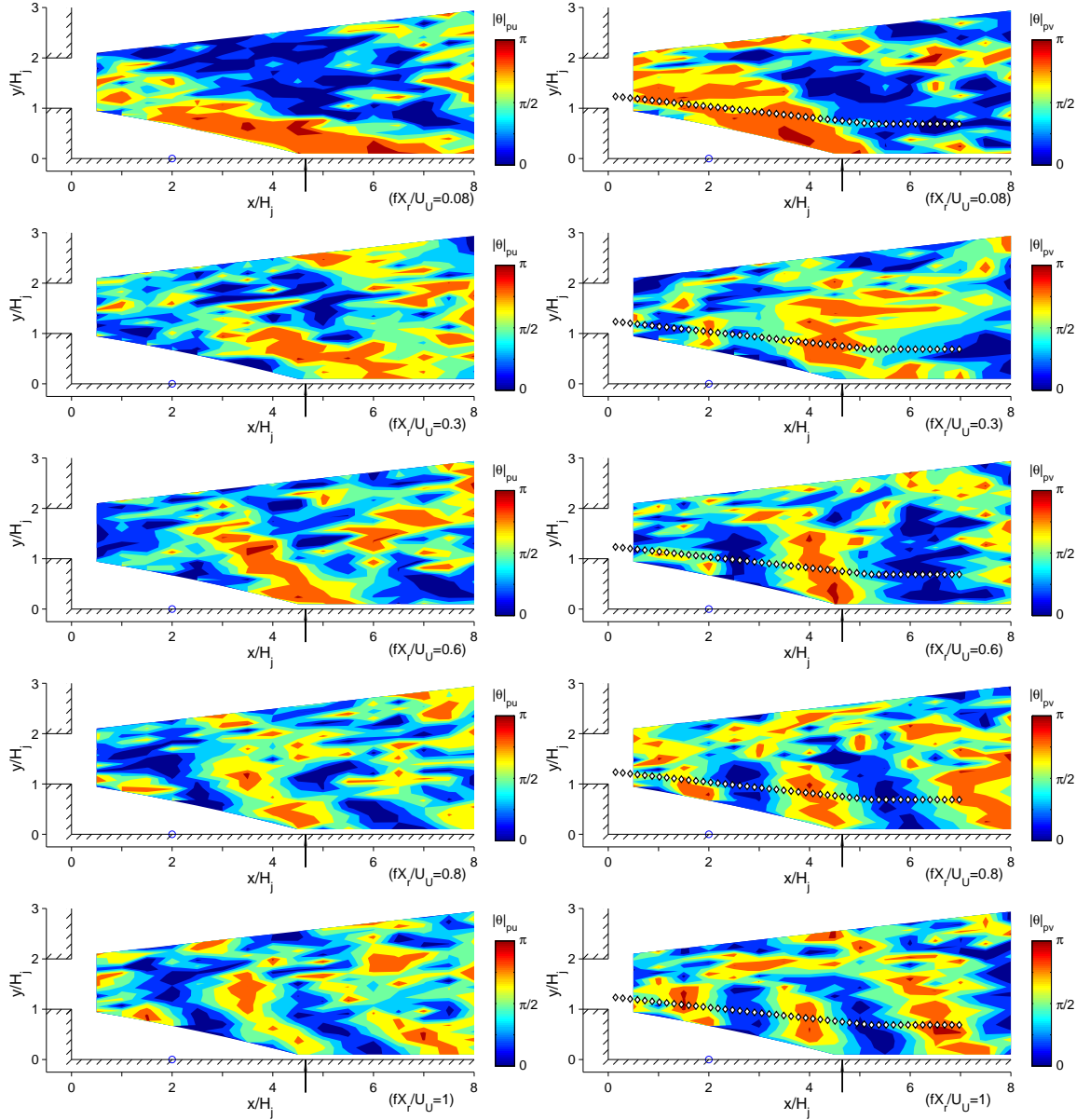


Figure 5.21: The phase angles of the cross spectra between the fluctuating wall pressure at $x_1/X_r \approx 0.4$ and fluctuating streamwise velocities, (left) $|\theta|_{pu}$ and (right) $|\theta|_{pv}$, for an offset jet with $H_s/H_j = 1.0$ and $Re \approx 44\,000$ for frequencies of $fX_r/U_U = 0.08$ to 1.0 .

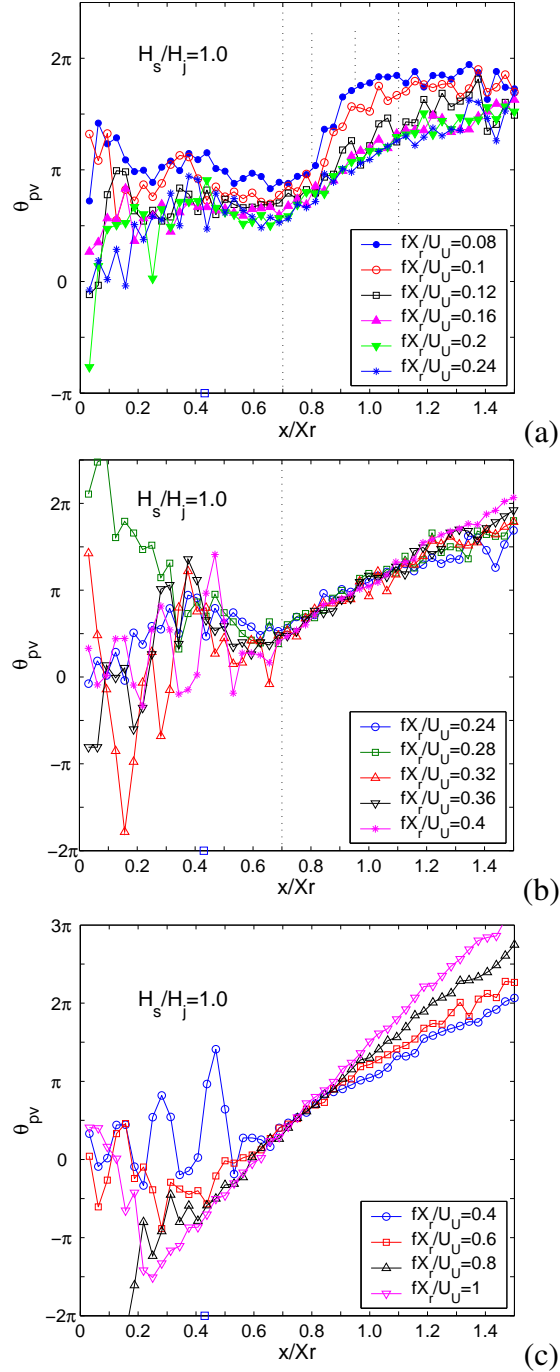


Figure 5.22: Distributions of the phase angles of the cross spectra of the fluctuating pressure and vertical fluctuating velocity for an offset jet with $H_s/H_j = 1.0$ and $Re \approx 44\,000$.

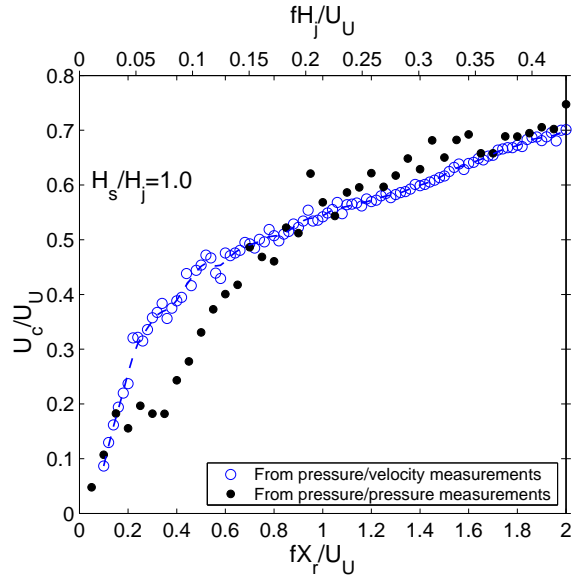


Figure 5.23: Distributions of the convection velocities computed using the phase angles of the cross spectra $\circ \theta_{pv}$ and $\bullet \theta_{pp}$ in the attachment region $0.8 \leq x/X_r \leq 1$ for different frequencies for an offset jet with $H_s/H_j = 1.0$ and $Re \approx 44\,000$.

0.4 are similar suggesting the wavelength of the fluctuations with these frequencies are similar. Eigenvectors of mode 1 for larger frequencies $fX_r/U_U \geq 0.6$ are also similar suggesting a constant wavelength for these frequencies but different from the wavelength for the fluctuations with $0.2 \lesssim fX_r/U_U \lesssim 0.4$.

The convection velocity in the reattachment region $0.8 \leq x/X_r \leq 1.0$ calculated from the change in the phase angle with the streamwise position, $d\theta_{pv}/dx$, are shown in Fig. 5.23. The resulting velocities are in reasonable agreement to those calculated from the phase angle of the fluctuating wall pressure, $d\theta_{pp}/dx$, for frequencies of $fX_r/U_U \leq 0.2$ and $fX_r/U_U \geq 0.6$ ($fH_j/U_U \leq 0.04$ and $fH_j/U_U \geq 0.13$). The convection velocities based on the pressure cross spectra for $0.2 \leq fX_r/U_U \leq 0.6$ were significantly smaller. It seemed that the fluctuations of the wall pressure with these frequencies were associated with the motions near the wall which were different from the motions in the inner shear layer where the velocity measurement were taken.

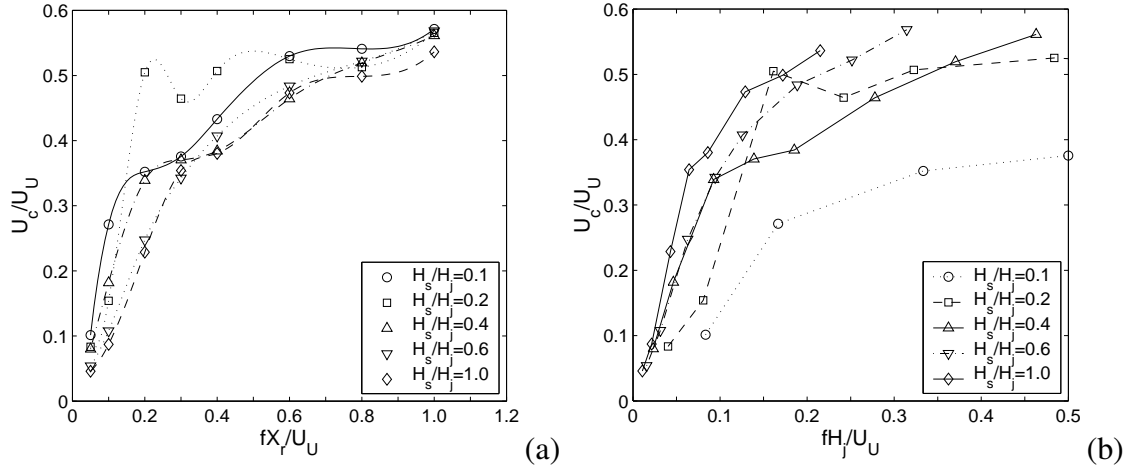


Figure 5.24: Distributions of the convection velocities in the attachment region $0.7 \leq x/X_r \leq 1.4$ for different frequencies for offset jets with $H_s/H_j = 0.1$ to 1.0 and $Re \approx 44\,000$.

The convection velocity calculated from θ_{pv} for offset jets with offset distance $H_s/H_j = 0.1$ to 1.0 are shown in Fig. 5.24. The results are presented in terms of fX_r/U_U and fH_j/U_U . The locations of the velocity measurements for jets with $H_s/H_j = 0.1$ to 0.6 started at $x/X_r = 0$ and $y/H_j = 1.25$ and ended at $x/X_r = 1.5$ and $y/H_j = 0.75$, similar to the case with $H_s/H_j = 1.0$. The convection velocity for all the jets were approximately $0.1U_U$ for the frequency of $fX_r/U_U = 0.1$. The convection velocity initially increased significantly with frequency. This increase with frequency became more gradual and approached the convection velocity of planar wall jet. The jet with offset distance $H_s/H_j = 0.2$ was different from other cases, the convection velocity increased to $0.5U_U$ without any transition. The cause of this is not known. The convection velocities for all the jets were similar for frequency $fX_r/U_U \geq 0.6$, indicating again the offset distance did not significantly affect the propagation velocity of the fluctuations with larger frequencies.

The characteristics of the three motions in the offset jet with $H_s/H_j \leq 1.0$ are summarized in Table 5.1. In the offset jet with $H_s/H_j = 0.2$, the characteristic frequency of the

Table 5.1: Summary of characteristic motions in offset attaching jets

| Motions | Length scales | Characteristic frequencies | Comments |
|-------------------------------------|----------------|---------------------------------|--|
| Structures in the inner shear layer | X_r or H_s | $fX_r/U_U \approx 0.6$ to 1.2 | generated due to K-H instability and reach maximum in fluctuations at $x \approx X_r$, contribute more than 40% to the pressure fluctuations at $x \approx X_r$ by integrating the spectrum; wave lengths of the fluctuations with these frequencies are similar at $x \approx X_r$; convection velocity $0.5 \sim 0.6U_U$ at $x \approx X_r$; fluctuations decrease after interacting with wall and gradually merge with wall jet like structures; |
| Flapping motions | X_r or H_s | $fX_r/U_U \approx 0.06$ to 0.1 | there are two regions with significant coherence separated by the reattachment location; fluctuations in these two regions approximately π out of phase; contribute $\sim 5\%$ to the fluctuating streamwise velocity in the inner shear layer at $x/X_r \approx 1$ for the offset jet with $H_s/H_j = 1$ |
| Wall jet like structures | H_j | $fH_j/U_U \approx 0.06$ to 0.08 | emerge and convect downstream after reattachment with $U_c/U_U \approx 0.5 \sim 0.6$, similar to the flow structures in planar wall jet; |

flapping motion coincides with the frequency of the wall jet type of structures. The difference in the convection velocity for the jet with $H_s/H_j = 0.2$ from the jets with other offset distances, shown in Fig. 5.24, might be related to this match of characteristic frequencies.

Chapter 6

Co-flowing Jets - Single Point Measurements

The effect of adding a co-flowing control jet on the development of offset planar attaching jets with offset distance of one jet height is initially examined using single point measurements. The results for cases with inner jet heights of $H'_j = 0.18H_j$ and $0.5H_j$ and a maximum velocity of $U'_o = 0.10U_o$ to U_o were studied. The experimental parameters of the jets determined from the profiles of the streamwise velocity measured at $x/H_j \approx 0.05$ using a single hot-wire (shown in Fig. A-2 in the appendix) are summarized in Table 6.1. The Reynolds number of the outer jet was approximately 44 000. The Reynolds number of the inner jet varied from 1300 to 14 000. The initial profile of the outer jet did not change when the inner jet velocity was changed.

6.1 Offset jet with a co-flowing jet of $H'_j/H_j = 0.5$

The distributions of the mean velocity vectors and the corresponding streamlines for a single offset jet and offset jets with a co-flowing jet with a height of $0.5H_j$ and velocity of $U'_o = 0.10U_o$ to $0.74U_o$ are shown in Fig. 6.1 and Fig. 6.2. The corresponding static wall pressure coefficient, C_P , and skin friction coefficient, C_f , are shown in Fig. 6.3 (a) and

Table 6.1: Summary of flow parameters of offset jet with a co-flowing jet.

| Case | H'_J/H_J | Re | Re' | U'_o/U_o | m'/m | M'/M |
|------|------------|-------|-------|------------|--------|--------|
| 1 | 0.5 | 35000 | 1320 | 0.10 | 0.04 | 0.003 |
| 2 | 0.5 | 39800 | 3520 | 0.20 | 0.09 | 0.017 |
| 3 | 0.5 | 42300 | 5780 | 0.28 | 0.14 | 0.039 |
| 4 | 0.5 | 41000 | 7550 | 0.38 | 0.19 | 0.072 |
| 5 | 0.5 | 42400 | 9780 | 0.47 | 0.24 | 0.111 |
| 6 | 0.5 | 40700 | 11750 | 0.59 | 0.30 | 0.174 |
| 7 | 0.5 | 38000 | 13930 | 0.74 | 0.39 | 0.281 |
| 8 | 0.18 | 41850 | 1700 | 0.27 | 0.04 | 0.010 |
| 9 | 0.18 | 43160 | 2920 | 0.42 | 0.06 | 0.026 |
| 10 | 0.18 | 42140 | 4420 | 0.63 | 0.10 | 0.062 |
| 11 | 0.18 | 43140 | 6240 | 0.86 | 0.14 | 0.115 |

(b), respectively. The streamlines here were determined from the velocity measurements at locations with streamwise spacing of H_j . These results show that when the maximum inner jet velocity was below $0.20U_o$, the inner jet separated from the wall near the jet exit due to the adverse pressure gradient along the wall. This results in a negative skin friction in this region. The inner jet seemed to be entrained into the outer jet and the merged jet attached to the wall at a location downstream of the reattachment point for the single offset jet. The attachment location moved downstream when the inner jet velocity was increased in these cases. The negative skin friction before the reattachment location was smaller than the single offset jet indicating the recirculating flow was less prominent as the co-flowing jet velocity increased. The curvature of the attaching jet with the co-flow was also more gradual than the offset jet without the co-flowing jet resulting in a decrease in the static wall pressure in the reattachment region. The skin friction increased gradually after the jets attached to the wall reaching a maximum at $x/H_j \approx 10$. The skin friction here was smaller than the wall jet and single offset jet, and the difference in the skin friction decreased gradually as the flow evolved downstream and became negligible at $x/H_j \approx 15$.

The development of the offset jet with a co-flowing jet appeared to change when the

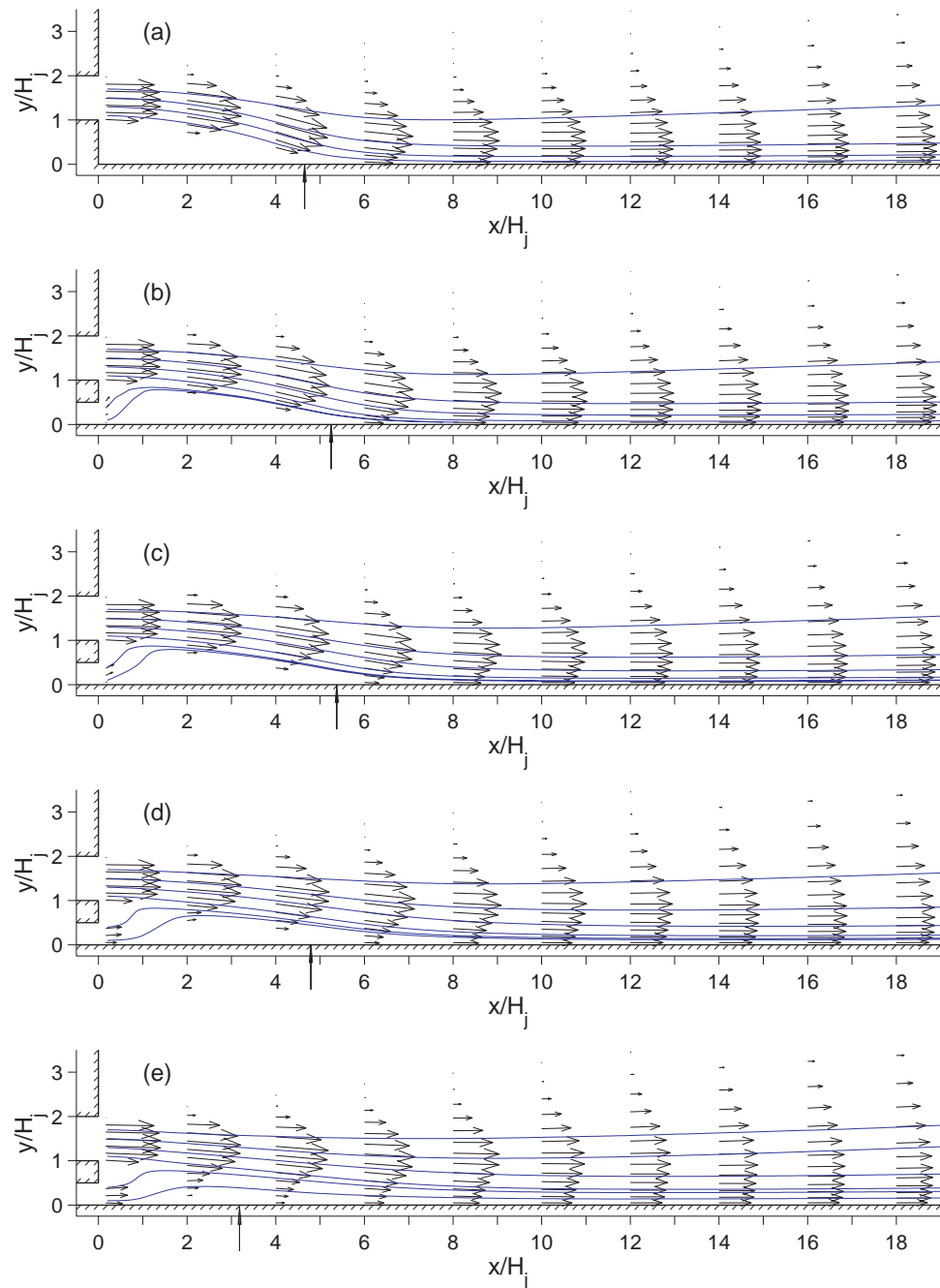


Figure 6.1: Distributions of the vectors and streamlines of the mean velocity for (a) a single offset jet and co-flowing jets with $H'_J/H_J = 0.5$ and U'_o/U_o of (b) 0.10, (c) 0.20, (d) 0.28, (e) 0.38, Reynolds numbers are given in Table. 6.1.

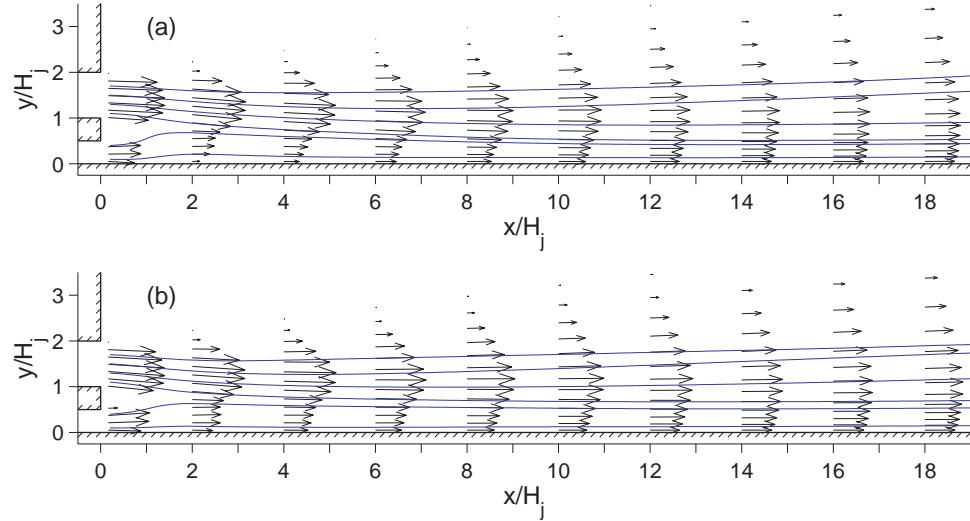


Figure 6.2: Distributions of the vectors and streamlines of the mean velocity for co-flowing jets with $H'_J/H_J = 0.5$ and U'_o/U_o of (a) 0.59 and (b) 0.74.

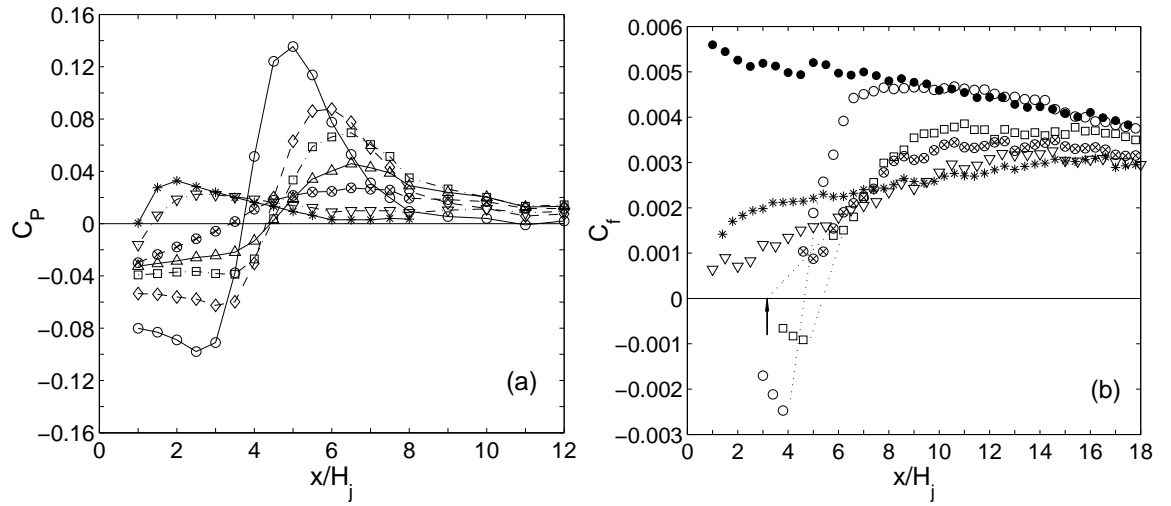


Figure 6.3: Distribution of (a) the static wall pressure coefficient and (b) the mean skin friction coefficient for ● a planar wall jet, ○ a single offset jet and co-flowing jets with $H'_J/H_J = 0.5$ and $U'_o/U_o = \diamond 0.10, \square 0.20, \triangle 0.28, \otimes 0.38, \nabla 0.59$ and * 0.74.

maximum velocity of the inner jet was $0.38U_o$. In this case, the bulk of the inner jet still appeared to curve away from the wall, but it did not appear to be entrained into the outer jet near the exit as was the case for the jet with $U'_o/U_o = 0.2$. Instead, the two jets seemed to develop parallel to each other near the jet exit and both jets then gradually curved toward the wall as the flow evolved downstream. The skin friction in the region $x/H_j \leq 4$ was small so it was not possible to measure it accurately. The visual observation of the oil film showed that the skin friction in the region $x/H_j < 3.2$ was approximately 0 and was positive in the region $x/H_j \geq 3.2$, so $x/H_j \geq 3.2$ was taken as the reattachment location in this jet. The negative pressure on the wall near the jet exit was also different from the cases with the smaller co-flowing velocities. The pressure near the exit was closer to atmospheric pressure than the pressure below the recirculating region for jet with $U'_o/U_o = 0.2$. The maximum in the static wall pressure further downstream was also much lower, because the streamline curvature associated with the outer jet attaching to the wall was smaller. The skin friction increased gradually after the jet reattached to the wall and approached the results for the planar wall jet as the inner jet was accelerated due to the momentum transfer from the outer jet. The skin friction did not however reach the skin friction for the planar wall jet in the region examined here.

The change in the skin friction was even more gradual when the velocity ratio U'_o/U_o was 0.59. In this case, the skin friction was clearly positive everywhere along the wall indicating that the inner jet did not separate from the wall, but there was still evidence of the inner jet being decelerated near the jet exit. The static pressure reached a local maximum near the jet exit at $x/H_j \approx 2.5$ due to the local curvature of the flow behind the splitter plate. This caused a deceleration of the inner jet near the wall. The maximum skin friction did not occur until $x/H_j \approx 13$ indicating the increase in the shear stress was more gradual and driven by momentum transfer across the flow rather than any acceleration of the flow near the wall during the reattachment process. When the velocity of the inner jet was $0.74U_o$, this trend continued and the maximum skin friction occurred even further

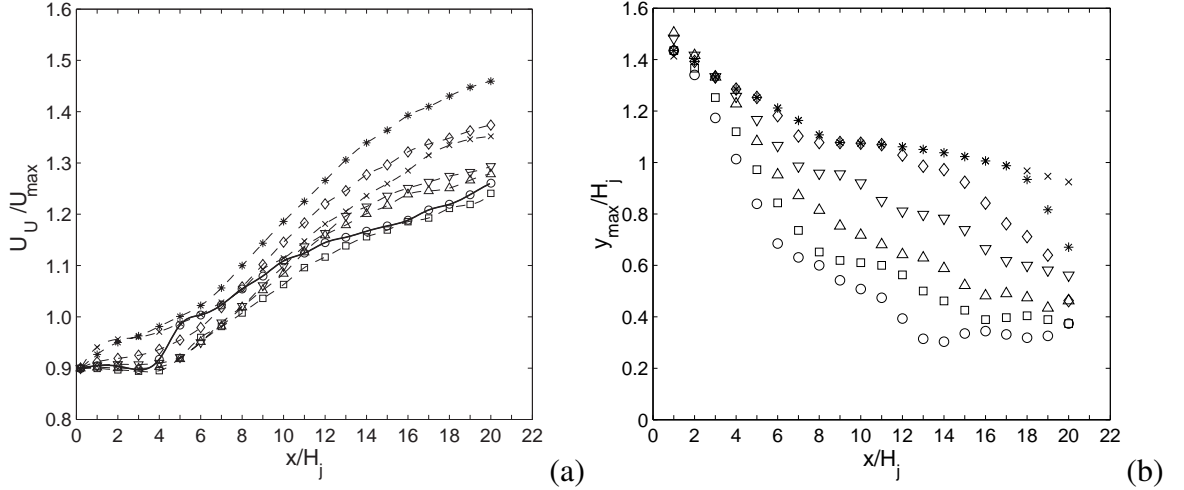


Figure 6.4: Distributions of (a) the maximum local streamwise velocity and (b) y_{max} for \circ the single offset jet and jets with velocity ratio $U'_o/U_o = \square 0.10, \triangle 0.20, \nabla 0.28, \diamond 0.38, *$ 0.59 and $\times 0.74$.

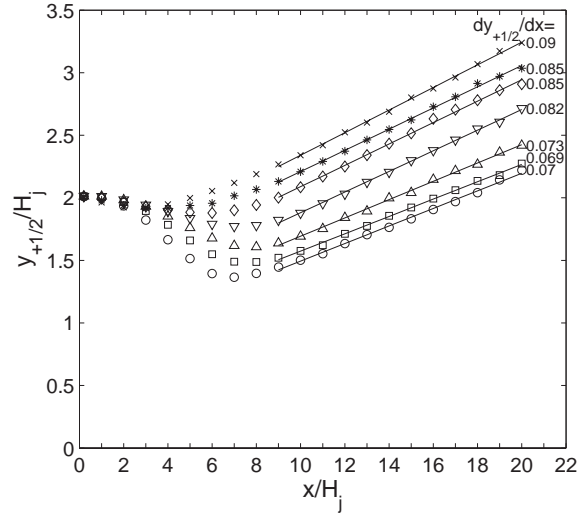


Figure 6.5: Distributions of the outer half jet width of the outer jet for \circ the single offset jet and jets with velocity ratio $U'_o/U_o = \square 0.10, \triangle 0.20, \nabla 0.28, \diamond 0.38, *$ 0.59 and $\times 0.74$.

downstream at $x/H_j \approx 16$.

The effect of the velocity of the inner jet on the reattachment of the upper jet can be characterized by examining the decay of the maximum local streamwise velocity and the height of this location above the wall shown in Fig. 6.4. The maximum velocities in the region $x/H_j \leq 4$ were approximately constant for jets with $U'_o/U_o \leq 0.28$ before decreasing significantly when the jet attached to the wall, similar to the single offset jet. For larger velocity ratios, $U'_o/U_o \geq 0.38$, where the inner jet did not appear to merge with the outer jet, the maximum velocity in the outer jet decayed gradually up to $x/H_j \approx 6$ (the approximate end of potential core of the outer jet) before decaying more rapidly in the region $x/H_j > 6$. For the case with the velocity ratio of 0.59, the maximum velocity in the outer jet decayed more rapidly than the jets with lower velocity ratios in the region $6 < x/H_j \leq 20$. The results show that all of the jets initially curved toward the wall. The value of y_{max} , the height of the the maximum velocity, decreased more quickly in the region $x/H_j \leq 6$ for the case with smaller co-flowing jet velocity, causing a smaller y_{max} at $6 < x/H_j < 16$ in these cases.

The effect of the velocity ratio on the growth of the outer jet can be characterized by examining the jet half width of the outer jet, $y_{+1/2}$, shown in Fig. 6.5. The distribution of the outer jet half width in the region $x/H_j \geq 9$ indicates that the flow went through two changes when the velocity ratio was increased, one between $U'_o/U_o \approx 0.20$ and 0.38 and a second between 0.59 and 0.74. The jet half width of all the jets grew approximately linearly in the region $x/H_j \geq 9$. The growth rates of the outer jet half width, $dy_{+1/2}/dx$, for the jets with $U'_o/U_o \leq 0.20$ were approximately 0.07, similar to those for the single offset jet, while the growth rate for jets with $U'_o/U_o \geq 0.28$ were significantly higher at 0.08 to 0.09 more similar to the values observed in a free jet, suggesting that the development of the outer shear layer is not as affected by the interaction with the wall in these cases at least in the regions studied here.

The profiles of the fluctuating streamwise and vertical velocities and Reynolds shear

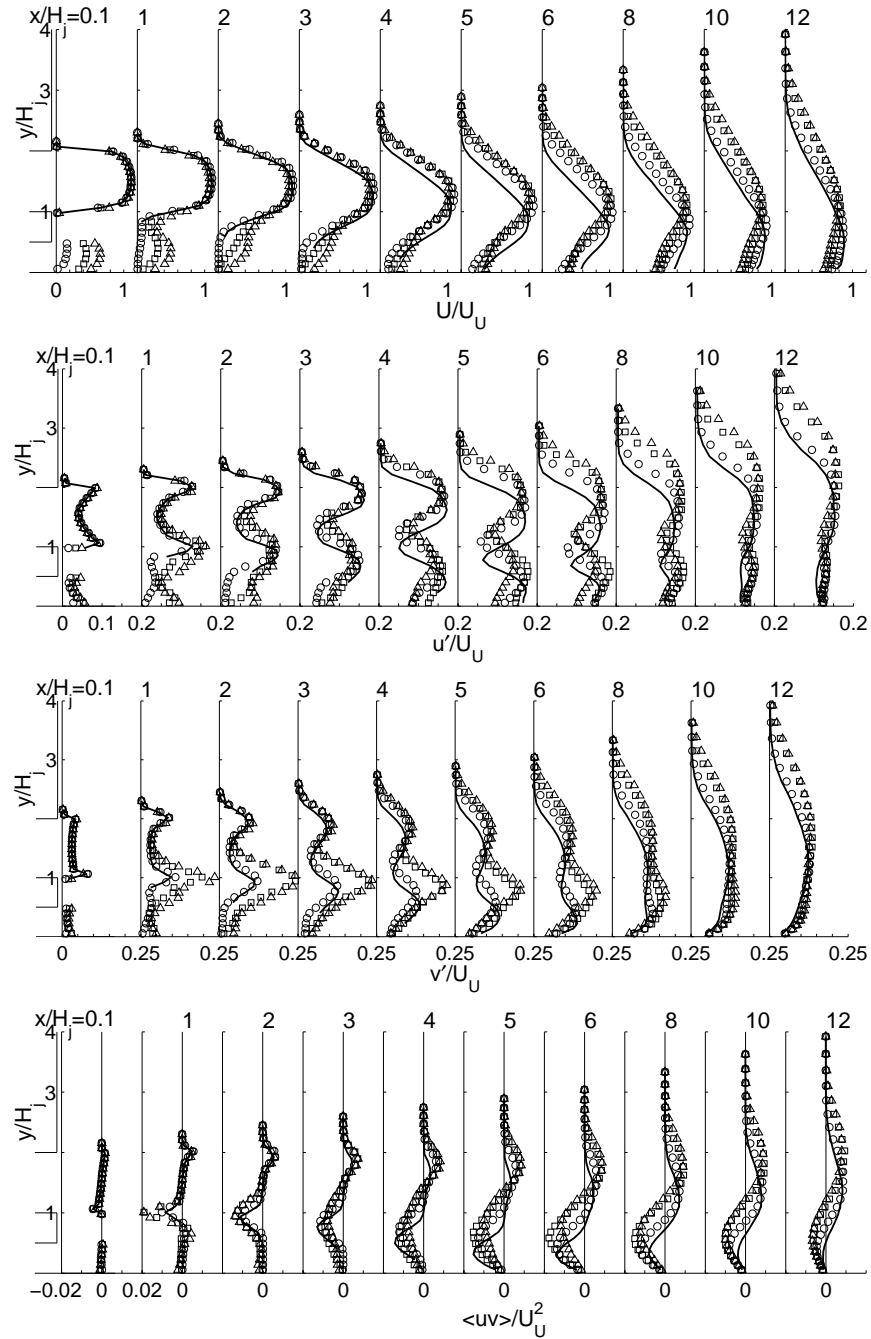


Figure 6.6: Profiles of the mean streamwise velocity, the fluctuating streamwise and vertical velocities and the Reynolds shear stress for — a single offset jet and jets with $H'_J/H_J = 0.5$ and $U'_o/U_o = \circ 0.20, \square 0.38$ and $\triangle 0.59$.

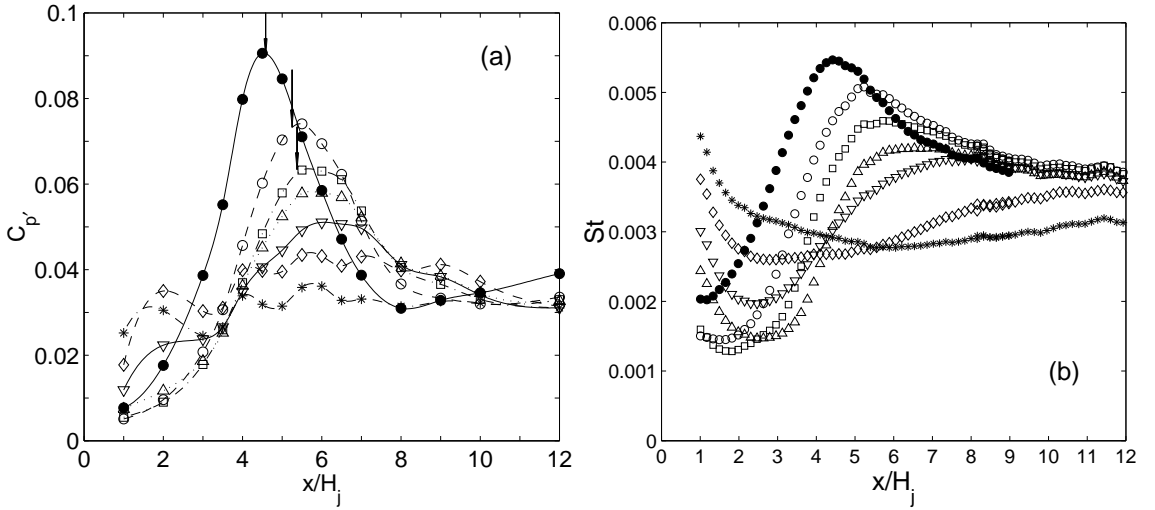


Figure 6.7: Distributions of (a) the fluctuating wall pressure coefficients and (b) the Stanton number for ● a single offset jet and co-flowing jets with $H'_J/H_J = 0.5$ and $U'_o/U_o = ○ 0.10$, $□ 0.20$, $△ 0.28$, $▽ 0.38$, $◊ 0.59$ and $* 0.74$.

stress for jets with velocity ratios $U'_o/U_o = 0.20$ to 0.59 and a single offset jet are shown in Fig. 6.6. When the velocity of the inner jet at the jet exit was smaller than $0.2U_o$, the fluctuating velocities in the region $x/H_j < 5$ became slightly smaller than those in the single offset jet. The results show that there was a significant increase in the vertical fluctuating velocity, v' , in the inner shear layer of the outer jet when the inner jet velocity was $0.38U_o$ or larger. In fact, the value of v' was larger than u' behind the splitter plate indicating that the presence of the inner jet has a dramatic impact on the vertical fluctuations in the inner shear layer in the outer jet. These vertical fluctuations were attenuated when the outer jet interacted with the wall and were largest between $x/H_j \approx 1$ to 3 .

The large increase in v' did not have a significant impact on the fluctuating pressure and the Stanton numbers in the region where the outer jet interacted with the wall as shown in Fig. 6.7. The fluctuating wall pressure and the Stanton number did increase slightly near jet exit ($x/H_j \lesssim 2$) when the inner jet velocity was increased. This was likely caused by the continuous development of inner jet along the wall. The maxima in the fluctuating wall

pressure and Stanton number were smaller where the outer jet interacted with the wall in the cases with larger inner jet velocity despite the dramatic increase in the turbulence in the inner shear layer of the offset jet. This suggests the turbulent structures developed in the flow for the cases with the large inner jet velocities were attenuated before they interacted with the wall in the jets with $H'_j/H_j = 0.5$.

6.2 Single point spectral measurements

The dynamics of the large scale flow structures in the offset jet with a co-flowing jet were initially studied by examining the spectra of fluctuating velocities and fluctuating wall pressure. The spectra of the fluctuating wall pressure for single offset jet ($U'_o/U_o = 0$) with $H_s/H_j = 1$ and co-flowing jets with $U'_o/U_o = 0.20, 0.38$ and 0.59 are shown in Fig. 6.8. The fluctuations at $x/H_j = 1$ near the jet exit were concentrated in the low frequency range $fX_r/U_U \lesssim 0.25$ ($fH_j/U_U \lesssim 0.05$) for jet with $U'_o/U_o = 0.20$ similar to the spectra for the single offset jet. The peak associated with the flow structures in the inner shear layer of the outer jet has a frequency of $fH_j/U_U \approx 0.2$, and can be found in all the cases suggesting that this characteristic frequency was determined by the offset distance or the ratio between the offset distance and the size of the outer jet. There was however a sharp peak in the spectra at $fH_j/U_U \approx 0.42$ for the jets with $U'_o/U_o = 0.38$ and 0.59 in the region $x/H_j \lesssim 7$. This corresponds to a frequency of $fH_c/U_U \approx 0.23$ when the frequency is normalized using the splitter plate height. This is similar to the wake structures downstream of a bluff body (Roshko, 1954) suggesting the fluctuations are associated with wake like structures. The sharp peak in the spectra gradually diminished and disappeared as flow evolved downstream. The peaks were more prominent for jets with larger velocity ratios and developed over a longer distance indicating the wake like structures have larger kinetic energy for higher velocity ratios.

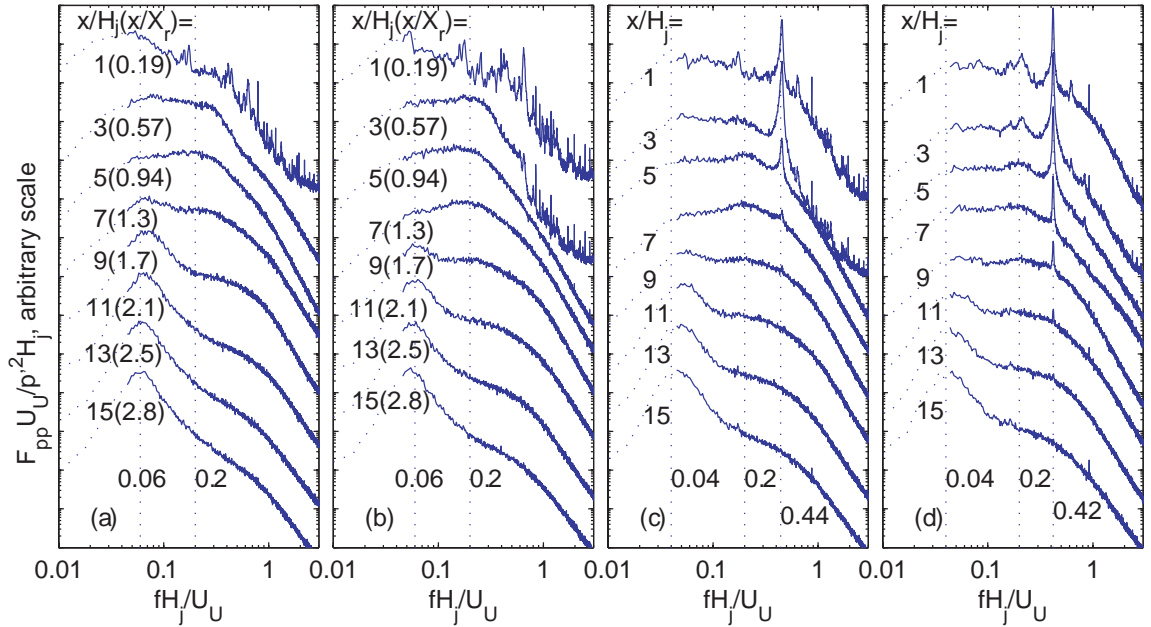


Figure 6.8: The spectra of the fluctuating wall pressure for (a) the single offset jet with $H_s/H = 1$ and offset jet with a co-flowing jet with $H_s/H_j = 1$, $H'_j/H_j = 0.5$ and $U'_o/U_o =$ (b) 0.20, (c) 0.38 and (d) 0.59.

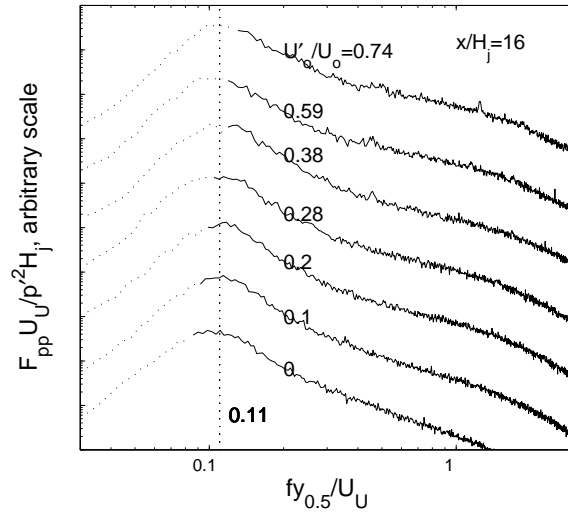


Figure 6.9: The spectra of the fluctuating wall pressure for offset jet with a co-flowing jet with $H_s/H_j = 1$, $H'_j/H_j = 0.5$ and $U'_o/U_o = 0$ to 0.74 measured at $x/H_j = 16$, frequency is normalized using outer jet half width $y_{+1/2}$ measured at $x/H_j = 16$.

The structures associated with the inner shear layer (at $fH_j/U_U \approx 0.2$) gradually diminished as flow evolved downstream, and a low frequency peak associated with the wall jet mode began to emerge. For the case with $U'_o/U_o = 0$, the low frequency peak emerged at $x/H_j \approx 7$. This location gradually shifted to $x/H_j \approx 11$ when inner jet velocity was increased to $U'_o/U_o = 0.59$ indicating the increase in the inner jet velocity shifted the location where the wall-jet like structures interacted with the wall. The characteristic frequency of these wall-jet like structures also decreased from $fH_j/U_U \approx 0.07$ to 0.04 as the inner jet velocity increased. The pressure spectra measured at $x/H_j = 16$ for offset jet with co-flowing jet with $U'_o/U_o = 0$ to 0.74 are shown in Fig. 6.9. Here the frequency was normalized using the outer half width, $y_{+1/2}$. The characteristic frequency are all $fy_{+1/2}/U_U \approx 0.11$ indicating the difference in the frequency of the wall jet structures was associated with a difference in the length scale of the flow.

The spectra of fluctuating velocities and wall pressure for offset jet with a co-flowing jet with $U'_o/U_o = 0.20$ are shown in Fig. 6.10. The spectra of fluctuating velocities in this case were similar to the spectra for the single offset jet except that there was a small peak at $fH_j/U_U \approx 0.5$ to 0.6 for $1 \lesssim y/H_j \lesssim 1.5$ in the region $x/H_j \leq 4$. It is thought this is associated the wake structures generated behind the splitter plate based on the spatial location. The high frequency sharp peak was not observed in the pressure spectra indicating these structures did not interact with the wall.

The spectra of streamwise and vertical fluctuating velocities and fluctuating wall pressure for an offset jet with a co-flowing jet of $H'_j/H_j = 0.5$ and $U'_o/U_o = 0.38$ are shown in Fig. 6.11. There is a sharp peak in the spectra of fluctuating velocities at $fH_j/U_U \approx 0.44$ and an apparent harmonic in the region $x/H_j \leq 4$. The peak was particularly large in F_{vv} measured at $y/H_j \approx 1$ where the rms value of the vertical fluctuations was the largest. The sharp peak decreased in magnitude as the flow evolved downstream and seemed to disappear at $x/H_j = 8$, where a low frequency peak emerged in the spectra. The sharp peak can also be found in the pressure spectra indicating these structures interacted with the wall in

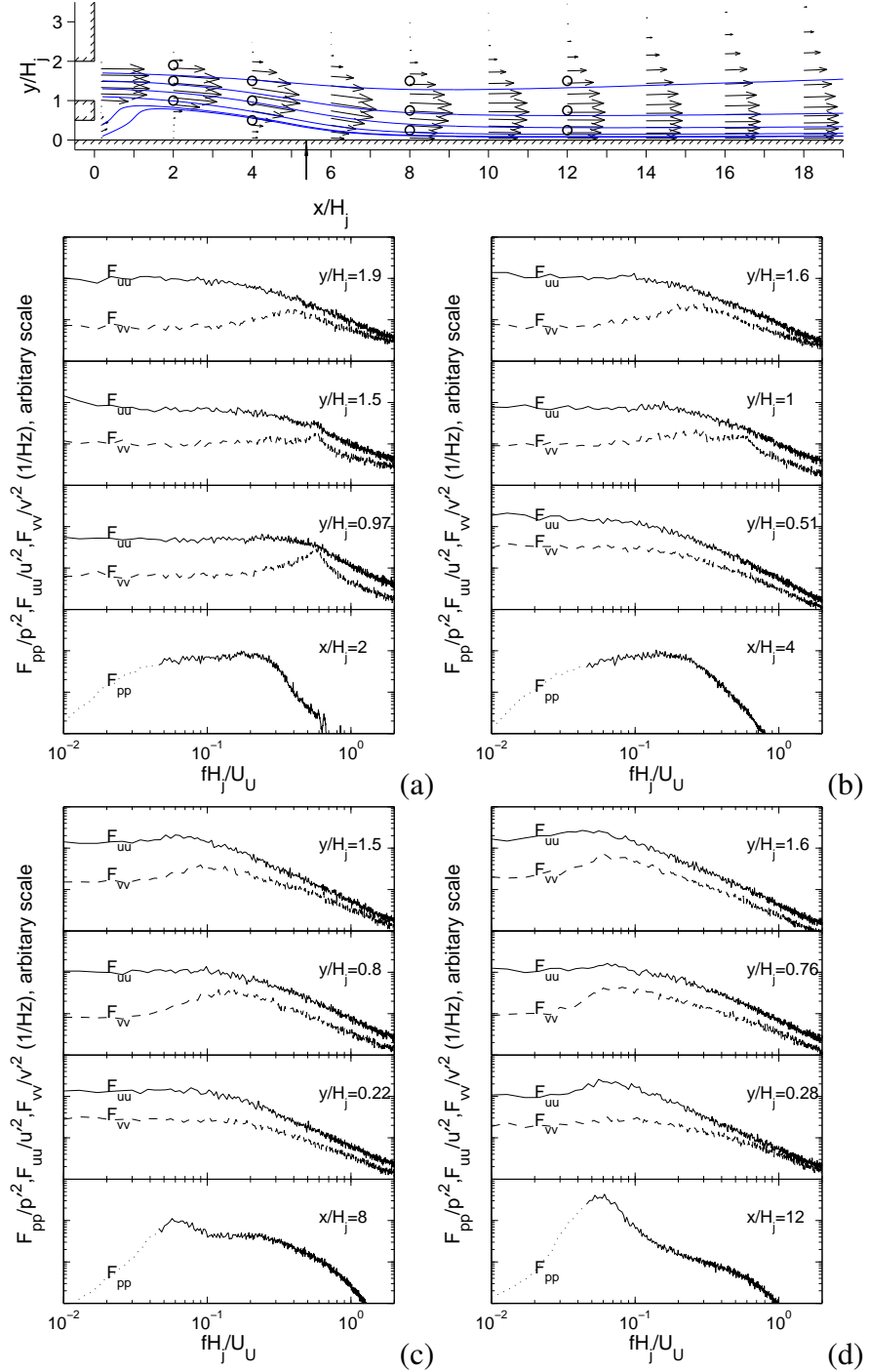


Figure 6.10: Spectra of fluctuating wall pressure and fluctuating streamwise and vertical fluctuating wall pressure measured at different distance above wall at x/H_j = (a) 2, (b) 4, (c) 8 and (d) 12 for an offset jet with $H_s/H_j = 1$ and a co-flowing jet with $H'_j/H_j = 0.5$ and $U'_o/U_o = 0.20$.

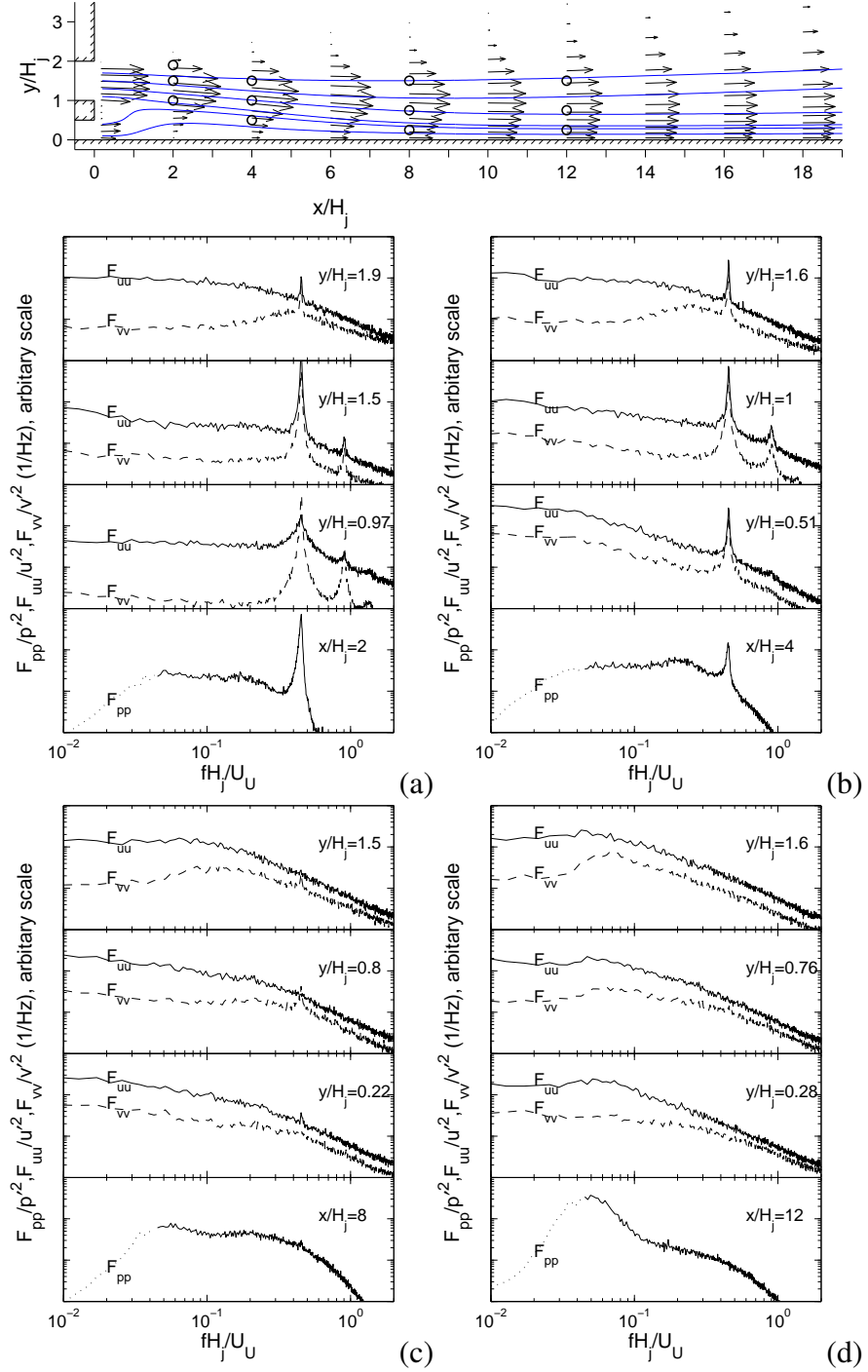


Figure 6.11: Spectra of fluctuating wall pressure and fluctuating streamwise and vertical fluctuating wall pressure measured at different distance above wall at $x/H_j =$ (a) 2, (b) 4, (c) 8 and (d) 12 for an offset jet with $H_s/H_j = 1$ and a co-flowing jet with $H'_j/H_j = 0.5$ and $U'_o/U_o = 0.38$.

the region $x/H_j \leq 4$.

6.3 Offset jet with a co-flowing jet of $H'_J/H_J = 0.18$

The distributions of the mean velocity vectors and the corresponding streamlines for a single offset jet and co-flowing jets with inner jet height of $0.18H_j$ and ratios of maximum streamwise velocity, U'_o/U_o , of 0.27 and 0.63 are shown in Fig. 6.12. In both cases, the inner jet separated from the wall and merged into the outer jet. This was different from the jets with $H'_J/H_J \approx 0.5$ where the inner jet with a maximum velocity of $0.59U_o$ continued to develop along the wall. The outer jet curved toward the wall in the current cases with $H'_J/H_J = 0.18$ and $U'_o/U_o \geq 0.63$. This was significantly different from the jets with $H'_J/H_J \approx 0.5$ where the outer jet did not curve to the wall when $U'_o/U_o \geq 0.59$, and the two jets instead developed parallel to each other.

The static wall pressure coefficient, C_P , and skin friction coefficient, C_f , for co-flowing jets with $U'_o/U_o = 0.27$ to 0.86 are shown in Fig. 6.13. The outer jet curved toward the wall in the current cases causing a broad peak in static wall pressure in the region $2 \leq x/H_j \leq 7$. A recirculation region was formed for the jets with $H'_J/H_J \approx 0.18$ and $U'_o/U_o \leq 0.42$ as indicated by the negative skin friction. For the offset jet with the inner jet velocity of $U'_o = 0.63U_o$, the inner jet separated and reattached to the wall before it was entrained in the outer jet. The skin friction was small in the separation region so it is not clear whether a recirculation region was formed. The inner jet with $U'_o = 0.86U_o$ did not separate from the wall. In this case, the skin friction decreased as the inner jet curved away from the wall in the region $x/H_j \leq 2.5$, and then gradually increased as the inner jet curved back toward the wall in the region $x/H_j > 2.5$. The skin friction increased as the outer jet approached the wall for all the jets with a co-flowing jet with $H'_J/H_J = 0.18$ and there was little difference among the jets at $x/H_j \approx 7$. The skin friction then increased gradually to approach the skin friction of the planar wall jet and single offset jet at $x/H_j \approx 10$.

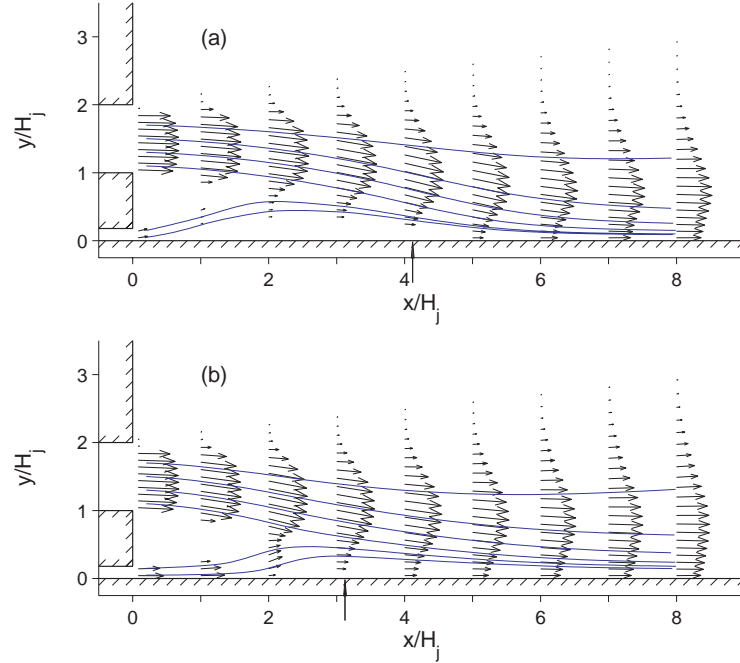


Figure 6.12: Distributions of the vectors and streamlines of the mean velocity for co-flowing jets with size ratio $H'_J/H_J \approx 0.18$ and velocity ratios $U'_o/U_o =$ (a) 0.27 and (b) 0.63.

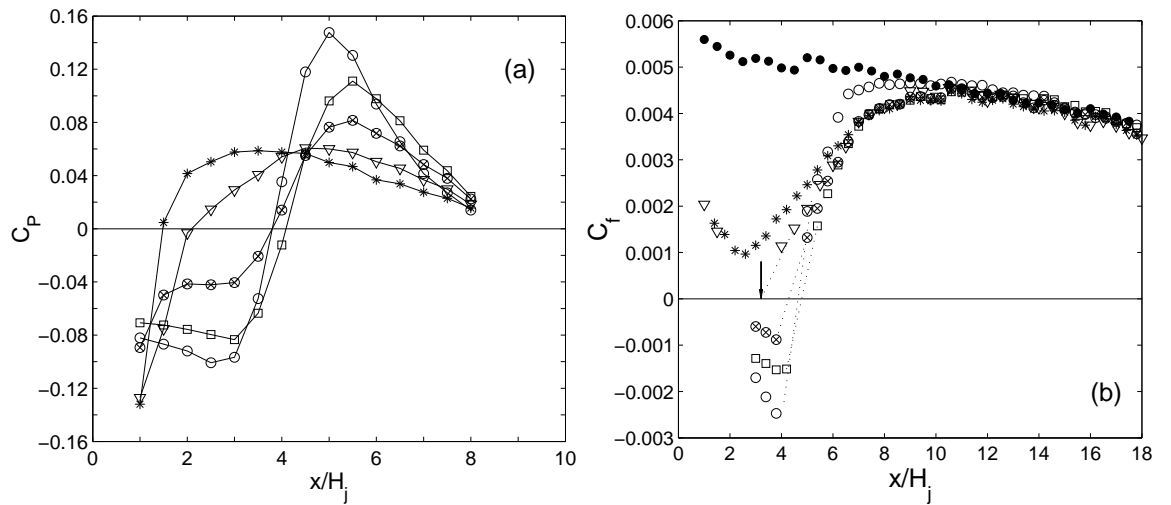


Figure 6.13: Distributions of (a) the static wall pressure coefficient and (b) the skin friction coefficient for co-flowing jets with size ratio $H'_J/H_J \approx 0.18$ and velocity ratios $U'_o/U_o = \circ$ 0, \square 0.27, \otimes 0.42, ∇ 0.63 and $*$ 0.86, and \bullet for the planar wall jet.

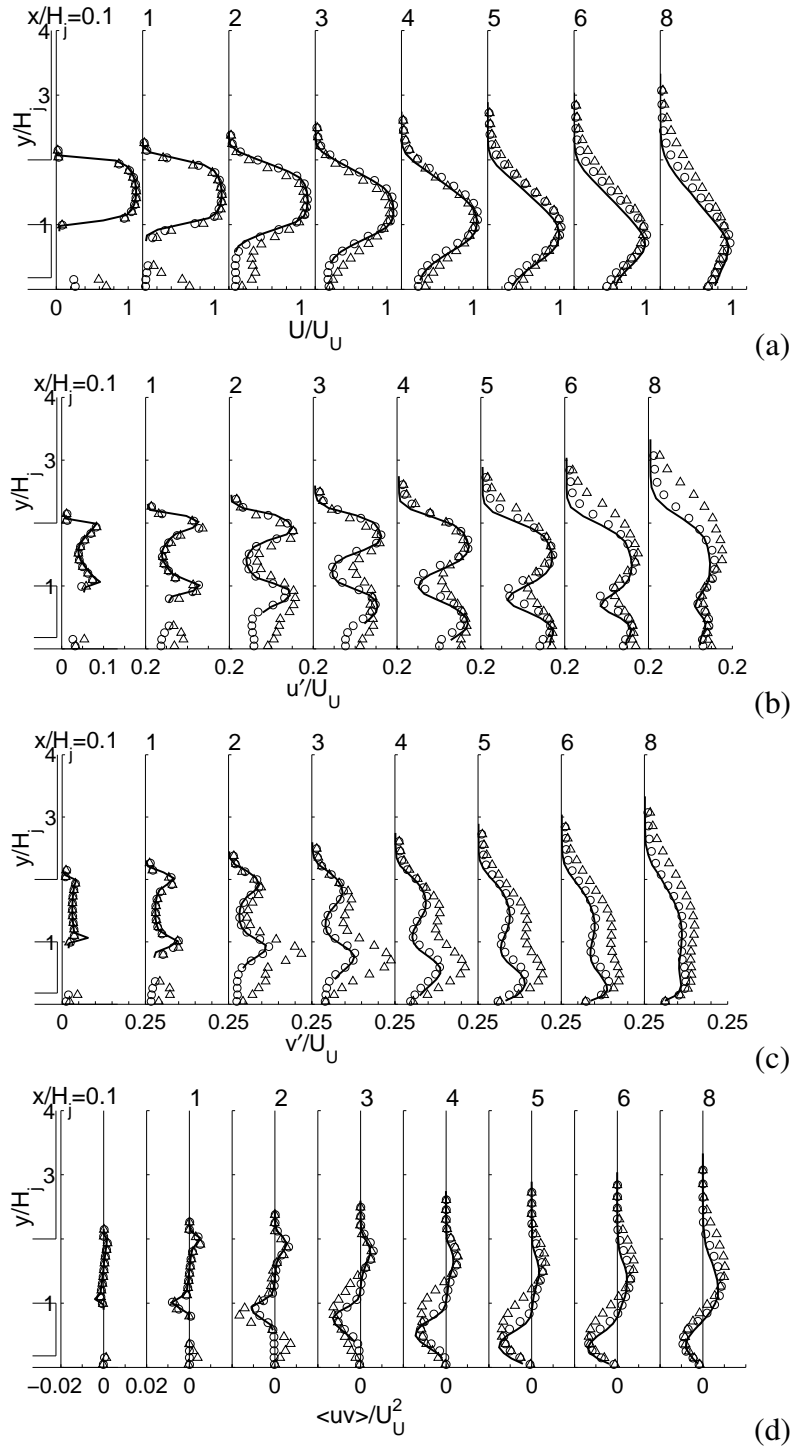


Figure 6.14: Profiles of (a) the mean streamwise velocity, (b) u' , (c) v' and (d) $\langle uv \rangle$ for — the single offset jet and jets with $H'_J/H_J = 0.18$ and $U'_o/U_o = \circ 0.27$ and $\triangle 0.63$.

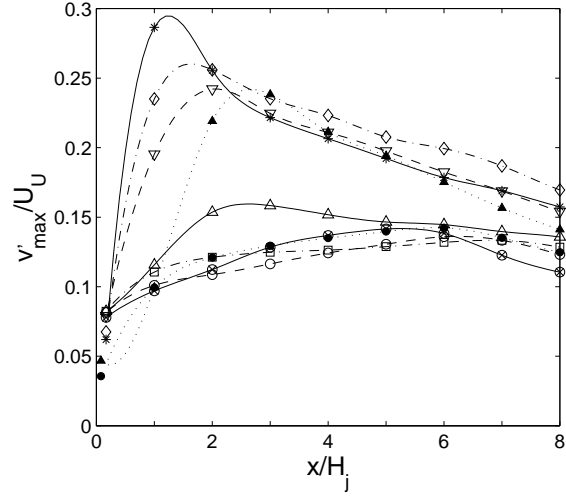


Figure 6.15: The distributions of the local maximum vertical fluctuating velocity along the inner shear layer for \otimes the single offset jet with $H_s/H_j = 1$ and co-flowing jets with $H'_j/H_j = 0.5$ and $U'_o/U_o = \circ 0.1, \square 0.2, \triangle 0.28, \nabla 0.38, \diamond 0.59, *$ 0.74 and co-flowing jets with $H'_j/H_j = 0.18$ and $U'_o/U_o = \bullet 0.27$ and $\blacktriangle 0.63$.

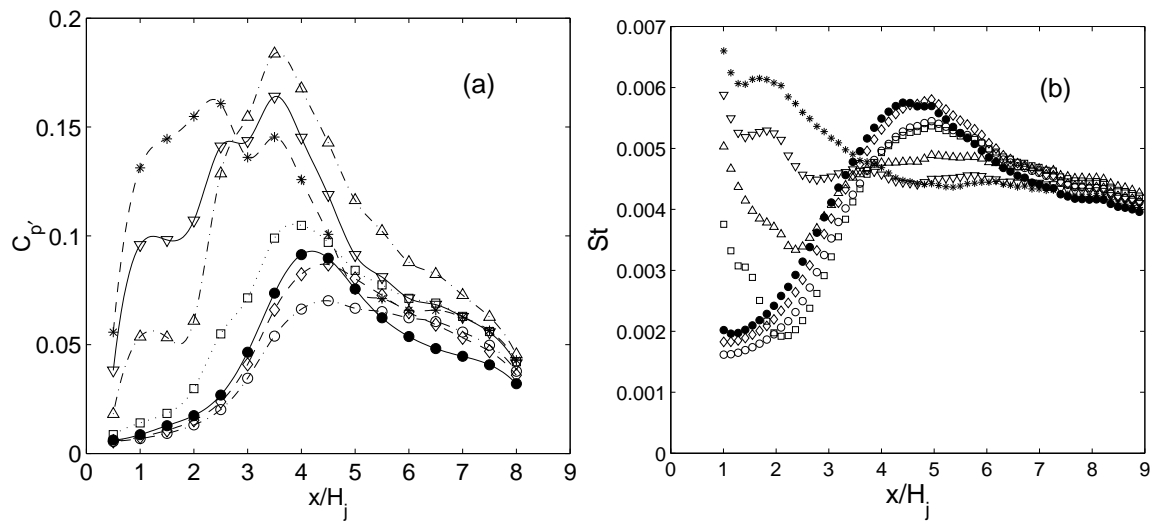


Figure 6.16: Distributions of (a) the fluctuating wall pressure coefficients and (b) the Stanton number for \bullet the single offset jet with $H_s/H_j = 1$ and co-flowing jets with $H'_j/H_j = 0.18$ and $U'_o/U_o = \diamond 0.1, \circ 0.27, \square 0.42, \triangle 0.63, \nabla 0.86$ and $*$ 1.

The distributions of the fluctuating streamwise and vertical velocities and Reynolds shear stress for jets with $H'_J/H_J = 0.18$ and $U'_o/U_o = 0, 0.27$ and 0.63 are shown in Fig. 6.14. The fluctuating velocities, particularly v' and Reynolds shear stress increased dramatically when U'_o/U_o increased to 0.63 , similar to the jets with $H'_J/H_J = 0.5$ with a similar velocity ratio. The distributions of the maximum vertical fluctuating velocity along the inner shear layer for the jets with $H'_J/H_J = 0.18$ and 0.5 are shown in Fig. 6.15. For the larger velocity ratios, $U'_o/U_o \gtrsim 0.4$, v'_{max} increased dramatically and reached a maximum value $0.3U_U$ near the jet exit, while the jets with smaller velocity ratios increased gradually to a maximum less than $0.15U_U$ near the reattachment point. The size of the splitter plate also seemed to play a minor role, v'_{max} was larger for the smaller splitter plate thickness for the same velocity ratio. The maximum local vertical fluctuations decreased gradually as the flow evolved downstream and the difference between the jets with different splitter plate thickness became smaller.

The distributions of the fluctuating wall pressure coefficient and the Stanton number for the co-flowing jet with $H'_J/H_J = 0.18$ and $U'_o/U_o = 0$ to 1 are shown in Fig. 6.16. The peak in the fluctuating wall pressure initially became broader and the maximum p' decreased in magnitude and occurred at a slightly downstream location when U'_o/U_o increased to 0.27 , similar to the case with $H'_J/H_J = 0.5$. When the velocity of the inner jet was $0.63U_o$, the maximum fluctuating wall pressure was significantly larger, nearly twice the maximum p' observed for the single offset jet. The location of this peak also shifted upstream to $x/H_J \approx 3.5$. This is different from the co-flowing jet with $H'_J/H_J = 0.5$ where the maximum fluctuating wall pressure continued to decrease when the inner jet velocity was increased. This indicates the flow went through a transition between $U'_o/U_o = 0.27$ and 0.63 for the co-flowing jets with $H'_J/H_J = 0.18$ that was not observed in the jet with $H'_J/H_J = 0.5$. Thus, another mechanism emerged and became dominant in offset jets with $H'_J/H_J = 0.18$ and $U'_o/U_o = 0.63$.

The peak in the Stanton number associated with the reattachment process in the region

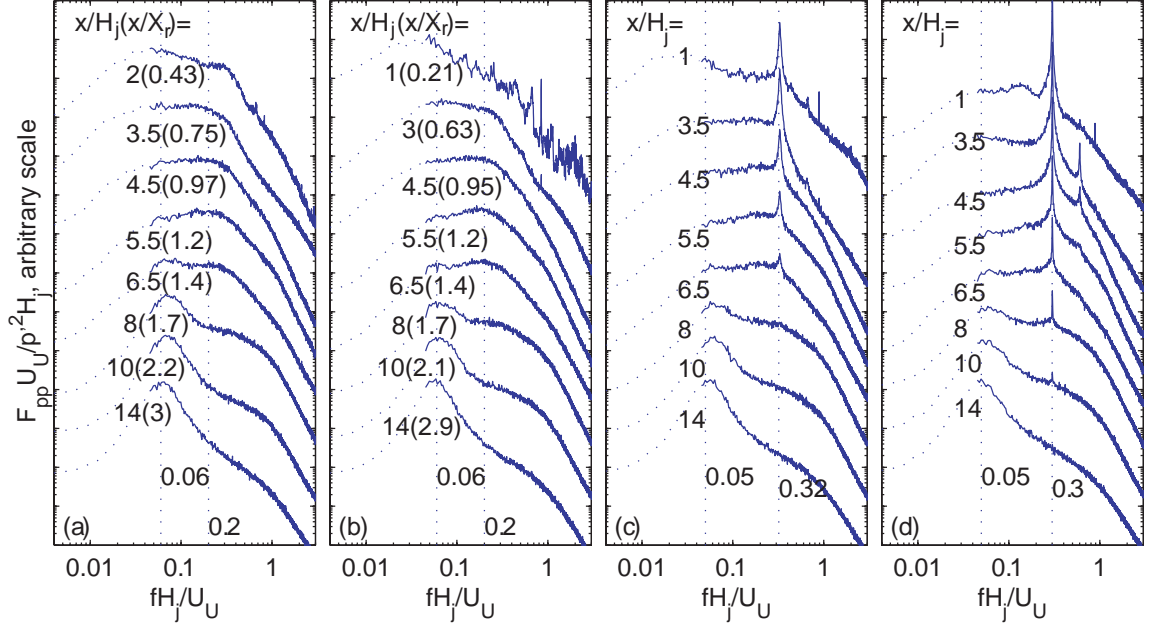


Figure 6.17: The spectra of the fluctuating wall pressure for (a) the single offset jet with $H_s/H_j = 1$ and co-flowing jets with $H'_j/H_j = 0.18$ and $U'_o/U_o =$ (b) 0.27, (c) 0.42 and (d) 0.63.

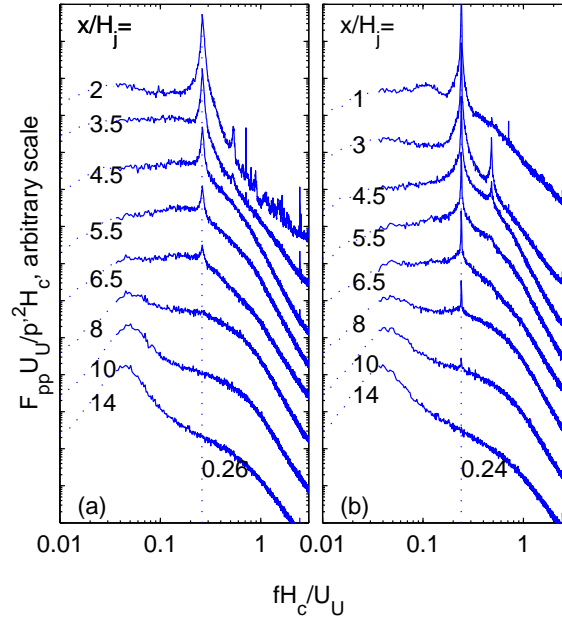


Figure 6.18: The spectra of the fluctuating wall pressure for co-flowing jets with $H'_j/H_j = 0.18$ and $U'_o/U_o =$ (a) 0.42 and (b) 0.63.

$4 \lesssim x/H_j \lesssim 6$ continued to decrease as the velocity ratio U'_o/U_o increased from 0 to 1. The Stanton number in the region $x/H_j \lesssim 3.5$ only decreased slightly when U'_o/U_o increased from 0 to 0.27, similar to the fluctuating wall pressure, but increased significantly in the region near the jet exit, $x/H_j \lesssim 2$ when the velocity ratio was further increased to $U'_o/U_o = 0.63$. This increase in the heat transfer near the jet exit was likely caused in part by the development of inner jet along the wall. When the velocity of the inner jet further increased to $U'_o > 0.63U_o$, the heat transfer in the region $x/H_j \lesssim 3$ increased further and another peak in the heat transfer emerged at $x/H_j \approx 1.5$ to 2 coinciding with the location with large increases in the fluctuating wall pressure. This suggests the increases in the turbulent fluctuations in the region $x/H_j \lesssim 3$ for large velocity ratios ($U'_o > 0.63U_o$) may cause an increase in the heat transfer on the wall.

The spectra of the fluctuating wall pressure for co-flowing jets with $H'_J/H_J = 0.18$ and $U'_o/U_o = 0, 0.27, 0.42$ and 0.63 plotted against fH_j/U_U are shown in Fig. 6.17. For the co-flowing jet with velocity ratios $U'_o/U_o \leq 0.27$, the spectra were similar to the single offset jet, where the characteristic frequency near attachment point was $fH_j/U_U \approx 0.2$. For the co-flowing jet with velocity ratios $U'_o/U_o \geq 0.42$, there is only one dominant peak in the spectra at $fH_j/U_U \approx 0.3$ in the near field. This corresponded to $fH_c/U_U \approx 0.24$ to 0.26 when the frequency was normalized using the splitter plate thickness as shown in Fig. 6.18. This frequency is similar to the frequency of the wake structures generated downstream of a bluff body. This peak was particularly strong and broad for the case with $U'_o/U_o = 0.63$ likely caused by the merging of the shear layer structures and the wake-like structures behind the splitter plate. The merged structures dramatically increased vertical motion of the outer jet, thus the fluctuating wall pressure and the heat transfer near the exit increased significantly for jet with $U'_o/U_o \geq 0.63$.

6.4 Effect of mass flow and momentum flux ratios

The attachment location, X_r/H_s , obtained from surface oil visualization for the co-flowing jet with two jet height ratios are shown in Fig. 6.19 in terms of the ratios of the maximum streamwise velocity, U'_o/U_o , mass flow rates, m'/m , and momentum flux, M'/M , at the jet exits. When the velocity ratio was less than 0.15 to 0.2, X_r/H_s increased when the inner jet velocity increased, and the attachment length seemed to be determined by the ratio of the mass flow rate. Thereafter the momentum ratio seemed to better capture the trend. When the velocity ratio was $U'_o/U_o \gtrsim 0.2$ and $M'/M \lesssim 0.07$, X_r/H_s decreased gradually to $x/H_j \approx 3$. For $M'/M \gtrsim 0.11$, the inner jet continued to develop along the wall and there was no separation and reattachment occurred.

The maximum static wall pressure coefficient also changed when the inner jet velocity changed. The maximum static wall pressure for the co-flowing jet with two jet height ratios are shown in Fig. 6.20, plotted against the ratios of the maximum streamwise velocity, mass flow rate and momentum of the two jets. The maximum static wall pressure decreased approximately linearly with the mass flow rate of the inner jet when the mass flow ratio was less than 0.2. In these cases, the peak in the static wall pressure was caused by the curvature of the outer jet.

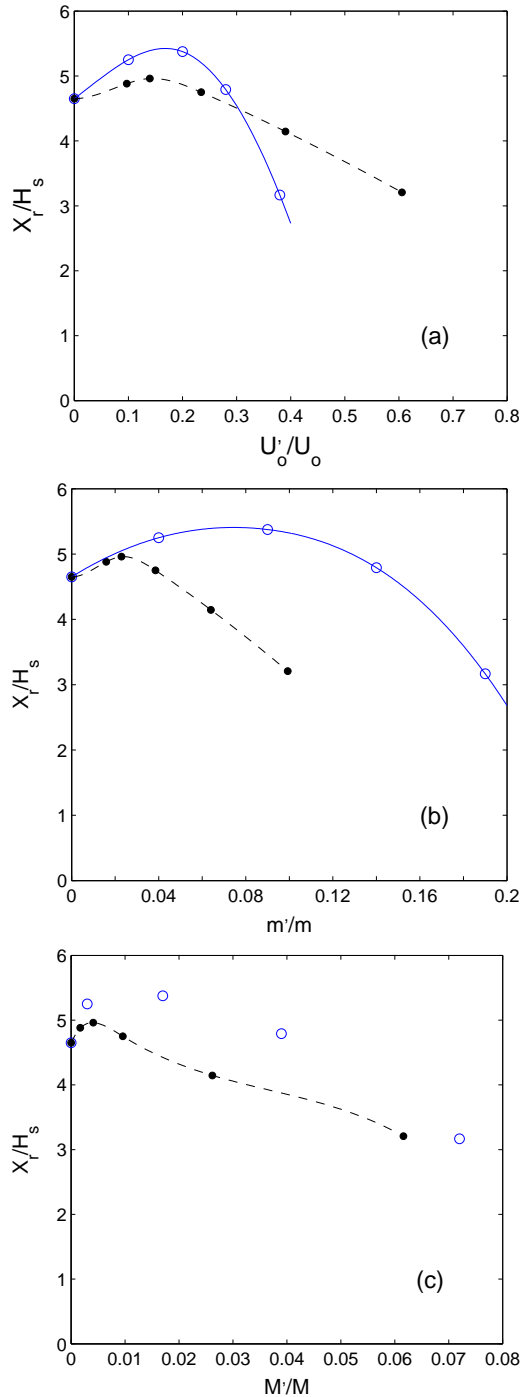


Figure 6.19: Effect of the ratios of the (a) maximum velocity, (b) mass flow rate and (c) streamwise momentum on the reattachment location for co-flowing jets with height ratio of $H'_j/H_j = \circ 0.5$ and $\bullet 0.18$.

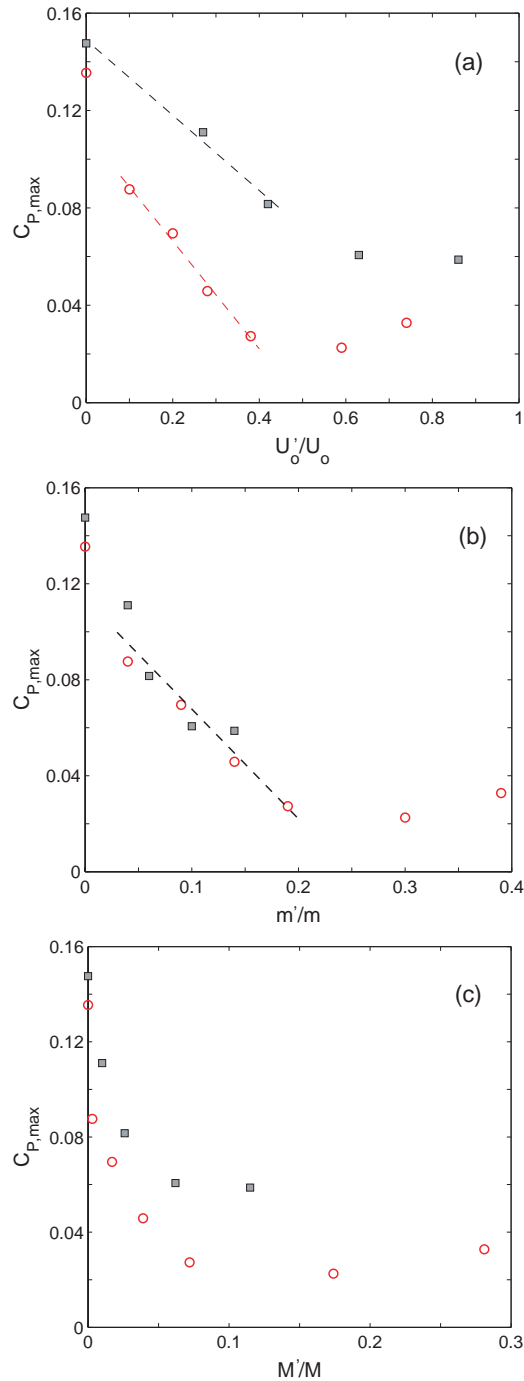


Figure 6.20: Effect of the ratios of the (a) maximum velocity, (b) mass flow rate and (c) streamwise momentum on the maximum static wall pressure coefficient for co-flowing jets with height ratio of $H'_j/H_j = \circ 0.5$ and $\blacksquare 0.18$.

Chapter 7

Co-flowing Jets - Multi-point Measurements

The previous chapter showed that the addition of a co-flowing jet can cause significant changes in the flow structures in an offset attaching jet depending on the co-flowing jet height and velocity. In the jets with large velocity ratios, periodic motions are found in the flow that seemed to be associated with wake structures behind the splitter plate. In this chapter, the results of two-point and two-time measurements of fluctuating wall pressure and fluctuating velocities are presented to further clarify the effect of the co-flowing jet on the development of the large scale structures in the main jet. The cases with $U'_o/U_o \leq 0.2$ are discussed first. The results for higher velocity ratios with inner jet heights of $0.5H_j$ and $0.18H_j$ were then discussed.

7.1 Effect of co-flowing jet with $U'_o/U_o \leq 0.2$

A comparison of the two-point and two-time correlation coefficients of fluctuating wall pressure determined for the single offset jet with $H_s/H_j = 1.0$ and co-flowing jets with a velocity ratio of 0.2 and $H'_j/H_j = 0.5$ are shown in Fig. 7.1. The measurements are reported for cases when the reference microphone was located at $x_1/H_j = 5, 9$ and 12. The

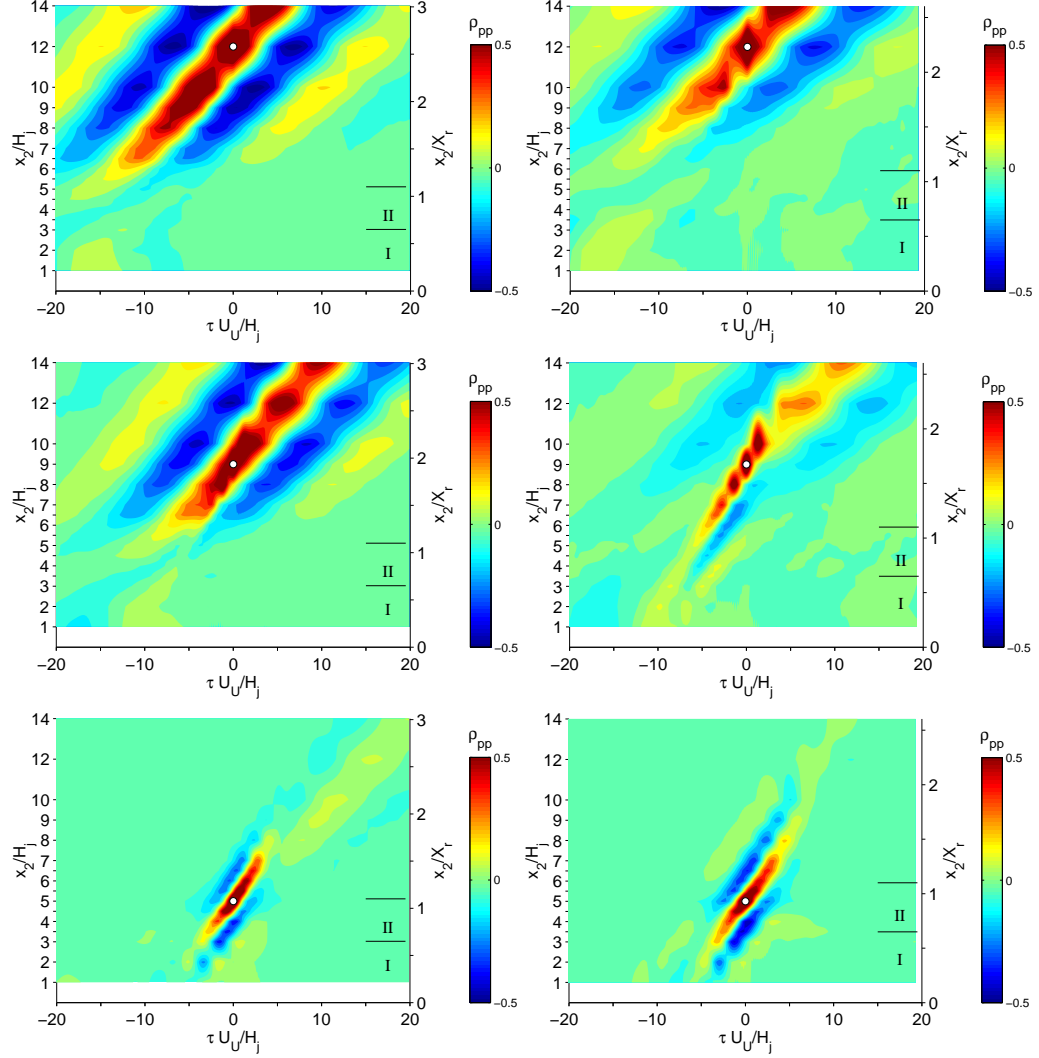


Figure 7.1: Correlation coefficients of the fluctuating wall pressure for (left) the single offset jet with $H_s/H_j = 1.0$ and (right) the co-flowing jets with velocity ratio of $U'_o/U_o \approx 0.2$ and $H'_j/H_j = 0.5$ for reference locations at $x_1/H_j = 12, 9$ and 5 (from top to bottom) indicated using \circ .

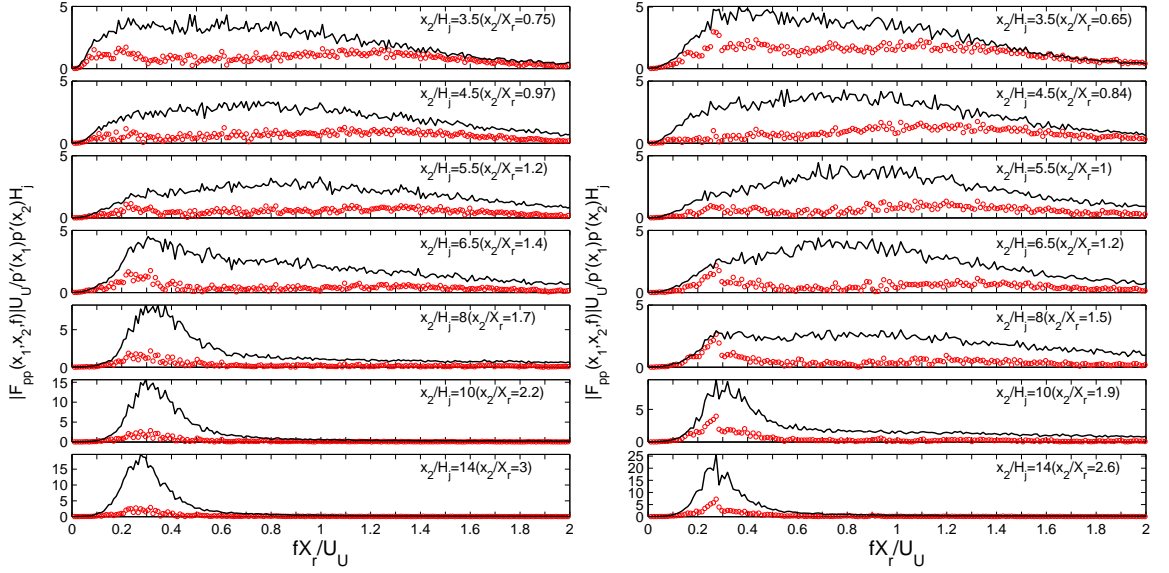


Figure 7.2: The \circ cross spectra of fluctuating wall pressure with reference location at $x_1/H_j = 2$ ($x_1/X_r \approx 0.4$) and — the auto spectra at x_2 for (left) single offset jet and (right) co-flowing jets with $U'_o/U_o \approx 0.2$, $H_s/H_j = 1$ and $H'_j/H_j = 0.5$.

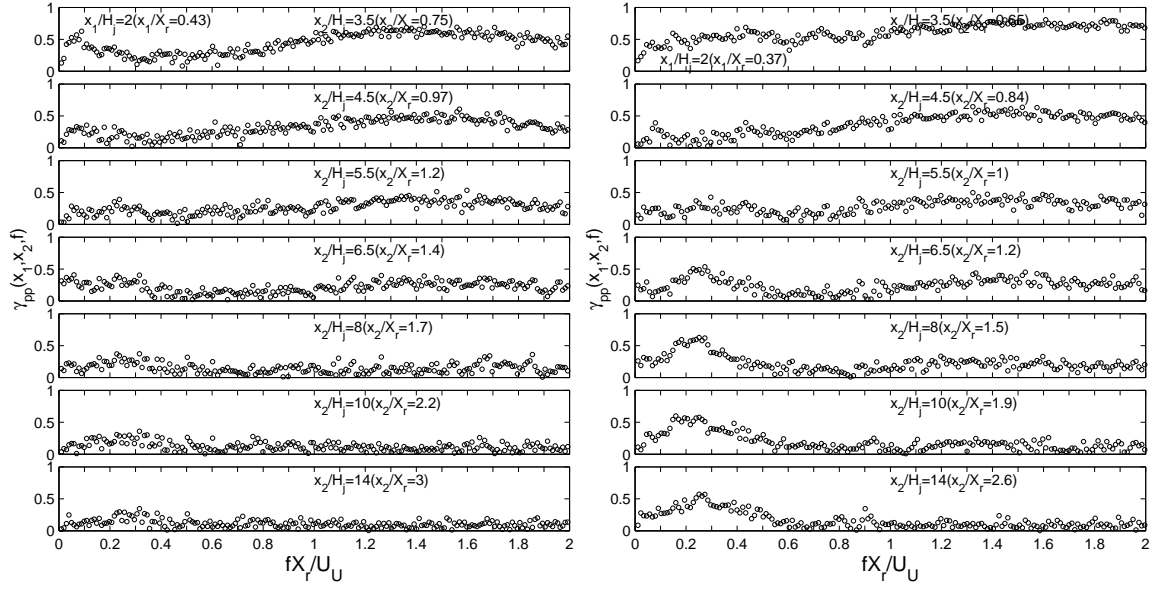


Figure 7.3: The coherence of fluctuating wall pressure with the reference location at $x_1/H_j = 2$ ($x_1/X_r \approx 0.4$) for (left) the single offset jet and (right) the co-flowing jets with $U'_o/U_o \approx 0.2$ and $H'_j/H_j = 0.5$.

locations of other microphones in the region $1 \leq x_1/H_j \leq 14$ are marked using the tick marks on the left vertical axis in the figure. The results show that when the co-flowing jet was added, the correlations below the recirculation region were quite similar to the case without the co-flow. The region associated with the inner shear layer structures seemed to extend downstream and the wall jet structures seemed to occur further downstream.

The magnitude of the cross spectra between the fluctuating wall pressure at a reference location at $x_1/H_j = 2$ ($x_1/X_r = 0.43$) and points at $x_2/H_j = 3.5$ to 14 ($x_2/X_r = 0.75$ to 3) are shown in Fig. 7.2. The auto spectra at the different downstream locations are also shown. The cross spectra for the co-flowing jets were similar to the single offset jet except there were slight differences in the magnitude of the peaks. The coherence computed from the results is shown in Fig. 7.3. There was a maximum in the coherence throughout the region $x/H_j \leq 14$ at $fX_r/U_U \leq 0.3$ ($fH_j/U_U \leq 0.06$) when the co-flowing jet was added that was not evident when the co-flow was not present. This was the characteristic frequency of the wall jet in the single offset jet measurement. This may suggest that the motions causing fluctuations in the wall jet region may be more related to those in the region near the jet exit when the co-flowing jet was added.

The change in the phase angle between the pressure at x_1/X_r and the downstream positions for different frequencies in the single offset jet with $H_s/H_j = 1.0$ and the offset jet with a co-flowing jet with $U'_o/U_o \approx 0.2$ are shown in Fig. 7.4. The reference location was again $x_1/H_j = 2$. The phase angles in the co-flowing jets at all the frequencies did not change significantly in the region $x_2/X_r < 0.5$, particularly for frequencies $fX_r/U_U \geq 0.4$. Thus, the fluctuations were approximately in phase in this region. The location of the phase jump for the low frequency structures, $fX_r/U_U = 0.2$ and 0.3, shifted downstream from $x/X_r \approx 0.7$ to 0.9 indicating the location where the motions started to interact with wall shifted downstream when the co-flowing jet was added.

The phase angles for all frequencies changed approximately linearly in the streamwise direction in the attachment region $0.9 < x_2/X_r < 1.2$ in the offset jet with the co-flowing

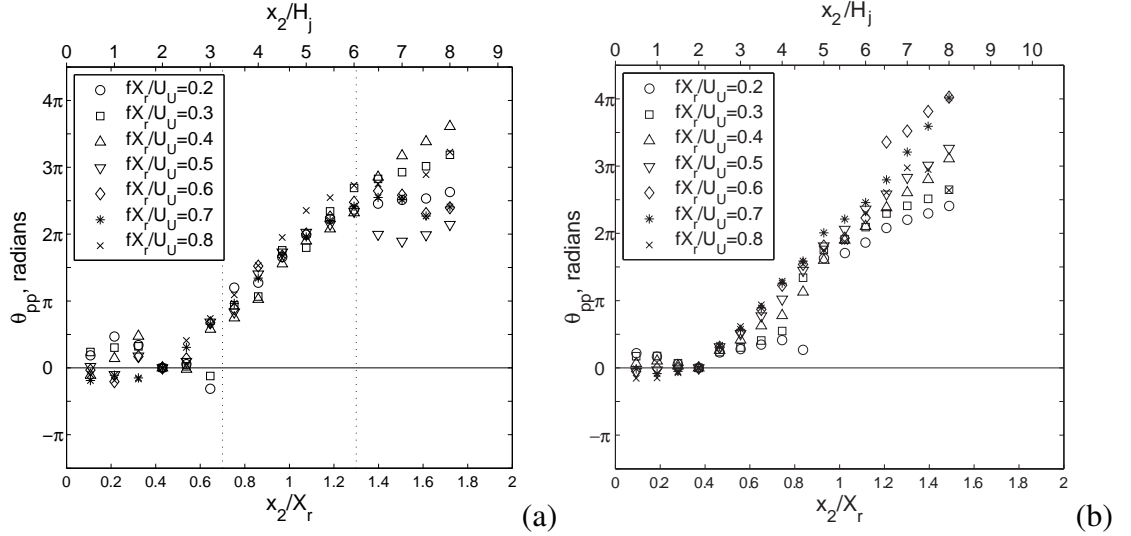


Figure 7.4: The phase angle of the fluctuating wall pressure between $x_1/H_j = 2$ ($x_1/X_r \approx 0.4$) and different streamwise position x_2 for frequencies of $0.2 \leq fX_r/U_U \leq 0.8$ for (a) single offset jet and (b) co-flowing jets with $U'_o/U_o \approx 0.2$ and $H'_j/H_j = 0.5$.

jet. This indicates that fluctuations with these fluctuations were convected along the wall. The convection velocities in the reattachment region are shown in Fig. 7.5. The convection velocity here were calculated from the phase angle with streamwise position in the region $0.7 \leq x/X_r \leq 1.3$ for single jet and $0.9 \leq x/X_r \leq 1.2$ for the offset jet with a co-flowing jet. The convection velocity for the the offset jet with a co-flowing jet was 30% to 50% higher than the single offset jet for frequencies $0.2 \leq fX_r/U_U \leq 0.4$ indicating the co-flowing jet increased the propagation velocity of these motions in the reattachment region. The convection velocities of the motions with frequency $0.6 \leq fX_r/U_U \leq 0.8$ were similar in the two flows. The convection velocity for fluctuations in the jet with the co-flowing jet reached a maximum at $fX_r/U_U \approx 1.2$, earlier than the single offset jet.

The phase angles between the pressure fluctuations with frequencies $fH_j/U_U \leq 0.13$ measured at $x_1/H_j = 8$ and points in the region $7 \leq x_2/H_j \leq 14$ also changed linearly with streamwise position. These phase angles were not shown but the convection velocities calculated using the slopes are shown in Fig. 7.6. The convection velocity for the

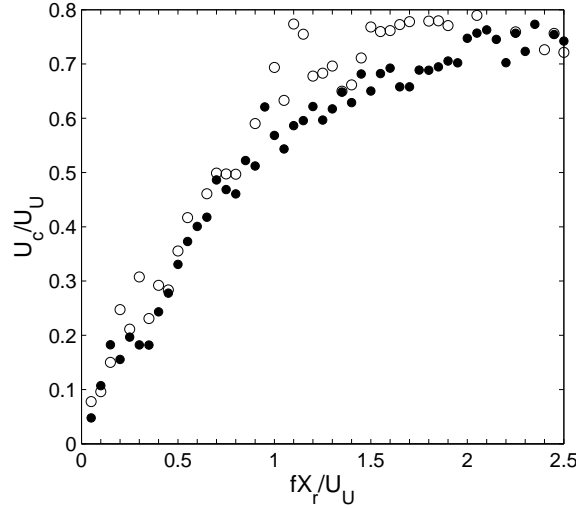


Figure 7.5: The convection velocity for different frequencies computed from $d\theta_{pp}/dx_2$ ● for the single offset jet with $H_s/H_j = 1.0$ and ○ for the offset jet with $H_s/H_j = 1.0$ and a co-flowing jet with $U'_o/U_o \approx 0.2$ and $H'_j/H_j = 0.5$, both for the region $0.9 \leq x/X_r \leq 1.2$ ($4.5 \lesssim x/H_j \lesssim 6$).

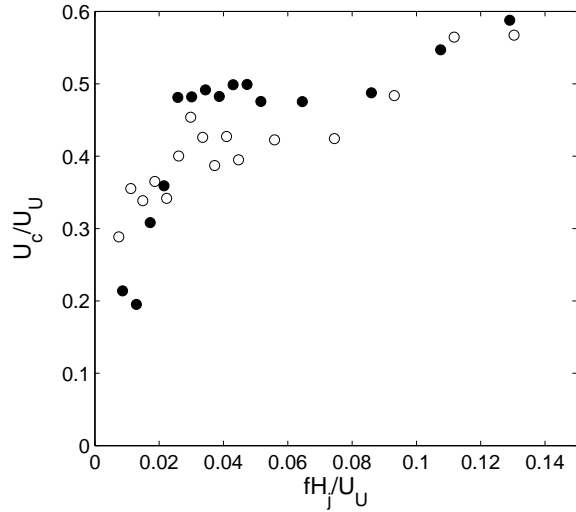


Figure 7.6: The convection velocity for different frequencies computed from $d\theta_{pp}/dx_2$ ● for a single offset jet with $H_s/H_j = 1.0$ and ○ for an offset jet with $H_s/H_j = 1.0$ and a co-flowing jet with $U'_o/U_o \approx 0.2$ and $H'_j/H_j = 0.5$, both for the region $7 \leq x/H_j \leq 14$.

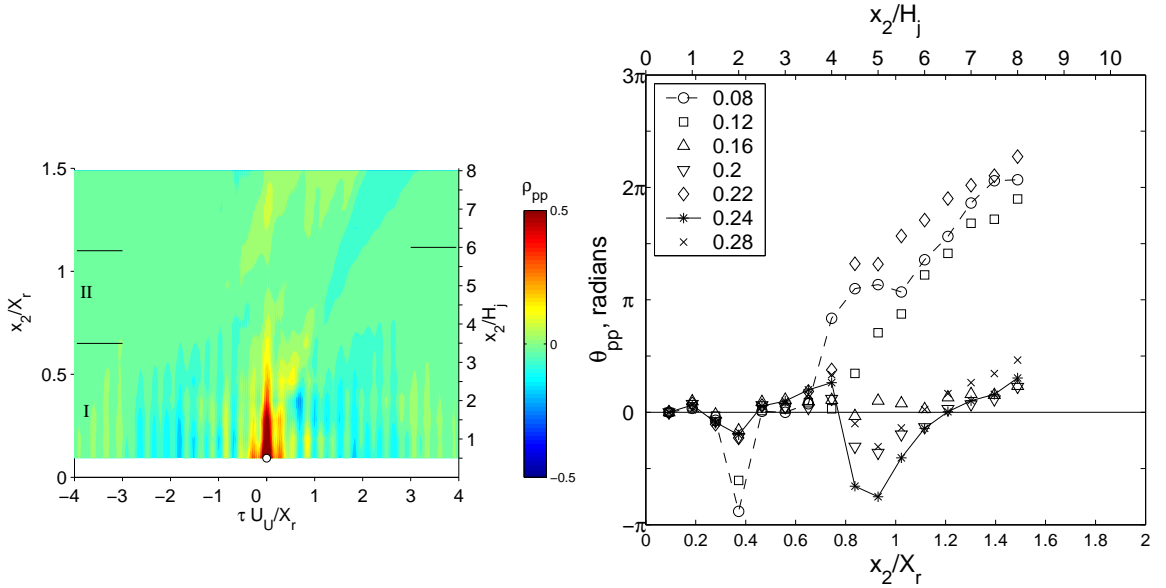


Figure 7.7: Correlation coefficient and phase angles for frequencies of $0.08 \leq f X_r / U_U \leq 0.28$ of the fluctuating wall pressure in the region $x_2/H_j \leq 8$ for $x_1/H_j = 0.5$ in the offset jet with $H_s/H_j = 1.0$ and co-flowing jet with $H'_j/H_j = 0.5$ and $U'_o/U_o \approx 0.2$.

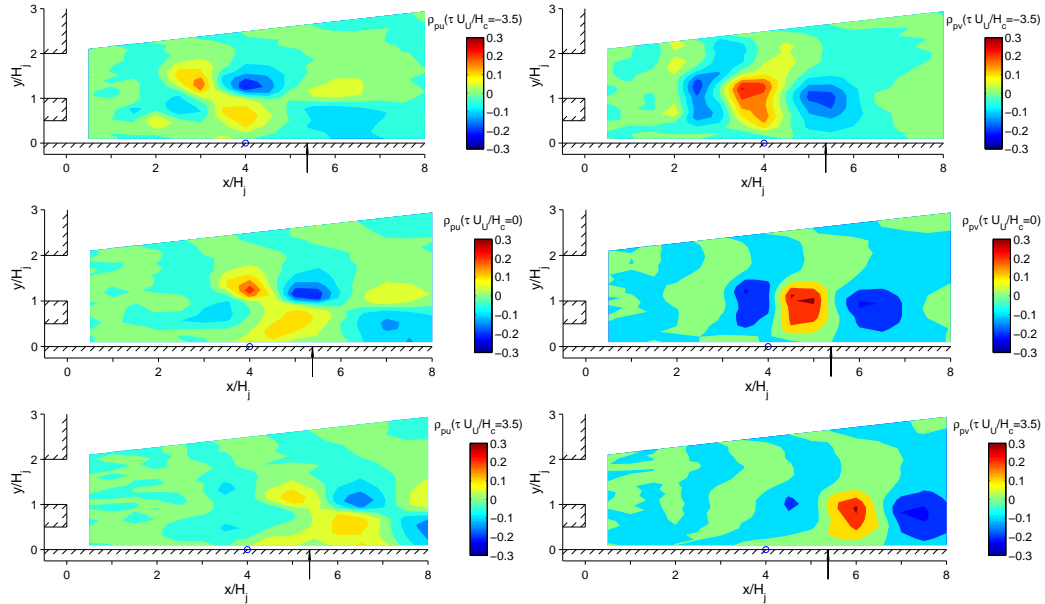


Figure 7.8: Correlation coefficients of fluctuating wall pressure and fluctuating velocities, ρ_{pu} (left) and ρ_{pv} (right), at three different time when $x_1/H_j = 4$ for the offset jet with $H_s/H_j = 1.0$ and a co-flowing jet with $H'_j/H_j = 0.5$ and $U'_o/U_o \approx 0.2$.

frequencies $fH_j/U_U \approx 0.04$ to 0.08 ($fX_r/U_U \approx 0.2$ to 0.4) in the co-flowing jets were approximately 10% lower than those in the single offset jet. The convection velocities of the higher frequency fluctuations $fH_j/U_U \approx 0.13$ were similar in the two flows.

The phase angle between the fluctuating wall pressure at $x_1/H_j = 0.5$ and the pressure at different streamwise positions in the co-flowing jets are shown in Fig. 7.7. The fluctuations in the region $x/X_r \leq 0.7$ were well correlated. The phase difference for frequencies $0.16 \leq fX_r/U_U \leq 0.28$ when the co-flowing jet was present were smaller than the case without the co-flowing jet. The phase angle for fluctuations with $0.16 \leq fX_r/U_U \leq 0.28$ decreased gradually in the region $0.2 \lesssim x/X_r \lesssim 0.4$ indicating the fluctuations still propagate upstream.

Examples of the two point correlation coefficient, ρ_{pu} and ρ_{pv} , for different time intervals in offset jet with a co-flowing jet of $U'_o/U_o \approx 0.2$ are shown in Fig. 7.8. These contours were generated based on velocity measurements at 16 by 20 equally spaced locations at $x/H_j \leq 8$. The reference microphone was located near the attachment location $x_1/H_j = 4$ ($x_1/X_r \approx 0.75$). The correlation of the velocities and the wall pressure showed that the large scale structures in the inner shear layer of the main jet were well correlated with the wall pressure and the development of these structures were similar to those observed in the single offset jet.

The coherence of the fluctuating wall pressure at $x_1/H_j = 4$ and the vertical fluctuating velocities for the single offset jet and offset jet with a co-flowing jet of $U'_o/U_o \approx 0.2$ are shown in Fig. 7.9. The coherence at the frequency of $fX_r/U_U = 0.08$ decreased when the co-flowing jet was added indicating the low frequency unsteadiness of the offset jet decreased when the co-flowing jet was added. The coherence at the frequency of $fX_r/U_U = 0.3$, or $fH_j/U_U \approx 0.06$ which is the characteristic frequency of the wall jet structures, increased slightly in the region $x/H_j \gtrsim 3$ when the co-flowing jet was added. The coherence for higher frequency $fX_r/U_U \geq 0.6$ was similar for offset jets with and without the co-flowing jet, indicating the change in the inner shear layer structures was

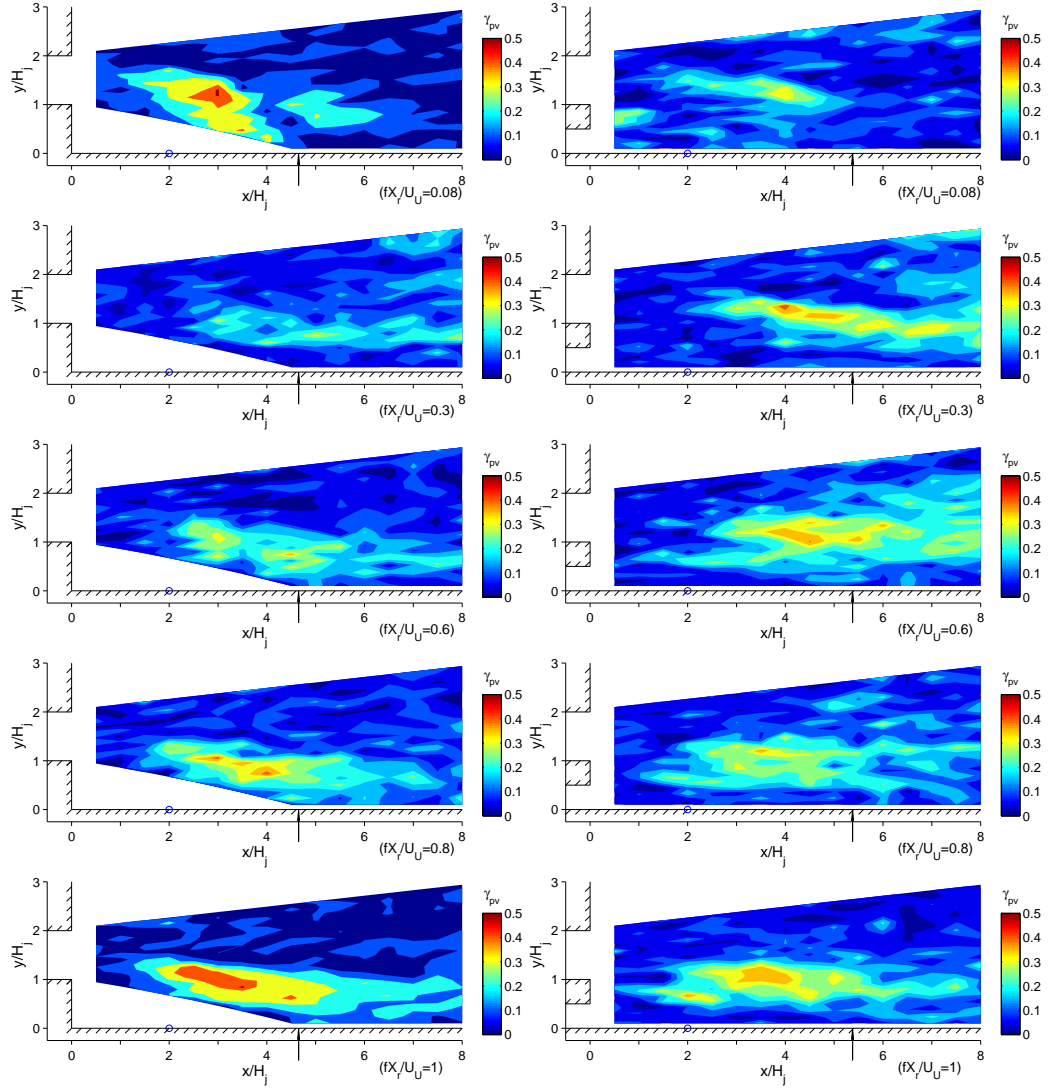


Figure 7.9: Coherence of the fluctuating wall pressure at $x_1/H_j = 4$ and fluctuating vertical velocity, γ_{pv} , of different frequencies for (left) single offset jet with $H_s/H_j = 1.0$ and (right) the offset jet with a co-flowing jet of $U'_o/U_o \approx 0.2$.

small when co-flowing jet of $U'_o/U_o \approx 0.2$ was added.

7.2 Effect of co-flowing jet with velocity $U'_o/U_o \geq 0.35$

The single point measurements showed that strong periodic motions were generated in the flow when the velocity of the co-flowing jet was greater than $0.2U_o$. The reattachment length of the offset jet also started to decrease when $H'_j/H_j = 0.5$. Two-point and two-time measurements of fluctuating wall pressure and velocities were performed to study the causes of this and the evolution of the structures in these flows.

7.2.1 Offset jet with a co-flowing jet of $H'_j/H_j = 0.5$

The two-point and two-time correlations of the fluctuating pressure for the co-flowing jet with $H'_j/H_j = 0.5$ and $U'_o/U_o = 0.38$ determined for $x_1/H_j = 1, 6.5, 9$ and 12 are shown in Fig. 7.10. The wall pressure fluctuations were well correlated near the jet exit due to the periodic motions that corresponded to the sharp peak observed in the pressure spectra. These results show these structures traveled downstream. The correlation from these motions gradually decreased in the region $x/H_j > 5$ indicating the role of these structures in causing the wall pressure fluctuations were diminishing in this region. The correlation coefficients for the fluctuating wall pressure determined for the pressure at $x_1/H_j = 6.5, 9$ and 12 were similar to the single offset jet. This suggests that the flow structures in the inner shear layer of the main jet and the wall jet structures still existed in the flow. The transition between these two types of structures seemed to occur at $x/H_j \approx 10$ to 12 , downstream of the transition location for the offset jet with a lower velocity co-flowing jet.

The changes in the coherence and the phase angles of the cross spectra with frequency for the fluctuating wall pressure measured in the co-flowing jets with velocity ratio of 0.38 are shown in Fig. 7.11. Here, the frequency was normalized using the thickness of the splitter plate, H_c . The distributions of the coherence showed that there were three types of

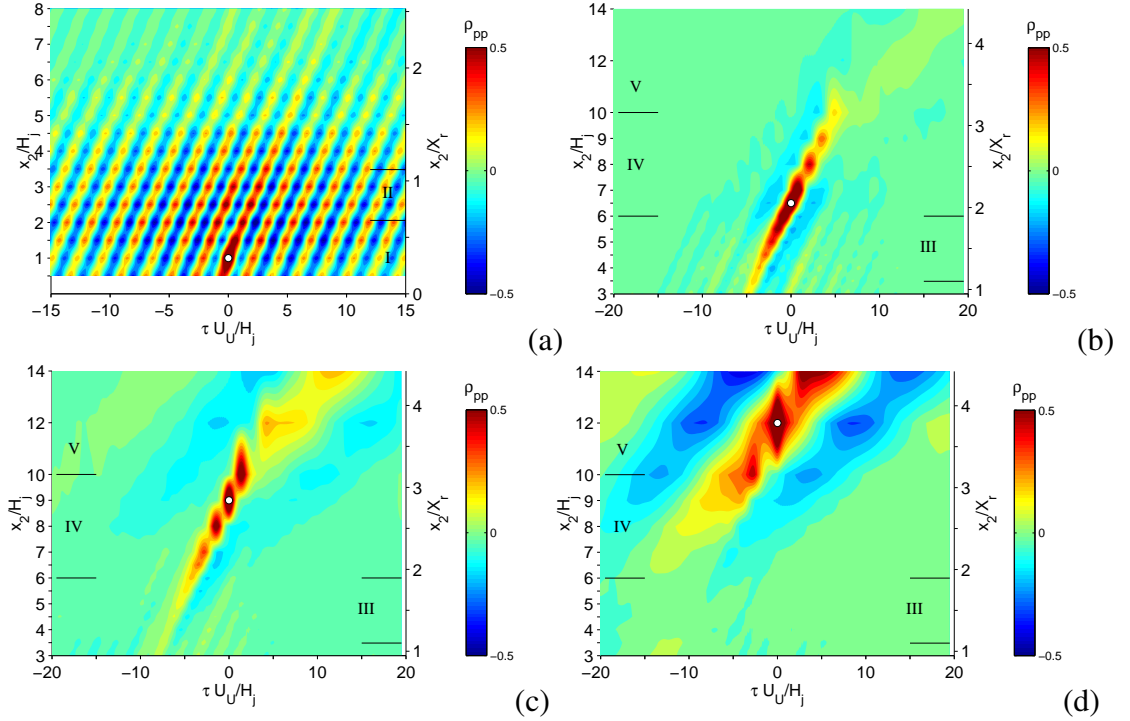


Figure 7.10: Correlation coefficient of fluctuating wall pressure for the offset jet with a co-flowing jet of $H'_j/H_j = 0.5$ and velocity ratio of $U'_o/U_o \approx 0.38$, when the reference location is at x_1/H_j = (a) 1, (b) 6.5, (c) 9 and (d) 12.

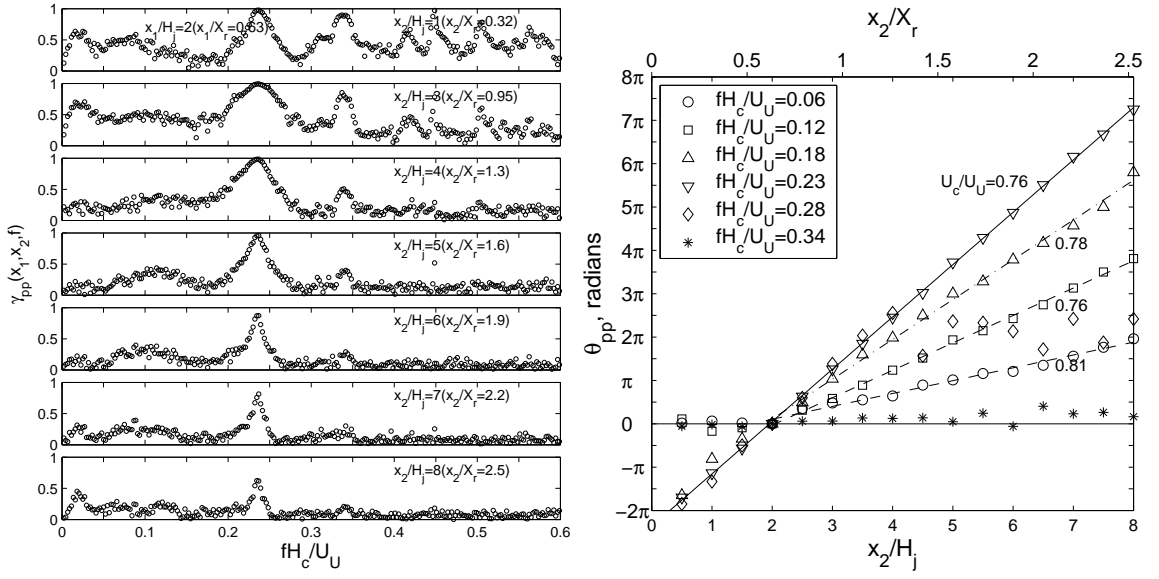


Figure 7.11: The coherence and the phase angles of fluctuating wall pressure with reference to $x_1/H_j = 2$ ($x_1/X_r \approx 0.63$) for the offset jet with $H_s/H_j = 1.0$ and a co-flowing jet with $H'_j/H_j = 0.5$ and $U'_o/U_o \approx 0.38$.

motions in this flow. There was a strong peak at $fH_c/U_U \approx 0.23$ that seems associated with the wake structures behind the splitter plate. There was also a broad peak at $fH_c/U_U \approx 0.08$ to 0.12 (or $fX_r/U_U \approx 0.7$ to 1.1) that corresponds to the frequency of the inner shear layer structures in the single offset jet. There was another low frequency peak at $fH_c/U_U \approx 0.02$ to 0.03 ($fH_j/U_U \approx 0.05$). There was also a series of sharp peaks occurred at $fH_c/U_U \gtrsim 0.34$. The role of these peaks are discussed below.

The phase angle for fluctuations with frequency of $fH_c/U_U \approx 0.23$ increased linearly with streamwise separation distance in the region $x_2/H_j \leq 8$ indicating the structures are convected downstream. The convection velocity was approximately $0.76U_U$. The fluctuations with frequencies $fH_c/U_U \lesssim 0.23$ are convected at a similar velocity in the region $2 \leq x/H_j \leq 8$. The phase of the fluctuations with the frequency $fH_c/U_U \approx 0.34$ did not change with position in the region $x/H_j \leq 8$. Thus, these motions cause fluctuations that do not propagate downstream but seem to be in phase throughout the region.

The development of the structures in the flows can be examined using the correlation of the fluctuating wall pressure and fluctuating velocities measured directly above the microphone. The correlations for the offset jet with a co-flowing jet of $U'_o/U_o \approx 0.38$ are shown in Fig. 7.12. At $x/H_j = 2$, the streamwise fluctuating velocities above and below $y/H_j \approx 0.9$ were well correlated with the wall pressure. The fluctuations in these two parts of the flow were out of phase with each other while the vertical fluctuating velocities were in phase, suggesting the periodic passage of the rolling flow structures generated behind the splitter plate. The pressure-velocity correlations decreased as the flow evolved downstream indicating that the periodic motions generated behind the splitter plate were diminishing. The structures appeared to interact with the wall in the region $6 \leq x/H_j \leq 8$ and this interaction further attenuated the periodic motions. Evidence of the inner shear layer structures in the lower part of the main jet became more apparent at $x/H_j \gtrsim 6$. Eventually the correlations developed into a manner similar to those in a planar wall jet like the cases without co-flow. This transition occurred at a downstream location $x/H_j \approx 10$ to 12 .

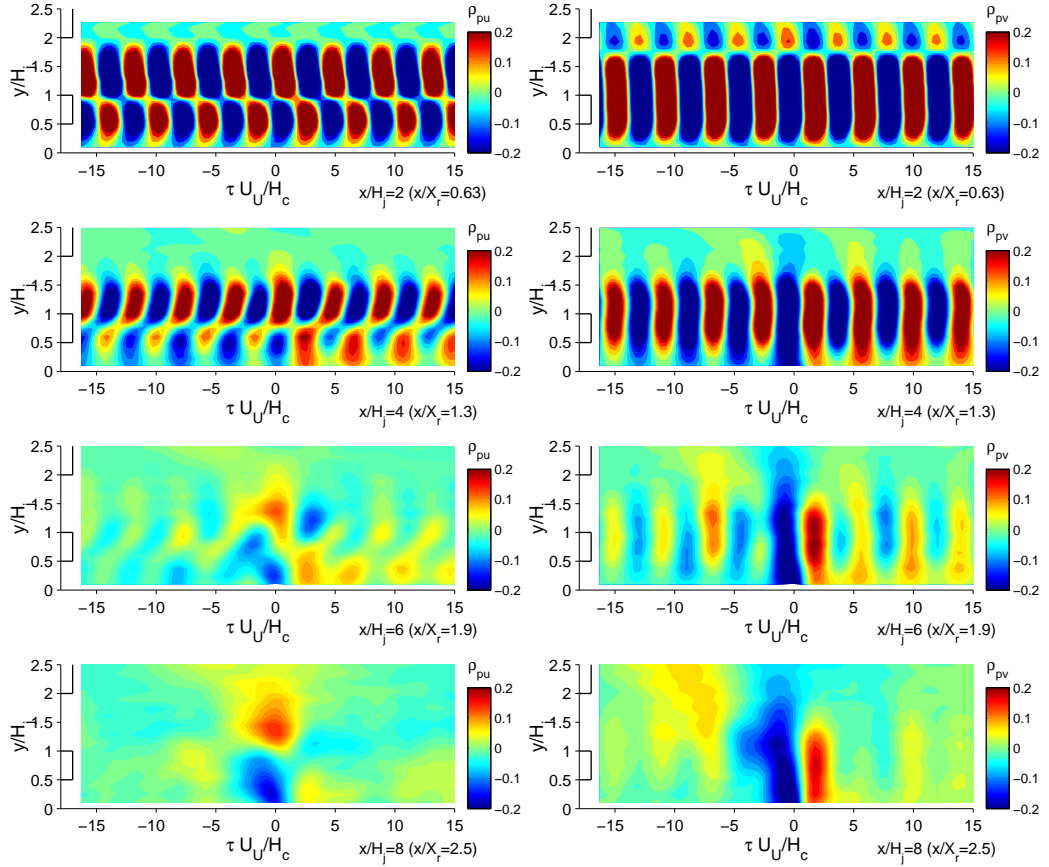


Figure 7.12: Correlation coefficients of the fluctuating wall pressure and the fluctuating velocities above the microphone, ρ_{pu} (left) and ρ_{pv} (right), measured at $x/H_j = 2, 4, 6$ and 8 for the offset jet with a co-flowing jet of $H'_j/H_j = 0.5$ and velocity ratio of $U'_o/U_o \approx 0.38$.

The development of the flow structures can also be examined using the contours of the correlation coefficient at different time intervals shown in Fig. 7.13. Here the reference microphone was located at $x/H_j = 4$, slightly downstream of the attachment point. The contours showed that periodic structures were generated behind the splitter plate and these structures convected downstream at a convection velocity of $U_c \approx 0.75U_U$. The correlations decreased gradually in the region $x/H_j \approx 4$ to 8 , suggesting again these periodic motions were diminishing.

The correlations of the fluctuating wall pressure and velocities in the region near the exit

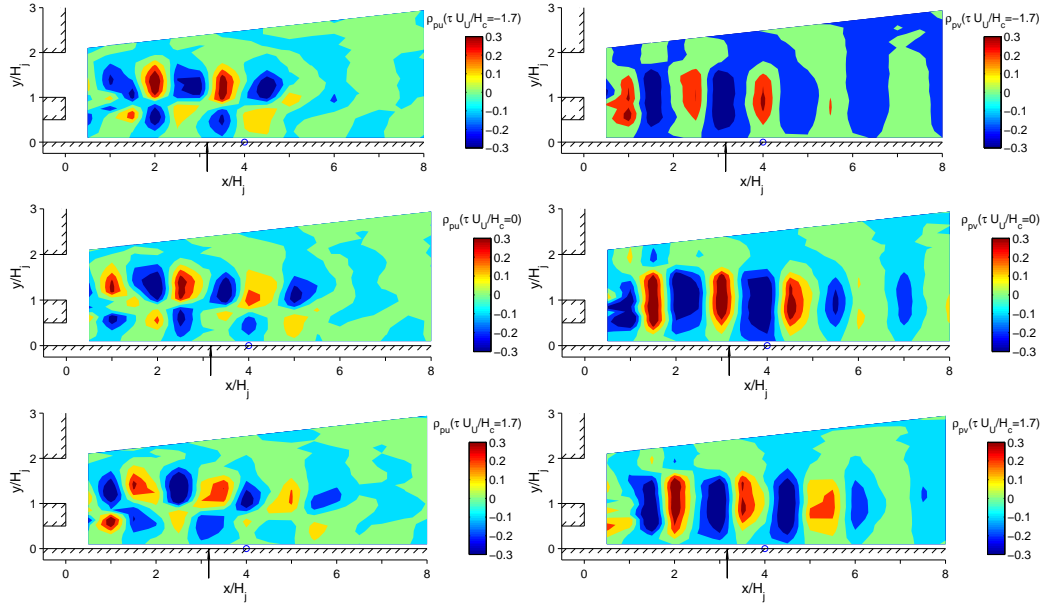


Figure 7.13: Correlation coefficients of fluctuating wall pressure at $x_1/H_j = 4$ and fluctuating velocities, (left) ρ_{pu} and (right) ρ_{pv} , for three different time delays in the offset jet with $H_s/H_j = 1.0$ and a co-flowing jet with $H'_j/H_j = 0.5$ and $U'_o/U_o \approx 0.38$.

become more prominent when the velocity of the inner jet was further increased to $U'_o/U_o > 0.38$ indicating the periodic motions become stronger. The characteristic frequency of the periodic motions were twice as large as those of the inner shear layer structures. These periodic motions increased the mixing between the two jets and thus likely decreased the reattachment length. The periodic motion also decreased the interaction between inner shear layer structures and the wall. As a result, the fluctuating pressure and the heat transfer in the reattachment region decreased.

7.2.2 Offset jet with a co-flowing jet of $H'_j/H_j = 0.18$

The periodic motions generated behind the splitter plate has a characteristic frequency of $f H_c/U_U \approx 0.23$. When the thickness of the splitter plate was changed to $H_c/H_j = 0.82$, the frequency of the wake like structures became similar to the frequency of the structures in the inner shear layer. The measurements of the pressure spectra showed that the two peaks

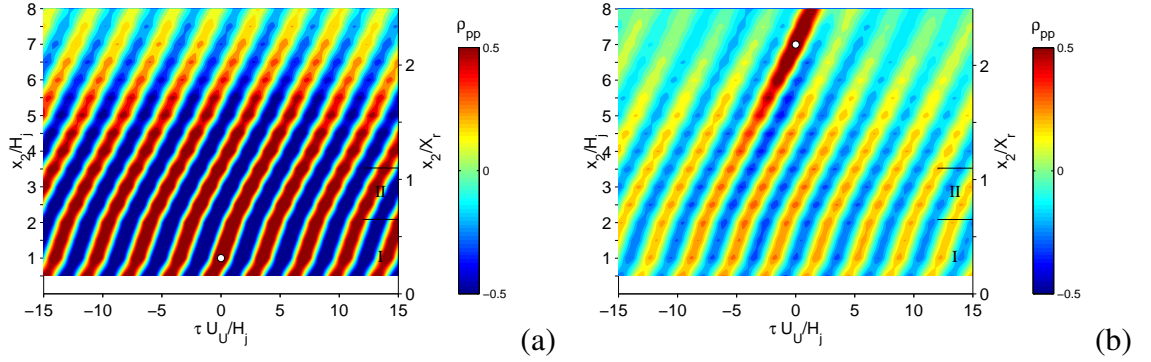


Figure 7.14: Correlation coefficient of fluctuating wall pressure for the offset jet with a co-flowing jet of $H'_j/H_j = 0.18$ and velocity ratio of $U'_o/U_o \approx 0.63$ when the reference location is at x_1/H_j = (a) 1 and (b) 7.

merged together and fluctuating wall pressure and heat transfer significantly increased. The changes in the large scale structures in the flow are considered here.

The correlation coefficients of the fluctuating wall pressure for the jets with $H'_j/H_j = 0.18$ and $U'_o/U_o = 0.63$ (case 10 in Table. 6.1) for $x_1/H_j = 1$ and 7 are shown in Fig. 7.14. The results showed strong periodic pressure fluctuations were generated close to the jet exits and were convected downstream. The convection velocity in region I ($x/X_r \leq 0.65$) seems to be larger than those in other regions. The correlation gradually decreased as the flow evolved downstream. There were no obvious fluctuations with other time scale found in the region $x/H_j \leq 8$ suggesting again that there was only one dominant flow structures in this region of the flow.

The coherence and the phase angles of the fluctuating wall pressure for jets with $U'_o/U_o \approx 0.63$ and $H'_j/H_j = 0.18$ are shown in Fig. 7.15. There was a low frequency peak at $fH_c/U_U \approx 0.07$ ($fH_j/U_U \approx 0.08$) that was similar to the frequency of the wall jet structures in the single offset jet. There was a strong peak at $fH_c/U_U \approx 0.23$ that was broader than the peak in the case with $H'_j/H_j = 0.5$. This is likely associated with the strong coherent motions due to the coincidence in the frequencies of the inner shear layer structures and the wake like structures.

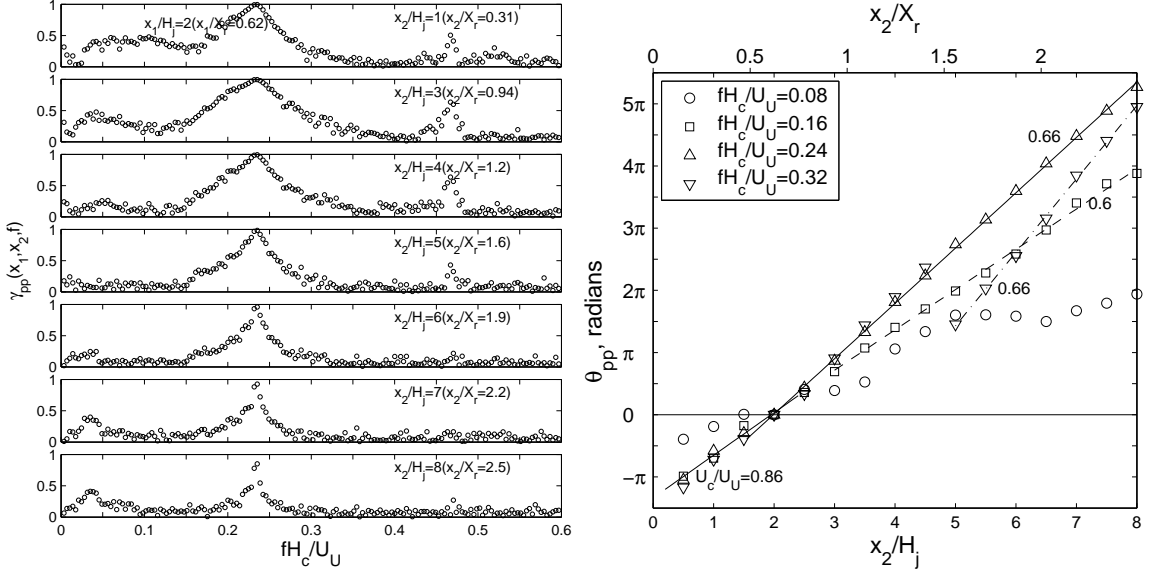


Figure 7.15: The coherence and the phase angles of fluctuating wall pressure with reference to $x_1/H_j = 2$ ($x_1/X_r \approx 0.62$) for the offset jet with $H_s/H_j = 1.0$ and a co-flowing jet with $H'_j/H_j = 0.18$ and $U'_o/U_o \approx 0.63$.

The phase angle of the cross spectra for the wake structures ($fH_c/U_U = 0.24$) increased linearly with streamwise position in the regions but the slope changed at the end of region I ($x/X_r \approx 0.65$). The convection velocity for the fluctuations with $fH_c/U_U = 0.24$ decreased from $0.86U_U$ to $0.66U_U$ at this location. The fluctuations with other frequencies in the bound $0.15 \lesssim fH_c/U_U \lesssim 0.3$ are also convected at $U_c \approx 0.66U_U$.

The correlation coefficients between the fluctuating wall pressure and the fluctuating velocity at locations above the microphone for the jets with $H'_j/H_j = 0.18$ and $U'_o/U_o \approx 0.63$ are shown in Fig. 7.16. Here, the time scale was normalized using the thickness of the splitter plate, H_c . The time interval between the adjacent passing structures were similar to the offset jet with a co-flowing jet of $H'_j/H_j = 0.5$, further confirming that the length scale of these structures was the thickness of the splitter plate. The centers of these structures are at $y/H_j \approx 0.5$ that are closer to the wall than those in the jet with $H'_j/H_j = 0.5$ where it was $y/H_j \approx 0.9$. This might be one of the reasons that the structures affect the

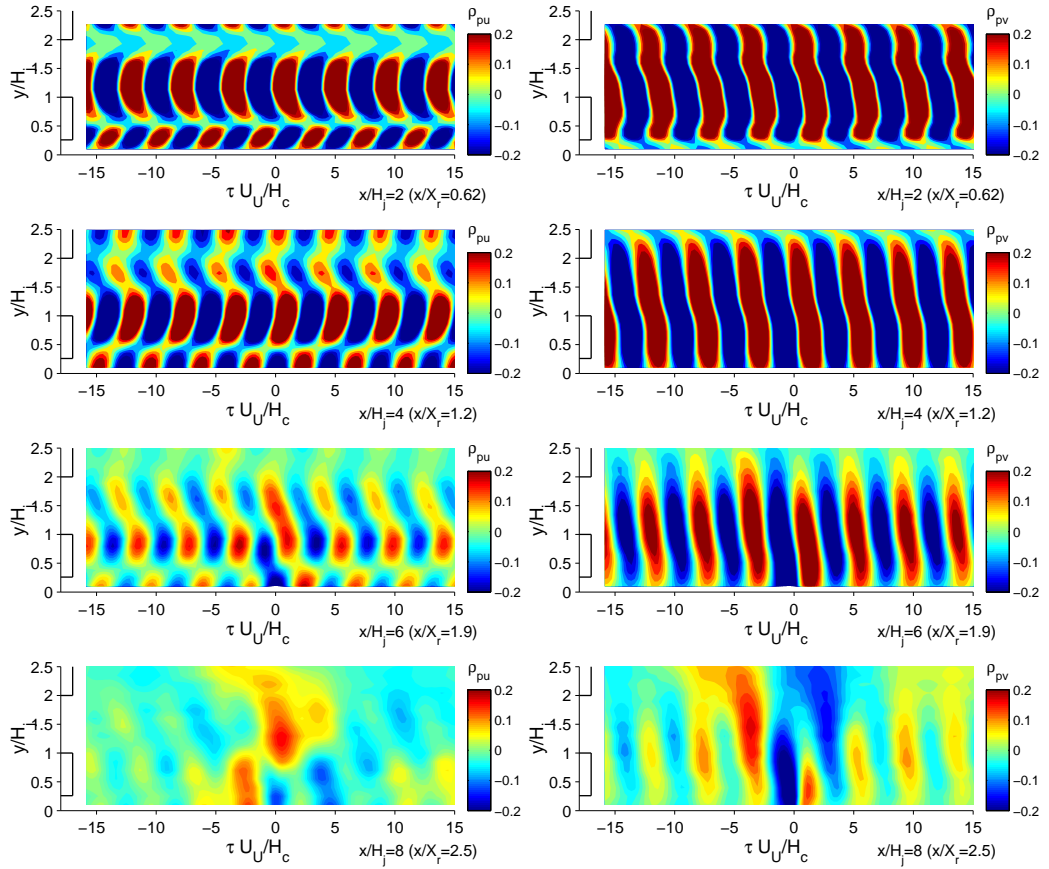


Figure 7.16: Correlation coefficients of fluctuating wall pressure and fluctuating velocities above the microphone, ρ_{pu} (left) and ρ_{pv} (right), measured at $x/H_j = 2, 4, 6$ and 8 for the offset jet with H_s/H_j a co-flowing jet of $H'_j/H_j = 0.18$ and velocity ratio of $U'_o/U_o \approx 0.63$.

wall much more in this case. Fluctuations with the same frequency formed in the outer part of the main jet. These fluctuations were coupled with the fluctuations in the wake with a phase difference. This appeared to propagate downstream at the same velocity. The correlations between the fluctuating wall pressure and velocities decreased as the flow evolved downstream indicating the diminishing of these structures.

The development of the flow structures was also shown in the correlation coefficient contours at different time intervals in Fig. 7.17. Periodic structures behind the splitter plate were more coherent than the case with $H'_j/H_j = 0.5$. There appeared to be two parts in the

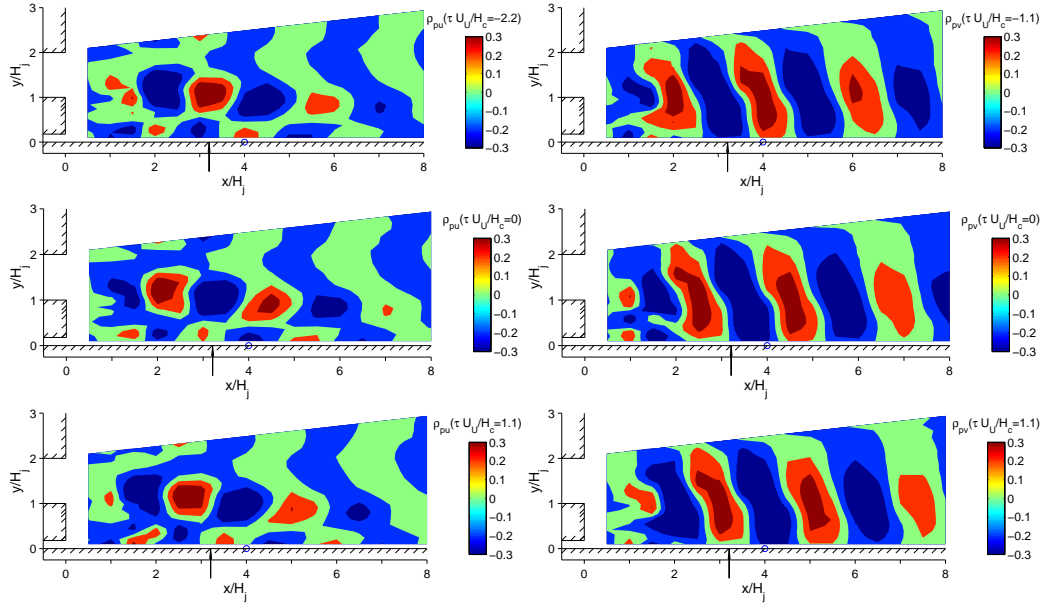


Figure 7.17: Correlation coefficients of fluctuating wall pressure at $x_1/H_j = 4$ and fluctuating velocities, (left) ρ_{pu} and (right) ρ_{pv} , at three different time delays for the offset jet with $H_s/H_j = 1.0$ and a co-flowing jet with $H'_j/H_j = 0.18$ and $U'_o/U_o \approx 0.63$.

flow. Wake like structures dominated the fluctuations in both parts of the flow. There was a phase difference in the vertical fluctuations in the inner and the outer part of the flow. The size of the inner part of the flow decreased gradually from approximately $2H_j$ near the jet exits to H_j at $x = 8H_j$, while the outer part grew at the same time. The phase difference in the vertical fluctuations seemed to decrease as the flow evolved downstream.

Chapter 8

Conclusions

An experimental study on the development of turbulent planar offset attaching jets was performed for jets with offset distance less than approximately 1.0 jet height and Reynolds numbers of 21 800 to 54 500. This includes measuring the flow field, static and fluctuating wall pressure, skin friction and heat transfer from the wall to the jet. The results showed that the development of the offset jet varied with offset distance in this range. For example, the normalized reattachment length (X_r/H_s) is approximately constant when the offset height is less than $0.3H_j$, and decreases gradually when offset height is increased further similar to jets with larger offset distances. The magnitude of the velocity and pressure fluctuations at the reattachment point increased as the offset distance increases. This is associated with a decrease in θ/H_s similar to other reattaching flows. The results here show this is due in part to the fact that the inner shear layer has a longer distance to develop before interacting with wall. The maximum heat transfer rate from the wall to the jet decreases when the offset distance increases (or θ/H_s decreases) suggesting the maximum heat transfer is not just related to the magnitude of the turbulent fluctuations. The change in Stanton number with Reynolds number also changed with offset height from $St \propto Re^{-0.36}$ for $H_s/H_j = 0.2$ to $St \propto Re^{-0.24}$ for $H_s/H_j = 1.0$, suggesting again there is a change in the development of the jet with offset height.

The results showed that the development of the jets can be divided into five regions, three defined by the reattachment process and two with the wall jet flow, as defined on section 4.1. The transition location between regions III and IV cannot be determined in terms of X_r or H_j but depends on H_s . Two-point and two-time correlation measurements show that flow structures change from those in the inner shear layer of the offset jet with characteristic frequencies of $fX_r/U_U \approx 0.6 - 1.2$ to the flow structures similar to those in a developed planar wall jet. The inner shear layer structures gradually merge with the wall jet like structures after attaching to the wall due to the difference in the convection velocity. The transition location shifts downstream when the offset distance (H_s) increases, likely caused by the changes in the magnitude of the fluctuations in the inner shear layer or the changes in the convection velocities of the flow structures. In the wall jet region, the skin friction coefficient is similar to the Stanton number suggesting the momentum and the heat transfer between the jet and the wall are driven by similar turbulent transport process.

The phase angles of the cross spectra of the fluctuating wall pressure or the cross spectra of the fluctuating wall pressure and velocities with the frequencies of $fX_r/U_U \approx 0.6$ to 1.2 change approximately linearly with the streamwise position near the reattachment point. These suggest that the wave length for the fluctuations associated with the reattaching flow are similar, resulting in different convection velocities for fluctuations with different frequencies. The convection velocity determined using phase angles of the cross spectra for fluctuating wall pressure (θ_{pp}) does not always agree with the convection velocity determined using the phase angles of the cross spectra for the fluctuating wall pressure and the fluctuating vertical velocity (θ_{pv}). For example, the convection velocities for fluctuations near the attachment location with frequencies of $0.25 \lesssim fX_r/U_U \lesssim 0.6$ determined using θ_{pp} are less than those determined using θ_{pv} . The convection velocity determined from the slope of the locus of the main positive peak in the cross correlation contour is only a measure of the propagation velocity of the fluctuations with frequencies larger than the

characteristic frequency of the dominant motion in the flow. The dominant motion propagates with a smaller propagation velocity. The results show that there is another periodic motion with very low frequency $fX_r/U_U \approx 0.06$ to 0.1 that is associated with a flapping motion. There appears to be two regions in the jet separated at the reattachment location and the vertical fluctuations in these two regions are approximately π out of phase. The frequencies of this flapping motion are similar to the characteristic frequencies of a flapping shear layer in other reattaching flows, *e.g.* flows over backward facing steps or bluff bodies. These low frequency motions are likely similar in nature. Measurements of the coherence and phase angle of the cross spectra between fluctuating wall pressure and velocities should be extended to these reattaching flows to confirm this argument.

The development of the offset attaching planar jets with a co-flowing jet was also studied. The results showed that both the mass and momentum flux of the inner jet and the height of the inner jet affected the development of the jet. When the momentum flux of the co-flowing jet added between the main jet and the wall was less than approximately 7% of the momentum of the main jet, the co-flowing jet separated from the wall and merged with the main jet instead of continuing to develop along the wall. The reattachment location moved downstream when the velocity of the co-flowing jet increased from 0 to approximately $0.2U_U$, while at the same time the static and fluctuating wall pressure and the heat transfer from the wall to the jets all decreased gradually.

The growth rates of the outer half jet width in the region away from the jet exit for the jets with $U'_o/U_o \leq 0.2$ were similar to the single offset jet while the growth rate for jets with $U'_o/U_o \geq 0.3$ were similar to the values observed in a free jet, suggesting that the development of the flow is not as affected by the interaction with the wall in these cases. The characteristic frequencies of all the flows at $x/H_j = 16$ in the wall jet region scaled with the outer half jet width, $fy_{+1/2}/U_U \approx 0.11$, indicating the fluctuations in all the flow are similar in the region away from the jet exits.

The measurements of the structures suggested that wake like structures with a characteristic frequency of $fH_c/U_U \approx 0.23$ are generated behind splitter plate when the velocity of the co-flowing jet with $U'_o > 0.2U_o$. The vertical fluctuating velocity increases dramatically and the reattachment location shifts closer to the exit due to the enhanced mixing. In the jets with $H'_j/H_j = 0.5$, the maximum in the fluctuating wall pressure and heat transfer associated with the reattaching process gradually decrease when the velocity of the inner jet is increased. This is different from the jets with $H'_j/H_j = 0.18$, where the maximum in the fluctuating wall pressure and heat transfer increase with the velocity of the inner jet. The frequencies of the wake like structures and inner shear layer structure seemed to coincide in the jets with $H'_j/H_j = 0.18$ and strong structures were generated and the fluctuating wall pressure and heat transfer were dramatically increased. The results indicate that the thickness and the shape of the splitter plate between the two jets are important in designing the air ring and can be used to modify the surface fluctuations or the heat transfer from the wall to the jet. Efforts were also taken to draw the conclusions from the parametric studies to reduce the systematic error. The estimated uncertainties in all the measurement are reasonably small and will not affect the conclusions.

The flow used in the current investigation captured many of the key features of the annular flow used in the blown film manufacturing process. For example, the wall pressure fluctuations in the reattachment region were dominated by the high frequency fluctuations associated with the large scale flow structures in the inner shear layer of the outer jet in both flows. Both flows then transitioned from a reattaching flow to a flow similar to a planar wall jet. These flow structures convected along the wall with a velocity of $U_c \approx 0.5U_U$ to $0.6U_U$ in the wall jet region. The development of the large scale flow structures in the actual cooling flow was also affected by other factors that were not simulated in the current investigations, such as the vibrations of the film. The characteristic frequencies of the dominant flow structures were 1 to 2 order of magnitude higher than those observed in the measurement of the film bubble instability (Pirkle & Braatz, 2003; Gao & Ewing, 2005).

Thus, it is not clear if the vibrations of the film have a significant direct effect on the flow structures because the disturbances have different time scales from the flow structures.

Chapter 9

Recommendations

The measurements of the offset planar attaching jet were focused on the cases with the offset distance less than $1.2H_j$ in the current investigation. Different motions were found in the flow, however, it will be useful to extend the measurements to higher offset distances to examine the interactions among these motions. For example, when the offset distance was approximately 3 to 4 jet heights, the characteristic frequency of the wall jet like structure may coincide with the frequency of the inner shear layer structures, and this could result in a flow that will behave differently.

Two-point and two-time measurements of the fluctuating wall pressure and velocities for the offset jet with a co-flowing jet in the region $x/H_j \leq 8$ revealed the emergence and growth of wake like structures. It will be useful to extend these measurements to the region $x/H_j > 8$ to examine the decay of these wake like structures and their effects on the evolution of the wall jet like structures.

The changes in the Reynolds stress terms ($\langle u^2 \rangle$, $\langle v^2 \rangle$ and $\langle uv \rangle$) in the offset jet with a co-flowing jet should be further examined by estimating the terms in the Reynolds average equations. Comparisons of the turbulence productions will be helpful to further understand the flows.

Linear stochastic estimation (Tung & Adrian, 1980) will be helpful to visualize the

flow fields. LSE provides estimates of the conditional averaged velocity that can be used to characterize the changes in the instantaneous fluctuating velocities from the instantaneous fluctuating wall pressure. This requires the correlations between the fluctuating wall pressure and velocities that were presented and discussed in Chapter 5 and 7. LSE provides a way of remotely estimating the flow field, particular in the regions where there are good correlations between the fluctuating velocities and wall pressure.

The recirculating flow was studied by measuring the wall pressure in the current investigation. The velocity in the recirculating region was not measured due to the limitation of the hot-wire anemometry. It will be useful to characterize the flow field directly using PIV or LDV to clarify the relationship between the fluctuations in the recirculation region and the wall jet region.

The three dimensional growth of the large scale structures in offset attaching planar jets with and without a co-flowing jet can be of significant importance in the development of the flow. The two-time and two-point measurements of wall pressure and velocity in the y-z plane have been taken at a number of streamwise locations for different jets. The data will be analyzed in the future.

Bibliography

- ABDALLA, I. & YANG, Z. 2005 Numerical study of a separated-reattached flow on a blunt plate. *AIAA Journal* **43**, 2465–2474.
- ADAMS, E. & JOHNSTON, J. 1988a Effects of the separating shear layer on the reattachment flow structure Part 1: Pressure and turbulence quantities. *Experiments in Fluids* **6**, 400–408.
- ADAMS, E. & JOHNSTON, J. 1988b Effects of the separating shear layer on the reattachment flow structure Part 2: Reattachment length and wall shear stress. *Experiments in Fluids* **6**, 493–499.
- BAUGHN, J., HOFFMAN, M., TAKAHASHI, R. & LAUNDER, B. 1984 Local heat transfer downstream of an abrupt expansion in a circular channel with constant wall heat flux. *Journal of Heat Transfer* **106**, 789–796.
- BAUGHN, J., HOFFMAN, M., TAKAHASHI, R. & LEE, D. 1987 Heat transfer downstream of an abrupt expansion in the transition Reynolds number regime. *Journal of Heat Transfer* **109**, 37–42.
- BERKOOZ, G., HOLMES, P. & LUMLEY, J. 1993 The proper orthogonal decomposition in the analysis of turbulent flows. *Annual Review of Fluid Mechanics* **25**, 539–575.
- BEUTHER, P. 1980 Experimental investigation of the axisymmetric turbulent buoyant plume. PhD Thesis, The State University of New York at Buffalo, Buffalo, NY.

- BHATTACHARJEE, S., SCHEELKE, B. & TROUTT, T. 1986 Modification of vortex interactions in a reattaching separated flow. *AIAA Journal* **24**, 623–629.
- BOURQUE, C. 1967 Reattachment of a two-dimensional jet to an adjacent flat plate. *Advances in Fluidics, F.T. Brown (Eds.), ASME Press, NY*.
- BOURQUE, C. & NEWMAN, B. 1960 Reattachment of a two-dimensional jet to an adjacent flat plate. *Aeronautical Quarterly* **11**, 201–232.
- BRADSHAW, P. & WONG, F. 1972 The reattachment and relaxation of a turbulent shear layer. *Journal of Fluid Mechanics* **52**, 113–135.
- BREDBERG, J., PENG, S. & DAVIDSON, L. 2002 An improved $k-\omega$ turbulence model applied to recirculating flows. *International Journal of Heat and Fluid Flow* **23**, 731–743.
- BREMHORST, K. & AGNEW, N. 1999 Surface heat transfer and flow structures of steady and fully pulsed radial reattaching jets. *International Journal of Heat and Fluid Flow* **20**, 280–289.
- BROWN, J. & NAUGHTON, J. 1999 The thin-oil-film equation. *Technical Report NASA/TM 1999-208767, NASA-Ames Research Center*.
- BRUUN, H. 1995 *Hot-wire Anemometry*. Oxford: Oxford University Press.
- CASTRO, I. & HAQUE, A. 1987 The structure of a turbulent shear layer bounding a separation region. *Journal of Fluid Mechanics* **179**, 439–468.
- CATTAFESTA, L., WILLIAMS, D., ROWLEY, C. & ALVID, F. 2003 Review of active control of flow-induced cavity resonance. *AIAA paper 2003-3567*.
- CHAMPAGNE, H. & SLEICHER, C. 1967 Turbulence measurements with inclined hotwires. part 2: Hot-wire response equation. *Journal of Fluid Mechanics* **28**, 177–182.

- CHAMPAGNE, H., SLEICHER, C. & WEHRMANN, O. 1967 Turbulence measurements with inclined hot-wires. part 1: Heat transfer experiments with inclined hot-wire. *Journal of Fluid Mechanics* **28**, 153–176.
- CHANDRSUDA, C. & BRADSHAW, P. 1981 Turbulent structure of a reattaching mixing layer. *Journal of Fluid Mechanics* **110**, 171–194.
- CHERRY, N., HILLIER, R. & LATOUR, M. 1984 Unsteady measurements in a separated and reattaching flow. *Journal of Fluid Mechanics* **144**, 13–46.
- CHUN, K. & SUNG, H. 1996 Control of turbulent separated flow over backward-facing step by local forcing. *Experiments in Fluids* **21**, 417–426.
- CHUN, K. & SUNG, H. 1998 Visualisation of a locally-forced separated flow over a backward-facing step. *Experiments in Fluids* **25**, 133–142.
- CHUN, S. & SUNG, H. 2003 Large-scale vortical structure of turbulent separation bubble affected by unsteady wake. *Experiments in Fluids* **34**, 572–584.
- COLEMAN, H. & STEELE, W. 1998 *Experimentation and Uncertainty Analysis for Engineers*, second ed.. New York, NY: John Wiley & Sons.
- CRAFT, T. 1998 Developments in a low-Reynolds-number second-moment closure and its application to separating and reattaching flows. *International Journal of Heat and Fluid Flow* **19**, 541–548.
- DAVIS, J. 1996 *Carbon and Alloy Steels*. ASM International.
- DEJOAN, A. & LESCHZINER, M. 2004 Large eddy simulation of periodically perturbed separated flow over a backward-facing step. *International Journal of Heat and Fluid Flow* **25**, 581–592.

- DRIVER, D. & SEEGMILLER, H. 1985 Features of a reattaching turbulent shear layer in divergent channel flow. *AIAA Journal* **23**, 163–171.
- DRIVER, D., SEEGMILLER, H. & MARVIN, J. 1987 Time-dependent behavior of a reattaching shear layer. *AIAA Journal* **25**, 914–919.
- EATON, J. & JOHNSON, J. 1981 A review of research on subsonic turbulent flow reattachment. *AIAA Journal* **19**, 1093–1100.
- FARABEE, T. & CASARELLA, M. 1986 Measurements of fluctuating wall pressure for separated/reattached boundary layer flows. *ASME Journal Vibration, Acoustics, Stress, Reliability Design* **108**, 301–307.
- FORLITI, D. & STRYKOWSKI, P. 2005 Controlling turbulence in a rearward-facing step combustor using countercurrent shear. *Journal of Fluids Engineering* **127**, 438–448.
- GAD-EL-HAK, M. 1996 Modern developments in flow control. *Applied Mechanics Reviews* **49**, 365–379.
- GAD-EL-HAK, M. & BUSHNELL, D. 1991 Separation control: Review. *Journal of Fluids Engineering* **113**, 5–30.
- GAO, N. & EWING, D. 2005 Investigation of the large-scale flow structures in the cooling jets used in the blown film manufacturing process. *Journal of Fluids Engineering* **127**, 978–985.
- GAO, N. & EWING, D. 2006 Investigation of the effect of confinement on the heat transfer to round impinging jets exiting a long pipe. *International Journal of Heat and Fluid Flow* **27**, 33–41.
- GAO, N., LI, S. & EWING, D. 2005 Investigation of cooling jets used in blown film manufacturing process. *International Polymer Processing* **20**, 68–77.

- GAO, N., SUN, H. & EWING, D. 2003 Heat transfer to impinging round jets with triangular tabs. *International Journal of Heat and Mass Transfer* **46**, 2557–2569.
- GARRISON, T. & ACKMAN, M. 1998 Development of a global interferometer skin-friction meter. *AIAA Journal* **36** (1), 62–68.
- GEORGE, W., BEUTHER, P. & LUMLEY, J. 1978 Processing of random signals. *Proc. Dynamic Flow Conf. Marseille* pp. 757–799.
- GHANEH-FARD, A., CARREAU, P. & LAFLEUR, P. 1996 Study of instabilities in film blowing. *AIChE Journal* **42**, 1388–1396.
- GHANEH-FARD, A., CARREAU, P. & LAFLEUR, P. 1997 Study of kinematics and dynamics of film blowing of different film blowing of different polyethylenes. *Polymer Engineering Science* **37**, 1148–1163.
- GLAUSER, M. 1987 Coherent structures in the axisymmetric turbulent jet mixing layer. PhD Thesis, The State University of New York at Buffalo, Buffalo, NY.
- GLAUSER, M. & GEORGE, W. 1992 Application of multipoint measurements for flow characterization. *Experimental Thermal and Fluid Science* **5**, 617–632.
- GLAUSER, M., LEIB, S. & GEORGE, W. 1987 Coherent structures in the axisymmetric jet mixing layer. In *Turbulent Shear Flows 5* (ed. Durst), pp. 134–145. Springer-Verlag.
- HALL, J. 2005 The role of the large-scale structures in the development of turbulent wall jets. PhD Thesis, McMaster University, Hamilton, Canada.
- HASAN, M. 1992 The flow over a backward-facing step under controlled perturbation: laminar separation. *Journal of Fluid Mechanics* **238**, 73–96.

- HASAN, M. & KHAN, A. 1992 On the instability characteristics of a reattaching shear layer with nonlaminar separation. *International Journal of Heat and Fluid Flow* **13**, 224–231.
- HEENAN, A. & MORRISON, J. 1998 Passive control of pressure fluctuations generated by separated flow. *AIAA Journal* **36**, 1014–1022.
- HOCH, J. & JIJI, M. 1981 Two-dimensional turbulent offset jet boundary interaction. *Journal of Fluids Engineering* **103**, 154–161.
- HUDY, L., NAGUIB, A. & HUMPHREYS, W. 2003 Wall-pressure-array measurements beneath a separating/reattaching flow region. *Physics of Fluids* **15**, 706–717.
- INAOKA, K., NAKAMURA, K. & SENDA, M. 2004 Heat transfer control of a backward-facing step flow in a duct by means of miniature electromagnetic actuators. *International Journal of Heat and Fluid Flow* **25**, 711–720.
- JOVIC, S. & DRIVER, D. 1995 Reynolds number effects on the skin friction in separated flows behind a backward facing step. *Experiments in Fluids* **18**, 464–467.
- KASAGI, N. & MATSUNAGA, A. 1995 Three-dimensional particle-tracking velocimetry measurement of turbulence statistics and energy budget in a backward-facing step flow. *International Journal of Fluid and Heat Flow* **16**, 477–485.
- KIM, D., YOON, S., LEE, D. & KIM, K. 1996 Flow and heat transfer measurements of a wall attaching offset jet. *International Journal of Heat and Mass Transfer* **39**, 2907–2913.
- KIM, H. & LEE, S. 2002 The structure of turbulent shear flow around a two-dimensional porous fence having a bottom gap. *Journal of Fluids and Structures* **16**, 317–329.

- KIYA, M. & SASAKI, K. 1983 Structure of a turbulent separation bubble. *Journal of Fluid Mechanics* **137**, 83–113.
- KIYA, M. & SASAKI, K. 1985 Structure of large-scale vortices and unsteady reverse flow in the reattaching zone of a turbulent separation bubble. *Journal of Fluid Mechanics* **154**, 463–491.
- KIYA, M., SHIMIZU, M. & MOCHIZUKI, O. 1997 Sinusoidal forcing of a turbulent separation bubble. *Journal of Fluid Mechanics* **342**, 119–139.
- LE, H., MOIN, P. & KIM, J. 1997 Direct numerical simulation of turbulent flow over a backward-facing step. *Journal of Fluid Mechanics* **330**, 349–374.
- LEE, I. & SUNG, J. 2001 Characteristics of wall pressure fluctuations in separated and reattaching flows over a backward-facing step, Part 1: time-mean statistics and cross spectral analyses. *Experiments in Fluids* **30**, 262–272.
- LEE, I. & SUNG, J. 2002 Multiple-arrayed pressure measurement for investigation of the unsteady flow structure of a reattaching shear layer. *Journal of Fluid Mechanics* **463**, 377–402.
- LI, S., GAO, N. & EWING, D. 2005 Experimental investigation of effect of the bubble cone on the cooling jets used in the blow film manufacturing process. *International Polymer Processing* **20**, 432–440.
- LI, Y. & NAGUIB, A. 2003 An oscillating hot-wire technique for resolving the magnitude and direction of velocity measurements using single hot-wire sensors. *Experiments in Fluids* **34**, 597–606.
- LIU, T., CATTAFESTA, L. & RADETSKY, R. 2000 Photogrammetry applied to wind tunnel testing. *AIAA Journal* **38** (6), 964–971.

- LUND, T. 1986 Augmented thrust and mass flow associated with two-dimensional jet reattachment. *AIAA Journal* **24**, 1964–1970.
- MANCEAU, R., PARNEIX, S. & LAURENCE, D. 2000 Turbulent heat transfer predictions using the v^2 -f model on unstructured meshes. *International Journal of Heat and Fluid Flow* **21**, 320–328.
- MI, J., NOBES, D. & NATHAN, G. 2001 Mixing characteristics of axisymmetric free jets issuing from a contoured nozzle, an orifice plate and a pipe. *Journal of Fluids Engineering* **123**, 878–883.
- NASR, A. & LAI, J. 1997 Comparison of flow characteristics in the near field of two parallel plane jets and an offset plane jet. *Physics of Fluids* **9**, 2919–2931.
- NASR, A. & LAI, J. 1998 A turbulent plane offset jet with small offset ratio. *Experiments in Fluids* **24**, 47–57.
- NAUGHTON, J. 2005 *Personal communications*.
- NAUGHTON, J., ROBINSON, J. & DURGESH, V. 2003 Oil-film interferometry measurement of skin friction - analysis summary and description of matlab program. In *ICIASF 2003 Record, 20th International Congress on Instrumentation in Aerospace Simulation Facilities*, pp. 169–178. IEEE-03CH37501, IEEE.
- NAUGHTON, J. & SHEPLAK, M. 2002 Modern developments in shear stress measurement. *Progress in Aerospace Science* **38**, 515–570.
- NAUGHTON, J., VIKEN, S. & GREENBLATT, D. 2006 Skin friction measurements on the NASA hump model. *AIAA Journal* **44**, 1255–1265.
- NOZAKI, T., HATTA, K., NAKASHIMA, M. & MATSUMURA, H. 1979 Reattachment flow issuing from a finite width nozzle. *Bulletin of JSME* **22**, 340–347.

- NOZAKI, T., HATTA, K., SATO, N. & MATSUMURA, H. 1981 Reattachment flow issuing from a finite width nozzle, Report 2: Effect of initial turbulence intensity. *Bulletin of JSME* **24**, 363–369.
- PANASONIC 2006 www.panasonic.com/industrial/components/pdf/em06_wm61_a_b_dne.pdf. Omnidirectional Back Electret Condenser Microphone Cartridge Series WM-61A and WM-61B, Panasonic Corporations.
- PELFREY, J. & LIBURDY, J. 1986 Mean flow characteristics of a turbulent offset jet. *Journal of Fluids Engineering* **108**, 82–88.
- PERRY, A. 1982 *Hot-wire Anemometry*. Oxford: Clarendon Press.
- PIRKLE, J. & BRAATZ, R. 2003 Dynamic modeling of blown-film extrusion. *Polymer Engineering and Science* **43**, 398–418.
- RHEE, G. & SUNG, H. 2000 Numerical prediction of locally forced turbulent separated and reattaching. *Fluid Dynamics Research* **26**, 421–436.
- ROOS, F. & KEGELMAN, J. 1986 Control of coherent structures in reattaching laminar and turbulent shear layers. *AIAA Journal* **24**, 1956–1963.
- ROSHKO, A. 1954 Turbulent wakes from vortex streets. *NACA Report 1191*.
- ROWLEY, C. & WILLIAMS, D. 2006 Dynamics and control of high-Reynolds-number flow over open cavities. *Annual Review of Fluid Mechanics* **38**, 251–276.
- RUDERICH, R. & FERNGOLZ, H. 1986 An experimental investigation of a turbulent shear flow with separation, reverse flow, and reattachment. *Journal of Fluid Mechanics* **163**, 283–322.
- SAATHOFF, P. & MELBOURNE, W. 1997 Effects of free-stream turbulence on surface pressure fluctuations in a separation bubble. *Journal of Fluid Mechanics* **337**, 1–24.

- SAROHIA, V. & MASSIER, P. 1977 Control of cavity noise. *Journal of Aircraft* **14**, 833–837.
- SAWYER, R. 1960 The flow due to a two-dimensional jet issuing parallel to a flat plate. *Journal of Fluid Mechanics* **9**, 543–560.
- SAWYER, R. 1963 Two-dimensional reattachment jet flows including the effect of curvature on entrainment. *Journal of Fluid Mechanics* **17**, 481–498.
- SCARANO, F., BENOCCI, C. & RIETHMULLER, M. L. 1999 Pattern recognition analysis of the turbulent flow past a backward facing step. *Physics of Fluids* **11**, 3808–3818.
- SEIFERT, A., DARABI, A. & WYGNANSKI, I. 1996 Delay of airfoil stall by periodic excitation. *Journal of Aircraft* **33**, 691–698.
- SHABBIR, A., BEUTHER, P. & GEORGE, W. 1996 X-wire response in turbulent flows of high-intensity turbulence and low mean velocities. *Experimental Thermal and Fluid Science* **12**, 52–56.
- SIDIROPOULOS, V. 2000 The Effect of Air Cooling on the Film Blowing Process. PhD Thesis, McMaster University, Hamilton, Canada.
- SIDIROPOULOS, V. & VLACHOPOULOS, J. 2000 The effects of dual-orifice air-ring design on blown film cooling. *Polymer Engineering Science* **40**, 1611–1618.
- SIGURDSON, L. 1995 The structure and control of a turbulent reattaching flow. *Journal of Fluid Mechanics* **298**, 139–165.
- SIMPSON, R. 1989 Turbulent boundary-layer separation. *Annual Review of Fluid Mechanics* **21**, 205–232.
- SMITS, A. 1987 A visual study of separation bubble. In *Flow visualization II* (ed. W. Merzkirch), pp. 247–251. Washington DC: Hemisphere.

- SONG, H., YOON, S. & LEE, D. 2000 Flow and heat transfer characteristics of a two-dimensional oblique wall attaching offset jet. *International Journal of Heat and Mass Transfer* **43**, 2395–2404.
- SPAZZINI, P., IUSO, G., ONORATO, M., ZURLO, N. & DI-CICCA, G. 2001 Unsteady behavior of back-facing step flow. *Experiments in Fluids* **30**, 551–561.
- SUKSANGPANOMRUNG, A., DJILALI, N. & MOINAT, P. 2000 Large-eddy simulation of separated over a blunt rectangular plate. *International Journal of Heat and Fluid Flow* **21**, 655–663.
- SUN, H. 2002 The development of three-dimensional wall jet. PhD Thesis, McMaster University, Hamilton, Canada.
- TANAKA, T. & TANAKA, E. 1978a Experimental studies of a radial turbulent jet(3rd report: Flow before an attachment point of attaching jet flow). *Bulletin of JSME* **21**, 665–672.
- TANAKA, T. & TANAKA, E. 1978b Experimental studies of a radial turbulent jet(4th report, flow at and after an attaching point of attaching jet flow). *Bulletin of JSME* **21**, 1349–1356.
- TANAKA, T. & TANAKA, E. 1981 Experimental studies of a radial turbulent jet(5th report, attaching jet flow from a inclined nozzle on an adjacent offset disc plate). *Bulletin of JSME* **24**, 82–88.
- TANAKA, T., TANAKA, E. & INQUE, Y. 1986a Study on control of radial attaching jet flow (3rd report, flow before reattachment point). *Bulletin of JSME* **29**, 2482–2486.
- TANAKA, T., TANAKA, E. & NAGAI, K. 1986b Study on control of radial attaching jet flow (1st report, effect of control flow on main jet flow near a nozzle). *Bulletin of JSME* **29**, 1135–1140.

- TANAKA, T., TANAKA, E. & NAGAYA, S. 1986c Study on control of radial attaching jet flow (2nd report, effect of control flow on pressure distributions). *Bulletin of JSME* **29**, 2049–2054.
- TIHON, J., LEGRAND, J. & LEGENTILHOMME, P. 2001 Near-wall investigation of backward-facing step flows. *Experiments in Fluids* **31**, 484–493.
- TUNG, T. & ADRIAN, R. 1980 Higher-order estimates of conditional eddies in isotropic turbulence. *Physics of Fluids* **23**, 1469–1470.
- TUTU, N. & CHEVARY, R. 1975 Cross-wire anemometry in high intensity turbulence. *Journal of Fluid Mechanics* **71**, 785–800.
- VAKILI, A. & GAUTHIER, C. 1994 Control of cavity flow by upstream mass-injection. *Journal of Aircraft* **31**, 169–174.
- VOGEL, J. & EATON, J. 1985 Combined heat transfer and fluid dynamic measurements downstream of a backward-facing step. *Journal of Heat Transfer* **107**, 922–929.
- WEE, D., YI, T., ANNASWAMY, A. & GHONIEM, A. 2004 Self-sustained oscillations and vortex shedding in backward-facing step flows: Simulations and linear instability analysis. *Physics of Fluids* **16**, 3361–3373.
- WU, J., LU, X., DENNY, A., FAN, M. & WU, J. 1998 Post-stall flow control on an airfoil by local unsteady forcing. *Journal of Fluid Mechanics* **371**, 21–58.
- YOSHIOKA, S., OBI, S. & MASUDA, S. 2001a Organized vortex motion in periodically perturbed turbulent separated flow over a backward-facing step. *International Journal of Heat and Fluid Flow* **22**, 301–307.
- YOSHIOKA, S., OBI, S. & MASUDA, S. 2001b Turbulence statistics of periodically perturbed separated flow over backward-facing step. *International Journal of Heat and Fluid Flow* **22**, 393–401.

- ZAMAN, K. 1992 Effect of acoustic excitation on stalled flows over an airfoil. *AIAA Journal* **30**, 1492–1499.

Appendix A: Velocity profiles of the offset and free jets

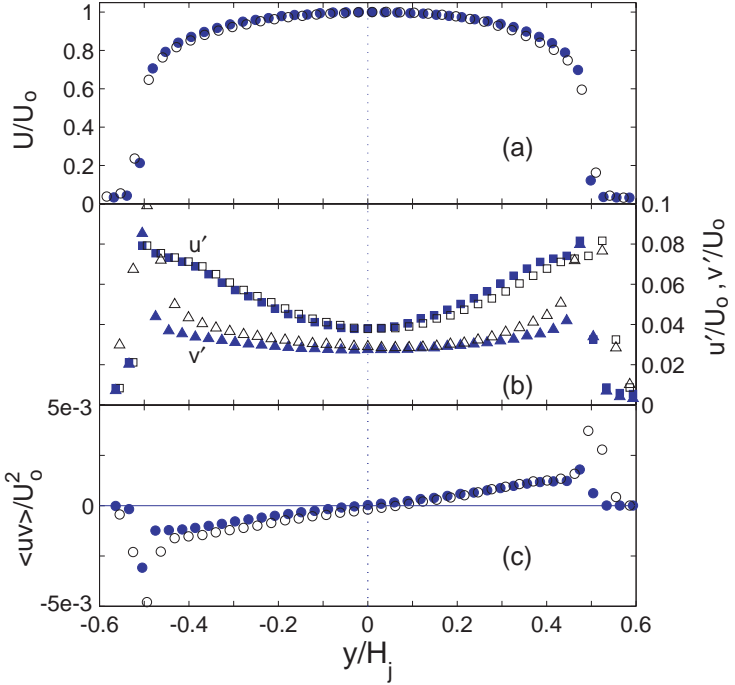


Figure A-1: Distributions of (a) the mean streamwise velocity (b) the fluctuating velocity and (c) the Reynolds shear stress for a planar free jet at $x \approx 0.05H_j$ measured using the jet with $H_j = 0.38\text{cm}$ (solid symbols) and the jet with $H_j = 0.19\text{cm}$ (open symbols), U_o represents the maximum streamwise velocity.

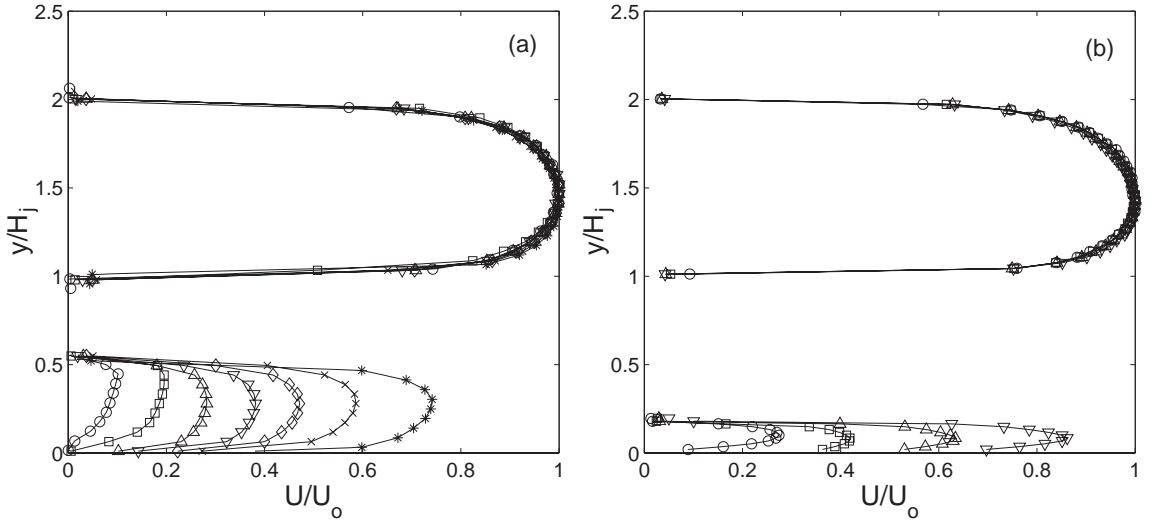


Figure A-2: Profiles of the mean velocity measured using a single hot-wire at $x \approx 0.05H_j$ for an offset attaching planar jet with $H_s/H_j = 1$ and (a) $H'_j/H_j = 0.5$ with $U'_o/U_o = \bigcirc 0.1, \square 0.2, \triangle 0.28, \nabla 0.38, \diamond 0.47, \times 0.59, *$ 0.74, and (b) $H'_j/H_j = 0.18$ with $U'_o/U_o = \bigcirc 0.27, \square 0.42, \triangle 0.63, \nabla 0.86$.

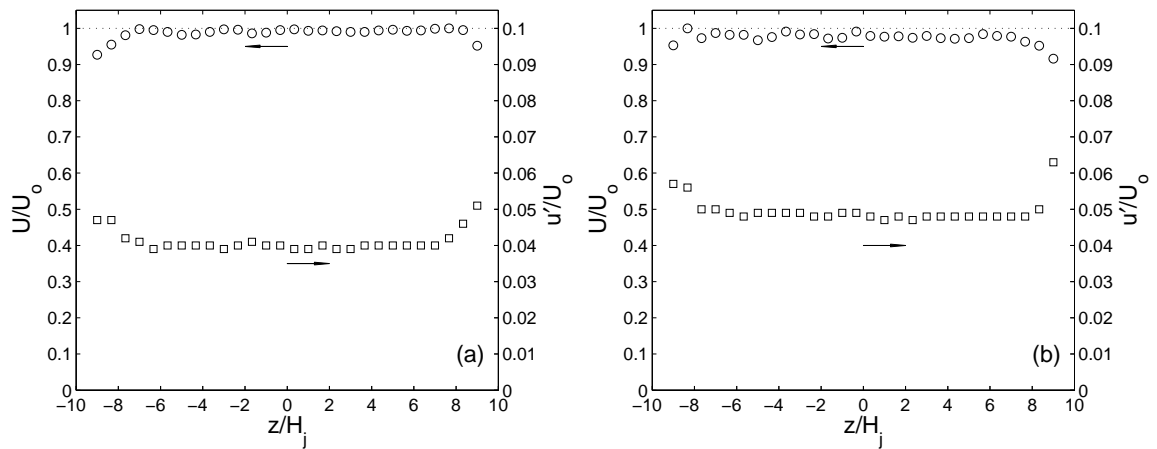


Figure A-3: Profile of mean and fluctuating streamwise velocity for a free jet along centerline of the jet, $y = H_j/2$, at the jet exit for $Re \approx 44\,000$.

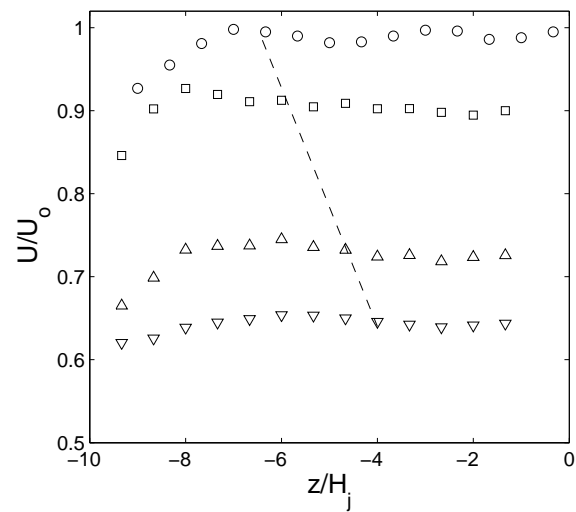


Figure A-4: Profile of mean streamwise velocity for a planar free jet along centerline of the jet, $y = H_j/2$, at $x/H_j = \circ 0, \square 6, \triangle 12, \nabla 18$ for $Re \approx 44\,000$.

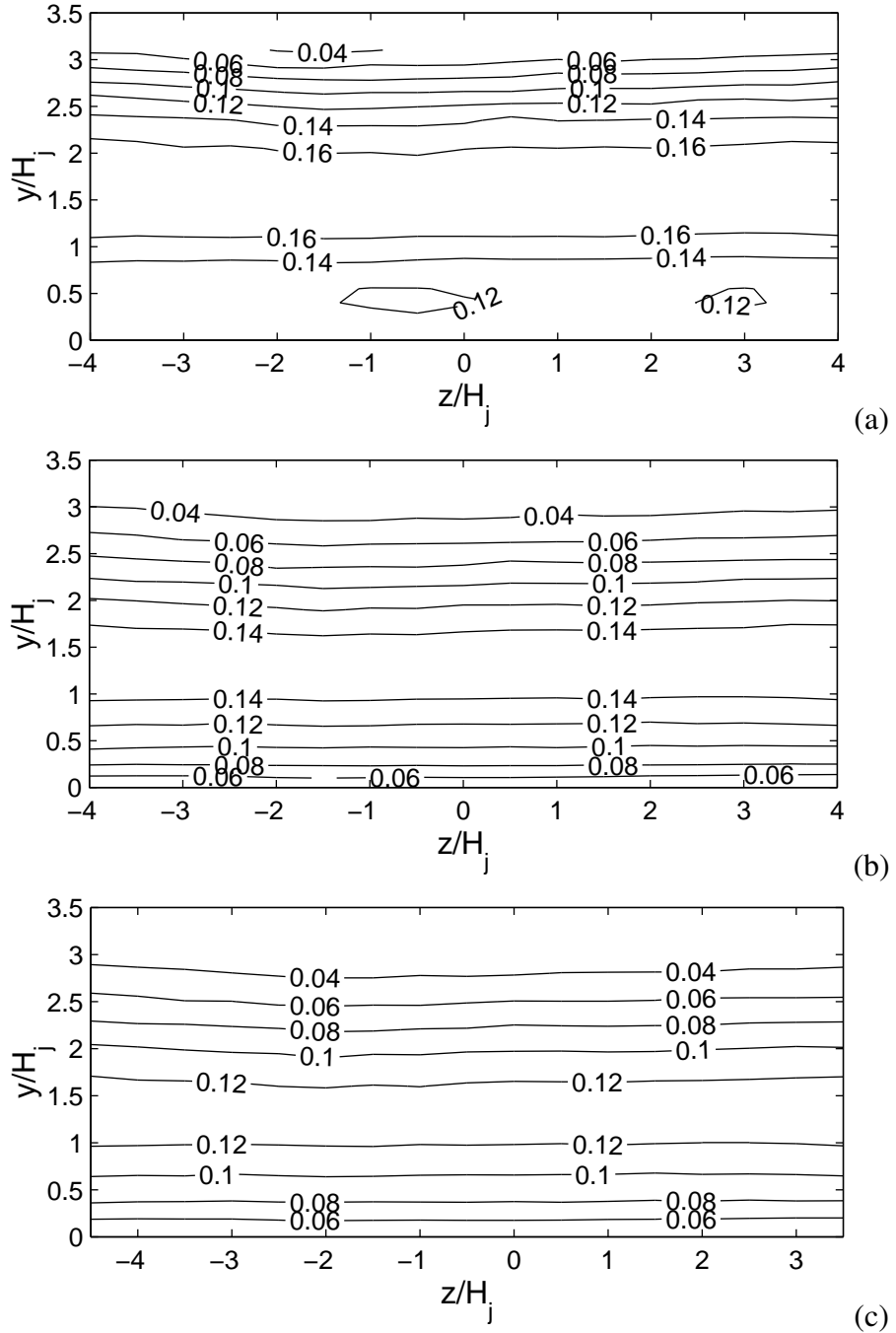


Figure A-5: Contours of fluctuating velocities (a) u'/U_{max} , (b) v'/U_{max} and (c) w'/U_{max} for an offset attaching jet with $H_s/H_j = 1$ at $x/H_j = 12$ for $Re \approx 44\,000$.

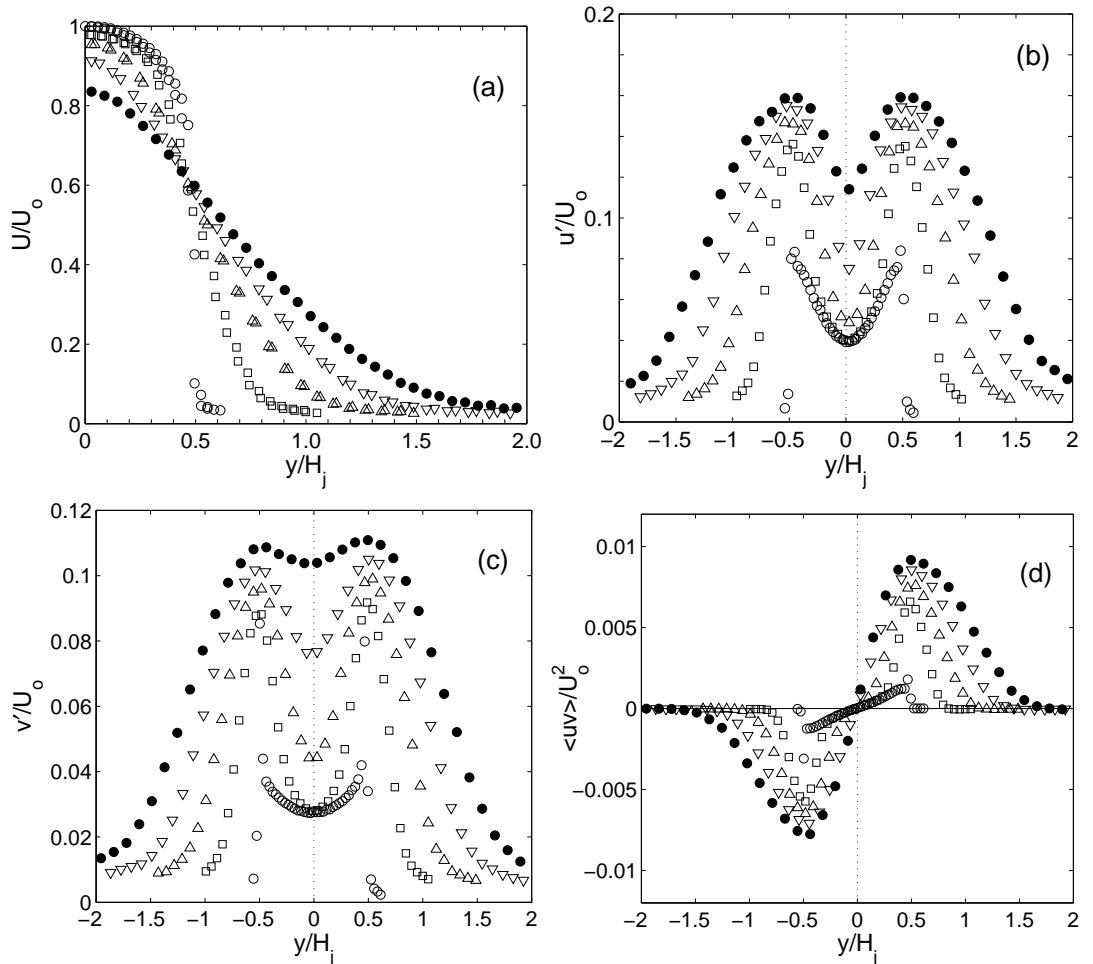


Figure A-6: Profiles of the mean streamwise velocity and turbulent stresses of a planar free jet measured using the jet with $H_j = 0.38\text{cm}$ at $x/H_j = \circ 0, \square 2, \triangle 4, \nabla 6, \bullet 8$ for $Re \approx 44000$.

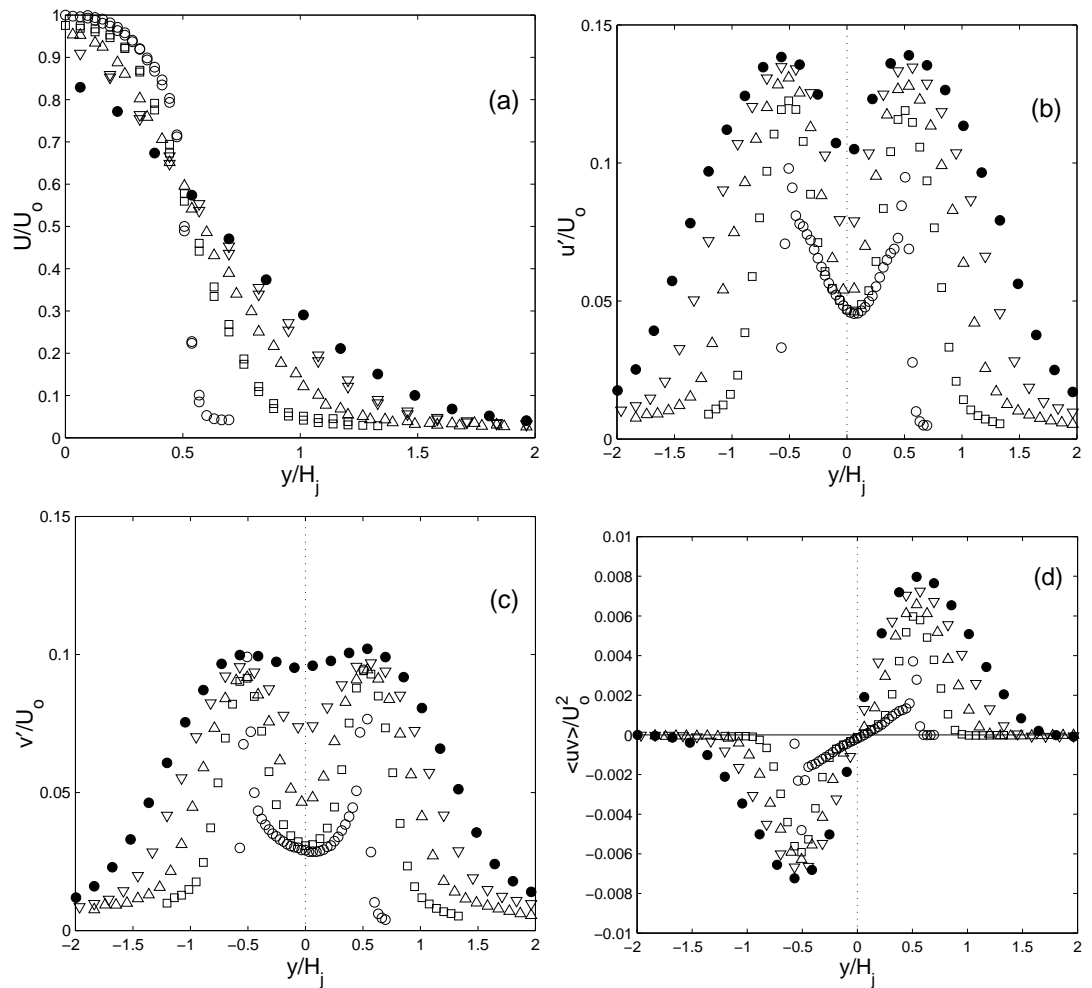


Figure A-7: Profiles of the mean streamwise velocity and turbulent stresses of a planar free jet measured using the jet with $H_j = 0.19\text{cm}$ at $x/H_j = \circ 0, \square 2, \triangle 4, \nabla 6, \bullet 8$ for $Re \approx 44000$.

Appendix B: Heat flux losses

The heat balance for the foil shown in Fig. B-1 can be written as

$$\dot{q}_{elec}wdx = \dot{q}_{conv}wdx + \dot{q}_{rad}wdx + \dot{q}_{cond}wdx + \dot{q}_{lat}hw, \quad (\text{B-1})$$

where h is the thickness of the foil, w is the width of the foil, the \dot{q}_{elec} is the total Joulean heat flux, \dot{q}_{conv} is the heat flux removed by convective heat transfer, \dot{q}_{los} is the heat loss through the bottom of the foil and \dot{q}_{cond} is the lateral conduction heat loss within the foil due to the temperature gradient given by

$$\dot{q}_{cond} = k \frac{dT}{dx}. \quad (\text{B-2})$$

Dividing equation B-1 by wdx yield

$$\frac{\dot{q}_{conv}}{\dot{q}_{elec}} + \frac{\dot{q}_{rad}}{\dot{q}_{elec}} + \frac{\dot{q}_{los}}{\dot{q}_{elec}} + k \frac{d}{dx} \left(\frac{dT}{dx} \right) \frac{h}{\dot{q}_{elec}} = 1, \quad (\text{B-3})$$

The radiation from the upper surface to the room can be evaluated using

$$\dot{q}_{rad} = \varepsilon \sigma (T_w^4 - T_\infty^4). \quad (\text{B-4})$$

The emissivity, ε , of the top surface is approximately 0.96 (Gao *et al.*, 2003; Gao & Ewing, 2006). The bottom heat loss was estimated by estimating the heat transfer out of the bottom of the cavity, given by

$$\dot{q}_{los} = k_a \frac{T_b - T_\infty}{D} + \varepsilon_b \sigma (T_b^4 - T_\infty^4), \quad (\text{B-5})$$

where $D = 3cm$ was the depth of the air gap, and T_b was the temperature of the bottom surface of the plexiglas plate measured using a thermocouple. The bottom of the plexiglass plate was covered with paper so the emissivity, ε_b , was approximately 1. T_b was higher than the room temperature but the difference was less than $5^\circ C$ in all cases.

The last three terms on the left of the equation evaluated for a typical case of an offset attaching jet is shown in Fig. B-2. The lateral conduction was evaluated using a central difference scheme at every pixel corresponding to dx of $1.1mm$.

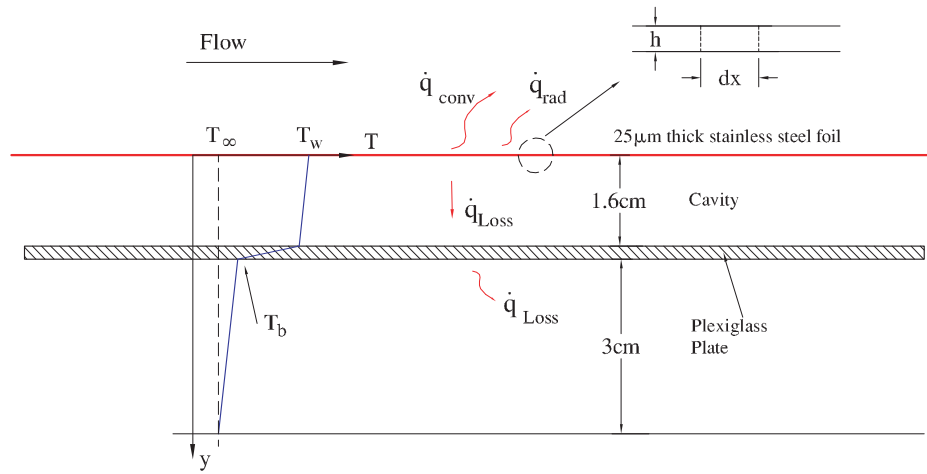


Figure B-1: Illustration of the heat losses.

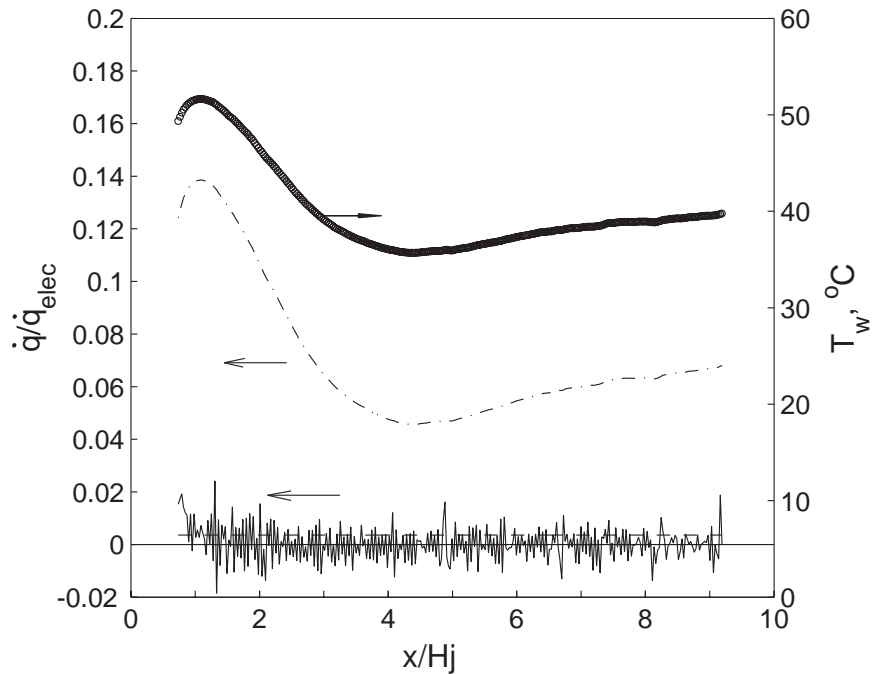


Figure B-2: Distribution of wall temperature for a typical offset jet with $H_s/H_j = 1$ and $Re = 44000$ and the estimated radiation heat loss from the top of the wall, —— heat loss through bottom air gap ($T_b = T_\infty + 5^\circ C$) and — lateral conduction within the foil.

Appendix C: Uncertainties in Stanton number

The uncertainty of the reported Stanton number was estimated following approach outlined by Coleman & Steele (1998). The uncertainty of measurement results was the square root of the summation of the square of the systematic errors and the random errors. When an experimental result, r , is a function of J measured variable X_i ,

$$r = r(X_1, X_2, \dots, X_J), \quad (\text{C-1})$$

the uncertainty in the results is given by

$$\xi_r^2 = \left(\frac{\partial r}{\partial X_1} \right)^2 \xi_{X_1}^2 + \left(\frac{\partial r}{\partial X_2} \right)^2 \xi_{X_2}^2 + \dots + \left(\frac{\partial r}{\partial X_J} \right)^2 \xi_{X_J}^2, \quad (\text{C-2})$$

where ξ_{X_i} is the uncertainty of the experimental variable X_i . For the Stanton number

$$St = \frac{q_{conv}}{(T_w - T_j)\rho c_p U_U}, \quad (\text{C-3})$$

$$\left(\frac{\xi_{St}}{St} \right)^2 = \left(\frac{\xi_{U_U}}{U_U} \right)^2 + \left(\frac{\xi_{(T_w - T_j)}}{T_w - T_j} \right)^2 + \left(\frac{\xi_{\dot{q}_{conv}}}{\dot{q}_{conv}} \right)^2. \quad (\text{C-4})$$

The uncertainty in the mean velocity at the jet exit, ξ_{U_U}/U_U , was 3% for 95% confidence interval, discussed in Chapter 3. The top of the foil was coated with candle-soot black paint.

In order to reduce the systematic error in the measurements, a calibration experiment was performed to determine the emissivity of the painted foil by measuring a painted isothermal surface with the infrared camera and a thermocouple with the Fluke thermometer for a series of temperatures from 50° to 80° . The temperatures measured by the infrared camera were adjusted by changing the emissivity of the painted surface to match the results from the thermometer. The emissivity of the painted surface was found to be $\varepsilon \approx 0.96 \pm 0.01$. This process also effectively calibrated the infrared camera against the thermometer and the majority of the systemic error in $T_w - T_j$ cancelled out. The systemic error in $T_w - T_j$ was estimated to be less than $0.2^\circ C$.

The random errors in T_w and T_j are $\pm 0.25^\circ C$ and $\pm 0.1^\circ C$, respectively. The total error in $T_w - T_j$ was thus less than $0.4^\circ C$. The minimum temperature difference, $T_w - T_j$, was approximately $10^\circ C$ at the reattachment region, so the uncertainty in the temperature measurements, $\xi_{(T_w - T_j)} / (T_w - T_j)$, was less than 4% for 95% confidence interval.

The random error of the convective heat flux is given by

$$\left(\frac{\xi_{\dot{q}_{conv}}}{\dot{q}_{conv}} \right)^2 = \left(\frac{\xi_{\dot{q}_{elec}}}{\dot{q}_{elec}} \right)^2 + \left(\frac{\xi_{\dot{q}_{rad}}}{\dot{q}_{rad}} \right)^2, \quad (\text{C-5})$$

where \dot{q}_{elec} and its uncertainty are given by

$$\dot{q}_{elec} = \frac{IU}{A}, \quad (\text{C-6})$$

$$\left(\frac{\xi_{\dot{q}_{elec}}}{\dot{q}_{elec}} \right)^2 = \left(\frac{\xi_I}{I} \right)^2 + \left(\frac{\xi_U}{U} \right)^2 + \left(\frac{\xi_A}{A} \right)^2. \quad (\text{C-7})$$

The random error in the current (I), voltage (U) and area (A) are approximately 2% determined by the gauges that were used. The random error in the total heat flux is thus less than 3.5%. The systematic error caused by neglecting the lateral conduction was less than 1%. It was also assumed that the heat flux was generated uniformly over the foil. However, the distributions of the foil temperature were between $25^\circ C$ to $55^\circ C$, the electrical resistivity of the foil was thus not uniform which would lead to uneven heating. The electrical resistivity of 304 stainless steel for different temperature was shown in Fig. C-1. The electrical resistivity varied less than approximately 2.5% due to the temperature difference. The systematic error associated with the uneven heating was less than 2.5%. The uncertainty in the total heat flux, $\xi_{\dot{q}_{elec}} / \dot{q}_{elec}$, was less than 4.5% for 95% confidence interval.

The radiation heat flux, \dot{q}_{rad} , and its uncertainty are given by

$$\dot{q}_{rad} = \varepsilon \sigma (T_w^4 - T_\infty^4), \quad (\text{C-8})$$

$$\left(\frac{\xi_{\dot{q}_{rad}}}{\dot{q}_{rad}} \right)^2 = \frac{(4\varepsilon\sigma T_w^3 \xi_{T_w})^2 + (4\varepsilon\sigma T_\infty^3 \xi_{T_\infty})^2}{\varepsilon^2 \sigma^2 (T_w^4 - T_\infty^4)^2}. \quad (\text{C-9})$$

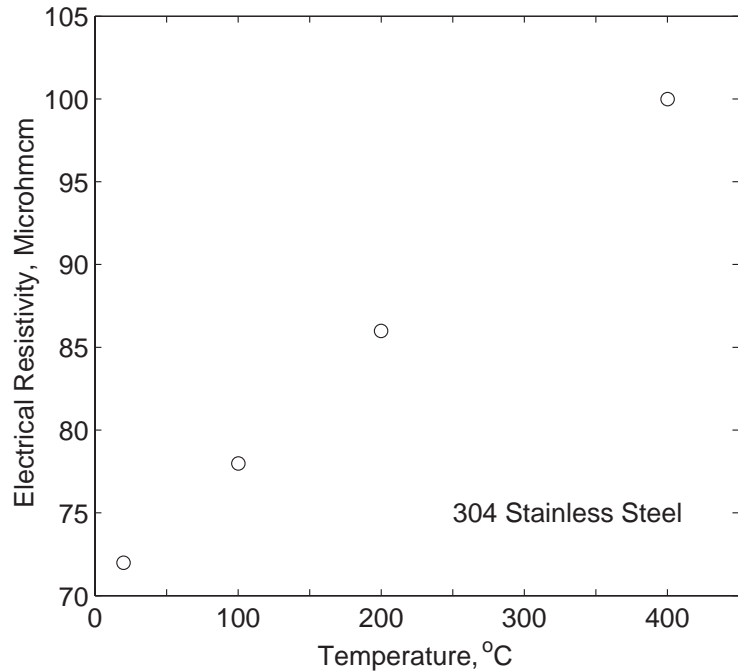


Figure C-1: Electrical resistivity of 304 Stainless steel for different temperatures (Davis, 1996).

The maximum wall temperature, $55^{\circ}C$ was used to evaluate the uncertainty, it was found the uncertainty in the radiation heat flux, $\xi_{\dot{q}_{rad}}/\dot{q}_{rad}$, was less than 1% for 95% confidence interval.

According to equation C-4, the uncertainty for the Stanton number was less than $\pm 7\%$ for 95% confidence interval.

Appendix D: POD analysis of fluctuating wall pressure for an offset attaching jet with $H_s/H_j = 1$

Proper Orthogonal Decomposition (POD) was used to characterize the fluctuating pressure field in region $x/X_r \lesssim 1.7$. The method of using POD to examine the large scale flow structures was reviewed by Berkooz *et al.* (1993). POD is a statistical technique that extracts the information of large scale flow structures from the fluctuating field. It decomposes the fluctuating field into a finite number of empirical orthogonal functions by optimizing energetic features of the flow.

Sixteen equally spaced microphones in the streamwise direction were used in the current investigation. For a stationary flow (that the flow is homogeneous in time), the POD reduces to a harmonic decomposition. It is easiest to first Fourier transform the fluctuating field in time and compute the matrix of single line cross spectra, $\Phi(x, x', f)$. The POD is then applied to the transformed field (Glauser & George, 1992). In the current case where the microphones were located in one dimensional array in the streamwise direction, this is given by

$$\int_{-\infty}^{\infty} \Phi(x, x', f) \psi^{(n)}(x', f) dx' = \lambda^{(n)}(f) \psi^{(n)}(x, f), \quad (\text{D-1})$$

where $\psi^{(n)}(x, f)$ and $\lambda^{(n)}(f)$ are the eigenvector and the eigenspectrum for the n-th mode.

The contribution of the n-th mode to the mean square fluctuations is

$$\varepsilon^{(n)} = \frac{\int_f \lambda^{(n)}(f) df}{\sum_{m=1}^N \int_f \lambda^{(m)}(f) df}, \quad (\text{D-2})$$

where N is the number of total modes that was determined by the amount of sensors. The contribution of the n-th mode to the cross-spectra is given by (Glauser *et al.*, 1987)

$$\Phi^{(n)}(x, x', f) = \lambda^{(n)}(f) \psi^{(n)}(x, f) \psi^{(n)*}(x', f). \quad (\text{D-3})$$

The contents of fluctuating energy in each mode, the eigenspectra for the first 3 energy containing modes and the real part of the eigenvectors for selected frequencies of the first

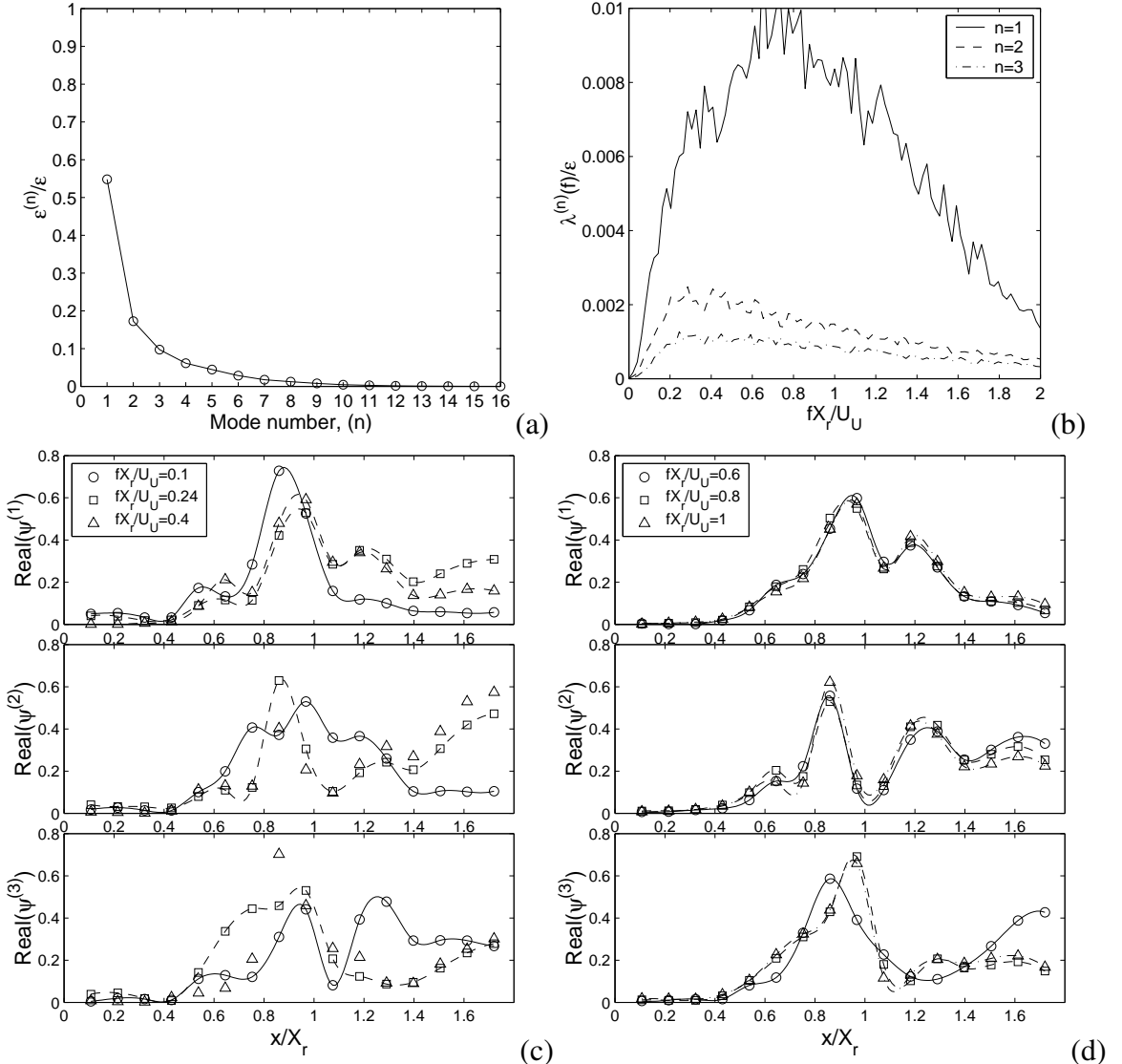


Figure D-1: The (a) modal energy contain $\varepsilon^{(n)}/\varepsilon$, (b) eigenspectra for the first 3 modes, $\lambda^{(n)}/\varepsilon$, and (c) real part of the eigenvectors for selected frequencies for offset jet with $H_s/H_j = 1.0$.

3 modes were shown in Fig. D-1. The first mode contains more than 55% of the total fluctuating energy. The fluctuating energy in mode 1 concentrated in frequency bands of $0.2 \lesssim fX_r/U_U \lesssim 0.4$ and $0.6 \lesssim fX_r/U_U \lesssim 1.0$, while the fluctuations in the second and the third modes are primarily in the low frequency $0.2 \lesssim fX_r/U_U \lesssim 0.4$. The eigenvectors of mode 1 for lower frequency $0.2 \lesssim fX_r/U_U \lesssim 0.4$ were very similar, and the larger frequency $fX_r/U_U \geq 0.6$ were very similar, likely corresponding to the two dominant forms of motions discussed in the main text.